THE UNIVERSITY *of* EDINBURGH

Magneto-Structural Investigations of Calix[*n*]arene-Supported Metal Clusters

Lucinda Wilson

A Thesis Submitted for the Degree of Doctor of Philosophy

School of Chemistry

Faculty of Science and Engineering

The University of Edinburgh

March 2024

For Grandad

Abstract

The synthesis of new molecular magnetic materials is not trivial. Ligand design, reaction conditions and serendipity all contribute to the synthesis of stable, tuneable magnetic molecules with interesting physical properties. Such clusters have been known to display fascinating magnetic behaviour, such as single-molecule magnetism or enhanced magnetocaloric effects. Developing a comprehensive understanding of the structure-property relationships of these molecules proffers one strategy to attaining species with attractive magnetic behaviour. Calix[*n*]arenes are cyclic, usually bowl-shaped, polyphenolic molecules which have been touted as excellent ligand candidates, in part due to their capacity for metal complexation and subsequent cluster formation. The dominant structure-directing role of the calix[*n*]arene also means that, in many cases, analogous structural topologies can be made with different metals and with metals in a variety of oxidation states, allowing detailed magneto-structural studies.

Chapter 1 reviews the coordination chemistry of polymetallic clusters synthesised from *p*-*tert*-butylcalix[4]arene (H_4TBC[4]) in literature. The coordination preferences and assembly behaviours of these clusters show consistent trends, allowing prevailing architectures to be established.

Chapter 2 describes a series of novel polymetallic clusters of nuclearities $\{Mn^{III}_2Mn^{II}_2\}$, $\{Mn^{III}_5Mn^{II}_2\}$, $\{Mn^{III}_4Mn^{II}_6\}$ and $\{Cu^{II}_{16}\}$, which are supported by 2,2'-bis-*p*-*tert*-butyl-calix[4]arene (BisTBC[4], H_8L), where two TBC[4] moieties are linked directly *via* a methylene bridge. Examination of these structures reveals adherence to the coordination bonding rules expected for TBC[4]. Magnetic studies show weak antiferromagnetic exchange between metal ions in most cases, with DFT calculations revealing the importance of both relevant bond parameters and metal oxidation states on the value of *J*.

Chapter 3 reports the synthesis and characterisation of the high-nuclearity truncated octahedron $\{Cu^{II}_{24}\}$ and its $\{Cu^{II}_8\}$ 'building block'. Both are supported by *p*-*tert*-butyl-thiacalix[4]arene (TC[4]A), where the methylene bridges of TBC[4] have been replaced with sulfur, and magnetic studies reveal strong antiferromagnetic exchange interactions. The proclivity of TC[4]A to house M^{II} ions prompted the investigation of mixed-calix[*n*]arene syntheses, yielding clusters $\{Mn^{III}_2Mn^{II}_4\}$ and $\{Mn^{III}_6Mn^{II}_4Cu^{II}_4\}$, supported by TBC[4] and TC[4]A, and $\{Co^{II}_4\}$, supported by TBC[8] and TC[4]A. The favoured metalloligand motifs of

distinct calix[*n*]arenes are upheld giving access to novel architectures, all of which display increased competitive exchange with respect to the homo-calix Cu^{II} clusters.

Chapter 4 builds on the work of the previously yielded TBC[4] clusters, reporting novel clusters of familiar topologies across the 3*d* and 3*d*-4*f* series' ($\{Cu^{II}_9\}$, $\{Cu^{II}_7Gd^{III}_2\}$, $\{Mn^{III}_3Na_6\}$ and the related BisTBC[4]-supported $\{Mn^{III}_6Na_6\}$). Attempts to construct large, high-symmetry TBC[4]-supported clusters by applying high-temperature, high-pressure conditions yielded $\{Fe^{III}_{18}\}$ and $\{Fe^{III}_{28}\}$. Magnetic studies reveal significant spin frustration effects arising from the high-symmetry, and dominant antiferromagnetic behaviour.

Chapter 5 presents the key conclusions and future outlooks derived from the body of this work.

Lay Summary

This thesis uses a family of compounds known as calixarenes to investigate the magnetic properties of metallic molecules. Calixarenes contain a number of oxygen atoms which can bind directly to metal atoms. They are also the correct shape and size to bind many metal atoms together, making an assembly of magnetic metal centres that can communicate magnetically to one another. This can either be accumulative, making highly magnetic structures, or diminishing, where they cancel each other out. In the case of the latter, molecules can also be 'frustrated'; there is no trivial magnetic orientation that will minimise its energy and so they magnetically arrange in non-trivial positions. By changing the calixarene type, the metal type and/or the conditions of the reactions used to combine them, we can access numerous different magnetic species and investigate how their structures influence the properties they exhibit.

Acknowledgements

Firstly, I would like to give a huge thank you to my supervisor, Prof. Euan Brechin, who has been exceptionally generous with his time, wisdom and pub recommendations. Thank you for the endless support, opportunities and encouragement, which have been instrumental in helping me complete this project. I really couldn't have done it, or enjoyed it so much, without you. Ta.

To the Brechin group, old and new. You're an amazing group of people to work with, which is lucky since during the pandemic you're pretty much the only people I saw! Special thanks to Marco for getting me started on my calixarene journey, Alvaro for being the best lab encyclopaedia there is, and Eri, who keeps me going when I want to give up (or gives up with me so we can go get a drink - Κουπα!). Also to Dan, Emily, Angelos, Mukesh, Abhi, Annabel and Yuning, for the games, the pub nights and for putting up with the state of my desk.

I would also like to thank Prof. Scott Dalgarno, for looking at the buckets of crystals I sent your way and always having a crack at them no matter how dodgy they looked, and Dr Gary Nichol, for taking the time for my endless crystal submissions, emails and questions. To Dr Murray Low, I would like to thank you for your support throughout the end of my undergraduate degree and your encouragement at the start of my PhD. I have thoroughly enjoyed my teaching experiences (both delivering and receiving) throughout my studies and a huge part of that is thanks to you.

To all my family, thank you for the love and support over the years. To Mum and Dad, there aren't enough words to thank you for everything you've helped me with, getting me through the tough bits and cheering me on through the good bits. And to Grandma (x2) and Grandad, for being incredible role models and the reasons I wanted to do a PhD here in the first place. Thank you all for showing me Edinburgh.

And lastly to Stefan, who has been there through everything and without whom, this thesis wouldn't have happened. You've cared, encouraged and believed in me endlessly, and I can't thank you enough.

Declaration

I hereby declare that except where specific reference is made to other sources, the work contained in this thesis is the original work of the author. It has been composed by the candidate and has not been submitted, in whole or in part, for any other degree, diploma, or other qualification.

Lucinda Wilson

Table of Contents

Format of Thesis

Each chapter of this thesis is made up of contributions to peer-reviewed papers, which have already been published or submitted for publication. To fulfil the requirements of The University of Edinburgh regarding the publication and submission of a thesis for the degree of PhD, they have been reformatted accordingly.

Chapter 1: Introduction

The coordination chemistry of *p-tert*-butylcalix[4]arene.

Chapter 2: Magneto-structural correlations of bis-calixarene-supported clusters

Structural and magnetic studies of a series of Mn^{II}, Mn^{III} and Cu^{II} clusters supported by bis-calix[4]arene ligand(s).

Chapter 3: Magneto-structural correlations of thiacalix[4]arene-supported clusters

Structural and magnetic studies of a series of homo-calix/mixed-calix clusters supported by thia-calixarene ligand(s).

Chapter 4: Exploring spin frustration in TBC[4]-supported clusters

Structural and magnetic studies of a series of tricapped trigonal $[M_9]$ prisms and high-symmetry Fe^{III} clusters supported by *p-tert*-butylcalix[4]arene ligand(s).

Chapter 5: Conclusions and future perspectives

External collaborator contributions

X-ray crystallography: Prof. Scott Dalgarno (Heriot-Watt University), Dr Laura McCormick McPherson and Prof. Simon Coles (University of Southampton), Dr Simon Teat (Lawrence Berkeley National Laboratory).

EPR measurements: Adam Brookfield, Dr Muralidharan Shanmugam and Prof. Eric McInnes (University of Manchester).

DFT calculations: Reshma Jose, Dr Mukesh Singh and Prof. Gopalan Rajaraman (IIT Bombay).

High-field magnetic measurements: Dr Daniel Cutler and Prof. Hiroyuki Nojiri (Tohoku University).

Magnetic fitting: Prof. Jürgen Schnack (Bielefeld University), Prof. Stergios Piligkos (University of Copenhagen). Where indicated collaborators used bespoke fitting software. All other fitting was performed by the author using PHI v3 software (N. F. Chilton, R. P. Anderson, L.D. Turner, A. Soncini and K. S. Murray, *J. Comput. Chem.*, 2013, **34**, 1164-1175).

Publications

In preparation:

"A stellated cuboctahedron of Fe^{III}"
Lucinda R. B. Wilson, Angelos. B. Canaj, Daniel J. Cutler, Laura J. McCormick McPherson, Simon J. Coles, Hiroyuki Nojiri, Marco Evangelisti, Jürgen Schnack, Scott J. Dalgarno and Euan K. Brechin, *Angew. Chem. Int. Ed.*, 2024, Submitted.

"Calix[4]arene-supported trigonal and square prisms of Mn and Na"
Lucinda R. B. Wilson, Scott J. Dalgarno and Euan K. Brechin, *Dalton Trans.,* 2024, To Be Submitted.

"A $[Cu^{II}_{24}]$ truncated octahedron"
Lucinda R. B. Wilson, Gary S. Nichol, Scott J. Dalgarno and Euan K. Brechin, *Chem. Comm.,* 2024, To Be Submitted.

2024:

"Magnetic exchange, anisotropy and excitonic fluctuations in a $[Ni^{II}_{7}]$ Anderson wheel"
Emily H. Payne, Lucinda R. B. Wilson, Mukesh K. Singh, Gary S. Nichol, J. R. Stewart, V. Garcia-Sakai, R. A. Ewings, Harry Lane, Jürgen Schnack, Chris Stock and Euan K. Brechin, *Inorg. Chem. Front.*, 2024, **11**, 515-525.

2023:

"A bis-calix[4]arene-supported $[Cu^{II}_{16}]$ cage"
Lucinda R. B. Wilson, Marco Coletta, Mukesh K. Singh, Simon J. Teat, Adam Brookfield, Muralidharan Shanmugam, Eric J. L. McInnes, Stergios Piligkos, Scott J. Dalgarno and Euan K. Brechin, *Dalton Trans.*, 2023, **52**, 8956-8963.

2022:

"The coordination chemistry of *p-tert*-butylcalix[4]arene with paramagnetic transition and lanthanide metal ions: an Edinburgh Perspective"
Lucinda R. B. Wilson, Marco Coletta, Marco Evangelisti, Stergios Piligkos, Scott J. Dalgarno and Euan K. Brechin, *Dalton Trans.*, 2022, **51**, 4213-4226.

2021:

"Oxidation state variation in bis-calix[4]arene supported decametallic Mn clusters"
Lucinda R. B. Wilson, Marco Coletta, Reshma Jose, Gopalan Rajaraman, Scott J. Dalgarno and Euan K. Brechin, *Dalton Trans.*, 2021, **50**, 17566-17572.

"$[(V^{IV}O)_2M^{II}_5]$ (M = Ni, Co) Anderson wheels"
Hector W. L. Fraser, Emily H. Payne, Arup Sarkar, Lucinda R. B. Wilson, Dmitri Mitcov, Gary S. Nichol, Gopalan Rajaraman, Stergios Piligkos and Euan K. Brechin, *Dalton Trans*., 2021, **50**, 12495-12501.

Conferences Attended

2023:

- Joseph Black Conference 2023, The University of Edinburgh, UK
  Oral communication

- 6th EaStChem Conference for Early Career Researchers (ECECR), The University of Edinburgh, UK
  Poster presentation

2022:

- 16th International Conference on Calixarenes (Calix 2022), Tulane University, New Orleans, USA
  Poster presentation

- Joseph Black Conference 2022, The University of Edinburgh, UK
  Poster presentation

2021:

- International conference on Molecule-Based Magnets (ICMM), The University of Manchester, UK (Online)
  Poster presentation

- RSC Scottish Dalton Meeting, The University of St Andrews, UK (Online)
  Poster presentation

Awards and Funding

- **HEA (Fellow):** Awarded Fellowship status of the Higher Education Academy
  2024

- **RSC travel grant:** Funding provided to visit Prof. Stergios Piligkos at the University of Copenhagen and be trained in specific magnetic modelling software
  2023

- **Charles Rupert McIntyre PGR Prize, The University of Edinburgh:** Prize rewards research excellence based on research outputs and exchange of knowledge with collaborators and the wider academic community
  2023

- **C David Gutsche Travel Award:** Student engagement prize awarded at Calix 2022
  2022

- **Principal's Career Development Scholarship, The University of Edinburgh:** Teaching-based scholarship awarded to PhD candidates
  2020

Abbreviations

Ac	Alternating current
ASU	Asymmetric unit
BVS	Bond Valence Sums
CSD	Cambridge Structural Database
CW	Curie-Weiss
DFT	Density Functional Theory
Dc	Direct current
JT	Jahn-Teller
LnM	Lanthanide metal
MCE	Magnetocaloric effect
SMM	Single-molecule magnet
TM	Transition metal
VTVB	Variable-temperature-variable-field
ZFS	Zero-field splitting

Ligand abbreviations

H_4C[4]	calix[4]arene
H_4TBC[4]	*p-tert*-butylcalix[4]arene
H_8TBC[8]	*p-tert*-butylcalix[8]arene
H_4TC[4]A	*p-tert*-butylcalix[4]arene
BisTBC[4]	2,2'-bis-*p-tert*-butylcalix[4]arene
Me-deaH_2	*N*-methyldiethanolamine
pdmH_2	pyridine-2,6-dimethanol
hmpH	2-(hydroxymethyl)pyridine

Chapter 1: Introduction

The coordination chemistry of *p*-*tert*-butylcalix[4]arene

1.1 The importance of calix[*n*]arenes

The synthesis of polymetallic clusters involving paramagnetic metal ions is of great synthetic interest. Those that exhibit interesting magnetic behaviour have potential applications in fields such as information storage, magnetic refrigeration and spintronics.[1] Ligand design is key to understanding and controlling the synthesis of these species; a ligand capable of directing cluster formation enables meticulous investigation into structure-property relationships.

Since their synthetic accessibility was developed (chiefly) by Gutsche and co-workers,[2] the *p*-*tert*-butylcalix[*n*]arenes have played a pivotal role in the development of supramolecular chemistry for a multitude of reasons.[3] Examples for this include the fact that different ring sizes deliver disparate cavity shapes and volumes, and synthetic alteration allows one to exploit features such as water solubility whilst utilising the hydrophobic environment presented by the host. Indeed, *p*-*tert*-butylcalix[4]arene (H_4TBC[4], Figure 1.1) is recognised for its incredible versatility as a compound/material. A search for literature concerned with H_4TBC[4] returns over 2500 hits, clearly showing that this molecule has found utility across many different settings. This is due, in part, to its ability to form self-assembled supramolecular structures,[4–6] its vast potential for functionalisation at both the upper- and lower-rims,[2] and its proclivity to form polynuclear metal clusters that display interesting magnetic properties.[7] A comparatively recent and noteworthy development in H_4TBC[4] chemistry, and one that demonstrates its true versatility, is that it sublimes to form a

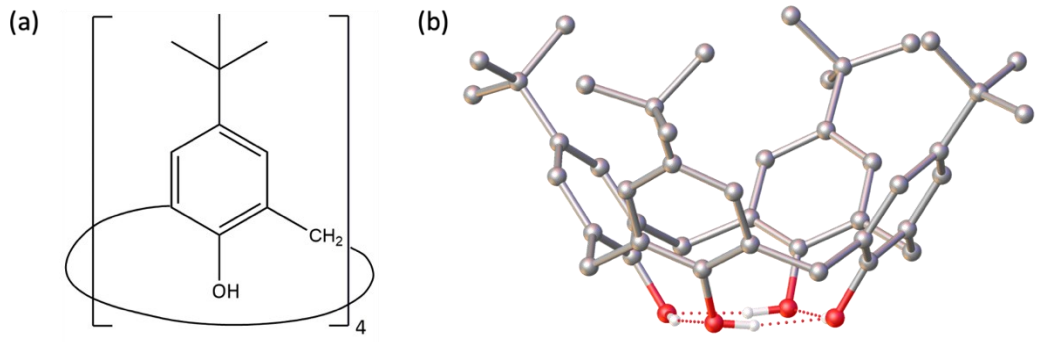

Figure 1.1 The chemical structure (a) and single-crystal X-ray structure (b) of H_4TBC[4], where the dashed lines represent hydrogen bonding.[7] Colour code: C- grey, O - red, H - white.

seemingly non-porous organic solid as shown in Figure 1.2.[8,9] Atwood, Barbour and co-workers found that sublimation under reduced pressure afforded a guest-free offset dimer, a low-density kinetic form, in which the constituent H_4TBC[4] molecules assemble within a bilayer (Figure 1.2) akin to many of its solvates.[10–12] Inspection of the space-filling representation of the low-density form shows the structure to be non-porous, yet gas molecules (O_2, N_2, CO_2) are capable of travelling through the material, coming to rest in the host cavities within the bilayer, and allowing for purification of H_2 from gas mixtures, for example.[9] This led to other related studies with the larger H_5TBC[5],[13] and to a general understanding of how such cavity-containing molecules behave in the organic solid state, which is of particular interest for gas storage applications.

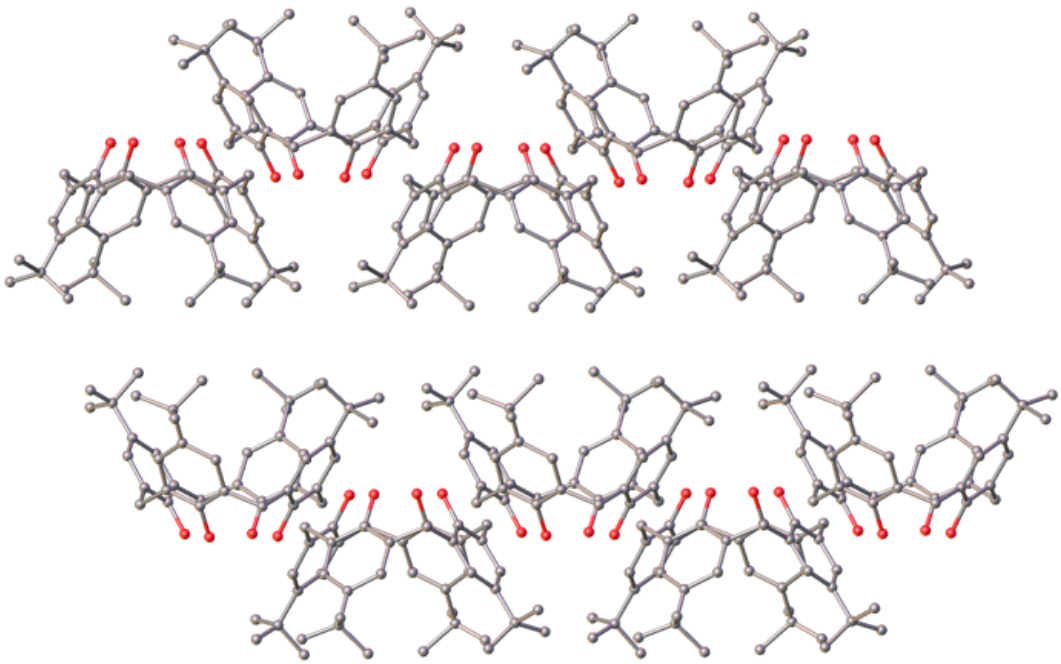

Figure 1.2 The offset dimer found in the low-density kinetic form of H_4TBC[4], assembled within an alternating bilayer.[8] Colour code: C - grey, O - red. H atoms omitted for clarity.

1.2 TBC[4]-supported polymetallic clusters of paramagnetic ions

Brechin, Dalgarno and co-workers began working on the coordination of H_4TBC[4] with paramagnetic transition metal (TM) and lanthanide metal (LnM) ions in 2008. As a ligand, H_4TBC[4] presented (i) ideal chemical functionality through the tetraphenolic lower-rim which is predisposed for metal ion binding, (ii) a well-understood structural platform with a structurally directing shape for crystal engineering, (iii) a highly soluble compound when deprotonated under ambient conditions, and (iv) a molecule that would structurally isolate or 'dilute' paramagnetic clusters in the solid state. Furthermore, noting that many air-sensitive TBC[4]-supported coordination compounds have previously been synthesised (but are beyond the scope for inclusion here), it was anticipated that this platform would afford air-stable species.

1.2.1 Homometallic clusters

The first use of H_4TBC[4] to isolate a large nuclearity cluster containing paramagnetic ions was in 2008, with the publication of the complex (cation)[$V^{III}V^{IV}_5O_6(OMe)_8$(TBC[4])(MeOH)] (**1**, cat = Et_4N^+, NH_4^+, pyridinium, Et_3NH^+).[14] This was made with the specific intention of examining magnetic properties. Complex **1** (Figure 1.3) is made *via* the solvothermal reaction

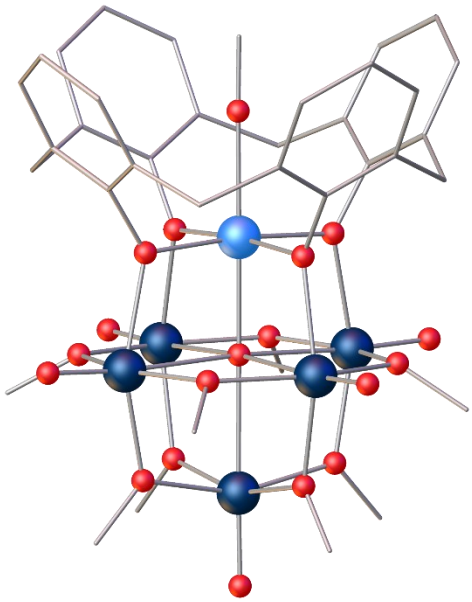

Figure 1.3 The molecular structure of the anion of complex **1**.[14] Colour code: V^{IV} - dark blue, V^{III} - light blue, C - grey, O - red. H atoms and ^{t}Bu groups omitted for clarity.

of $VOSO_4$ and H_4TBC[4] in a basic MeOH solution under anaerobic conditions. Its metallic skeleton describes a mixed-valent [$V^{III}V^{IV}_5$] octahedron, and its metal-oxygen core a [$V^{III}V^{IV}_5O_{19}$] Lindqvist-like polyoxovanadate, with the sole μ_5-TBC[4] ligand capping the V^{III} vertex and further bridging to four V^{IV} ions. Magnetic susceptibility and magnetisation measurements, combined with DFT calculations, suggested the presence of weak ferromagnetic exchange between the V^{III}-V^{IV} ions and stronger antiferromagnetic exchange between the V^{IV}-V^{IV} ions. An analogue of **1** can be made *via* sequential oxidation and reduction of hexavanadate ($[V_6O_{13}]^{2-}$) to yield [^{n}Bu$_4$N][$V^{III}V^{IV}_5O_6$(OMe)$_8$(TBC[4])(MeCN)] (**1a**). This complex exhibited improved solubility in polar organic solvents, rendering it compatible for small molecule activation studies by which [^{n}Bu$_4$N][$V^{IV}_5V^{V}O_7$(OMe)$_8$(TBC[4])] (**1b**), [($V^{IV}_4V^{V}_2O_7$(OMe)(TBC[4])] (**1c**) and [$V^{III}V^{IV}_4V^{V}O_6$(OMe)$_8$(OP(Me)$_2$Ph)] (**1d**) were obtained.[15,16]

This was a very encouraging result, showcasing the potential of H_4TBC[4] as a ligand for the construction of paramagnetic TM clusters of variable oxidation states. From a synthetic viewpoint one can consider the [V^{III}(TBC[4])]$^{1-}$ unit in **1**, for example, as a metalloligand generated *in situ*, which bridges to further metal moieties *via* the deprotonated phenolic O-atoms, in this case the [$(V^{IV}O)_5O$(OMe)$_8$] fragment. In turn, this suggests that the *in situ* formation of analogous [TM/LnM(TBC[4])]$^{n+/-}$ metalloligands would be a profitable route for the self-assembly of a breadth of homo- and heteronuclear 3*d*/4*f* complexes. Ligand design is key in molecular magnetism since, in most cases it dictates, or at least influences, cluster topology, metal ion geometries and bond lengths and bond angles – the key structural features describing the way metal ions interact with one another. Whilst initial reactions with any flexible ligand, *i.e.* one that has the ability to coordinate in different ways, produces clusters with structures that cannot be fully predicted, the construction of even small families of polymetallic cages allows identification of the key building blocks. It is at this point the synthetic chemist can influence structure and the resultant physical properties through judicious changes to reaction conditions. Therefrom, characterisation of multiple family members allows for the development of quantitative magneto-structural correlations and for the exploitation of those properties for specific applications.

The tetraphenolic lower rim of H_4TBC[4] would appear to be an ideal host for Jahn-Teller (JT) distorted octahedral TM ions such as Mn^{III} and Cu^{II} whose preference is for four short equatorial bonds and two long axial bonds, and for the oxophilic LnM ions. The ability of Mn to commonly exist in three different oxidation states (Mn^{II}, Mn^{III} and Mn^{IV}) in polymetallic

clusters, and the structural variability this affords, also offers an ideal playground for developing magneto-structural relationships. Reaction of $MnX_2 \cdot 4H_2O$ (X = Cl, Br) and H_4TBC[4] in a basic dmf/MeOH solution affords a mixed-valent cluster of formula $[Mn^{III}_2Mn^{II}_2(OH)_2(TBC[4])_2(dmf)_6]$, (**2**, Figure 1.4).[7,17] The base-assisted aerial oxidation of the Mn^{II} ions is immediately evident upon a colour change from pale pink to deep purple. The complex comprises a planar diamond or butterfly-like $[Mn^{III}_2Mn^{II}_2(\mu_3\text{-}OH)_2]$ core in which the wings are Mn^{III} ions and the body is Mn^{II} ions. This is a common structural type in Mn chemistry (and TM^{III} chemistry in general), but the oxidation state distribution observed in **2** is rather unusual, being reversed from the norm, in which the body ions are almost always +3.[18,19] The Mn^{III} ions in **2** are in distorted octahedral geometries, with the JT axes defined by the O_{dmf}-Mn-OH vector. The four equatorial coordination sites are occupied by the O-atoms of the TBC[4] ligand, two of which bridge in a μ-fashion to the central Mn^{II} ions. These moieties are connected to each other and to the Mn^{II} ions by two centrally located $\mu_3\text{-}OH^-$ ions. The remaining equatorial sites on the Mn^{II} ions are occupied by dmf ligands. An alternative description of **2** is two $[Mn^{III}(TBC[4])]^{1-}$ metalloligands encapsulating a $[Mn^{II}_2(OH)_2(dmf)_4]^{2+}$ fragment. The extended structure of **2** shows a bilayer type arrangement that is similar to that observed for the dmf solvate of H_4TBC[4], in which each H_4TBC[4] cavity lies opposite ^{t}Bu groups from a neighbouring bilayer.

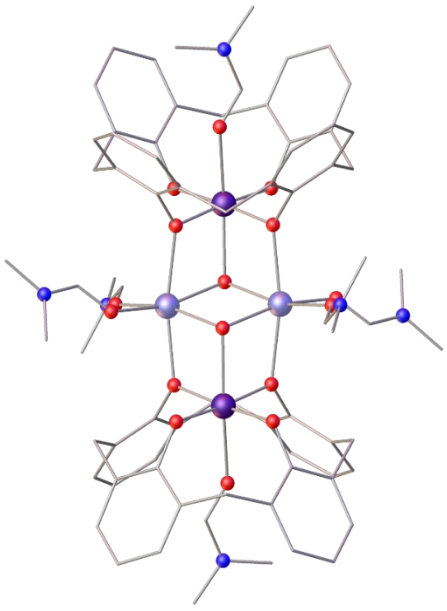

Figure 1.4 The molecular structure of complex **2**.[7] Colour code: Mn^{III} - dark purple, Mn^{II} - light purple, C - grey, O - red, N - blue. H atoms and ^{t}Bu groups omitted for clarity.

Several analogues of **2** can be made by either changing the solvent bonded to the Mn^{II} ions, *e.g.* $[Mn^{III}_2Mn^{II}_2(OH)_2(TBC[4])_2(dmf)_4(H_2O)_2]$ (**2a**), $[Mn^{III}_2Mn^{II}_2(OH)_2(TBC[4])_2(dmf)_4(EtOH)(H_2O)]$ (**2b**), $[Mn^{III}_2Mn^{II}_2(OH)_2(TBC[4])_2(dmso)_6]$ (**2c**), or by swapping out the $H_4TBC[4]$ for the non-butylated $H_4C[4]$, *e.g.* $[Mn^{III}_2Mn^{II}_2(OH)_2(C[4])_2(MeOH)_6]$ (**2d**). The coordinated solvent can also be replaced with bidentate chelates such as 2,2'-bipyridine, $[Mn^{III}_2Mn^{II}_2(OH)_2(TBC[4])_2(bpy)_2]$ (**2e**) or linear linkers such as 4,4'-bipyridine to form chains of butterflies, *e.g.* $[Mn^{III}_2Mn^{II}_2(OH)_2(TBC[4])_2(bpy)_2]_n$ (**2f**) whose magnetic properties are analogous to **2**.[20]

Perhaps more interesting is the ability to sequentially swap out the body Mn^{II} ions in **2** for LnM^{III} ions. Reaction of $Mn(NO_3)_2{\cdot}4H_2O$, $LnM(NO_3)_3{\cdot}6H_2O$ and $H_4TBC[4]$ in a basic dmso/EtOH solution, followed by slow diffusion with MeCN, affords a family of complexes of general formula $[Mn^{III}_2Mn^{II}LnM^{III}(OH)_2(TBC[4])_2(NO_3)(solvent)_6]$, **3** (LnM = Y (**3a**), Gd (**3b**), Tb (**3c**), Dy (**3d**), Ho (**3e**)).[21] Alternatively a dmf/EtOH solvent combination followed by slow diffusion with ^{i}PrOH produces $[Mn^{III}_2Mn^{II}LnM^{III}(OH)_2(TBC[4])_2(NO_3)(dmf)_4(^{i}PrOH)_2]$, **4** (LnM = Gd (**4a**), Dy (**4b**)). Complex **3b** (Figure 1.5) contains a butterfly-like $[Mn^{III}_2Mn^{II}Gd^{III}(OH)_2]$ core that is entirely analogous to that of **2** but with one Mn^{II} ion replaced with a Gd^{III} ion. The Gd^{III} ion

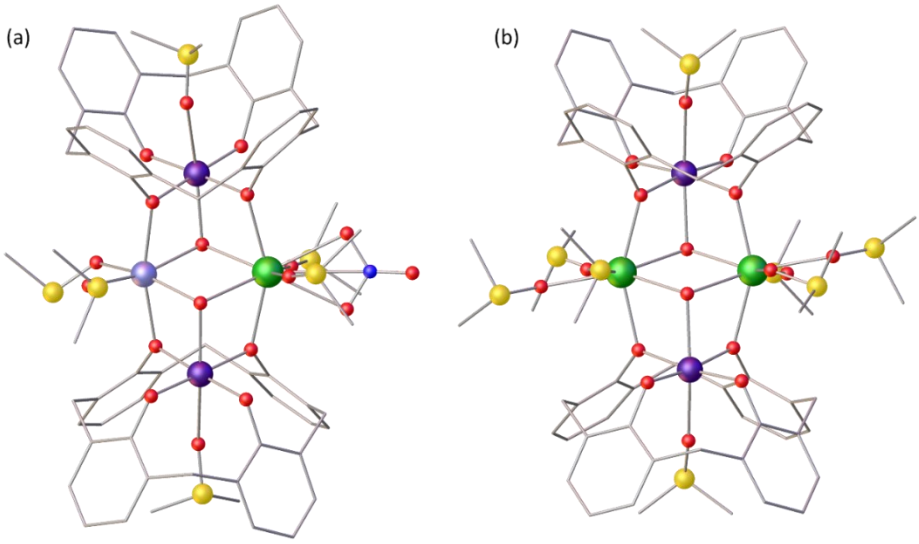

Figure 1.5 The molecular structure of complex **3b** (a) and the cation of **5b** (b).[21] Colour code: Mn^{III} - dark purple, Mn^{II} - light purple, Gd^{III} - green, S - yellow, N - blue, C - grey, O - red. H atoms and ^{t}Bu groups omitted for clarity.

sits in a distorted square antiprismatic geometry with its coordination sphere completed by two dmso molecules, a bidentate NO_3^- anion, and two μ_3-OH^- ions. The latter connect the Mn^{III}-LnM^{III} (wing-body) and LnM^{III}-LnM^{III} (body-body) ions, whilst the NO_3^- anion ensures the charge balance is maintained following the introduction of the LnM^{III} cation. A comparison of the structures **2** and **3**/**4** shows that the presence of the larger LnM ion skews the relative orientation of the two TBC[4] ligands. Thus, in **2** the TBC[4] ligands are co-planar, whereas in **3**/**4** they present a more clamshell-like appearance with the two O_4 planes forming an angle of ~7° with respect to one another. There is also a marked change in the angles found between the constituent metal centres upon moving from **2** to **3**/**4**, and the $Mn^{III}\cdots Mn^{III}$ distance increases from ~5.7 to ~5.8 Å.

A second type of butterfly can be selectively isolated by employing different reaction conditions, where the use of the dmso/MeOH solvent combination is key.[21] Thus, the reaction of $MnCl_2{\cdot}4H_2O$, $LnMCl_3{\cdot}6H_2O$ and H_4TBC[4] in a basic dmso/MeOH solution, followed by slow diffusion with ^{i}PrOH vapour, affords the isostructural series $[Mn^{III}_2LnM^{III}_2(OH)_2(TBC[4])_2(dmso)_8]Cl_2$, **5** (LnM = Y (**5a**), Gd (**5b**), Tb (**5c**), Dy (**5d**), Ho (**5e**)). The metallic skeleton in **5** (Figure 1.5) is related to **2** through the exchange of both Mn^{II} ions for LnM^{III} ions. In the main, the structures of **3**/**4** and **5** are analogous, with the only major difference being in the coordination number and geometry of the LnM^{III} ions. In **5**, the LnM^{III} ions are seven coordinate and in distorted pentagonal bipyramidal geometries, possessing three terminally bonded dmso ligands. The introduction of two LnM^{III} ions has re-introduced a co-planar arrangement of the O_4 planes of the TBC[4]s, and the $Mn^{III}\cdots Mn^{III}$ distance shows a further increase from ~5.8 to ~5.9 Å. Complex **5** is cationic, with Cl^- counter ions maintaining charge balance. Examination of the extended structures in **3**-**5** reveals assembly into a bilayer arrangement akin to that in **2** and H_4TBC[4] solvents. The ability to change almost every aspect of the structure of **2** - only the central μ_3-OH ions remain in **3**-**5** – points towards the exceptional structural stability of this motif, and the dominant role played by TBC[4] in structure formation.

The exchange of Mn^{II} ions for Gd^{III} in **2**-**5** provides the perfect opportunity to study both the relative importance of the nature and magnitude of exchange on the overall magnetic properties of the complexes, and the transferability of spin-Hamiltonian parameters between complexes, which provides additional confidence in their reliable determination. The direct current (dc) molar magnetic susceptibilities (in the form of their χT products) and variable-

temperature-variable-field (VTVB) magnetisation (*M*) data of complexes **2**, **3b** and **5b** are shown in Figure 1.6. From inspection of the χT data it is clear that increasing Gd^{III} content decreases the magnitude of the exchange, as one might expect from the replacement of magnetic *d*-orbitals with magnetic *f*-orbitals. In addition, the magnetisation of **2** displays notable nesting of isofield lines, indicative of significant magnetic anisotropy, which appears larger than that observed for **3b** and **5b** in turn. The data for the three complexes were fitted simultaneously using spin-Hamiltonian (1.1) with the exchange coupling scheme shown in the insets of Figure 1.6, where the summation indices *i, j* run through the constitutive metal centres, *D* is the uniaxial single-ion anisotropy parameter for Mn^{III}, $\hat{S}$ is a spin operator, *S* is the total spin, μ_B is the Bohr magneton, and *J* is the isotropic exchange interaction parameter.

$$\widehat{H} = \sum_i D_i\left(\hat{S}_{z,i}^2 - S_i(S_i+1)/3\right) + \mu_B B \sum_i g_i \hat{S}_i - 2\sum_{i,j<1} J_{i,j}\hat{S}_i \cdot \hat{S}_j \qquad (1.1)$$

This results in the best-fit parameters $J_{MnII\text{-}MnIII}$ = +0.893 cm^{-1}, $J_{MnII\text{-}MnII}$ = -0.909 cm^{-1}, $J_{MnIII\text{-}GdIII}$ = +0.075 cm^{-1}, $J_{MnII\text{-}GdIII}$ = -0.164 cm^{-1}, $J_{GdIII\text{-}GdIII}$ = -0.006 cm^{-1} and D_{MnIII} = -4.219 cm^{-1}, with all *g*-factors fixed to *g* = 2.00. Thus, the Mn^{II}-Mn^{III} interaction is ferromagnetic, the Mn^{II}-Mn^{II} interaction is antiferromagnetic, the Mn^{III}-Gd^{III} interaction is weakly ferromagnetic, the Mn^{II}-Gd^{III} interaction is weakly antiferromagnetic and the Gd^{III}-Gd^{III} interaction is very weakly antiferromagnetic/paramagnetic. With these parameters, the spin ground state of **2**, when only the isotropic part of spin-Hamiltonian (1.1) is considered, is *S* = 7 with numerous low-lying excited spin-states present (80 in the first 20 cm^{-1}) due to the weak exchange (Figure 1.7). These are significantly admixed, permitting numerous thermal relaxation pathways for magnetisation relaxation. This is manifested in the dynamic susceptibility measurements where out-of-phase (χ") alternating current (ac) susceptibility signals are only observed at the highest frequencies (1000 Hz) and lowest temperatures (1.8 K) investigated.[21]

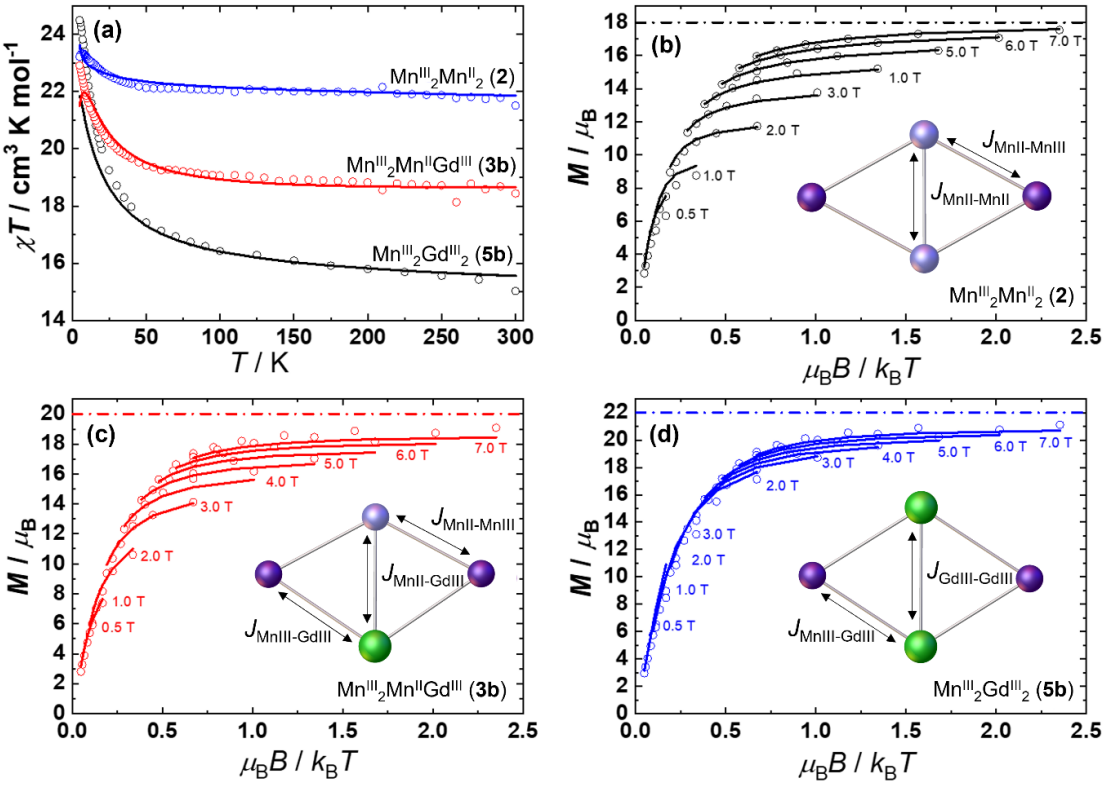

Figure 1.6 (a) χT products for complexes **2** ($[Mn^{III}_2Mn^{II}_2]$), **3b** ($[Mn^{III}_2Mn^{II}Gd^{III}]$) and **5b** ($[Mn^{III}_2Gd^{III}_2]$) measured with B = 0.1 T in the indicated temperature range. (b-d) VTVB magnetisation data plotted against $\mu_B B/k_B T$. The dotted lines show the saturation magnetic moment expected for a ferromagnetic ground state. Solid lines are a simultaneous fit of all the experimental data to spin-Hamiltonian (1.1), with each exchange coupling scheme shown in the respective inset.[21] Colour code: Mn^{III} - dark purple, Mn^{II} - light purple, Gd^{III} - green.

For **3b**, the ground state spin of the isotropic part of spin-Hamiltonian (1.1), is an S = 3 state, and for **5b** it is the ferromagnetic S = 11 state (Figure 1.7). In both cases, the ground states again lie in very close proximity to several excited spin states. In **3b** many more eigenstates (200) are located in the same energy window (20 cm^{-1}), and for **5b** approximately 200 eigenstates are located within just the first 5 cm^{-1}. This of course is a direct consequence of the very weak exchange mediated by the Gd^{III} ions. As we move from **2** to **3b** to **5b** we remove two and four ferromagnetic exchange interactions (Mn^{III}-Mn^{II}), which in the context of this molecule are relatively strong interactions and replace them with two (**3b**) and four (**5b**) very weak ferromagnetic interactions that are more than an order of magnitude smaller. We also replace the antiferromagnetic Mn^{II}-Mn^{II} interaction with the weaker antiferromagnetic Mn^{II}-

Gd^{III} interaction and yet weaker antiferromagnetic Gd^{III}-Gd^{III} exchange. The result is the presence of many more magnetisation relaxation pathways, as reflected in the appearance of diminishing signals (**2** > **3b** > **5b**) in out-of-phase ac susceptibility measurements. Indeed, no χ" component is observed for **5b**.[21]

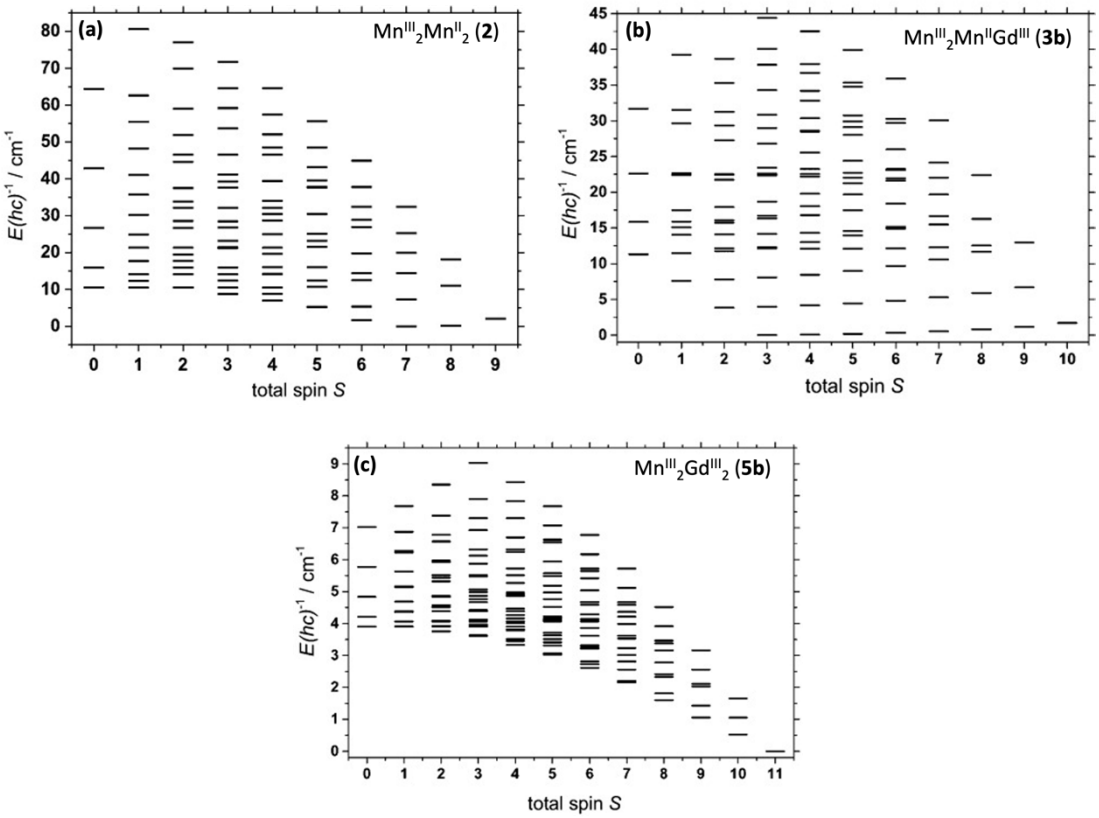

Figure 1.7 The energy spectra of **2** (a), **3b** (b) and **5b** (c) at zero magnetic field for the isotropic (1.1) with the best-fit parameters described in the text.[21]

Inclusion of the anisotropic Tb^{III} and Dy^{III} ions in the form of complexes **3c** ([Mn_3Tb]), **3d** ([Mn_3Dy]), **5c** ([Mn_2Tb_2]) and **5d** ([Mn_2Dy_2]) introduces an antiferromagnetic Dy/Tb-Mn^{III} interaction. Interestingly, this has little or no effect upon the out-of-phase ac susceptibility signals for [Mn_3LnM], the tails of the same frequency χ" component shifting to slightly lower temperatures, albeit with a larger magnitude. This trend continues to the [Mn_2LnM_2] family where the Tb analogue displays a much-diminished χ" signal and where the Dy species shows no out-of-phase component at all. Thus, it can be concluded that it is the exchange between the metal ions that is the prerequisite for observing single-molecule magnet (SMM)

behaviour at higher temperatures. Indeed, the butterfly topology ensures a move away from an exchange-coupled molecule towards a paramagnet with increasing LnM encapsulation.

The self-assembly of [Mn_4] (**2**) can be perturbed through the use of (competing) co-ligands. For example, the use of phosphinates allows for the transformation of the butterfly into an unusual [$Mn^{III}Mn^{II}]_2$ dimer of dimers.[22] Addition of sodium phenylphosphinate to the reaction mixture used to form **2** affords [$Mn^{III}Mn^{II}$(TBC[4])(O_2P(H)Ph)$(dmf)_2(MeOH)_2]_2$ (**6**) (Figure 1.8a), which is best described as consisting of two [$Mn^{III}Mn^{II}$] moieties held together by two bridging phosphinate ligands. In effect, complex **6** is an elongated version of complex **2** in which the two μ_3-OH^- ions have been replaced with two much larger μ_3-bridging phosphinates. The magnetic core of **6** thus consists of two [Mn^{III}-$(\mu$-O$)_2$-Mn^{II}] dimers linked *via* two three-atom O-P-O bridges. The remaining coordination sites on the Mn^{II} ions are filled by a combination of dmf and MeOH molecules, the latter of which are H-bonded to two of the monodentate TBC[4] O-atoms. In the extended structure, molecules of **6** pack in the familiar bilayer array seen for **2** and H_4TBC[4] solvates. Magnetic susceptibility measurements are consistent with those observed for **2** showing competing ferro- (Mn^{III}-Mn^{II}) and

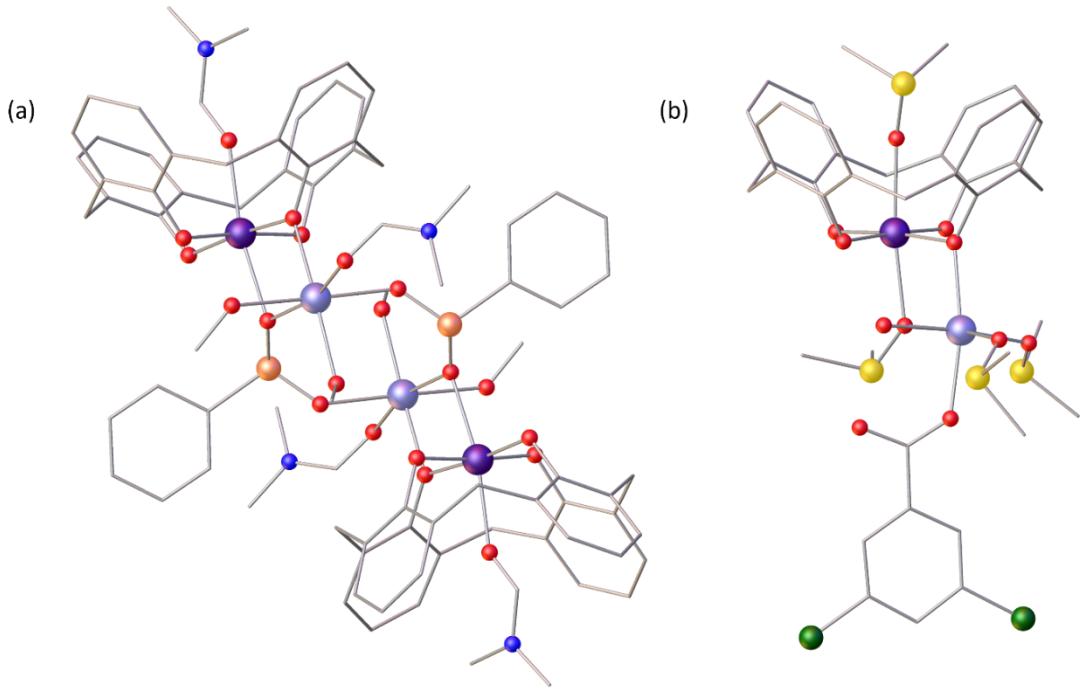

Figure 1.8 The molecular structure of complex **6** (a)[22] and complex **7** (b).[23] Colour code: Mn^{III} - dark purple, Mn^{II} - light purple, Cl - dark green, P - pale orange, S - yellow, N - blue, C - grey, O - red. H atoms and ^{t}Bu groups omitted for clarity.

antiferromagnetic (Mn^{II}-Mn^{II}) exchange interactions, $J_{MnIII\text{-}MnII}$ = +5.14 cm^{-1} and $J_{MnII\text{-}MnII}$ = -8.47 cm^{-1}. In an isotropic model, the spin ground state of complex **6** is an S = 6 state with multiple low-lying excited states.[22]

The [Mn_4] butterfly can be completely split into its respective dimers through the use of carboxylate co-ligands in place of phosphinates. Reaction of $MnCl_2{\cdot}4H_2O$ with H_4TBC[4] and Na(dcb) (dcbH = sodium 3,5-dichlorobenzoate) in a basic dmso solution affords [$Mn^{III}Mn^{II}$(TBC[4])(dcb)(μ-dmso)(dmso)$_3$(H_2O)] (**7**) (Figure 1.8b).[23] From inspection of Figure 1.8, it is clear that **7** resembles one half of the 'parent' molecule **2**, but where the terminally bonded dcb ligand blocks the dimerisation. Rather unusually the Mn^{III} and Mn^{II} ions are connected by a μ-dmso ligand as well as the phenolic O-atom from TBC[4]. The remaining sites on the Mn^{II} ion are occupied by terminally coordinated dmso molecules. Analysis of the extended structure shows that the molecules pack in a head-to-head bilayer akin to the packing found in H_4TBC[4] solvates. The carboxylates interdigitate between the cavities of the TBC[4] moieties of symmetry equivalents of **7** within each layer, forming alternating up-down chain type assemblies along the *c*-axis. Closer inspections reveals that individual layers are bridged by halogen···halogen interactions between the symmetry equivalent molecules, with two crystallographically unique Cl···Cl distances of ~3.3 and ~4.2 Å.[23]

Magnetic studies reveal the expected weak ferromagnetic exchange between the Mn^{III}-Mn^{II} ions in the dimer, consistent with that seen for **2**-**4** and **6**. The magnetic susceptibility and magnetisation data of **7** were simultaneously fitted to spin-Hamiltonian (1.1) affording the best-fit parameters $J_{MnIII\text{-}MnII}$ = +0.38 cm^{-1} and D_{MnIII} = -3.34 cm^{-1} with g = 2.00. Complex **7** does display frequency-dependent out-of-phase (χ") signals in ac susceptibility measurements performed in the 1.8-10 K range in zero applied dc field and a 3.5 G ac field oscillating in the 50-1000 Hz frequency range suggestive of SMM behaviour, but no peaks were observed down to 1.8 K.[23]

A complementary co-ligand for H_4TBC[4] in Mn chemistry is 2-(hydroxymethyl)pyridine (hmpH). Typically, hmp^- acts as a μ-bridge, chelating to one Mn centre through N- and O-atoms and bridging to the second metal *via* the alkoxide. This is nicely illustrated in the complex [$Mn^{III}_2Mn^{II}_2$(hmp)$_6$$Br_2$($H_2O$)$_2$]$^{2+}$ whose metal-oxygen butterfly core is identical to **2** but with the oxidation state distribution reversed, *i.e.* Mn^{II} ions in the wings and Mn^{III} ions in the body.[18,24] In this topology the exchange interactions are all ferromagnetic, leading to an S

= 9 ground state. The two cluster ligand moieties/building blocks should therefore be complementary, and we reasoned that their simple addition should result in the self-assembly of a structurally related complex. Indeed, the reaction of $MnCl_2 \cdot 4H_2O$, H_4TBC[4] and hmpH in a basic dmf/EtOH mixtures produces $[Mn^{III}_3Mn^{II}_2(OH)_2(TBC[4])_2(hmp)_2(dmf)_6](H_3TBC[4])$ (**8**) (Figure 1.9).[25]

The metallic skeleton of **8** describes two vertex-sharing $[Mn^{III}_2Mn^{II}]$ triangles. The two μ_3-OH ions lie at the centre of these triangles, but not in the same plane and thus perhaps a more accurate description of the $[Mn^{III}_2Mn^{II}(OH)]$ moiety is that of a partial cubane. The TBC[4] ligands are fully deprotonated and each house a Mn^{III} ion in the centre of their phenolic pocket with two O-atoms terminally coordinated and two bridging to the other Mn ions in the partial cubane. The hmp ions chelate to the Mn^{II} ions and use their alkoxide arm to bridge to the central Mn^{III} ion. All the Mn ions are six-coordinate, the remaining coordination sites being filled with dmf molecules. The μ_3-OH ions are H-bonded to the terminally bonded O-atoms of the TBC[4] ligands, with the latter also H-bonded to H_2O molecules of crystallisation. Charge balance is maintained through the presence of one $(H_3TBC[4])^{1-}$ anion per Mn_5 cluster. The presence of this anion, which crystallises orthogonal to the cation, prevents the formation of the expected bilayer array.

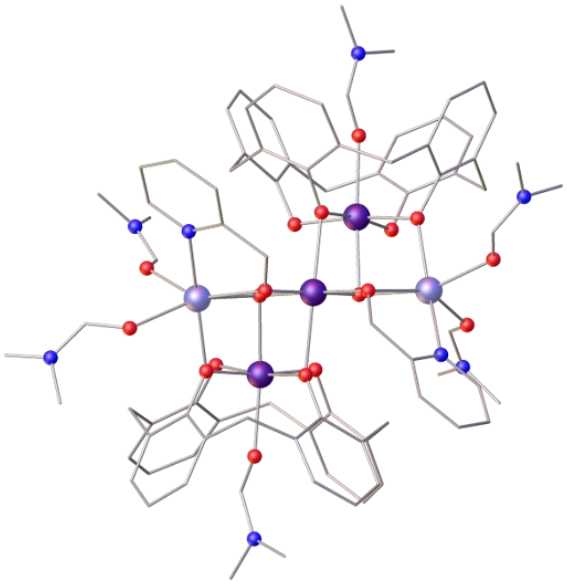

Figure 1.9 The molecular structure of the metallic cluster cation of complex **8**.[25] Colour code: Mn^{III} - dark purple, Mn^{II} - light purple, N - blue, C - grey, O - red. H atoms and ^{t}Bu groups omitted for clarity.

A simultaneous fit of the magnetic susceptibility and magnetisation data of **8** to the full spin-Hamiltonian (1.1) reveals ferromagnetic exchange between nearest neighbours (Figure 1.10), $J_{MnIII\text{-}MnII}$ = +0.348 cm^{-1}, $J_{MnIII\text{-}MnIII}$ = +2.553 cm^{-1}, D_{MnIII} = -2.111 cm^{-1} with a g fixed at g = 2.00. Considering just the isotropic parameters, this leads to a spin ground state S = 11. The nature and magnitude of the exchange interactions found resembles those observed for both **2** and $[Mn^{III}_2Mn^{II}_2(hmp)_6Br_2(H_2O)_2]^{2+}$.[24] Ac susceptibility studies in the 1.8-10.0 K range in a 3.5 G field oscillating at frequencies up to 1000 Hz display frequency-dependent out-of-phase signals indicative of SMM behaviour. An Arrhenius plot constructed from these data affords U_{eff} = 42 K with τ_0 = 1.125 x 10^{-10} s.[25]

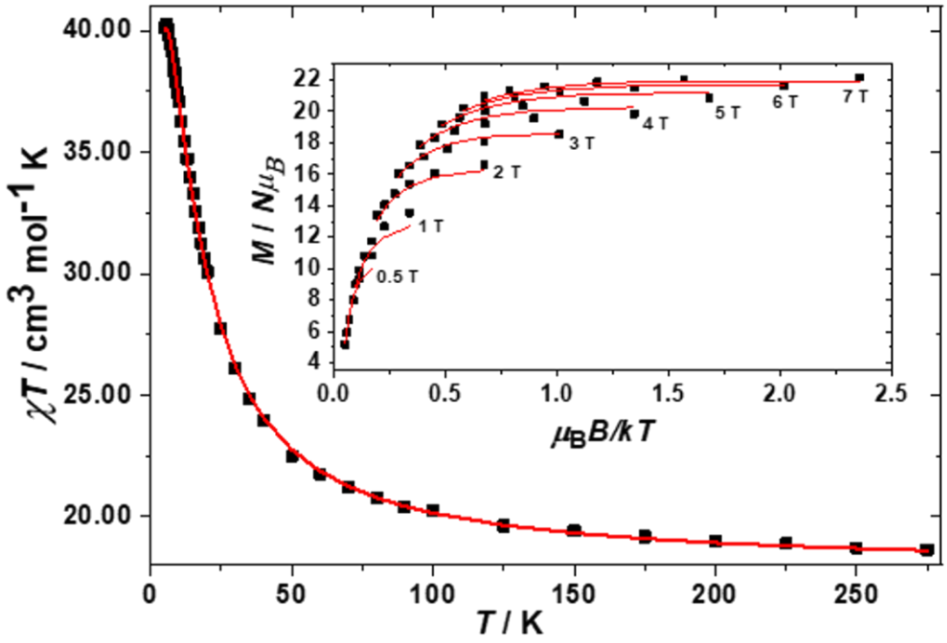

Figure 1.10 Plot of the χT product of **8** *vs* T in the 275 - 5 K temperature range in an applied field of B = 0.1 T. Inset: Plot of reduced magnetisation in the 2.0 to 7.0 K T range at the indicated field strengths. The solid red lines are the best fit of the experimental data to spin-Hamiltonian (1.1).[25]

Phosphinates and alkoxides such as hmpH work very well as co-ligands in Mn-TBC[4] chemistry because they have been successfully employed as the primary bridging ligands in Mn chemistry in their own right and can therefore compete with H_4TBC[4]. Another very good example that fits into this category are the phenolic oximes (Scheme 1.1), that have previously been employed to make a variety of cages, including $[Mn^{III}_3]$ and $[Mn^{III}_6]$ SMMs.[26–

[28] The general phenolic oxime skeleton can be readily altered at various positions *via* the formal substitution of either aromatic or oximic H-atoms for aliphatic or aromatic substituents.

The ten ligands shown in Scheme 1.1 were synthesised and used to construct a family of eight octametallic $[Mn^{III}_7Mn^{II}]$ (**9**) clusters (Figure 1.11).[29] Reaction of H_4TBC[4] with ligands $H_2\mathbf{L}^{\mathbf{IV\text{-}VII}}$ and either $MnCl_2{\cdot}4H_2O$ or $Mn(NO_3)_2{\cdot}4H_2O$ in a basic dmf/MeOH solvent mixture results in formation of $[Mn^{III}_7Mn^{II}(TBC[4])_2(\mathbf{L}^{\mathbf{IV}})_3(\mu_4\text{-}O)_2(\mu_3\text{-}O)(\mu\text{-}OMe)_2(\mu\text{-}OH)(dmf)_2(H_2O)_2]$ (**9a**), $[Mn^{III}_7Mn^{II}(TBC[4])_2(\mathbf{L}^{\mathbf{V}})_3(\mu_4\text{-}O)_2(\mu_3\text{-}O)(\mu\text{-}OMe)_3(dmf)_2(H_2O)(MeOH)]$ (**9b**), $[Mn^{III}_7Mn^{II}(TBC[4])_2(\mathbf{L}^{\mathbf{VI}})_3(\mu_4\text{-}O)_2(\mu_3\text{-}O)(\mu\text{-}OMe)_3(dmf)_2(H_2O)_{0.5}(MeOH)_{1.5}]$ (**9c**) and $[Mn^{III}_7Mn^{II}(TBC[4])_2(\mathbf{L}^{\mathbf{VII}})_3(\mu_4\text{-}O)_2(\mu_3\text{-}O)(\mu\text{-}OMe)_3(dmf)_2(H_2O)(MeOH)]$ (**9d**). Similar reactions with $H_2\mathbf{L}^{\mathbf{II\text{-}III}}$ afford $[Mn^{III}_7Mn^{II}(TBC[4])_2(\mathbf{L}^{\mathbf{II}})_3(\mu_4\text{-}O)_2(\mu_3\text{-}O)(\mu\text{-}OMe)_2(NO_3)(dmf)_3(H_2O)_{0.5}(MeOH)_{1.5}]$ (**9e**), $[Mn^{III}_7Mn^{II}(TBC[4])_2(\mathbf{L}^{\mathbf{II}})_3(\mu_4\text{-}O)_2(\mu_3\text{-}O)(\mu\text{-}OMe)_2(Cl)(dmf)_{3.5}(H_2O)_{0.5}(MeOH)]$ (**9f**), $[Mn^{III}_7Mn^{II}(TBC[4])_2(\mathbf{L}^{\mathbf{III}})_3(\mu_4\text{-}O)_2(\mu_3\text{-}O)(\mu\text{-}OMe)_2(NO_3)(dmf)_3(MeOH)]$ (**9g**) and $[Mn^{III}_7Mn^{II}(TBC[4])_2(\mathbf{L}^{\mathbf{III}})_3(\mu_4\text{-}O)_2(\mu_3\text{-}O)(\mu\text{-}OMe)_2(Cl)(dmf)_2(MeOH)_2]$ (**9h**).

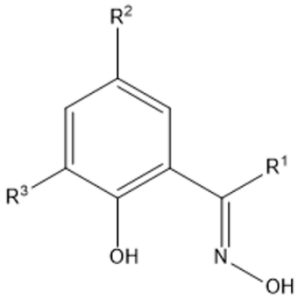

	R^1	R^2	R^3		R^1	R^2	R^3
I	H	H	H	**VI**	H	H	Et
II	Me	H	H	**VII**	H	H	Me
III	Et	H	H	**VIII**	H	^{t}Bu	H
IV	Ph	H	H	**IX**	H	H	^{t}Bu
V	H	H	^{i}Pr	**X**	H	^{t}Bu	^{t}Bu

Scheme 1.1 The ten phenolic oxime co-ligands ($H_2\mathbf{L}^{\mathbf{I\text{-}X}}$) explored as candidates for complementary cluster formation with H_4TBC[4].

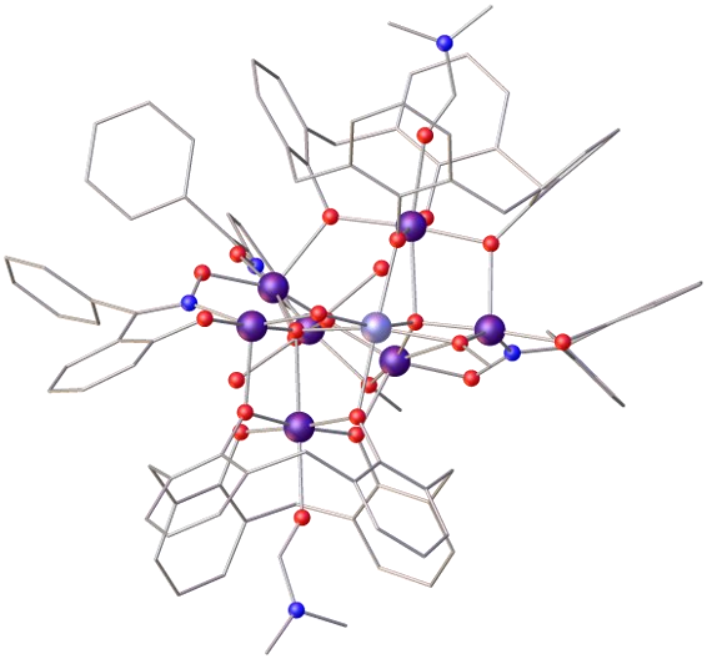

Figure 1.11 The molecular structure of complex **9a**. Colour code: Mn^{III} - dark purple, Mn^{II} - light purple, N - blue, C - grey, O - red. H atoms and ^{t}Bu groups omitted for clarity.[29]

The metallic skeleton common to **9a**-**d** describes a central, buckled [$Mn^{III}_5Mn^{II}$] triangle of edge-sharing triangles (Figure 1.12), capped top and bottom by an additional Mn^{III} ion. The metal-oxygen core of the triangle is an asymmetric [$Mn^{III}_5Mn^{II}(\mu_4\text{-}O)_2(\mu_3\text{-}O)(\mu\text{-}OMe)_2(\mu\text{-}OH)$] unit. The μ-$\mathbf{L}^{2-}$ ligands are also asymmetrically positioned around the triangle, two on one edge, one on the second edge and none on the edge containing the Mn^{II} ion. This is consistent with the doubly deprotonated phenolic oximes preference for Mn^{III}.[26–28] The μ_4-O^{2-} ions connect the triangle to the capping $[Mn^{III}(TBC[4])]^{-}$ moieties, three of whose four O-atoms also bond to Mn ions in the triangle. The fourth O-atom is terminally coordinated, with a second longer interaction to a five-coordinated Mn^{III} in the triangle. The Mn ions are all either five coordinate and square-based pyramidal, or six-coordinate and octahedral, with the remaining coordination sites being occupied by a combination of solvent molecules – dmf, H_2O or MeOH. The structures of **9e**-**h** are broadly similar but differ in two key aspects: (a) the position of the Mn^{II} ion in the triangle, and (b) the incorporation of a terminally coordinated chloride or nitrate to that Mn^{II} ion (Figure 1.12).

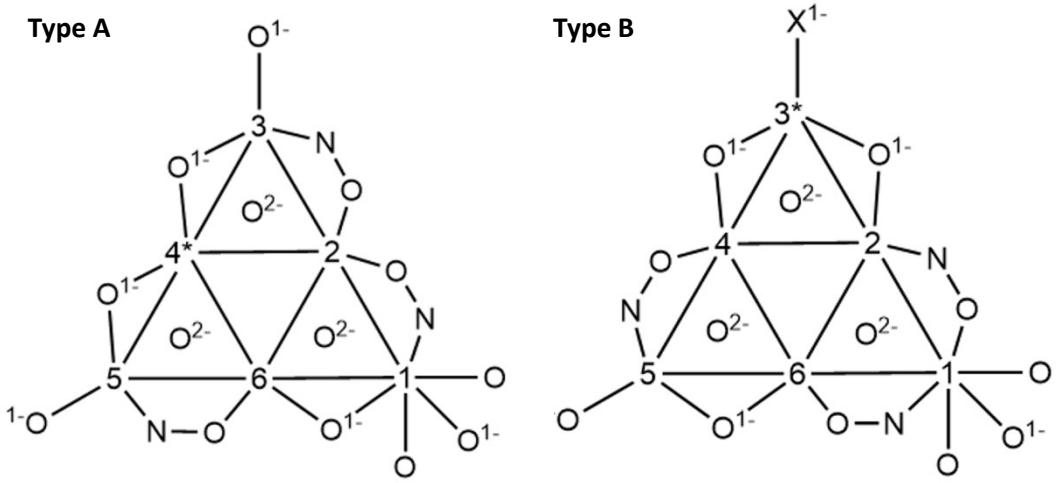

Figure 1.12 A schematic of the central [$Mn^{III}_5Mn^{II}$] triangle of triangles seen in the two distinct structure types, **A** and **B**, in **9**. Mn^{II} positioning is indicated by the *.

These structural differences lead to rather dramatic changes in the magnetic properties of **9a**-**d** (type **A**) and **9e**-**h** (type **B**), with χT values decreasing with decreasing temperature for the former, but increasing for the latter.[29] This behaviour is consistent with the presence of competing (weak) ferromagnetic and antiferromagnetic exchange interactions in both cases, but where the metal topology in structure type **B** gives rise to the stabilisation of a larger spin ground state than that for structure type **A**. Complexes **9e** and **9f** display frequency-dependent signals in out-of-phase (χ'') ac susceptibility measurements, suggestive of slow relaxation of the magnetisation and SMM behaviour. Data obtained by varying the frequency of oscillation of the ac field were fit to the Arrhenius equation, affording U_{eff} = 26.1 K, 28.5 K and τ = 9.63 x 10^{-9} s, 1.45 x 10^{-9} s, respectively.

The employment of a co-ligand with H_4TBC[4] has also generated novel topologies without their direct incorporation into the prevailing crystal structure. Indeed, the reaction of $MnCl_2{\cdot}4H_2O$, H_4TBC[4], NH_4ClO_4 and 1,4-butanediol (H_2bd) in a basic dmf/MeCN mixture, followed by slow diffusion with Et_2O vapour, affords the mixed-valent cluster [$Mn^{III}_8Mn^{II}_4$(TBC[4])$_4$(μ_4-O)$_2$(μ_3-OH)$_6$(μ-OH)$_4$(μ-Cl)$_2$(dmf)$_8$(H_2O)$_4$(MeCN)$_2$] (**10**) (Figure 1.13).[30] Analogous reactions repeated in the absence of the diol resulted in the formation of **2**, indicating the crucial role the co-ligand plays in the formation of **10**. Inspection of the central metal-oxygen core reveals a near-planar, mixed-valent [$Mn^{III}_6Mn^{II}_4$(μ_4-O)$_2$(μ_3-OH)$_6$(μ-OH)$_4$(Cl)$_2$] sheet-like structure reminiscent of the Brucite lattice, with two [Mn^{III}(TBC[4])]$^-$

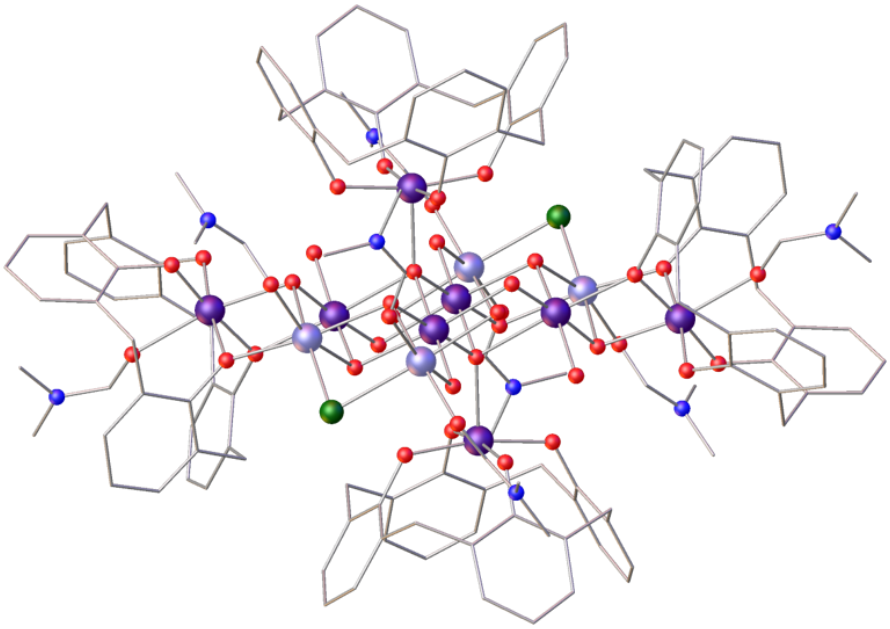

Figure 1.13 The molecular structure of complex **10**.[30] Colour code: Mn^{III} - dark purple, Mn^{II} - light purple, Cl - dark green, N - blue, C - grey, O - red. H atoms and ^{t}Bu groups omitted for clarity.

moieties sitting above/below the plane. The Mn ions within the plane are of distorted octahedral geometry, with the remaining coordination sites occupied by ligated dmf. The Mn^{III} of the plane-capping moiety is formally five-coordinate and square-pyramidal, with a MeCN molecule occupying the TBC[4] cavity without direct ligation, a feature redolent of the host-guest chemistry found in the MeCN solvate of H_4TBC[4].[31] The extended structure of **10** is dominated by the calixarenes - the 'coating' of the $[Mn^{III}(TBC[4])]^-$ caps results in head-to-head packing - and as such mimics a bilayer assembly. Magnetic susceptibility and magnetisation measurements suggested the presence of weak antiferromagnetic exchange interactions between constituent metal ions. A fit of the $1/\chi$ *versus* T data to the Curie-Weiss law supported this observation, affording the Weiss constant, θ = -10 K.[30]

The only other homometallic 3*d* cages known with H_4TBC[4] are an aesthetically pleasing family of $[Cu^{II}_9]$ (**11**) clusters of formula $[Cu^{II}_9(OH)_3(TBC[4])_3Cl_2(dmso)_{5.5}(EtOH)_{0.5}][Cu^{I}Cl_2]$ (**11a**) and $[Cu^{II}_9(OH)_3(TBC[4])_3(NO_3)_2(dmso)_6](NO_3)$ (**11b**) (Figure 1.14).[32] The former is formed from the reaction of $CuCl_2{\cdot}2H_2O$, H_4TBC[4] and NH_4ClO_4 in a basic dmso/EtOH solvent mixture. The latter results from a similar reaction using $Cu(NO_3)_2{\cdot}3H_2O$ in dmso/MeOH. The metallic core of **11a** describes a tricapped trigonal prism. The upper and lower triangular faces are each

capped by a Cl ion that resides within hydrophobic pockets generated by ligated solvent molecules. These faces are linked to each other *via* three μ-OH ligands along each vertical edge of the prism. The μ_5-TBC[4] ligands use all four μ-O atoms to chelate the face-capping Cu^{II} ions, forming a $[Cu(TBC[4])]^{2-}$ metalloligand which bridges to each of the Cu^{II} ions on the vertices of the square face of the prism. The Cu^{II} ions defining the trigonal prism are 5-coordinate, while the face-capping Cu^{II} ions are square planar. The cation in **11a** carries an overall charge of 1+, with charge balance maintained through the presence of the $[Cu^{I}Cl_2]^{1-}$ anion. The cation in **11b** is analogous to that of **11a**, the only difference being in the triangular face-capping anions. Two NO_3^- anions, one of which is disordered over two positions, reside on the upper and lower triangular faces of the prism.

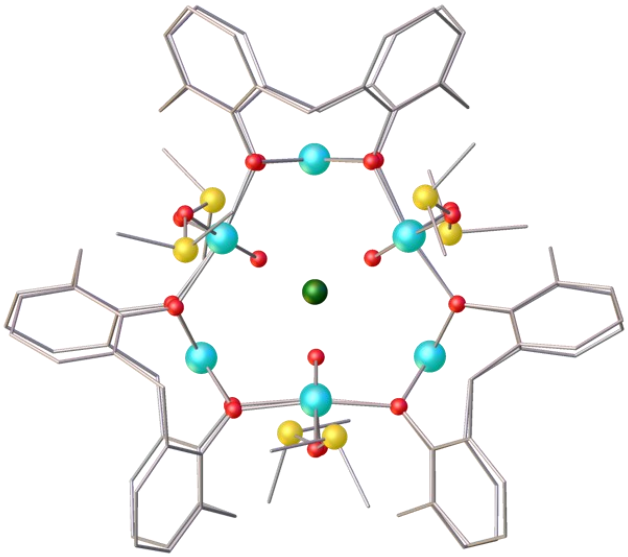

Figure 1.14 The molecular structure of the cluster cation in complex **11a**, viewed down the triangular face of the prism.[32] Colour code: Cu^{II} - turquoise, Cl - dark green, S - yellow, C - grey, O - red. H atoms, ^{t}Bu groups, non-coordinating dmso ligands and the $[Cu^{I}Cl_2]$ anion have been omitted for clarity.

One particularly interesting feature of these triangular clusters is that, despite their inherent inability to form bilayers akin to H_4TBC[4] solvates (due to their shape), they pack in 2D layers such that cavities (and spaces generated between TBC[4]s within each cluster) mimic classical H : G bilayer behaviour (Figure 1.15).

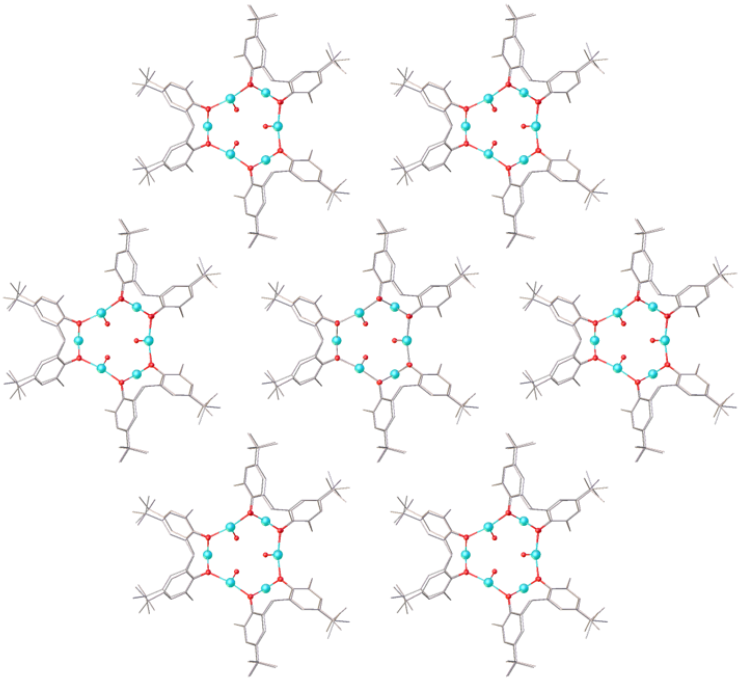

Figure 1.15 Organisation of triangular cluster **11a** into a 2D layer that mimics classical host-guest chemistry found in solvates of H_4TBC[4].[32] Colour code: Cu^{II} - turquoise, C - grey, O - red. H atoms, both non-coordinating and coordinating dmso ligands, and anions have been omitted for clarity.

Magnetic measurements reveal dominant antiferromagnetic exchange between the Cu^{II} ions, with a ground state of S = 3/2.[32] If one assumes that the larger Cu-O-Cu angles mediate stronger antiferromagnetic exchange,[33,34] and notes that (Cu-O(H)-Cu) > (Cu-O(TBC[4])-Cu), then a cartoon picture of the ground state is one of the Cu ions in the trigonal prism being 'spin-up' and the face capping Cu ions being 'spin-down'.

It is interesting to note that H_4TBC[4] produces just one main structure type per 3*d* metal in homoleptic species – an octahedron in $V^{III/IV/V}$ chemistry, a butterfly in $Mn^{II/III}$ chemistry and a tricapped trigonal prism in Cu^{II} chemistry. These are only perturbed in the presence of co-ligands. Perhaps strangely, bar those made for catalysis, there are no homo/polymetallic clusters of H_4TBC[4] with Cr^{III}, $Fe^{II/III}$, Co^{II} or Ni^{II} reported in the literature. On moving to homometallic and homoleptic 4*f* chemistry a single topology, a $[LnM^{III}_6]$ (**12**) octahedron, also dominates. The reaction of $LnMCl_3{\cdot}6H_2O$ and H_4TBC[4] in a basic dmf/ROH (R = Me, Et) solution produces $[LnM^{III}_6O_2(OH)_{3.32}(TBC[4])_2(HCO_2)_2Cl_{0.68}(dmf)_8(H_2O)_{0.5}]$ (LnM = Gd (**12a**), Tb (**12b**), Dy (**12c**), Ho (**12d**)) (Figure 1.16).[35]

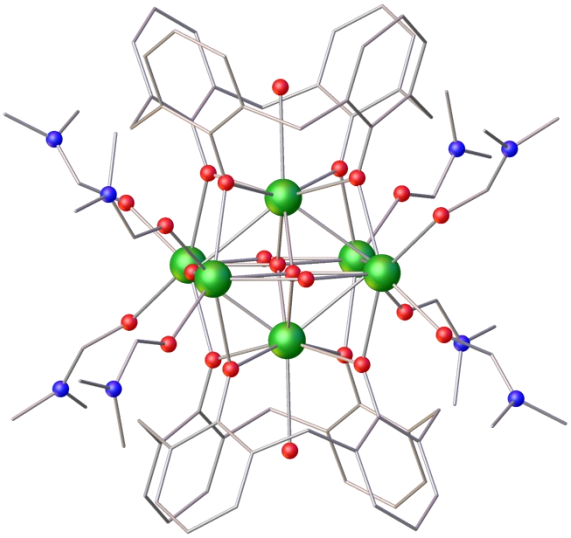

Figure 1.16 The molecular structure of the complex **12a**.[35] Colour code: Gd^{III} - green, N - blue, C - grey, O - red. H atoms, ^{t}Bu groups and disordered Cl/formate anions have been omitted for clarity.

The metallic skeleton of **12** describes a $[LnM^{III}_6]$ octahedron in which the six metal ions are connected internally by two μ_4-O^{2-} ions. The fully deprotonated TBC[4] ligands house the apical LnM ions within their lower-rim polyphenolic pockets, with each of the four O-arms further bridging to a LnM ion in the central metal square. The edges of this square are bridged by a disordered combination of formate (formed *via* the metal-assisted oxidation of MeOH), OH^- and Cl^- ions. The remaining coordination sites on the LnM ions are filled with dmf molecules. The apical LnM ions are either of nine-coordinate tricapped trigonal prismatic geometry when apical H_2O ligands are present, or square antiprismatic geometry in their absence. The LnM ions in the central square are all eight-coordinate with distorted square antiprismatic geometry. An alternative description of **12** is that of two $[LnM^{III}(TBC[4])]^{1-}$ metalloligands encapsulating a $[LnM^{III}_4O_2(OH)_{3.32}(HCO_2)_2Cl_{0.68}(dmf)_8(H_2O)_{0.5}]^{2+}$ fragment. Examination of the extended structures of **12a**-**d** shows that in contrast to the majority of clusters discussed above, neighbouring complexes pack in interdigitated layers in which upper-rim ^{t}Bu groups are sandwiched between the aromatic regions of TBC[4] molecules from adjacent layers. This may be caused by the increased coordination number and corresponding bulk of the LnM ions in the central square.

The magnetic properties of **12** are dominated by weakly antiferromagnetic nearest neighbour exchange, as one might expect. A simultaneous fit of the dc magnetic susceptibility and magnetisation data of the Gd analogue **12a** to the isotropic spin-Hamiltonian (1.1) assuming all $Gd^{III}\cdots Gd^{III}$ interactions to be equivalent afforded J = -0.06 cm^{-1} with g fixed at g = 2.00. There are no signs of slow magnetic relaxation in the ac susceptibility of **12a**-**d** down to 1.8 K and up to 1500 Hz, likely the result of the pseudo-octahedral metal-oxygen core and the crystallographic disorder where, in each case, the clusters are disordered over two closely related positions, with additional disorder in some of the coordinating ligands.

1.2.2 Heterometallic clusters

The first characterised methylene-bridged calix[*n*]arene-based 3*d*/4*f* molecules were a family of isostructural $[Mn^{III}_4LnM^{III}_4]$ (**13**) clusters, in which the replacement of one LnM^{III} ion for another invokes dramatic changes in the observed magnetic properties – from an enhanced magnetocaloric effect (MCE) in the isotropic Gd analogue to SMM behaviour in the anisotropic Dy and Tb versions. The reaction of $Mn(NO_3)_2{\cdot}4H_2O$ and $LnM(NO_3)_3.6H_2O$ with calix[4]arene ($H_4C[4]$) in a basic dmf/MeOH solvent mixture results in the formation of complexes of general formula $[Mn^{III}_4LnM^{III}_4(OH)_4(C[4])_4(NO_3)_2(dmf)_6(H_2O)_6](OH)_2$, (LnM = Gd (**13a**), Tb (**13b**), Dy (**13c**)) (Figure 1.17).[36,37]

The metallic skeleton in **13a** consists of a near-planar octametallic core describing an outer square of Mn^{III} ions encasing an inner square of Gd^{III} ions. The $[Mn_4]$ square has dimensions ~6.6 x 7.0 Å and the $[Gd_4]$ square ~3.9 x 3.9 Å, with the latter rotated ~45° with respect to the former. The central $[Gd^{III}_4(OH)_4(NO_3)_2]$ unit comprises the four Gd^{III} ions connected to each other *via* four μ_3-OH ions and two η^2,η^2,μ_3-NO_3 ions. The OH ions also bridge to the four $[Mn^{III}(C[4])(dmf)]$ corner units of the $[Mn_4]$ square. The μ_3-C[4] ligands are fully deprotonated with two O-atoms bonding terminally to the Mn^{III} ions and two μ-bridging to the central $[Gd_4]$ square. The Mn^{III} ions possess distorted octahedral geometries in $\{O_6\}$ coordination spheres with the JT axes described by the dmf-Mn-OH vector, *i.e.* across the diagonal of the $[Mn^{III}_4]$ square. The Gd^{III} ions are eight-coordinate and are in distorted square antiprismatic geometries, with their remaining coordination sites filled by a combination of H_2O and dmf molecules. The former form intramolecular H-bonds to the terminally bonded O-atoms of the C[4] ligands and intermolecular H-bonds to the OH anions and dmf molecules of crystallisation. In the extended structures of **13a**-**c** the cluster cations assemble in a pseudo-

capsule assembly to produce a dmf-rich microenvironment between the corner units of nearest neighbour cages.

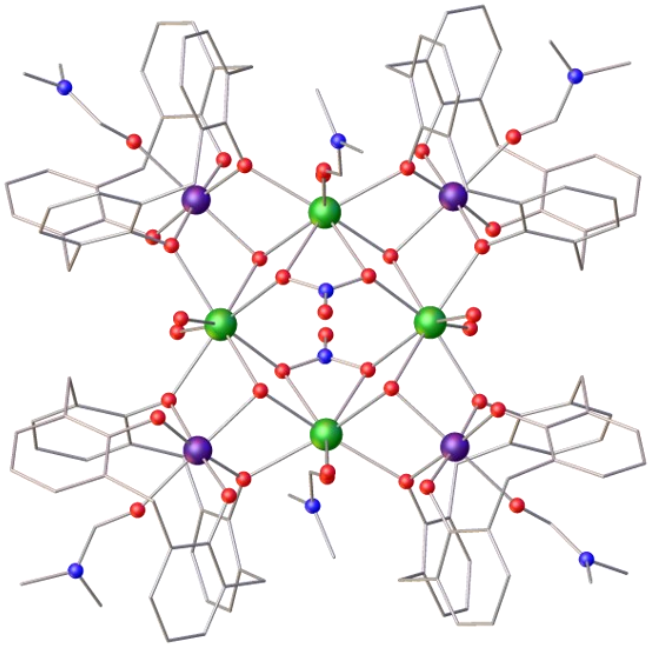

Figure 1.17 The molecular structure of the cation of complex **13a** viewed perpendicular to the $[Mn^{III}_4Gd^{III}_4]$ plane.[36] Colour code: Mn^{III} - dark purple, Gd^{III} - green, N - blue, C - grey, O - red. H atoms, ^{t}Bu groups, OH anions and dmf molecules have been omitted for clarity.

The presence of just LnM-LnM and LnM-Mn interactions and the absence of any Mn-Mn interactions results in a topology that displays extremely weak magnetic exchange interactions and thus population of several magnetic states, even at the lowest temperatures studied. For the Gd analogue **13a**, the room-temperature χT value of ~42.8 cm^3 K mol^{-1} is close to the spin-only (g = 2.00) value expected for an uncoupled $[Mn^{III}_4Gd^{III}_4]$ unit, ~43.5 cm^3 K mol^{-1} (Figure 1.18). This value stays essentially constant as the temperature is decreased until ~50 K, below which it increases to a maximum of ~60.5 cm^3 K mol^{-1} at 5 K, well below the value expected for a ferromagnetically coupled cluster with an isolated S = 22 ground state (253 cm^3 K mol^{-1}). This is also reflected in the magnetisation data which shows M increasing rather slowly with field reaching a maximum value of 40 μ_B at T = 1.8 K and B = 7 T (inset Figure 1.18).

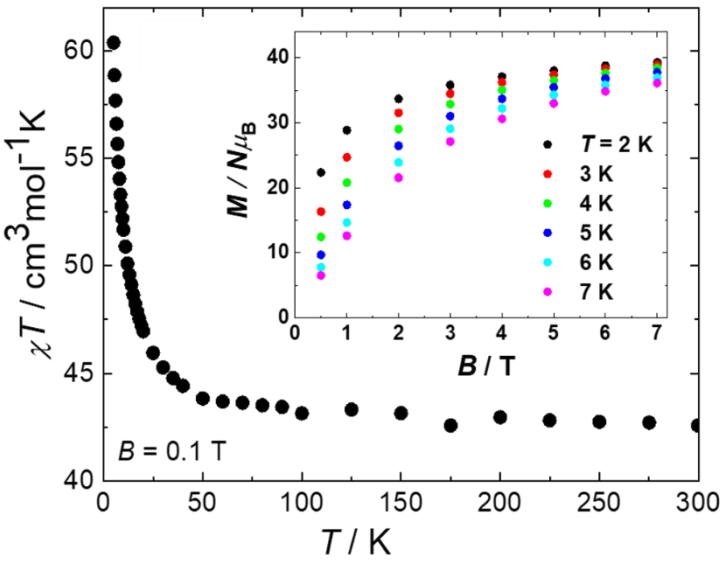

Figure 1.18 Temperature dependence (T = 5 - 300 K) of the dc susceptibility data for **13a** collected in an applied field, B = 0.1 T. Inset: magnetisation data of **13a** *versus* applied field for T = 2 - 7 K.[37]

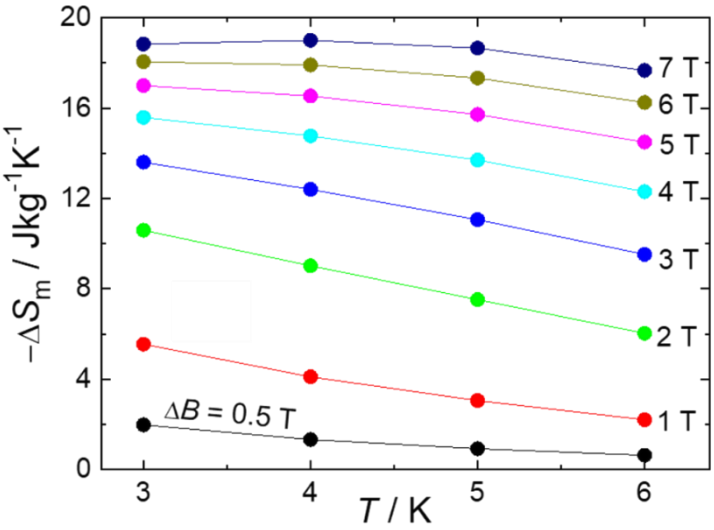

Figure 1.19 Temperature dependence of the magnetic entropy changes for **13a** in applied field changes, ΔB = 0.5 - 7 T.[37]

The combination of a large isotropic S and the population of multiple low-lying excited spin states suggests that **13a** should be an excellent candidate for application in cryogenic magnetic refrigeration. Determination of the magnetic entropy change, ΔS_m, from the magnetisation data *via* the Maxwell relations showed that $-\Delta S_m$ increases gradually with increasing ΔB, reaching a value of 19.0 J kg^{-1} K^{-1} at T = 4 K for a ΔB of 7 T, much larger than

the maximum allowable entropy for an isolated S = 22 spin ground state (R ln(2S + 1) = 3.8R = 9.0 J kg^{-1} K^{-1}) (Figure 1.19). This clearly demonstrates that the presence of low-lying excited spin states can have a very positive influence on the MCE.

Variable temperature and field heat capacity (C) experiments (Figure 1.20) reveal that data collected at temperatures below 1 K are strongly dependent on the applied field and span over three orders of magnitude in units of R for the investigated field changes. The zero-field curve achieves a maximum of ~4R for T = 0.8 K, while the field-independent lattice contribution has a value of (6 x 10^{-3})R for the same temperature. The relevant feature is the broad specific heat anomaly that shifts toward higher temperatures on increasing applied field, attributed to the field-splitting of the spin multiplets. This cannot be reproduced by a model based solely on a well-defined S = 22 spin ground state (which would not exceed ~1R). The excess experimental heat capacity can be explained by the contribution arising from the population of low-lying excited spin states. In the high-temperature range, a large field-independent contribution appears that can be attributed to the lattice phonon modes of the

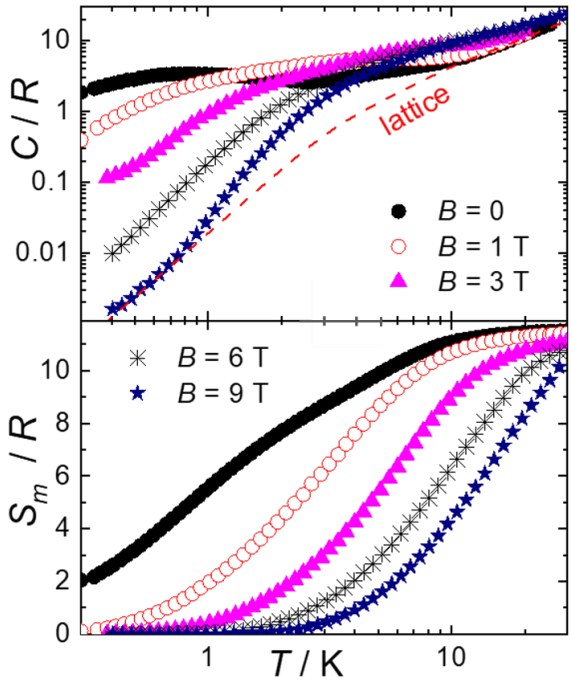

Figure 1.20 Top: temperature dependence of the heat capacity of **13a** normalised to the gas constant R collected for B = 0, 1, 3, 6, and 9 T. The dashed line is the fitted lattice contribution. Bottom: temperature dependence of the experimental magnetic entropy for several B, obtained from the respective magnetic contributions to the total heat capacity.[37]

crystal. The dashed line in the top panel of Figure 1.20 represents a fit to this contribution with the low-temperature Debye function, yielding a value of θ_D = 23 K, typical for this class of cluster complex.[38,39] The temperature dependence of the magnetic entropy S_m is shown in the bottom panel of Figure 1.20 for the corresponding applied fields. As further evidence of the participation of excited spin states, the experimental $S_m(T)$ far exceeds the value expected for an isolated S = 22 ground state, 3.8R.

The temperature dependence of the magnetic entropy changes of **13a** at the indicated applied-field changes ΔB are shown in Figure 1.21. The $\Delta S_m(T, \Delta B)$ curves are consistent with the preliminary estimates obtained from the magnetisation data, highlighting the importance of employing both types of data. Note that $-\Delta S_m$ reaches a value of 21.3 J kg^{-1} K^{-1} at liquid helium temperature for the field change, ΔB = 9 - 0 T. Analysis of the heat capacity data permits an estimation of the adiabatic temperature change ΔT_{ad}. The bottom panel of Figure 1.21 shows that the maximum in ΔT_{ad} gradually decreases and shifts to lower temperatures with decreasing field change ΔB, from ΔT_{ad} = 9.0 K for ΔB from 9 to 0 T at T = 4.4 K, to ΔT_{ad} =

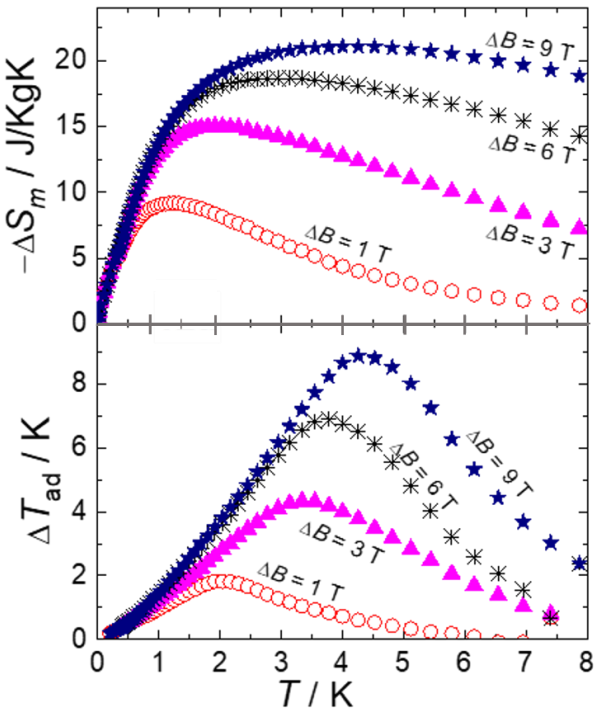

Figure 1.21 Top: temperature dependence of the magnetic entropy change of **13a** for the indicated applied-field changes ΔB. Bottom: temperature dependence of the adiabatic temperature change for **13a** for indicated ΔB. Both $\Delta S_m(T, \Delta B)$ and $\Delta T_{ad}(T, \Delta B)$ curves are obtained from the heat capacity data of Figure 1.20.[37]

2.0 K for Δ*B* from 1 to 0 T at T = 2.0 K. Thus the magnetic field dependence of the adiabatic temperature change increases from 1 to 2 K/*T*, respectively, making **13a** one of the finest refrigerants known in the liquid-helium temperature range.[40] By contrast, complexes **13b**-**c** display SMM behaviour, albeit at rather low temperatures, induced by the anisotropy of the LnM ions present.[36,37]

The sole remaining family of heterometallic TBC[4]-supported clusters reported in the literature are $[Fe^{III}_2LnM^{III}_2]$ (**14**) tetrahedra of general formula $[Fe^{III}_2LnM^{III}_2(O)(OH)(TBC[4])_2(dmf)_4(H_2O)_2(MeOH)_2]Cl$ (LnM = Gd (**14a**), Tb (**14b**), Dy (**14c**)) (Figure 1.22) and result from the reaction of $FeCl_2{\cdot}4H_2O$, $LnCl_3{\cdot}6H_2O$ and H_4TBC[4] in a basic dmf/MeOH solution.[41] The metallic core common to **14a**-**c** describes a distorted, asymmetric tetrahedron [Ln···Ln, ~3.9 Å; Fe···Fe, ~3.5 Å; Fe···Ln, ~3.4 Å] in which the four metal ions are connected *via* one central μ_4-O^{2-} ion [Fe-O-Fe, 144°; LnM-O-LnM, 101°; Fe-O-LnM, ~100°] and one edge-capping OH^- ion [Gd-O-Gd, ~117°]. The fully deprotonated TBC[4] ligands bond the symmetry equivalent Fe^{III} ions within their lower rim polyphenolic pockets, with two of the four O-atoms further bridging to the two symmetry inequivalent Gd^{III} ions. The magnetic core is thus $[Fe^{III}_2LnM^{III}_2(O)(OH)(OR)_4]$. The Fe^{III} ions are five coordinate and in distorted square-based pyramidal geometry, and the LnM^{III} ions are each eight-coordinate in square-

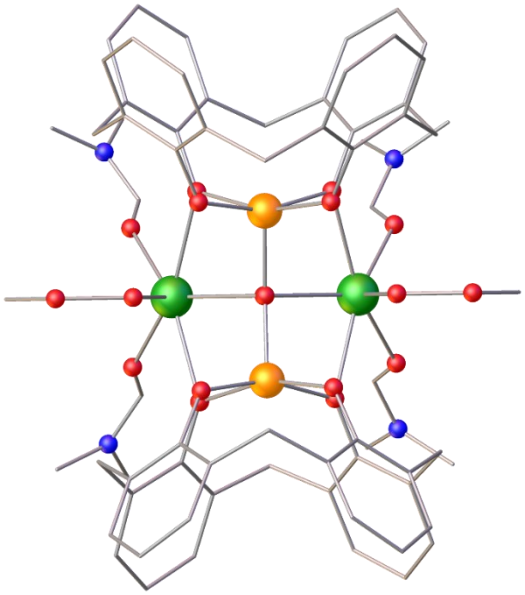

Figure 1.22 The molecular structure of the cation of complex **14a**.[41] Colour code: Cu^{II} - orange, Gd^{III} - green, N - blue, C - grey, O - red. H atoms, ^{t}Bu groups, anions and solvents of crystallisation have been omitted for clarity.

antiprismatic geometries with their coordination spheres completed by one MeOH, one H_2O and one dmf. Charge balance is maintained through the presence of one Cl per cluster unit. The Cl ions sit between neighbouring $[Fe_2Ln_2]$ clusters, H-bonded to the terminally bonded MeOH and H_2O molecules on one $[Fe_2LnM_2]$ cluster and to the bridging OH ion on its neighbour. Magnetic measurements show the presence of dominant antiferromagnetic exchange interactions. The susceptibility and magnetisation data of **14a** can be fitted employing a 3*J*-model to the isotropic part of spin-Hamiltonian (1.1) to afford the best-fit parameters $J_{Fe\text{-}Fe}$ = -85.0 cm^{-1}, $J_{Fe\text{-}Gd}$ = -0.05 cm^{-1} and $J_{Gd\text{-}Gd}$ = +0.01 cm^{-1} with *g* fixed at *g* = 2.00. **14b**-**c** show no evidence of SMM behaviour.

At first glance, clusters **1**-**14** might not appear to share much in common. However, visual inspection of their metallic skeletons (Figure 1.23) reveals some very interesting structural similarities. In homoleptic reactions the topology of the structures are dictated by the formation/presence of the $[TM/LnM(TBC[4])]^{n+/-}$ metalloligands which cap or encapsulate metal-oxyhydride fragments. For example, in **1** a single $[V^{III}(TBC[4])]^{1-}$ metalloligand caps a $[(V^{IV}O)_5O(OMe)_8]$ polyoxo-vanadate fragment, in **2**-**4** two $[Mn^{III}(TBC[4])]^{1-}$ metalloligands encapsulate a $[(Mn^{II}_xLnM^{III}_{2-x})(OH)_2]^{n+}$ fragment, and in **11** three $[Cu(TBC[4])]^{2-}$ metalloligands encapsulate three $[Cu_2(OH)]^{3+}$ dimers. The oxides and hydroxides in these units originate from the use of hydrated metal salts and base in wet solvents, and the self-assembled moieties this generates are entirely analogous to those commonly observed as building blocks in the coordination chemistry of those metal ions with other organic bridging ligands. For example, the $[TM_6]$ Lindqvist ion is ubiquitous in POM chemistry, $[TM_3]$ triangles and $[TM_4]$ butterflies are abundant in $Mn^{II/III}$ chemistry, and hydroxide-bridged $[TM_2]$ dimers are the most prevalent structural unit in Cu^{II} chemistry. A scan of Figure 1.23 reveals these structural building blocks to be present in all the clusters we have isolated. Thus, the combination of the $[TM/LnM(TBC[4])]^{n+/-}$ metalloligand and self-assembled metal oxy-hydroxide moieties conforming to known building blocks makes structure prediction/comparison a little simpler. The use of co-ligands can block the self-assembly process – as it does for compounds **6** and **7**, for example. However, it can also be entirely complementary, as observed for compounds **8** and **9** in which the use of alkoxides/H_4TBC[4] and oximes/H_4TBC[4] generates topologies comprising fused butterflies and triangles, respectively – structures one would expect from the homoleptic reactions.

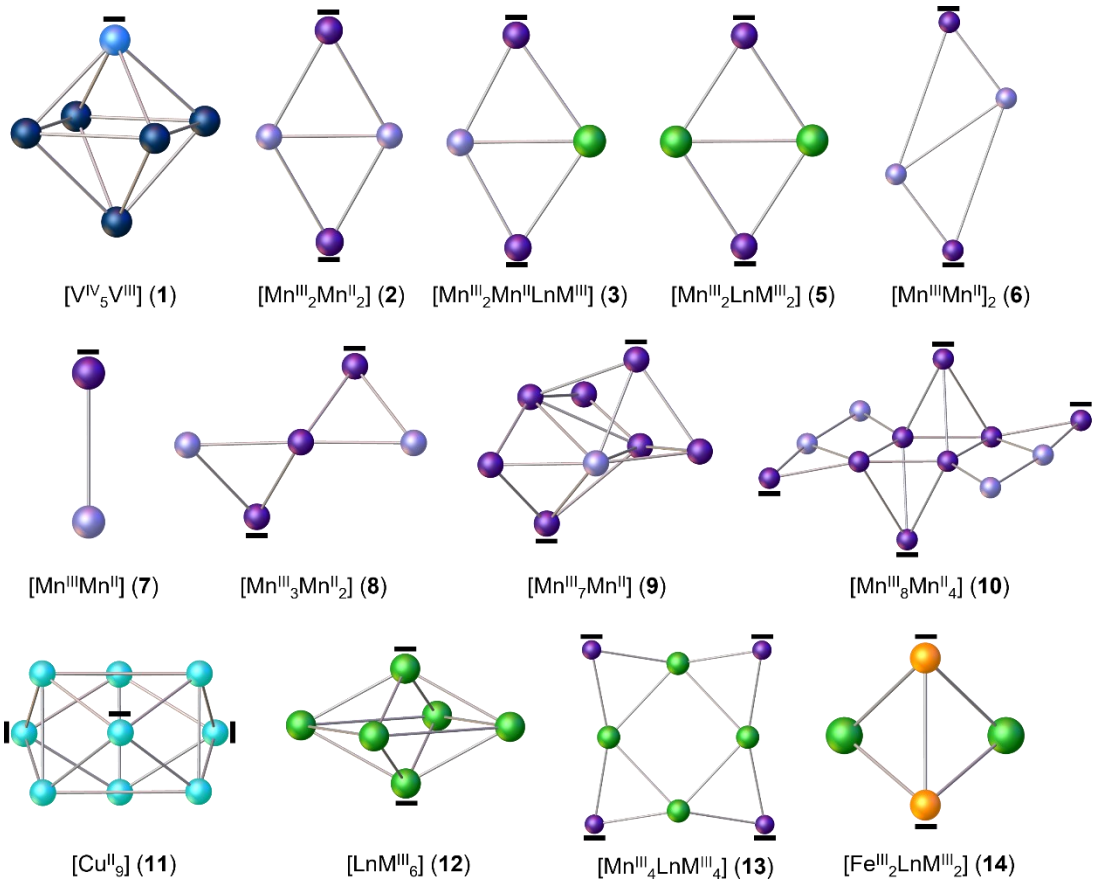

Figure 1.22 The metallic skeletons of complexes **1**-**14**. Colour code: V^{IV} - dark blue, V^{III} - light blue, Mn^{III} - dark purple, Mn^{III} - light purple, Cu^{II} - turquoise, Gd^{III} - green, Fe^{III} - orange. The solid black lines represent the metal ions housed within the calix[4]arene polyphenolic pocket and therefore highlight the position of the $[TM^{II/III}/LnM^{III}(TBC[4])]^{n+/-}$ metalloligand.

The analogous hierarchical self-assembly process is observed on moving to heterometallic clusters, where a clear bonding preference for certain metal ions in particular oxidation states by the calix[4]arene ligand is observed in competitive reaction media. Indeed, our experiments allow us to establish the key metal ion binding rules for H_4TBC[4] (and H_4C[4]), at least thus far. Under ambient conditions TBC[4]: (1) preferentially binds TM^{III} ions, (2) will bind TM^{II} ions in the absence of TM^{III} ions, and (3) will bind LnM^{III} ions in the absence of TM^{II} or TM^{III} ions. These rules translate logically to systems developed with synthetically altered calix[4]arenes, *e.g.* bis-calix[4]arenes tethered directly through one methylene bridge position (*vide infra*, Chapter 2).

1.3 Conclusions

p-tert-Butylcalix[4]arene (H_4TBC[4]) has proven to be an excellent ligand for the construction of polymetallic 3*d*, 4*f* and 3*d*-4*f* clusters containing paramagnetic metal ions, as reflected in the synthesis and characterisation of a large family of complexes, including [V_6] (**1**), [Mn_4] (**2**), [Mn_3LnM] (**3**, **4**), [Mn_2LnM_2] (**5**), [Mn_2]$_2$ (**6**), [Mn_2] (**7**), [Mn_5] (**8**), [Mn_8] (**9**), [Mn_{12}] (**10**), [Cu_9] (**11**), [LnM_6] (**12**), [Mn_4LnM_4] (**13**) and [Fe_2LnM_2] (**14**). It has been particularly successful in the construction of Mn^{III}-based clusters whose preference for an axially elongated (JT distorted) ligand field is ideally suited to the polyphenolic pocket of the calix[4]arene. These species display a breadth of fascinating magnetic behaviours ranging from slow relaxation of magnetisation and SMM behaviour to an enhanced magnetocaloric effect. The synthesis of families of related structures and the use of complementary co-ligands allows for quantitative magneto-structural correlations that can uncover the nature and magnitude of ferromagnetic and antiferromagnetic exchange interactions. The presence of just one major structure type per 3*d* or 4*f* metal ion in homoleptic clusters points to the dominant structure directing effect of H_4TBC[4], as does the unprecedented ability to swap out TM^{II} ions for LnM^{III} ions whilst maintaining structural integrity.

Structural analysis of the whole family of TBC[4]-supported clusters reveals common self-assembled moieties and has allowed development of empirical metal ion binding rules. Under ambient conditions H_4TBC[4] preferentially binds TM^{III} ions, will bind TM^{II} ions in the absence of TM^{III} ions, and will bind LnM^{III} ions in the absence of TM^{II} or TM^{III} ions. What governs/underpins these rules (*e.g.* electrostatics, ionic radii/size-matching, *etc.*), and how these rules can be broken, will require the isolation and characterisation of a broader family of complexes. It's clear, however, that the *in situ* formation of $[TM^{II/III}LnM^{III}(TBC[4])]^{n+/-}$ metalloligands is a very powerful methodology for the self-assembly of polymetallic cluster compounds. The following chapters detail work in this area, extending this chemistry to the related bis-calix[4]arenes (Chapter 2), thiacalix[4]arenes and their combination with H_4TBC[4] in heteroleptic reactions (Chapter 3) and to the judicious manipulation of reaction conditions to afford spin frustrated, high-symmetry topologies (Chapter 4).

1.4 References

(1) D. Gatteschi, R. Sessoli and J. Villain, *Molecular Nanomagnets*, Oxford University Press, 2006.

(2) C. D. Gutsche, in *Calixarenes : An Introduction*, RSC Publishing, Cambridge, 2nd ed., 2008, ch. 2, pp. 27-160.

(3) L. R. B. Wilson, M. Coletta, M. Evangelisiti, S. Piligkos, S. J. Dalgarno and E. K. Brechin, *Dalton Trans.*, 2022, **51**, 4213–4226.

(4) L. R. MacGillivray and J. L. Atwood, *Nature*, 1997, **389**, 469–472.

(5) S. J. Dalgarno, S. A. Tucker, D. B. Bassil and J. L. Atwood, *Science*, 2005, **309**, 2037–2039.

(6) P. Jin, S. J. Dalgarno, C. Barnes, S. J. Teat and J. L. Atwood, *J. Am. Chem. Soc.*, 2008, **130**, 17262–17263.

(7) G. Karotsis, S. J. Teat, W. Wernsdorfer, S. Piligkos, S. J. Dalgarno and E. K. Brechin, *Angew. Chem. Int. Ed.*, 2009, **48**, 8285–8288.

(8) J. L. Atwood, L. J. Barbour, A. Jerga and B. L. Schottel, *Science*, 2002, **298**, 1000–1002.

(9) J. L. Atwood, L. J. Barbour and A. Jerga, *Angew. Chem. Int. Ed.*, 2004, **43**, 2948–2950.

(10) G. D. Andreetti, R. Ungaro and A. Pochini, *J. Chem. Soc., Chem. Commun.*, 1979, **22**, 1005–1007.

(11) J. L. Atwood, L. J. Barbour and A. Jerga, *Chem. Commun.*, 2002, **24**, 2952–2953.

(12) E. B. Brouwer, G. D. Enright, K. A. Udachin, S. Lang, K. J. Ooms, P. A. Halchuk and J. A. Ripmeester, *Chem. Commun.*, 2003, **12**, 1416–1417.

(13) P. K. Thallapally, S. J. Dalgarno and J. L. Atwood, *J. Am. Chem. Soc.*, 2006, **128**, 15060–15061.

(14) C. Aronica, G. Chastanet, E. Zueva, S. A. Borshch, J. M. Clemente-Juan and D. Luneau, *J. Am. Chem. Soc.*, 2008, **130**, 2365–2371.

(15) R. L. Meyer, P. Miró, W. W. Brennessel and E. M. Matson, *Inorg. Chem.*, 2021, **60**, 13833–13843.

(16) A. A. Fertig, S. E. Cooney, R. L. Meyer, W. W. Brennessel and E. M. Matson, *Chem. Commun.*, 2022, **58**, 6004–6007.

(17) S. M. Taylor, G. Karotsis, R. D. McIntosh, S. Kennedy, S. J. Teat, C. M. Beavers, W. Wernsdorfer, S. Piligkos, S. J. Dalgarno and E. K. Brechin, *Chem. Eur. J.* 2011, **17**, 7521–7530.

(18) E. K. Brechin, J. C. Huffman, G. Christou, J. Yoo, M. Nakano and D. N. Hendrickson, *Chem. Commun.*, 1999, **9**, 783–784.

(19) L. M. Wittick, L. F. Jones, P. Jensen, B. Moubaraki, L. Spiccia, K. J. Berry and K. S. Murray, *Dalton Trans.*, 2006, **12**, 1534–1543.

(20) A. Fong, PhD Thesis, Heriot-Watt University, 2019.

(21) M. A. Palacios, R. McLellan, C. M. Beavers, S. J. Teat, H. Weihe, S. Piligkos, S. J. Dalgarno and E. K. Brechin, *Chem. Eur. J.,* 2015, **21**, 11212–11218.

(22) S. M. Taylor, R. D. McIntosh, C. M. Beavers, S. J. Teat, S. Piligkos, S. J. Dalgarno and E. K. Brechin, *Chem. Commun.*, 2011, **47**, 1440–1442.

(23) S. M. Taylor, J. M. Frost, R. McLellan, R. D. McIntosh, E. K. Brechin and S. J. Dalgarno, *CrystEngComm*, 2014, **16**, 8098–8101.

(24) J. Yoo, A. Yamaguchi, M. Nakano, J. Krzystek, W. E. Streib, L.-C. Brunel, H. Ishimoto, G. Christou and D. N. Hendrickson, *Inorg. Chem.*, 2001, **40**, 4604–4616.

(25) S. M. Taylor, R. D. McIntosh, S. Piligkos, S. J. Dalgarno and E. K. Brechin, *Chem. Commun.*, 2012, **48**, 11190–11192.

(26) R. Inglis, C. J. Milios, L. F. Jones, S. Piligkos and E. K. Brechin, *Chem. Commun.*, 2012, **48**, 181–190.

(27) R. Inglis, S. M. Taylor, L. F. Jones, G. S. Papaefstathiou, S. P. Perlepes, S. Datta, S. Hill, W. Wernsdorfer and E. K. Brechin, *Dalton Trans.*, 2009, **42**, 9157–9168.

(28) R. Inglis, L. F. Jones, C. J. Milios, S. Datta, A. Collins, S. Parsons, W. Wernsdorfer, S. Hill, S. P. Perlepes, S. Piligkos and E. K. Brechin, *Dalton Trans.*, 2009, **18**, 3403–3412.

(29) R. McLellan, M. A. Palacios, S. Sanz, E. K. Brechin and S. J. Dalgarno, *Inorg. Chem.*, 2017, **56**, 10044–10053.

(30) M. Coletta, M. A. Palacios, E. K. Brechin and S. J. Dalgarno, *Chemistry*, 2020, **2**, 253–261.

(31) Z. Asfari, A. Bilyk, C. Bond, J. M. Harrowfield, G. A. Koutsantonis, N. Lengkeek, M. Mocerino, B. W. Skelton, A. N. Sobolev, S. Strano, J. Vicens and A. H. White, *Org. Biomol. Chem.*, 2004, **2**, 387–396.

(32) G. Karotsis, S. Kennedy, S. J. Dalgarno and E. K. Brechin, *Chem. Commun.*, 2010, **46**, 3884–3886.

(33) V. H. Crawford, H. Wayne. Richardson, J. R. Wasson, D. J. Hodgson and W. E. Hatfield, *Inorg. Chem.*, 1976, **15**, 2107–2110.

(34) W. E. Hatfield, *Comments Inorg. Chem.*, 1981, **1**, 105–121.

(35) S. Sanz, R. D. McIntosh, C. M. Beavers, S. J. Teat, M. Evangelisti, E. K. Brechin and S. J. Dalgarno, *Chem. Commun.*, 2012, **48**, 1449–1451.

(36) G. Karotsis, M. Evangelisti, S. J. Dalgarno and E. K. Brechin, *Angew. Chem. Int. Ed.*, 2009, **48**, 9928–9931.

(37) G. Karotsis, S. Kennedy, S. J. Teat, C. M. Beavers, D. A. Fowler, J. J. Morales, M. Evangelisti, S. J. Dalgarno and E. K. Brechin, *J. Am. Chem. Soc.*, 2010, **132**, 12983–12990.

(38) M. Evangelisti, F. Luis, L. J. de Jongh and M. Affronte, *J. Mater. Chem.*, 2006, **16**, 2534–2549.

(39) M. Evangelisti and E. K. Brechin, *Dalton Trans.*, 2010, **39**, 4672–4676.

(40) C. Zimm, A. Jastrab, A. Sternberg, V. Pecharsky, K. Gschneidner, M. Osborne and I. Anderson, in *Advances in Cryogenic Engineering*, ed. P. Kittel, Springer US, Boston, MA, 1998, pp. 1759–1766.

(41) S. Sanz, K. Ferreira, R. D. McIntosh, S. J. Dalgarno and E. K. Brechin, *Chem. Commun.*, 2011, **47**, 9042–9044.

Chapter 2

Magneto-structural correlations of bis-calixarene-supported clusters

2.1 Introduction

In 2013, Fantini and co-workers derived a synthetic route to 2,2'-bis-*p*-*tert*-butylcalix[4]arene, hereafter referred to as BisTBC[4] or H_8L, an attractive new ligand where two TBC[4] macrocycles are tethered directly *via* the methylene bridge (Figure 2.1).[1] Having established the TBC[4] binding rules discussed in Chapter 1, it was of interest to begin successive investigations into BisTBC[4] cluster formation. Given that BisTBC[4] has double the number of phenol units, the expectation was to access higher nuclearity complexes whilst mimicking the binding behaviour of TBC[4] with respect to cluster formation. X-ray crystallography reveals that the isolated BisTBC[4] molecule exists in the *anti*-conformation, minimising steric hindrance between the ^{t}Bu groups of each H_4TBC[4] moiety.[2]

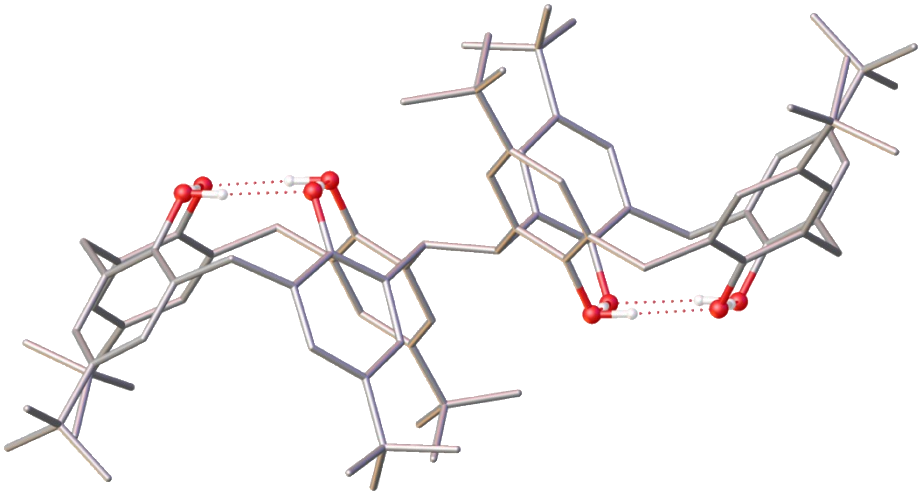

Figure 2.1 The single crystal X-ray structure of BisTBC[4] (H_8L) in the *anti*-conformation, where the dotted red lines represent hydrogen bonding. For clarity, only the phenolic H atoms are shown.[25] Colour code: C - grey, O - red, H - white.

Initial investigations revealed that upon deprotonation and coordination of metal ions, one TBC[4] moiety will invert to give the *syn*-conformation (Figure 2.2). This conformational inversion creates additional binding sites for the metal ions; four adjacent lower-rim oxygen atoms (two from each TBC[4] pocket) can accommodate further coordination, leading to double-capping behaviour and systematic increase of nuclearity.

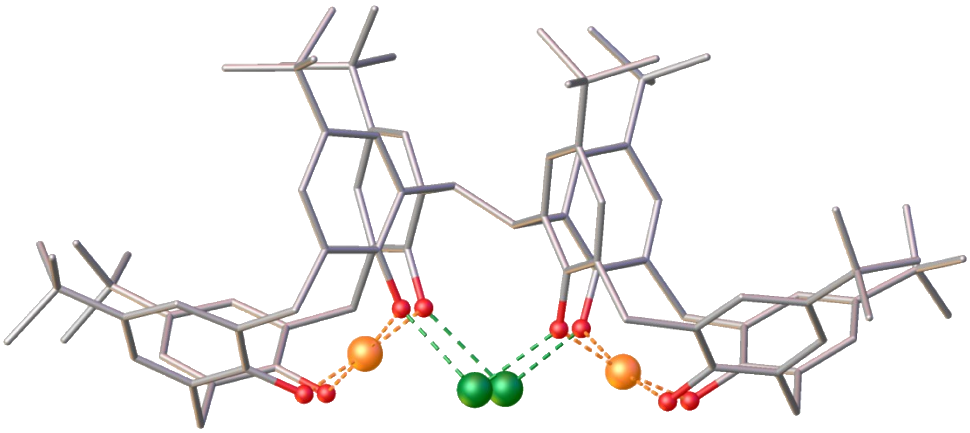

Figure 2.2 Conformational inversion to *syn*-L upon metal coordination. The orange ions depict metals housed in the tetraphenolic cavity and the green ions depict those housed in the additional binding sites created upon inversion. H atoms are omitted for clarity. Colour code: C - grey, O - red.

A search of the Cambridge Structural Database (CSD) reveals just five 3*d* and six 3*d*/4*f* BisTBC[4]-supported clusters published to date. Here, we extend this family to include five novel BisTBC[4]-supported 3*d* clusters and compare their syntheses, structures and magnetic properties to the relevant TBC[4]/BisTBC[4] literature.

2.2 Experimental

Materials and Syntheses

All chemicals were procured from commercial suppliers and used as received (reagent grade). Elemental analyses were performed on a Thermo Fisher Scientific Flash SMART instrument.

Synthesis of *p-tert*-butylcalix[4]arene (H_4TBC[4])

H_4TBC[4] was synthesised according to literature procedure.[3] *p-tert*-butylphenol (100 g, 0.665 mol), formaldehyde (37%, 60 mL) and a solution of NaOH (0.48 g, 12 mmol) in deionised water (4 mL) were heated to reflux under N_2, and water collected by means of a Dean-Stark apparatus until polymer formation (~120 °C). Upon cooling to room temperature, toluene (400 mL) and diphenyl ether (800 mL) were added. The reaction mixture was heated until toluene was removed, kept under reflux for 4 hours and then allowed to cool to room temperature. Ethyl acetate (600 mL) was added and the solution stirred under ambient conditions for 2 hours. The solution was filtered affording white crystals of H_4TBC[4] in 63.1% yield (68.1 g). ^{1}H NMR (500 MHz, $CDCl_3$): δ (ppm) 10.28 (s, 4H, ArOH), 7.08 (s, 8H, ArH), 4.27 (d, *J* = 12.8 Hz, 4H, Ar-CH_2-Ar), 3.52 (d, *J* = 11.7 Hz, 4H, Ar-CH_2-Ar), 1.24 (s, 36H, ^{t}Bu).

Synthesis of 2,2'-bis-*p-tert*-butylcalix[4]arene (H_8L)

H_8L was synthesised from H_4TBC[4] according to literature procedure in a 3-step reaction.[1]

1. Synthesis of tetramethoxy-*p-tert*-butylcalix[4]arene (TBC[4]OMe)

H_4TBC[4] (20 g, 30.9 mmol) was dissolved in a THF/dmf mixture (10:1 v/v, 110 mL). NaH (5 g, 0.208 mol) was added slowly whilst stirring. MeI (20 mL, 0.321 mol) was added and the solution heated at reflux for 2 hours, after which it was cooled to room temperature and MeOH added to destroy any unreacted NaH. Solvents were eliminated under reduced pressure and the resultant crude solid washed with water and dissolved in $CHCl_3$. The solution was dried over $MgSO_4$, filtered and concentrated under reduced pressure. The product was recrystallised from hot $CHCl_3$/MeOH, affording TBC[4]OMe as a white powder in 80.8% yield (17.6 g).

2. Synthesis of 2,2'-bis(tetramethoxy-*p*-*tert*-butylcalix[4]arene) (BisTBC[4]OMe)

n-BuLi (2.5 M in hexane, 11.3 mL, 28.4 mmol) was added to a stirred solution of TBC[4]OMe (10 g, 14.2 mmol) in dry THF (50 mL) under N_2, causing a rapid colour change from pale yellow to deep red. After 10 minutes, 1,2-dibromoethane (3.05 mL, 35.4 mmol) in dry THF (30 mL) was added dropwise over 40 minutes, with a concomitant colour change from deep red to yellow. The reaction mixture was stirred for 12 hours then quenched by the addition of H_2O, upon which volatiles were removed and the resultant solid dried under vacuum. The crude material was dissolved in $CHCl_3$ (300 mL), washed with brine (3 x 100 mL) and the organic layer separated and dried over $MgSO_4$. Solvent was removed under reduced pressure to form a gummy yellow solid left to dry thoroughly under vacuum. The crude product was recrystallised from hot $CHCl_3$/MeOH affording BisTBC[4]OMe as a white powder in 67.6% yield (6.76 g).

3. Synthesis of 2,2'-bis(*p*-*tert*-butylcalix[4]arene) (BisTBC[4], H_8L)

Cyclohexyl iodide (27.9 mL, 216 mmol, 45 equiv.) was added to a solution of BisTBC[4]OMe (6.76 g, 4.80 mmol, 1 equiv.) in dmf (150 mL). The solution was heated at reflux for 48 hours, with a concomitant colour change from pale yellow to dark orange. The solution was poured into H_2O (250 mL) and the resultant orange precipitate collected, washed thoroughly with H_2O and stirred in MeOH for 15 minutes. The resultant white solid was filtered, washed several times with MeOH and collected under reduced pressure. The crude product was recrystallised from hot $CHCl_3$/MeOH to afford BisTBC[4] in 71.2% yield (4.43 g). ^{1}H NMR (500 MHz, $CDCl_3$): δ (ppm) 10.42 (s, 8H, ArOH), 7.20 (d, *J* = 2.2 Hz, 4H, ArH), 7.02 (d, *J* = 2.3 Hz, 4H, ArH), 6.84 (d, *J* = 2.2 Hz, 4H, ArH), 5.81 (s, 1H, methine CHO), 4.26 (d, *J*=13.8 Hz, 2H, Ar-CH_2-Ar (H_{ax})), 4.19 (d, *J*, 14.0 Hz, 4H, Ar-CH_2-Ar (H_{ax})), 3.53 (d, *J* = 13.8 Hz, 2H, Ar-CH_2-Ar (H_{eq})), 3.42 (d, *J* = 13.9 Hz, 2H, Ar-CH_2-Ar (H_{eq})), 1.21 (s, 36H, ^{t}Bu), 1.09 (s, 36H, ^{t}Bu).

Synthesis of $[Mn^{III}_2Mn^{II}_2(L)(CH_3COO)(\mu_3\text{-}OH)(MeOH)_{1.4}(H_2O)_{1.6}(dmf)_3]\cdot 1.25dmf\cdot H_2O$ (15)

H_8L (200 mg, 0.154 mmol), $Mn(CH_3COO)_2\cdot 4H_2O$ (302 mg, 1.232 mmol) and NEt_3 (0.4 mL, 2.870 mmol) were dissolved in dmf/MeOH (1:1 v/v, 24 mL) and stirred for 2 hours. After filtration, the solution was allowed to evaporate slowly to afford dark purple crystals of **15** in 41% yield after 7 days. Elemental analysis (%) calculated for **15**: C, 62.97; H, 7.44; N, 3.00. Found: C, 62.57; H, 7.31; N, 2.59.

Synthesis of $[Mn^{III}_2Mn^{II}_2(L)(Me\text{-}deaH)(\mu_3\text{-}OMe)(H_2O)_2(dmf)_2]\cdot 4MeCN$ (16)

H_8L (200 mg, 0.154 mmol), $MnCl_2\cdot 4H_2O$ (31 mg, 0.154 mmol), Me-deaH_2 (0.12 mL, 1.078 mmol) and NEt_3 (0.4 mL, 2.870 mmol) were dissolved in dmf/MeOH (1:1 v/v, 24 mL) and stirred for 2 hours. After filtration, MeCN was diffused into the mother liquor affording dark purple crystals of **16** in 32% yield after 7 days. Elemental analysis (%) calculated for **16**: C, 64.76; H, 7.40; N, 4.89. Found: C, 64.49; H, 7.13; N, 4.56.

Synthesis of $[Mn^{III}_5Mn^{II}_2(L)(H_4L)(pdmH)_2(\mu_3\text{-}O)_2(\mu_3\text{-}OH)(dmf)_2(MeOH)_2]\cdot 7.5dmf$ (17)

H_8L (200 mg, 0.154 mmol), $MnCl_2\cdot 4H_2O$ (0.122 g, 0.616 mmol), pdmH_2 (0.171 g, 1.232 mmol) and NEt_3 (0.4 mL, 2.870 mmol) were dissolved in dmf/MeOH (1:1 v/v, 24 mL) and stirred for 2 hours. After filtration, the solution was allowed to evaporate slowly to afford dark purple crystals of **17** in 30% yield after 7 days. Elemental analysis (%) calculated for **17**: C, 67.26; H, 5.05; N, 3.94. Found: C, 66.85; H, 4.81; N, 3.73.

Synthesis of $[Mn^{III}_4Mn^{II}_6(L)_2(\mu_3\text{-}OH)_4(\mu\text{-}OH)_4(MeOH)_4(dmf)_4(MeCN)_2]\cdot MeCN$ (19)

H_8L (200 mg, 0.154 mmol), $MnCl_2\cdot 4H_2O$ (170 mg, 0.86 mmol) and NEt_3 (0.4 mL, 2.870 mmol) were dissolved in dmf/MeOH (1:1 v/v, 24 mL) and stirred for 2 hours. After filtration, MeCN was diffused into the mother liquor, affording dark purple crystals of **19** in 31% yield after 7 days. Elemental analysis (%) calculated for **19**: C, 62.64; H, 6.82; N, 2.58. Found: C, 62.18; H, 6.30; N, 2.05.

Synthesis of $[Cu^{II}_{16}(L)_2(Me\text{-}dea)_4(\mu_4\text{-}NO_3)_2(\mu\text{-}OH)_4(dmf)_{3.5}(MeOH)_{0.5}(H_2O)_2](H_6L)\cdot 16dmf\cdot 4H_2O$ (25)

H_8L (200 mg, 0.154 mmol), $Cu(NO_3)_2\cdot 3H_2O$ (0.250 g, 1 mmol), Me-deaH_2 (0.02 mL, 0.174 mmol) and NEt_3 (0.4 mL, 2.870 mmol) were dissolved in dmf/MeOH (1:1 v/v, 24 mL) and stirred for 2 hours. After filtration, the solution was allowed to evaporate slowly to afford dark brown crystals of **25** in 18% yield after 7 days. Elemental analysis (%) calculated for **25**: C, 58.06; H, 7.25; N, 5.03. Found: C, 57.82; H, 6.93; N, 4.69.

X-ray crystallography

Single crystal X-ray diffraction data for **15** were collected on a Rigaku 007HF equipped with Varimax confocal mirrors, a UG2 goniometer and HyPix 6000HE detector and operating with CuK_α radiation (1.54184 Å). Diffraction data for **16** and **25** were collected on a Bruker D8

diffractometer equipped with a PHOTON 100 detector and operating with synchrotron radiation (0.7749 Å). Diffraction data for **17** were collected on a Diamond Light Source I-19 diffractometer operating with synchrotron radiation (0.6889 Å). Diffraction data for **19** were collected on a Bruker Kappa APEXII DUO CCD diffractometer operating with CuK_α radiation (1.54178 Å). Crystal data for **15**-**17**, **19** and **25** are given in Tables S2.1-S2.3. Structures were solved using ShelXT/ShelXL and refined with version 2018/3 of ShelXL interfaced through Olex2.[4,5] All non-hydrogen atoms were refined anisotropically. Most hydrogen atom positions were calculated geometrically and refined using the riding model, but some hydrogen atoms were refined freely.

Powder X-ray diffraction data for **15**-**17**, **19** and **25** were collected on polycrystalline powders using a Bruker D8 ADVANCE with Cu radiation at 40 kV, 40mA and a Johansson monochromator, 2mm divergence slit and 2.5 degree Soller slits on the incident beam side, LynxEye detector and Bruker DIFFRAC software. Data were measured from 2θ = 2 - 30°; step size, 0.0101°. Freshly prepared crystalline powders were loaded into borosilicate capillaries with a 0.7 mm inside diameter and measured while spinning (Figure S2.1).

Magnetic data

Magnetic susceptibility and magnetisation data were collected on powdered microcrystalline samples using a Quantum Design MPMS XL SQUID magnetometer equipped with a 7 T dc magnet (**15**-**17** and **19**) and a Quantum Design PPMS DynaCool magnetometer equipped with a 9 T dc magnet (**25**). Susceptibility data were collected in the T = 298 - 2 K range under an applied magnetic field, B = 0.1 T. Magnetisation data were collected in the ranges T = 2 - 7 K and B = 0 - 7 T (**15**-**17**, **19**) and T = 2 - 10 K and B = 0 - 9 T (**25**). Data were modelled using PHI v3 software (**15**,**16**) and bespoke collaborator software (**25**, SP) – see Format of Thesis.

EPR spectroscopy

EPR spectra were measured on powder and solution (CH_2Cl_2/toluene) samples of **25**, at 10 and 20 K and over the 0 - 1.8 T field range, on a Bruker EMXPlus spectrometer.

Computational details

Density Functional Theory (DFT) calculations were performed on the full crystal structures of complexes **19** and **20**. The energies of each spin configuration were computed using a hybrid UB3LYP functional with the TZV basis set as implemented in Gaussian 16 software.[6,7] The

exchange interactions were estimated using the broken symmetry approach,[8] which has been shown to yield good numerical estimates of *J* values in polymetallic systems based on the extended pair-wise interaction model proposed by Ruiz and co-workers.[9–13] The spin-Hamiltonian used to estimate the exchange interactions is given in the supplementary information (Equation S2.1). We also estimated these using Yamaguchi's spin-projection formula for the model complex which yielded very similar results.[14]

DFT in conjunction with the broken symmetry approach was also used to estimate the magnetic exchange interactions in **25** using Gaussian 09.[15] The hybrid B3LYP functional[16–19] together with Ahlrichs TZV basis set was used for the Cu atoms, the SVP basis set for O and N atoms, and the SV basis set for C and H atoms.[6,7,20]

2.3 Results and Discussion

Structure descriptions

Reaction of H_8L with $Mn(CH_3COO)_2{\cdot}4H_2O$ in a basic dmf/MeOH mixture affords single crystals of formula $[Mn^{III}_2Mn^{II}_2(L)(CH_3COO)(\mu_3\text{-}OH)(MeOH)_{1.4}(H_2O)_{1.6}(dmf)_3]{\cdot}1.25dmf{\cdot}H_2O$ (**15**, Figure 2.3), following slow evaporation of the mother liquor. The crystals were found to be in a triclinic cell and structure solution was carried out in space group *P*-1. The ASU comprises the whole formula and pertinent bond parameters and BVS calculations are given in Table S2.4. Ligand L has undergone conformational inversion to accommodate the $[Mn^{III}_2Mn^{II}_2]$ distorted butterfly in **15**, which itself is reminiscent of the structure of the TBC[4]-supported $[Mn_4]$ (**2**, Chapter 1) in that the Mn^{III} ions bound within the TBC[4] cavities occupy the wings and the Mn^{II} ions occupy the body positions (Figure 2.3c).[21] The butterfly is asymmetric with just one

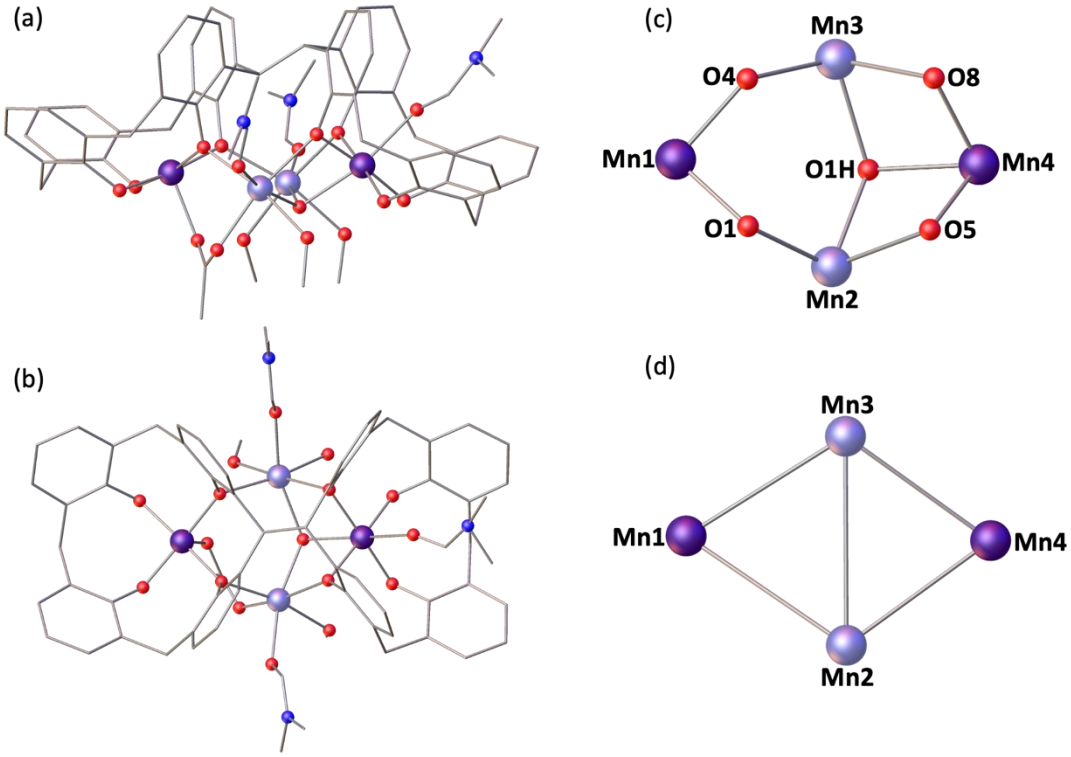

Figure 2.3 Single crystal X-ray structure (side-on (a); top-down (b)), cluster core (c) and metallic skeleton (d) of **15**. Colour code: Mn^{III} - dark purple, Mn^{II} - light purple, N - blue, C - grey, O - red. H atoms, ^{t}Bu groups of L and co-crystallised solvent molecules omitted for clarity.

μ_3-OH (O1H) present, bridging between Mn2, Mn3 and Mn4, and a single μ-CH_3COO ligand bridging between Mn1 and Mn2. The distorted octahedral geometries of the Mn^{II} ions (Mn2, Mn3) are completed by monodentate ligand molecules - one dmf and one disordered MeOH/H_2O molecule on Mn2 and one dmf and two disordered MeOH/H_2O molecules on Mn3. The cavity of the TBC[4] moiety connected to Mn4 is occupied by a dmf molecule, completing the JT distorted (JT vector O3D-Mn4-O1H) octahedral geometry at this metal centre whilst the second pocket remains empty, Mn1 being 5-coordinate and square pyramidal.

Examination of the extended structure of **15** (Figure S2.2-S2.3) reveals that the cluster packs in opposite layers as visible in the *bc* plane, forming a honeycomb-like arrangement down the *c*-axis with each centre filled by hydrophobic ^{t}Bu groups. Some significant intermolecular interactions are noteworthy; both the μ_3-OH and ligated MeOH/H_2O molecule bonded to Mn3 show H-bonding to the same non-coordinating dmf molecule. Each cluster, however, appears to be isolated from nearest neighbours and exhibits no short contact interactions. It is worth noting that partial occupancy water molecules also reside within the lattice, although do not appear to interact with the clusters.

Reaction of H_8L with $MnCl_2{\cdot}4H_2O$ and *N*-methyldiethanolamine (Me-deaH_2) in a basic dmf/MeOH mixture affords single crystals of formula $[Mn^{III}_2Mn^{II}_2(L)(Me\text{-}deaH)(\mu_3\text{-}OMe)(H_2O)_2(dmf)_2]{\cdot}4MeCN$ (**16**, Figure 2.4), following diffusion of MeCN into the mother liquor. The crystals were found to be in a monoclinic cell and structure solution was carried out in space group $P2_1/m$. The asymmetric unit (ASU) comprises half of the reported formula, with disorder associated with the positions of the μ_3-OMe, μ-Me-deaH and H_2O molecules ligated to the metal centres. This is due to the presence of a plane of symmetry bisecting the molecule through the Mn1-Mn2 plane. Pertinent bond parameters and BVS calculations are given in the Table S2.5.

As with **15**, L has undergone conformational inversion in **16** to support the $[Mn^{III}_2Mn^{II}_2]$ distorted butterfly. Mn1 and Mn2 are both in the third oxidation state, display distorted square pyramidal geometries and are located in the tetraphenolic cavities of L. The coordination spheres of Mn1 and Mn2 are completed *via* ligation to the O-atom (O6) of the μ-Me-deaH ligand and μ_3-OMe group (O5), respectively. An MeCN molecule occupies the cavity of the TBC[4] unit at a C···Mn distance of ~4 Å. The μ_3-OMe moiety also bridges Mn3

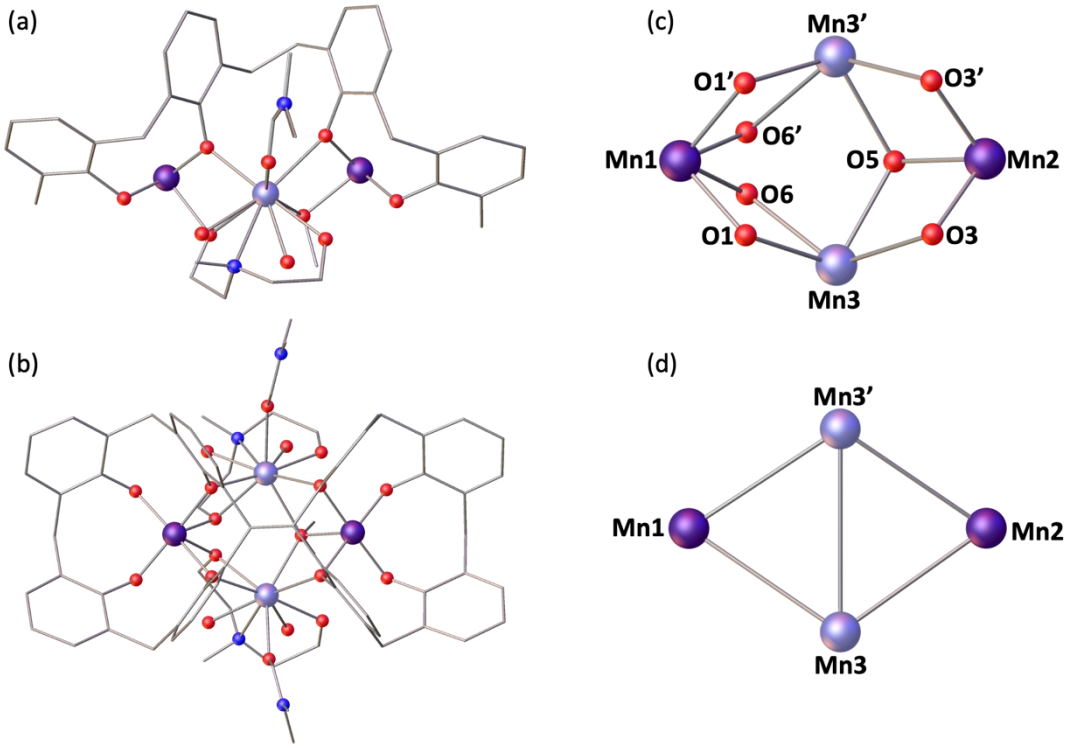

Figure 2.4 Single crystal X-ray structure (side-on (a); top-down (b)), cluster core (c) and metallic skeleton (d) of **16**. Colour code: Mn^{III} - dark purple, Mn^{II} - light purple, N - blue, C - grey, O - red. H atoms, ^{t}Bu groups of L and co-crystallised solvent molecules omitted for clarity.

(and symmetry equivalent Mn3') which is in the second oxidation state and is located in the additional binding site generated by L, such that two O-atoms from two distinct TBC[4] moieties are coordinated. Ligation is completed *via* the O- and N-atoms of the disordered bidentate Me-deaH ligand, the disordered H_2O and a single dmf molecule. Examination of the extended structure of **16** (Figure S2.4) shows that the cluster packs in opposite layers down the *a*-axis with no significant intermolecular interactions. Each cluster is well isolated from its neighbours and the closest M···M distance is ~9.1 Å between the Mn3 ions of distinct molecules.

It is worth noting that replacing H_4TBC[4] with H_8L in an otherwise analogous reaction to that of **2** does not provide a successful method of obtaining the $[Mn^{III}_2Mn^{II}_2]$ butterfly, which suggests the presence of the co-ligand, as in **15**-**16**, is essential in stabilising the perturbed L-supported butterfly motif. Further investigation of co-ligand influence on L-supported clusters

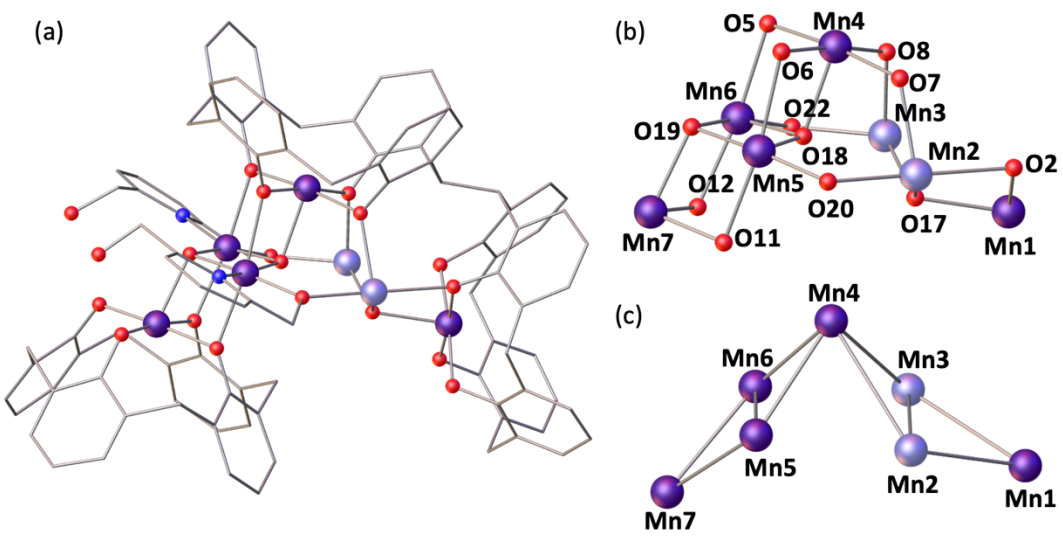

Figure 2.5 Partial single crystal X-ray structure (a), cluster core (b) and metallic skeleton of **17**. Colour code: Mn^{III} - dark purple, Mn^{II} - light purple, N - blue, C - grey, O - red. H atoms, ^{t}Bu groups of L, one TBC[4] moiety of *anti*-L and co-crystallised solvent molecules omitted for clarity.

through the reaction of H_8L with $MnCl_2{\cdot}4H_2O$ and 2,6-pyridinedimethanol ($pdmH_2$) in a basic dmf/MeOH mixture affords single crystals of formula $[Mn^{III}_5Mn^{II}_2(L)(H_4L)(pdmH)_2(\mu_3\text{-}O)_2(\mu_3\text{-}OH)(dmf)_2(MeOH)_2]{\cdot}7.5dmf$ (**17**, Figures 2.5 - 2.6a), following slow evaporation of the mother liquor. The crystals were found to be in a triclinic cell and structure solution was carried out in space group *P*-1. Pertinent bond parameters and BVS calculations are given in Table S2.6.

The $[Mn^{III}_5Mn^{II}_2]$ metallic skeleton describes two perpendicular, vertex sharing $[Mn_4]$ butterflies of distinct forms. One butterfly (Mn4-7) is homovalent and of the form $[Mn^{III}_4(\mu_3\text{-}O)_2(\mu\text{-}OR_L)_4]$. Two of the Mn^{III} ions (Mn4, Mn7) in this unit reside in the TBC[4] cavities of L, occupying the wing-tip positions of the butterfly as with **2**, **15** and **16**. The remaining Mn^{III} ions (Mn5, Mn6) are supported in the body positions of the butterfly by μ_3-O and μ-pdmH ligands, the latter of which also ligates to the Mn^{II} ions (Mn2, Mn3) in the body positions of the second butterfly. This butterfly (Mn1-4) is heterovalent and displays a rather unusual $[Mn^{III}_2Mn^{II}_2(\mu_3\text{-}OH)(\mu\text{-}OR_L)_3(OR_L)]$ unit, where just one μ_3-OH anion links Mn1, Mn2 and Mn3. The Mn^{III} ions (Mn1, Mn4) again reside within the TBC[4] pockets, corroborating the established ion binding rules. This latter butterfly is supported by the *syn*-L as is expected, since conformational inversion of L is what generates the additional binding sites.

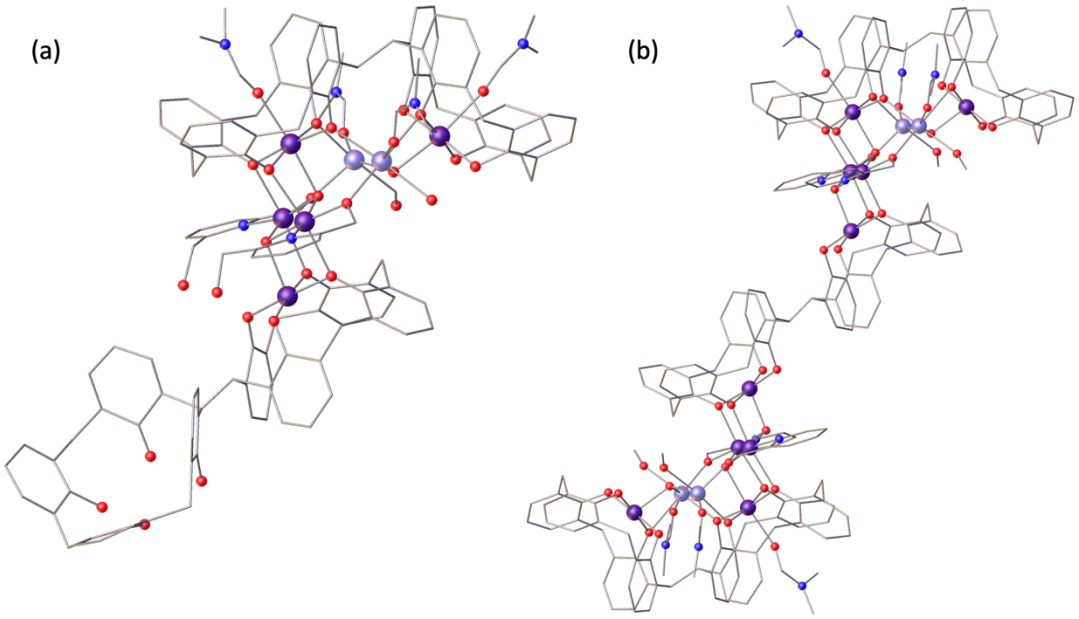

Figure 2.6 Single crystal X-ray structures of **17** (a) and **18** (b).[22] Colour code: Mn^{III} - dark purple, Mn^{II} - light purple, N - blue, C - grey, O - red. H atoms, ^{t}Bu groups of L and co-crystallised solvent molecules omitted for clarity.

Interestingly, the former homovalent butterfly is supported by one TBC[4] moiety from *syn*-L and one from *anti*-L. This partial inversion of L in **17** is also observed in the related (and previously published) complex $[Mn^{III}_{10}Mn^{II}_{4}(L)_3(hmp)_4(\mu_3\text{-}O)_4(\mu_3\text{-}OH)_2(MeOH)_4(dmf)_6]\cdot 4dmf$ (**18**, Figure 2.6b),[22] the ASU of which is very similar to **17**. The important distinction is, that whilst in **17** the 'spare' TBC[4] moiety of the *anti*-L is left empty, in **18** it goes on to bind another $[Mn^{III}_{5}Mn^{II}_{2}]$ unit with a third L ligand. This suggests that the inclusion of a slightly bulkier co-ligand (μ-pdmH in **17** compared to μ-hmp in **18**) prevents the cluster from continued growth.

Mn1, Mn4 and Mn7 are all five-coordinate and in distorted square pyramidal geometries, bound by four $\mu\text{-}OR_L$ phenolic oxygen atoms and a μ_3-OH (Mn1) / μ_3-O (Mn4, Mn7) bridge (Mn-O bond distances in the range ~1.90-2.18 Å). The remaining Mn^{III} ions (Mn5, Mn6) are six-coordinate and in JT distorted octahedral geometries. They are supported by two $\mu\text{-}OR_L$ phenolic oxygen atoms, each belonging to the TBC[4] moieties of distinct neighbouring L ligands, and the $R_LO\text{-}Mn\text{-}OR_L$ vectors of which define the JT axes (Mn-O bond distances in the range ~2.18-2.30 Å). Their coordination spheres are the same, each being completed by two μ_3-O bridges and a ligated μ-pdmH molecule (Mn-O bond distances in the range ~1.89-1.94

Å, Mn-N bond distances in the range ~2.11-2.14 Å), which chelates through just two of the three possible bonding modes (Figure S2.5). Mn2 is located in one of the additional binding sites that are generated upon the conformational inversion of L, such that it is bound by two phenolic oxygen atoms of different TBC[4] moieties within the same ligand. Mn2 is in a distorted octahedral geometry, with ligation completed through μ_3-OH, μ-pdmH, a terminal MeOH and a terminal dmf molecule (Mn-O bond distances in the range ~2.16-2.33 Å). Mn3 displays trigonal bipyramidal geometry, only making use of one of the two phenolic oxygen atoms of the additional binding site. We do not define the Mn3···O1 long contact in **17** as a formal bond due in part to its own extended length (~2.55 Å) but also the length of the analogous long contact in **18** (~2.65 Å). Ligation of Mn3 is then completed *via* μ_3-OH, μ-pdmH, a terminal MeOH and a terminal dmf molecule (Mn-O bond distances in the range ~2.10-2.25 Å). There are several intramolecular H-bonds throughout the cluster; both μ_3-O19 and the phenolic O9 H-bond to the uncoordinated arm of the pdmH co-ligand. Phenolic O-atoms (O3, O4) also H-bond with the nearest MeOH ligands whilst the protonated TBC[4] moiety H-bonds about the phenolic cavity as expected.

Examination of the extended structure of **17** reveals that the closest intermolecular interactions are between the ^{t}Bu groups of the calix[4]arene moieties (C···C, >3.6 Å). The clusters pack in a brickwork like pattern when viewed down the *b*-axis of the cell, with the 'empty' H_4TBC[4] units helping to isolate the $[Mn^{III}_5Mn^{II}_2]$ units from each other (Figure S2.6). Each cluster appears to be isolated from nearest neighbours and exhibits no short contact interactions. It is worth noting that the electron equivalent of 7.5 dmf molecules were removed after modelling of the crystallographic data and these will reside within the lattice.

Adjustment of reaction conditions and reactant stoichiometries in previously explored syntheses creates another path to access new topologies, yielding $[Mn^{III}_4Mn^{II}_6(L)_2(\mu_3\text{-}OH)_4(\mu\text{-}OH)_4(MeOH)_4(dmf)_4(MeCN)_2]\cdot MeCN$ (**19**, Figure 2.7). Herein, we outline the synthetic and structural similarities between this novel cluster and the related, previously published species $[Mn^{III}_6Mn^{II}_4(L)_2(\mu_3\text{-}O)_2(\mu_3\text{-}OH)_2(\mu\text{-}OMe)_4(H_2O)_4(dmf)_8]\cdot 4dmf$ (**20**).[23] Reaction of H_8L with $MnCl_2\cdot 4H_2O$ in a basic dmf/MeOH mixture affords single crystals of **19** following vapour diffusion of MeCN into the mother liquor.[24] The crystals were found to be in a monoclinic cell and structure solution was carried out in the space group $P2_1/n$. The ASU comprises half of the cluster, with an inversion centre located in the middle of the Mn5-O14-Mn5'-O14' rhombus. Pertinent bond lengths and angles and BVS calculations are given in Table S2.7.

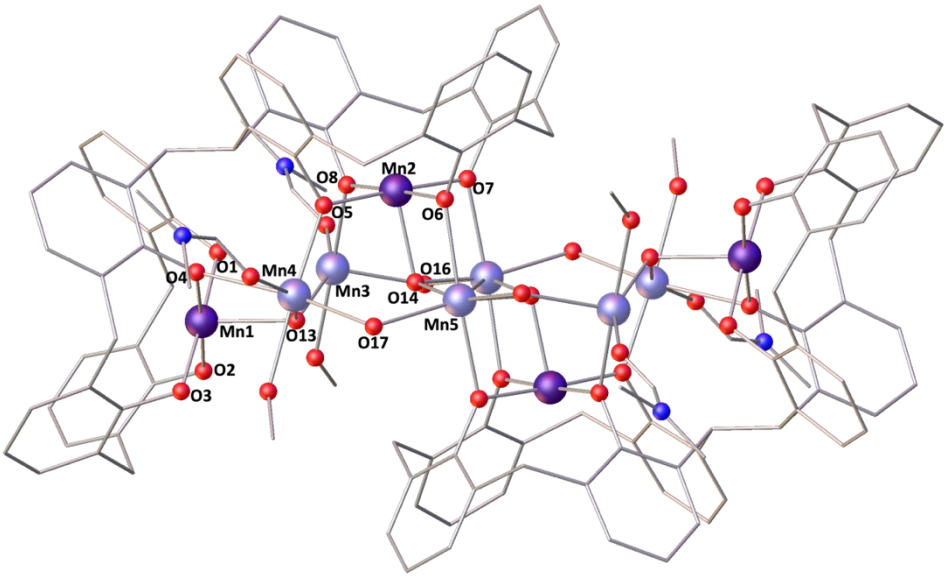

Figure 2.7 Single crystal X-ray structure of **19**. Colour code: Mn^{III} - dark purple, Mn^{II} - light purple, N - blue, C - grey, O - red. H atoms, ^{t}Bu groups of L and co-crystallised solvent molecules omitted for clarity.

Both L ligands are arranged such that one TBC[4] moiety in each has undergone inversion in order to accommodate a $[Mn^{II}_6Mn^{III}_4]$ metallic skeleton that describes three vertex-sharing $[Mn^{II}_2Mn^{III}_2]$ butterflies (Figure 2.8). These are of two types. The central butterfly (Mn2, Mn5, and symmetry equivalent) is of the form $[Mn^{III}_2Mn^{II}_2(\mu_3\text{-OH})_2(\mu\text{-OR}_L)_4]$, maintaining the 'reversed' butterfly motif seen in **2**, **15** and **16**, whereby the Mn^{III} ions occupy the wings and the Mn^{II} ions occupy the body. The peripheral butterflies (Mn1-4) appear rather asymmetric and are of the form $[Mn^{III}_2Mn^{II}_2(\mu_3\text{-OH})(\mu\text{-OR}_L)_4]$ with just one μ_3-bridging OH anion (O13) linking Mn1, Mn3 and Mn4. O13 forms a hydrogen bond with the neighbouring μ_3-OH ion in the central butterfly (O13···O14, ~2.83 Å). The metal oxygen core is completed by the presence of four 'external' μ-OH ions that link the Mn^{II} ions in the body positions of the central butterfly to the Mn^{II} ions in the body positions of peripheral butterflies (Mn5'-O16-Mn3; Mn5-O17-Mn4). Thus, as expected, the L ligands bind the Mn^{III} ions within their polyphenolic pockets with the Mn^{II} ions encapsulated between them, linked through multiple OH anions.

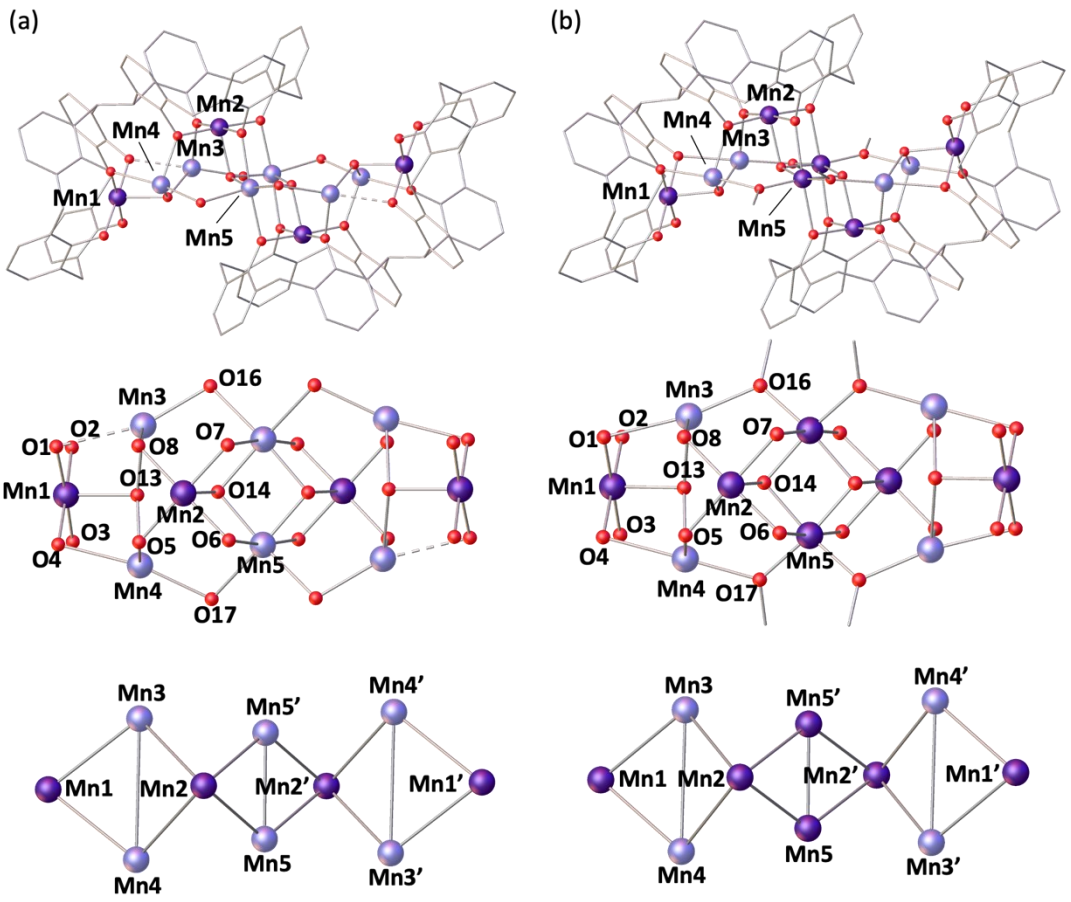

Figure 2.8 Single crystal X-ray structures (top), cluster cores (middle) and metallic skeletons (bottom) of **19** (a) and **20** (b).[23] Colour code: Mn^{III} - dark purple, Mn^{II} - light purple, C - grey, O - red. H atoms, ^{t}Bu groups of L and co-crystallised/ligated solvent molecules omitted for clarity. Dashed lines represent longer bond lengths (as discussed in text).

The Mn^{III} anions (Mn1, Mn2, and symmetry equivalent) are six-coordinate and in JT distorted octahedral geometries, with the JT axes defined by the HO-Mn-NCMe vector in each case. The acetonitrile molecules are disordered over two positions within the TBC[4] cavities, with Mn-N distances of ~2.34 Å and ~2.58 Å and N-Mn-O angles of ~169° and ~172°. The Mn^{II} ions are also six-coordinate but with rather different geometries. The two central Mn ions (Mn5) have $[Mn(OH)_4(OR_L)_2]$ coordination spheres with Mn-O bond lengths in the range ~1.99-2.29 Å, and *cis/trans* angles of ~78-98°/163-172°. Mn3 and Mn4 have their coordination spheres completed by one MeOH and one dmf, affording $[Mn(OH)_2(OR_L)_2(O_{solvent})_2]$ with (highly) distorted octahedral geometries. For both, five of the six Mn-O bond lengths fall in the range ~2.1-2.2 Å (Mn3) and ~2.1-2.3 Å (Mn4). The sixth bond, to the L O-atom, is much longer (Mn3-O1 = 2.577(7) Å and Mn4-O4 = 2.424(7) Å). A search of the CSD reveals that of over 93 000

Mn-O bond distance entries, only 325 are found to be between 2.5-2.6 Å, with 98.8% of the entries lying within the 1.8-2.5 Å range (Figure S2.7). *Cis/trans* angles are ~70-112°/154-176° (Mn3), and ~79-116°/154-175° (Mn4). The O-atoms of the terminally bonded MeOH molecules on Mn3 and Mn4 are H-bonded to the two terminally bonded OR_L atoms at distances of O15···O2, ~2.56 Å, and O18···O3, ~2.54 Å.

Examination of the extended structure of **19** reveals that clusters pack in a brickwork like pattern down the *b*-axis (Figure S2.8). The closest intermolecular interactions are between co-coordinated dmf molecules and the ^{t}Bu C-atoms at C···C distances ≥ 3.2 Å, and between neighbouring ^{t}Bu groups, C····C ≥ 3.8 Å. The closest M···M distance is ~12.3 Å between the Mn ions of distinct molecules, meaning they are structurally isolated thanks to the framework of the L ligands and overall shape of the assembly.

The structure of **19** is closely related to that of the previously published species $[Mn^{III}_6Mn^{II}_4(L)_2(\mu_3\text{-}O)_2(\mu_3\text{-}OH)_2(\mu\text{-}OMe)_4(H_2O)_4(dmf)_8]\cdot 4dmf$ (**20**). A comparison of the structures of **19** and **20** (Figure 2.8) reveals three significant differences: (a) the oxidation states of the central Mn5/Mn5' ions are different - Mn^{II} in **19** and Mn^{III} in **20**. (b) The bridging groups connecting Mn3/Mn4 to Mn5 are μ-OH in **19** but μ-OMe in **20**. (c) The O1-Mn3 distance in **19** is 2.577(7) Å compared to 2.436(4) Å in **20**. The former would be expected to have significant impact upon magnetic behaviour (*vide infra*). Note that **19** and **20** result from the methodical screening of reaction conditions, where changes in reagent stoichiometry and crystallisation conditions leads to the selective formation of either **19** or **20**. Indeed, the only major differences in the preparation of **19** and **20** comes in the ligand:metal ratio (1:6 (**19**), 1:8 (**20**)) and the method of crystallisation - MeCN diffusion into the dmf/MeOH mother liquor for **19** and slow evaporation of the dmf/MeOH solution for **20**.

Figure 2.9 shows that the structure of **19** is also related to the compounds $[Mn^{III}_6Mn^{II}_2Gd^{III}_2(L)_2(\mu_4\text{-}O)_2(\mu_3\text{-}OH)_2(\mu\text{-}OMe)_2(\mu\text{-}OH)_2(MeOH)_4(dmf)_8(NO_3)_2(H_2O)_2$ (**21**)[23] and $[Mn^{III}_4Mn^{II}_4(L)_2(\mu_3\text{-}OH)_2(\mu\text{-}OH)(\mu\text{-}Cl)(H_2O)(MeOH)(dmf)_4]$ (**22**),[25] which was the very first compound isolated with H_8L. The metallic skeleton of **21** describes three vertex-sharing $[Mn^{III}_2Mn^{II}_2Ln^{III}]$ butterflies, and that of **22** two vertex-sharing $[Mn^{III}_2Mn^{II}_2]$ butterflies. Indeed, from an inspection of **19-22** (Figures 2.8 and 2.9) it is clear to see that it is the $Mn^{III}L$ metalloligand that directs structure formation, with the additional Mn^{II}/Ln^{III} ions encapsulated within this framework connected *via* bridging hydroxides/alkoxides. What is

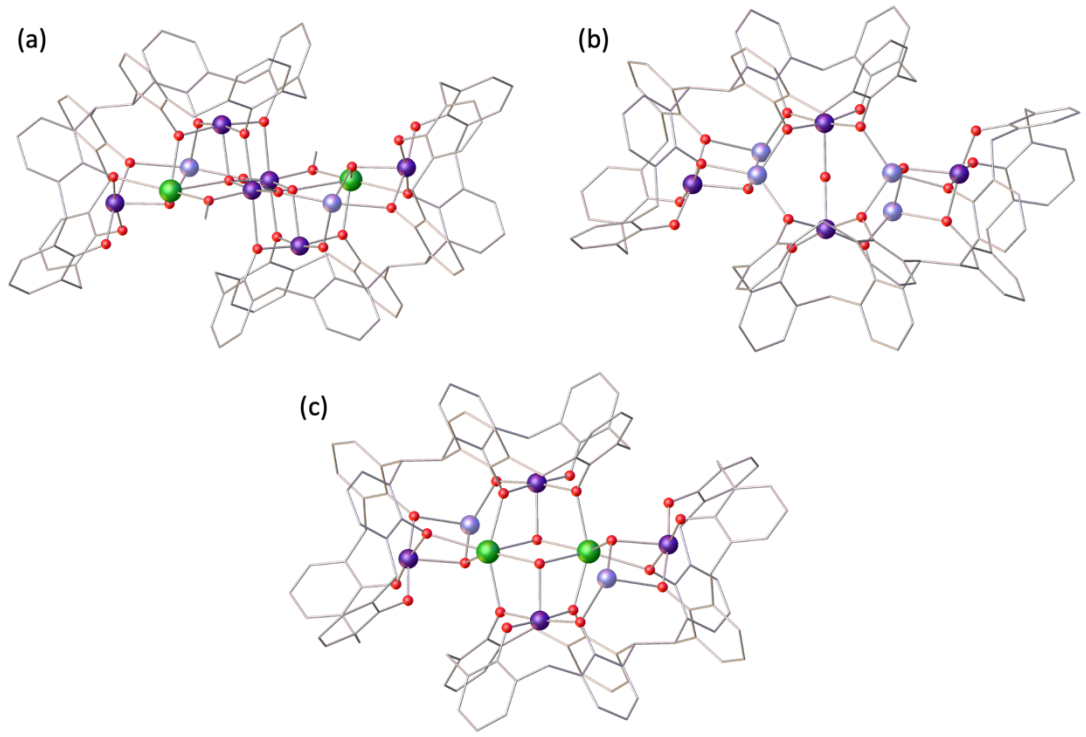

Figure 2.9 Single crystal X-ray structures of **21** (a),[23] **22** (b) and **23** (c).[25] Colour code: Mn^{III} - dark purple, Mn^{II} - light purple, Gd^{III} - green, C - grey, O - red. H atoms, ^{t}Bu groups of L and co-crystallised/ligated solvent molecules omitted for clarity.

also clear is that these encapsulated metal ions can be replaced whilst maintaining the general structure. This is illustrated by complex **22** undergoing selective Mn^{II}/Ln^{III} substitution to form $[Mn^{III}_4Mn^{II}_2Gd^{III}_2(L)_2(Cl)_2(\mu_3\text{-}OH)_4(MeOH)_2(dmf)_8]$ (**23**, Figure 2.9).[25] This mirrors the behaviour observed for TBC[4]. For example, the Mn^{II} ions in **2** can be replaced in a stepwise fashion with Ln^{III} ions, from $[Mn^{III}_2Mn^{II}_2]$ to $[Mn^{III}_2Mn^{II}Ln^{III}]$ and $[Mn^{III}_2Ln^{III}_2]$.[26] The isolation of multiple, structurally-related compounds is reflective of the versatility of the bis-calix[4]arene ligand for the construction of polymetallic clusters where subtle changes in reactants/conditions can be exploited to direct the nature of the metallic core and associated physical properties.

Replacing H_4TBC[4] with H_8L in the reaction yielding $[Cu^{II}_9]$ (**11**, *vide supra*) affords the previously published $[Cu^{II}_{13}(L)_2(NO_3)(\mu\text{-}OH)_8(dmf)_7](OH)$ (**24**) whose metallic skeleton describes a centred, tetracapped square prism (Figure 2.10).[25] The expansion from $[Cu_9]$ to $[Cu_{13}]$ is a result of the conformational flexibility of H_8L and so to explore this reaction space further we adapted the synthesis of **24** to include a co-ligand, namely Me-deaH_2.

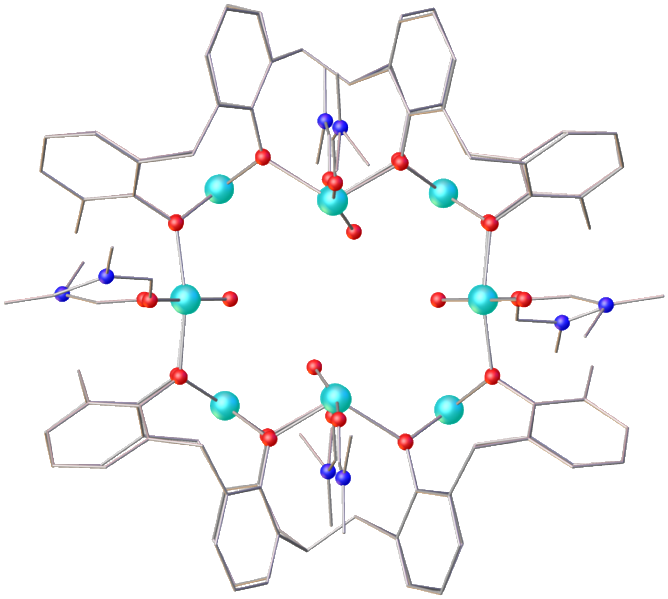

Figure 2.10 Single crystal X-ray structure of **24**.[25] Colour code: Cu^{II} - turquoise, N - blue, C - grey, O - red. H atoms, ^{t}Bu groups of L, co-crystallised solvent molecules and centred Cu^{II} ion omitted for clarity.

Reaction of H_8L with $Cu(NO_3)_2{\cdot}3H_2O$ and Me-deaH_2 in a basic dmf/MeOH mixture affords single crystals of formula $[Cu^{II}_{16}(L)_2(Me\text{-}dea)_4(\mu_4\text{-}NO_3)_2(\mu\text{-}OH)_4(dmf)_{3.5}(MeOH)_{0.5}(H_2O)_2](H_6L){\cdot}16dmf{\cdot}4H_2O$ (**25**, Figure 2.11-2.12), following slow evaporation of the mother liquor.[27] The crystals were found to be in a triclinic cell and structure solution was carried out in the space group *P*-1. The ASU comprises half of the cluster. Pertinent bond lengths and angles and BVS calculations are given in Table S2.8.

The metallic skeleton describes a tetracapped (Cu1-2 and symmetry equivalent) square prism (Cu3-6) in which the 'upper' and 'lower' square faces (as shown in Figure 2.12) are edge-capped by a $\{Cu_2\}$ (Cu7-8) moiety. The Cu ions in the upper and lower faces of the square prism are connected to each other by four μ-OH ions to form a $[Cu_8(OH)_4]$ central unit (Figure S2.9). The four face-capping Cu ions are housed in the polyphenolic pockets of the two fully deprotonated bis-calixarene ligands whose O-atoms further bridge to the Cu ions in the square prism (Cu3-Cu6; Figure S2.10). The L ligands thus wrap around the four square faces of the prism in the 'equatorial' plane, completely encapsulating the $[Cu_8(OH)_4]$ central unit. The upper and lower faces of the prism are connected to the $\{Cu_2\}$ edge-cap by a μ_4-NO_3 ion which connects Cu3-4 to Cu7-8. The latter are further bridged to each other and the Cu ions

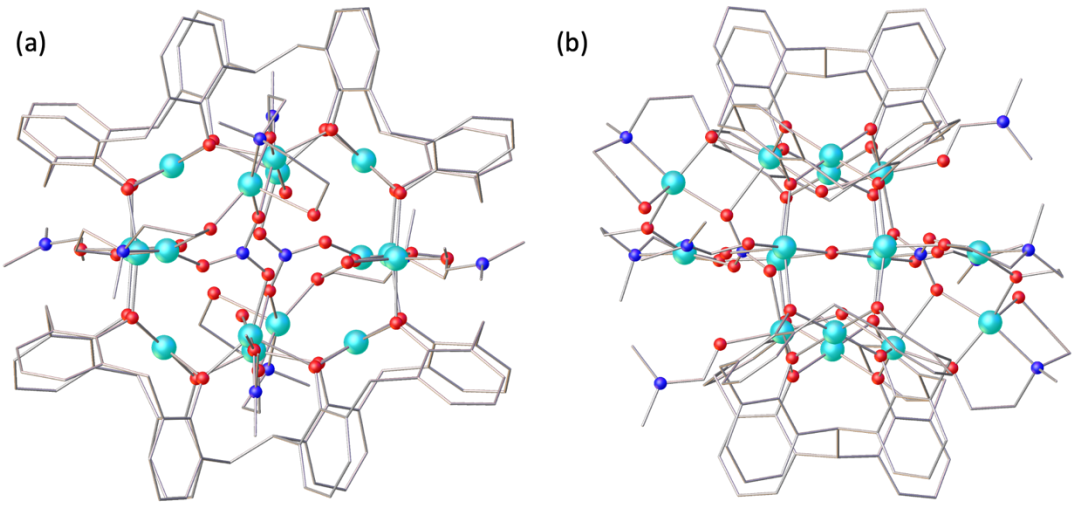

Figure 2.11 Orthogonal views of the single crystal X-ray structure of **25** shown face-on (a) and side-on (b)**.** Colour code: Cu^{II} - turquoise, N - blue, C - grey, O - red. H atoms, ^{t}Bu groups of L and co-crystallised solvent molecules omitted for clarity.

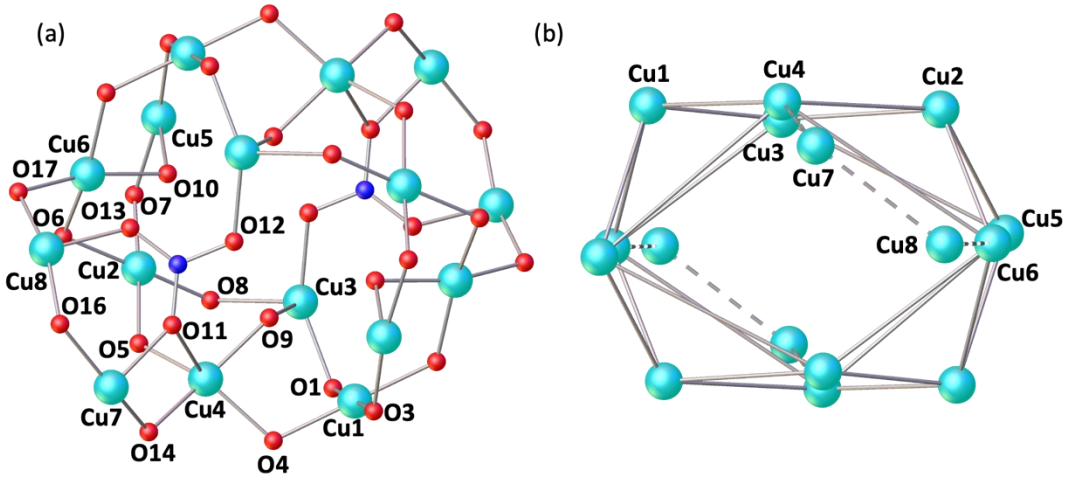

Figure 2.12 Cluster core (a) and metallic skeleton (b) of **25.** The eight Cu ions in the square prism are Cu3-6 and symmetry equivalent. The four face-capping Cu ions are Cu1-2. The four edge-capping Cu ions are Cu7-8. Colour code: Cu^{II} - turquoise, N - blue, O - red.

on the vertices of the square prism by two Me-dea ligands that bond in two different ways. The first μ_3-bridges, using one O-arm (O16) to link between Cu7-Cu8 and the other (O17) to link between Cu8 and Cu6 in the square prism. The second chelates to Cu7 with one O-arm terminally coordinated (O15) and one arm (O14) bridging to Cu4 in the square prism.

The Cu ions (Cu1-2) that sit in the tetraphenolic pocket of L are square planar with a fifth longer contact to a disordered molecule of dmf that fills the calixarene cavity. The Cu ions in the square prism (Cu3-6) are all five-coordinate and in distorted square pyramidal geometry (Cu3-5) or four-coordinate and in square planar geometry (Cu6), the remaining sites on Cu3 and Cu5 being occupied by dmf/H_2O molecules. The Cu ions in the edge-capping $\{Cu_2\}$ moiety (Cu7, Cu8) bonded to the Me-dea ligands are five-coordinate, square pyramidal $\{CuO_4N\}$ and four-coordinate, square planar $\{CuO_3N\}$ respectively.

The complex displays numerous intra- and intermolecular H-bonding interactions. The water molecule bonded to Cu5 is H-bonded to two O-atoms of the nitrate anion (O19···O12/O11, ~2.83-3.01 Å). O12 is also H-bonded to a μ-OH ion (O12···O9, ~2.95 Å), and the third O-atom in the nitrate anion (O13) is H-bonded to a dmf molecule bonded to Cu3 (O13···O18, ~3.00 Å). There is also a complex H-bonding network in the region of one of the two Me-dea co-ligands. The O-atoms (O15) belonging to the Me-dea ligand supporting Cu7 is H-bonded to a H_2O molecule of crystallisation (O15···O21, ~2.72 Å). The latter is also interacting with the lower-rim oxygen atom of the co-crystallised H_6L^{2-} ligand (O21···O26, ~2.72 Å). Upon symmetry expansion, it is possible to appreciate the importance of this network of H-bonds as it dictates the way compound **25** and the co-crystallised molecules pack, through the formation of H-bonded chains; the $[Cu_{16}]$ cluster is surrounded at its four 'corners' by co-crystallised H_6L^{2-} (Figures S2.11). This doubly deprotonated molecule affords overall charge balance, and although there are waters of crystallisation present (and therefore potentially OH^- counter ions), we favour the presence of this dianion for two reasons. (1) The intermolecular interactions discussed above; (2) refinement suggests each TBC[4] moiety in H_6L^{2-} is singly deprotonated, consistent with the highly acidic nature of H_4TBC[4] hydroxyl groups reported in literature.[28] The clusters are well isolated from each other, with the closest Cu···Cu distance being >12 Å between the Cu8 ions of distinct molecules. A search of the CSD shows that there are a total of thirteen $[Cu^{II}_{16}]$ clusters known, none of which have a topology similar to **25**.[29–39]

A comparison of the metallic skeletons of $[Cu_9]$, $[Cu_{13}]$ and $[Cu_{16}]$ shows striking similarities (Figure 2.13). $[Cu_9]$ is a tricapped trigonal prism in which the square faces are all capped by a Cu ion housed in the pocket of a TBC[4] moiety, with halide/nitrate anions capping the upper/lower triangular faces. $[Cu_{13}]$ is a centred, tetracapped square prism in which the 'equatorial' square faces are all capped by a Cu ion housed in the pocket of a TBC[4] moiety with nitrate anions capping the upper/lower triangular faces. $[Cu_{16}]$ has a structure analogous

to [Cu_{13}] but without the central ion, and with two additional {Cu_2} edge-capping moieties introduced through the presence of a co-ligand. These structural similarities reflect the dominant, structure-directing influence of the calix[4]arene ligands.

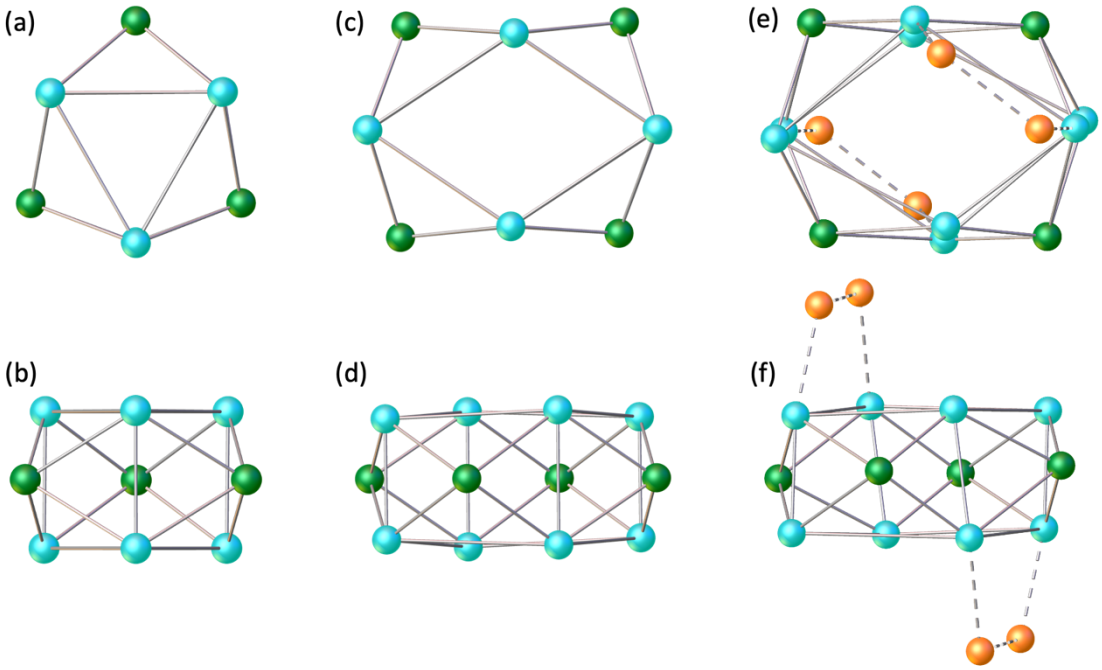

Figure 2.13 A comparison of the metallic skeletons of [Cu_9] (**11**, (a) and (b)), [Cu_{13}] (**24**, (c) and (d))[25] and [Cu_{16}] (**25**, (e) and (f)). The central, distorted Cu ion in [Cu_{13}] has been removed to aid comparison. [Cu_9] describes a tricapped trigonal prism, [Cu_{13}] a (centred) tetracapped square prism, and [Cu_{16}] a tetracapped square prism containing two additional {Cu_2} edge-caps. The Cu ions in the prisms are in turquoise, those housed in the tetraphenolic calixarene pocket in green and the edge-caps in orange.

Magnetic measurements

Direct current (dc) susceptibility studies were performed on polycrystalline samples of **15** and **16** over the temperature range T = 298 - 2 K, in an applied magnetic field B = 0.1 T (Figure 2.14), where $\chi_M = M/B$ and M is the magnetisation. The magnetic behaviour of both $[Mn^{III}_2Mn^{II}_2]$ complexes are similar and thus they can be considered here together. At 298 K, the $\chi_M T$ values of 13.63 cm^3 K mol^{-1} (**15**) and 13.79 cm^3 K mol^{-1} (**16**) are below that expected for the spin-only contributions of a $[Mn^{III}_2Mn^{II}_2]$ unit (14.75 cm^3 K mol^{-1}, g = 2.00). Upon cooling, the $\chi_M T$ product decreases steadily until approximately T = 100 K, where it decreases more rapidly, reaching values of 4.17 cm^3 K mol^{-1} (**15**) and 7.60 cm^3 K mol^{-1} (**16**) at T = 2 K. Variable-temperature-variable-field (VTVB) magnetisation data (Figure S2.12 (**15**), S2.13 (**16**)) show magnetisation rising slowly with increasing field, reaching maximum values of M = 7.29 μ_B (**15**) and M = 8.41 μ_B (**16**) at 7 T without saturating. This behaviour is indicative of weak, competing exchange interactions dominated by the antiferromagnetic contributions.

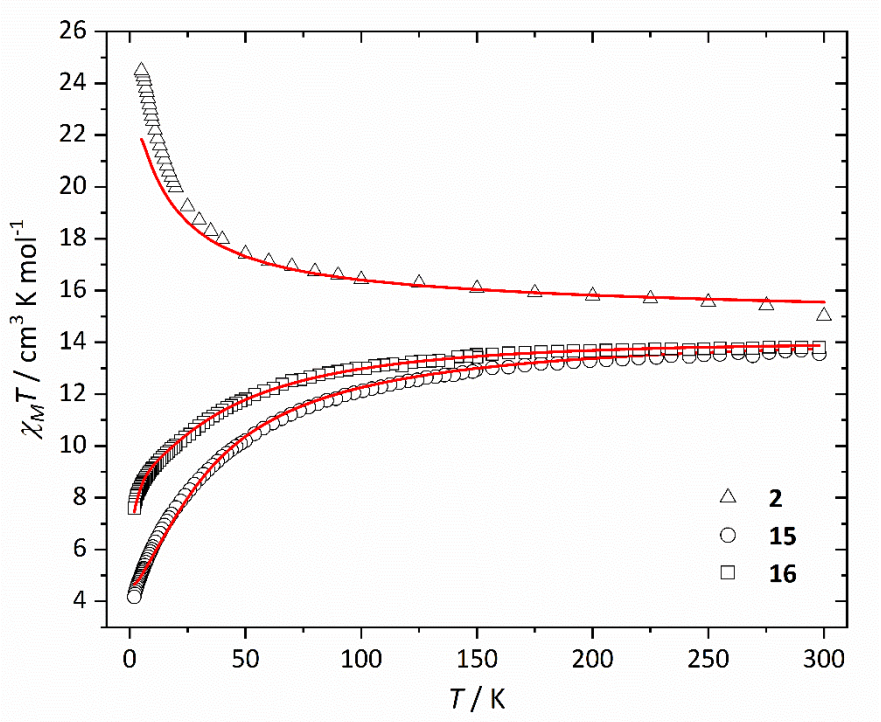

Figure 2.14 Experimental $\chi_M T$ *vs* T data for **15** (circles) and **16** (squares) measured in the T = 298 - 2 K temperature range in an applied field, B = 0.1 T. The equivalent data for **2** (triangles) is included for comparison.[21] The solid red lines are the best fits modelled using spin-Hamiltonian (2.1).

Qualitative comparison of the susceptibility data for **15** and **16** with respect to TBC[4]-supported $[Mn^{III}_2Mn^{II}_2]$ complex **2** (Figure 2.14) reveals that the perturbation of the butterfly driven by ligation of BisTBC[4] and the respective co-ligands promotes antiferromagnetic exchange.

The quantitative interpretation of the temperature dependence of the $\chi_M T$ product of **15** and **16** was performed by simultaneous fitting of the susceptibility and magnetisation data to spin-Hamiltonian (2.1), where the summation indices *i, j* run though the constituent metal ions, *D* is the uniaxial single-ion anisotropy parameter, $\hat{S}$ is a spin operator, *S* is the total spin, μ_B is the Bohr magneton, *g* is the *g*-factor (fixed at *g* = 2.00), and J_{ij} is the bilinear pairwise isotropic exchange interaction parameter.

$$\hat{H} = \sum_i D_i\left(\hat{S}_{z,i}^2 - S_i(S_i+1)/3\right) + \mu_B B \sum_i g_i \hat{S}_i - 2\sum_{i,j<1} J_{i,j}\hat{S}_i \cdot \hat{S}_j \qquad (2.1)$$

The asymmetry introduced by the ligation of the acetate on just one 'edge' of the butterfly in **15**, and the disorder of bridging ligands in **16,** prevents the same exchange pathways being modelled for both complexes. Observation of the crystal structure of **15** reveals 4 unique magnetic interaction pathways due to the asymmetry of the bridging ligands making up the butterfly. However, to avoid over-parameterisation we used a 2*J* model (Figure 2.15a), where *J* is the interaction between Mn^{III}-Mn^{II} ions (Mn1-Mn2, Mn1-Mn3, Mn2-Mn4, Mn3-Mn4) and *J'* is the interaction between Mn^{II}-Mn^{II} ions (Mn2-Mn3), and introduced a $D_{Mn(III)}$ parameter making the fit comparable to that of **2** in literature. This resulted in excellent agreement with

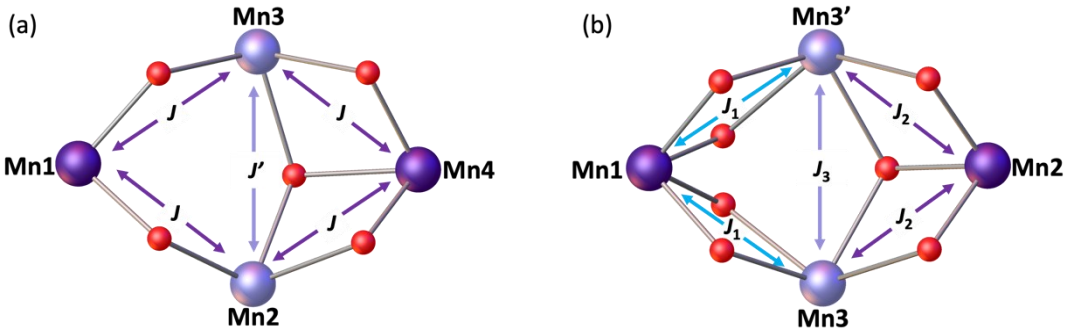

Figure 2.15 Schematic representation of the 2*J* (a) and 3*J* (b) models used to fit the experimental susceptibility data of **15** and **16** respectively, as discussed in text.

experimental data (Figure 2.14) with best-fit parameters J = -0.58 cm^{-1}, J' = -2.11 cm^{-1} and $D_{Mn(III)}$ = -2.83 cm^{-1}. However, the exchange parameters J and $D_{Mn(III)}$ are strongly correlated with a correlation coefficient >95%. Further fitting with the same model but no $D_{Mn(III)}$ parameter yielded a poorer agreement with the experimental magnetisation data but maintained the trend that J is less antiferromagnetic than J' (J = -0.80 cm^{-1}, J' = -1.69 cm^{-1}) with a correlation coefficient of ~60%. Fitting using the 2J model and fixing $D_{Mn(III)}$ at -4.219 cm^{-1}, the value given in the literature fit of **2**, also gave poorer agreement to the magnetisation data but maintained this trend (J = -0.22 cm^{-1}, J' = -3.04 cm^{-1}). Use of a single exchange parameter, both with and without $D_{Mn(III)}$, fails to satisfactorily reproduce the experimental data. Whilst these data are not robust enough to define absolute exchange parameters, they indicate exchange in the region of -0.80 ≤ J ≤ -0.22 cm^{-1} and -3.04 ≤ J' ≤ -1.69 cm^{-1} and as such the interaction between Mn^{II}-Mn^{II} ions will always be more antiferromagnetic than between Mn^{III}-Mn^{II} ions.

Observation of the crystal structure of **16** reveals three unique exchange pathways: between Mn^{III}-Mn^{II} ions bridged by the disordered μ-Me-deaH ligand (J_1, Mn1-Mn3, Mn1-Mn3'), between Mn^{III}-Mn^{II} ions bridged by the μ_3-OMe ligand (J_2, Mn2-Mn3, Mn2-Mn3') and between Mn^{II}-Mn^{II} ions (J_3, Mn3-Mn3') (Figure 2.15b). This 3J model gave excellent agreement with the experimental data (Figure 2.14) yielding best-fit parameters J_1 = -3.37 cm^{-1}, J_2 = +4.65 cm^{-1}, J_3 = -3.99 cm^{-1} and $D_{Mn(III)}$ = -2.14 cm^{-1}. Strong correlation between J_2 and J_3 (correlation coefficient > 95%) prompted further fits using the 2J model (J = J_1, J_2; J' = J_3), both with $D_{Mn(III)}$ free/$D_{Mn(III)}$ fixed at -4.219 cm^{-1}. Both gave poorer agreement to the experimental data without improving the correlation coefficient between exchange parameters (>95%, J = +1.29 cm^{-1}, J' = -4.63 cm^{-1}, $D_{Mn(III)}$ = -4.89 cm^{-1} ; >95%, J = +1.28 cm^{-1}, -4.65 cm^{-1}, $D_{Mn(III)}$ = -4.219 cm^{-1}). Use of a single exchange parameter, or any model that does not include a $D_{Mn(III)}$ parameter, fails to satisfactorily reproduce the experimental data for **16**. These data indicate exchange in the region of J ~ +1.29 cm^{-1} and J' ~ -4.64 cm^{-1}. Comparing the interaction parameters for **15** and **16** to those given for **2** (J = +0.89 cm^{-1}, J' = -0.91 cm^{-1}, $D_{Mn(III)}$ = -4.219 cm^{-1}) indicates a significant increase in antiferromagnetic contribution to the exchange in the BisTBC[4]-supported butterflies with respect to TBC[4]-supported butterflies.

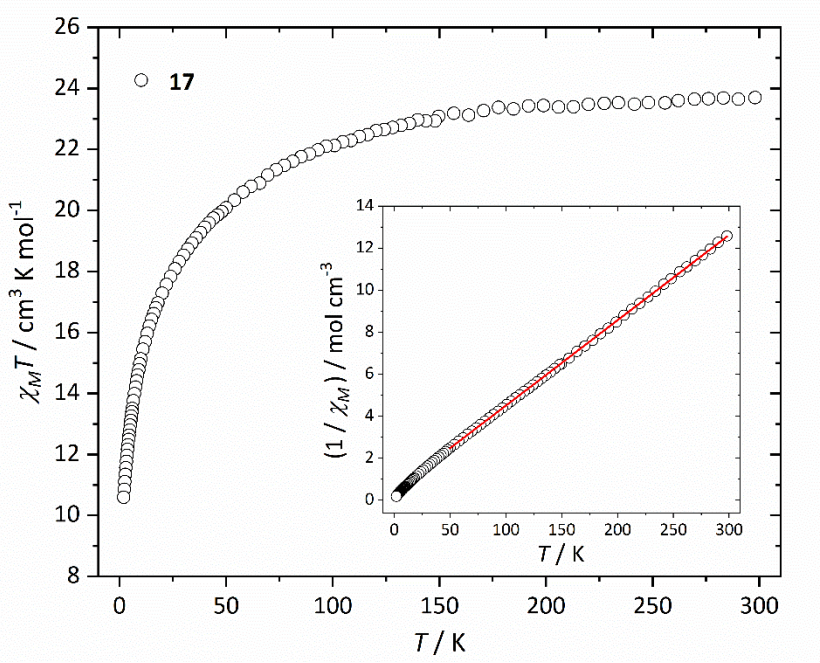

Figure 2.16 Experimental $\chi_M T$ *vs* *T* data for **17** measured in the *T* = 298 - 2 K temperature range and in an applied field, *B* = 0.1 T. Inset: Plot of $1/\chi_M$ *vs* *T* data in the same temperature range. The solid red line is a fit of the experimental data to the Curie-Weiss law in the range *T* = 298 - 50 K.

Dc magnetic susceptibility studies were also performed on a polycrystalline sample of **17** in an applied magnetic field *B* = 0.1 T, over the temperature range *T* = 298 - 2 K (Figure 2.16). At 298 K, the $\chi_M T$ value of 23.70 cm^3 K mol^{-1} is in agreement with the expected spin-only contributions to the susceptibility of a [$Mn^{III}_5Mn^{II}_2$] cluster (23.75 cm^3 K mol^{-1}, *g* = 2.00). Upon cooling, the $\chi_M T$ product decreases steadily until approaching approximately *T* = 100 K, where it decreases more rapidly to a value of 10.60 cm^3 K mol^{-1} at *T* = 2 K. Magnetisation data measured in the temperature range *T* = 2 - 7 K and field range *B* = 0 - 7 T shows *M* rising steadily with increasing *B*, reaching a maximum value of *M* = 14.7 μ_B at 7 T without reaching saturation (Figure S2.14). This behaviour is indicative of the presence of weak exchange interactions but the complexity and large nuclearity of **17** prevents a thorough quantitative analysis of the data. A fit of the inverse susceptibility data to the Curie-Weiss (CW) law, in the range *T* = 298 - 50 K, affords θ = -10.96 K and *C* = 24.6 cm^3 K mol^{-1} (inset of Figure 2.16), suggestive of weak, dominantly antiferromagnetic exchange.

Dc magnetic susceptibility studies were performed on a polycrystalline sample of **19** over the temperature range T = 298 - 2 K, in an applied magnetic field B = 0.1 T (Figure 2.17). At 298 K, the $\chi_M T$ value of 37.4 cm^3 K mol^{-1} is in agreement with the expected value for spin-only contributions to the susceptibility for a $[Mn^{III}_4Mn^{II}_6]$ unit (38.25 cm^3 K mol^{-1}, g = 2.00). Upon cooling, the $\chi_M T$ product decreases slowly until approximately T = 100 K, wherefrom it decreases more rapidly, reaching a value of 8.6 cm^3 K mol^{-1} at 2 K. VTVB magnetisation data (Figure S2.15) shows M rising slowly with increasing B, reaching a maximum value of M = 17.6 μ_B at 7 T but without saturating. Both are suggestive of the presence of weak, competing exchange interactions dominated by antiferromagnetic contributions. The large nuclearity of **19** and the presence of six different exchange interactions prevents a quantitative analysis of the susceptibility and magnetisation data. Previously published Mn complexes of H_4TBC[4] and H_8L show that the exchange interactions tend to be relatively weak, $J_{Mn(III)\text{-}Mn(II)}$ being weakly ferromagnetic, $J_{Mn(II)\text{-}Mn(II)}$ being weakly antiferromagnetic and $J_{Mn(III)\text{-}Mn(III)}$ being borderline anti/ferromagnetic.[25,26] In order to investigate this in more detail, we turn to theory (full details of the computational methodology is outlined in the experimental section of this chapter).

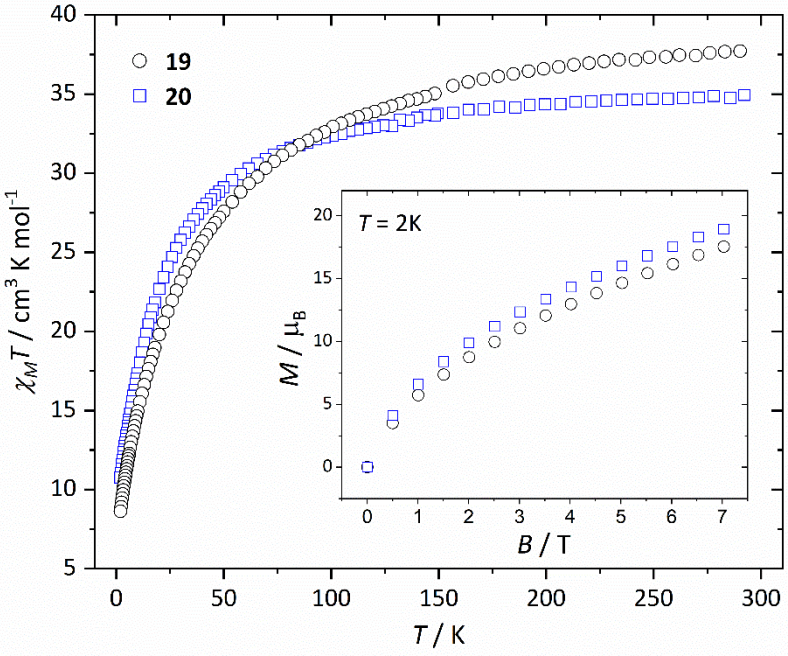

Figure 2.17 Experimental $\chi_M T$ *vs* T data for **19** (circles) measured in the T = 298 - 2 K temperature range and in an applied field, B = 0.1 T. Inset: Variable-temperature-variable-field (VTVB) magnetisation data of **19** at T = 2 K and B = 0 - 7 T. The equivalent data for complex **20** (squares) is added for comparison.[23]

Analysis of the structures of **19** and **20** reveals a total of six different exchange interactions ($J_{1\text{-}6}$), as shown in Figure 2.18. The magnitude and sign of the DFT calculated exchange constants is provided in Table 2.1, alongside pertinent structural information describing the bond distances and angles in each pairwise interaction. In each case the sign and magnitude of the *J* values obtained can be easily explained *via* magneto-structural correlations previously published for O-bridged $Mn^{II/III}$ complexes,[40–42] and are in close agreement with those calculated for a mixed-valent $[Mn^{III}_2Mn^{II}_2]$ cage published by Milios and co-workers.[43]

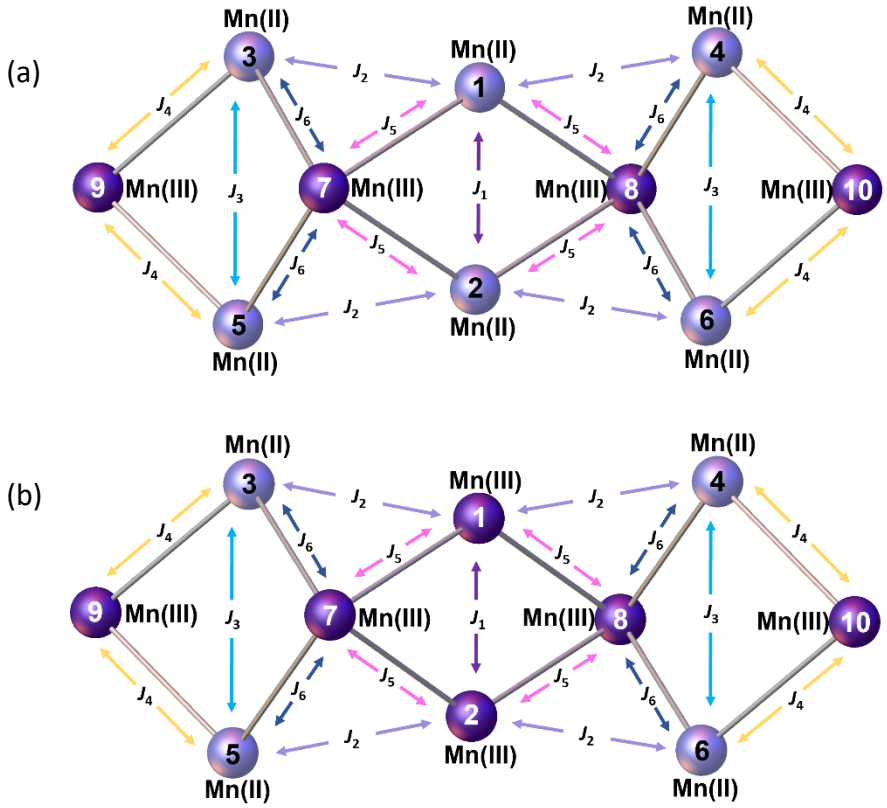

Figure 2.18 Schematic representation of the six different exchange interactions present in **19** (a) and **20** (b). The corresponding spin-Hamiltonian is given in the SI (Equation S2.1).

For complex **19**, the *J* values are all found to be weakly antiferromagnetic ($-0.2 \leq J \leq -4.8$ cm^{-1}), with J_1 the strongest and J_5 the weakest. J_1 is mediated between the two central Mn^{II} ions *via* two μ_3-OH bridges, with (short) Mn-O/Mn-Mn distances of ~1.99/3.00 Å and (relatively acute) Mn-O-Mn angles of ~97.7°. The J_2-J_5 interactions are more weakly antiferromagnetic than J_1 due to the larger Mn-O-Mn angles and larger Mn-O/Mn-Mn distances present. The

value of J_6, bridged by a single Mn^{III}-(μ-OR)-Mn^{II} unit is comparable to that of J_1 due to the large Mn-O-Mn angle (~116.0°). Magneto-structural correlations of such units predict antiferromagnetic exchange in the range of ~5 cm^{-1}.[44] Based on these *J* values complex **19** has an *S* = 2 ground state (Figure S2.16).

For complex **20**, the *J* values are found to be in a much larger range, with both ferro- and antiferromagnetic exchange being observed (+4.1 ≤ *J* ≤ -40.4 cm^{-1}). J_1, between the two central Mn^{III} ions connected by two μ_3-OH bridges, is the largest antiferromagnetic exchange present due to the small Mn-O-Mn angles (~97.6°) and short Mn-O (~1.92 Å) and Mn-Mn (~2.88 Å) distances. The large *J* value has been confirmed through calculations on a dinuclear model complex adapted from the X-ray structure (Figure S2.17). We note that the JT axes of the two Mn^{III} ions are oriented parallel to the bridging ligands, which can be classified as a type I structure based on detailed studies of the dinuclear $\{Mn^{III}_2(OR)_2\}$ motif. In this class of interactions, a large antiferromagnetic *J* contribution and a negligible ferromagnetic *J* contribution are expected, leading to strong antiferromagnetic coupling, as observed here.[40–42,45]

J_2 is ferromagnetic in nature, mediated between Mn^{II} and Mn^{III} ions *via* a single μ-OR bridge with a short Mn-O distance (~2.03 Å) and a large Mn-O-Mn angle (~122.8°). Interestingly, although J_3 (Mn^{II}-OH-Mn^{II}) is mediated *via* similar bridging angles and distances as that seen for J_2, it is weakly antiferromagnetic in nature, highlighting the important role played by the oxidation state of the Mn ion in controlling the sign and magnitude of the exchange. J_3, J_4 and J_6 are much more weakly antiferromagnetic in comparison to J_1 due to the larger Mn-O/Mn distances and larger Mn-O-Mn angles present, just as they were in **19**. J_5, between two Mn^{III} ions bridged by a μ_3-OH ion and a μ-OR group, is weakly ferromagnetic in nature. J_5 can be classified as a type II $\{Mn^{III}_2(OR)_2\}$ unit in which the JT axes of the Mn^{III} ions are oriented parallel to each other and lying along the μ-oxo bridge. This leads to borderline ferro/antiferromagnetic coupling dictated by Mn-O-Mn angle and Mn-O distances. The highly frustrated nature of the interactions in complex **20** precludes the identification of an isolated spin ground state.

From these calculations we can conclude that a change in oxidation state levels from $[Mn^{III}_6Mn^{II}_4]$ (**20**) to $[Mn^{III}_4Mn^{II}_6]$ (**19**) results in a significant decrease in the magnitude of some antiferromagnetic exchange contributions (J_1 = -4.8 cm^{-1} (**19**), -40.4 cm^{-1} (**20**)), a switch from ferromagnetic to antiferromagnetic in others (J_2 = -1.1 cm^{-1} (**19**), +3.1 cm^{-1} (**20**); J_5 = -0.2

cm^{-1} (**19**), +4.1 cm^{-1} (**20**)), and the loss of significant spin frustration. The computed spin density plots for the high spin state of complexes **19** and **20** are given in Figure S2.18, with the spin density plots for all the broken symmetries computed given in Figures S2.19-S2.20.

Table 2.1 List of DFT calculated exchange interactions, $J_{1\text{-}6}$, for compounds **19** and **20** together with pertinent structural information describing the bond distances and angles in each pairwise interaction. The grey shaded rows highlight the exchange interactions, J_1, J_2 and J_5 directly affected by the change in oxidation state of the two central Mn ions.

19				**20**			
	Bridging group	*d*(Mn⋯Mn) / Å	J_{DFT} / cm^{-1}		Bridging group	*d*(Mn⋯Mn) / Å	J_{DFT} / cm^{-1}
J_1	μ_3-OH (1.99 Å, 97.7°) μ_3-OH (1.99 Å, 97.7°)	3.00	-4.8	J_1	μ_3-O (1.92 Å, 97.6°) μ_3-O (1.92 Å, 97.6°)	2.88	-40.4
J_2	μ-OH (2.27 Å, 104.1°)	3.58	-1.1	J_2	μ-OMe (2.03 Å, 122.8°)	3.51	+3.1
J_3	μ_3-OH (2.21 Å, 128.4°)	3.98	-0.9	J_3	μ_3-OH (2.19 Å, 127.3°)	3.92	-1.6
J_4	μ_3-OH (2.18 Å, 102.3°) μ-OR_L (2.18 Å, 98.8°)	3.36	-0.9	J_4	μ_3-OH (2.15 Å, 101.1°) μ-OR_L (2.18 Å, 98.6°)	3.32	-0.8
J_5	μ_3-OH (2.05 Å, 101.1°) μ-OR_L (2.09 Å, 97.6°)	3.16	-0.2	J_5	μ_3-O (2.03 Å, 101.7°) μ-OR_L (2.13 Å, 95.8°)	3.16	+4.1
J_6	μ-OR_L (2.02 Å, 116.0°)	3.44	-4.1	J_6	μ-OR_L (2.04 Å, 116.4°)	3.45	-5.2

Dc magnetic susceptibility studies were performed on a polycrystalline sample of **25** over the temperature range T = 298 - 2 K, in an applied magnetic field B = 0.1 T (Figure 2.19). At 298 K, the $\chi_M T$ value of 5.9 cm^3 K mol^{-1} is below the expected value for spin-only contributions to the susceptibility for a [Cu$^{II}_{16}$] unit (7.26 cm^3 K mol^{-1}, g = 2.20; 6.00 cm^3 K mol^{-1}, g = 2.00). Upon cooling, the $\chi_M T$ product decreases rapidly until approximately T = 10 K where it reaches a 1.1 cm^3 K mol^{-1}. Further cooling then increases $\chi_M T$ to a value of 1.5 cm^3 K mol^{-1} at 2 K. The data are therefore suggestive of the presence of competing exchange interactions, in agreement with the range of Cu-O-Cu angles present, and previous magneto-structural correlations developed for smaller O-bridged Cu^{II} clusters.[46–51]

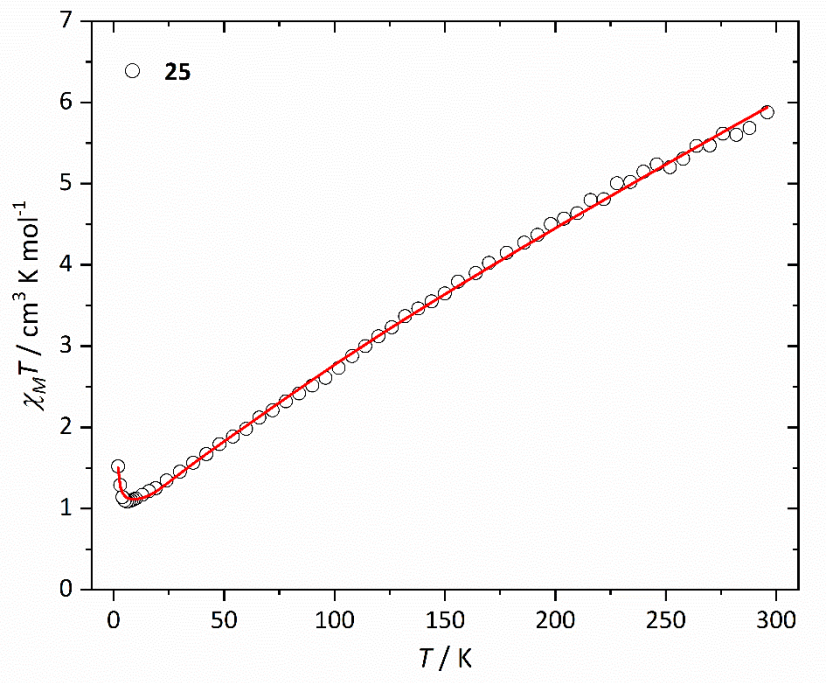

Figure 2.19 Experimental $\chi_M T$ *vs* T data for **25** (circles) measured in the T = 298 - 2 K temperature range and in an applied field, B = 0.1 T. The solid red line is the best fit modelled using spin-Hamiltonian (2.1) as discussed in text.

Based on the structure of **25**, four different isotropic exchange parameters could be considered to fit the experimental temperature dependence of the $\chi_M T$ product (Figure 2.20). We employed irreducible tensor operator algebra to block-diagonalise the matrix representation of the isotropic part of spin-Hamiltonian (2.1),[52] fixing the g-factor for all Cu^{II} centres to g = 2.00, affording only the four different isotropic exchange parameters as free fit parameters. This resulted in very good agreement with the experimental data with the best-

fit parameters J_1, J_2 and J_3 being strongly antiferromagnetic, *ca*. -70 to -100 cm^{-1}, and J_4 being ferromagnetic, *ca*. +20 cm^{-1}. However, all these exchange parameters are strongly correlated, with only the correlation coefficients between J_4 and the others being less than 95%. Use of a single exchange parameter fails to satisfactorily reproduce the experimental data at all temperature regimes. Use of a model containing two different exchange parameters ($J_{1\text{-}3} = J$, $J_4 = J'$; Figure 2.20) results in a very good agreement with the experimental data (Figure 2.19); J = -122 cm^{-1} and J' = 22 cm^{-1} with a correlation coefficient of 87%. With these best-fit parameters the spin ground state of **25** is an S = 1 spin-state, with excited S = 0, 0 and 2 states lying 23, 35 and 46 cm^{-1} above the ground state, respectively, followed by a quasi-continuum of states (Figure 2.21). The exchange constants in the [Cu_{12}] prism of **25** are similar to the values found in [Cu_{13}] (**24**), which are all antiferromagnetic and in the range -66 ≤ J ≤ -84 cm^{-1}.[25] Employing the same isotropic model to fit the VTVB magnetisation data of **25** was not possible. This is because the VTVB magnetisation of **25** presents significant nesting (Figure S2.21) when plotted against B/T, which indicates anisotropy splittings of the same order of magnitude as the experimental conditions (T = 2 - 10 K, and B = 1 - 9 T). Given that the individual Cu^{II} centres are devoid of anisotropy (bar the g-factor), the observed anisotropy splittings can only originate (within the spin-Hamiltonian formalism) from magnetic

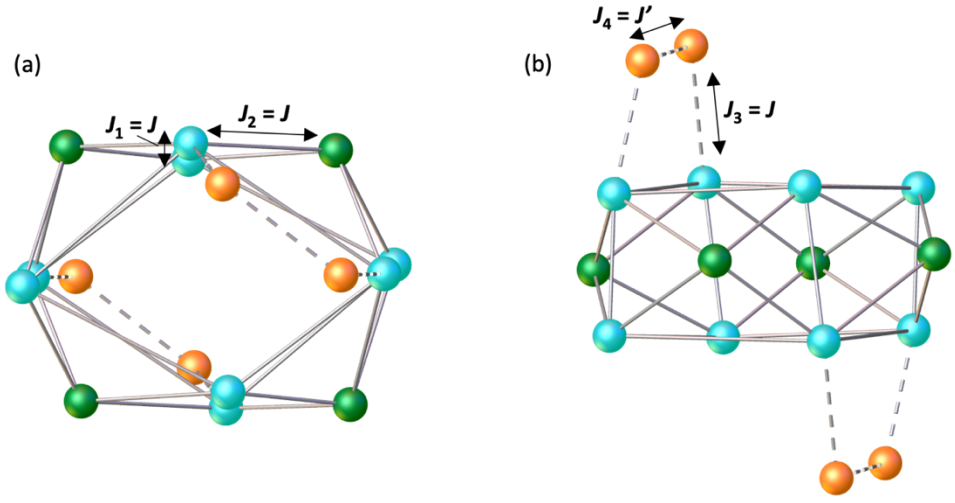

Figure 2.20 Schematic representation of the different exchange interactions present in **25**, used to model the experimental susceptibility data as discussed in text. The Cu ions in the prisms are in turquoise, those housed in the tetraphenolic calixarene pocket in green and the edge-caps in orange.

exchange.[53-58] The experimental data do not allow for the determination of these exchange contributions to anisotropy.

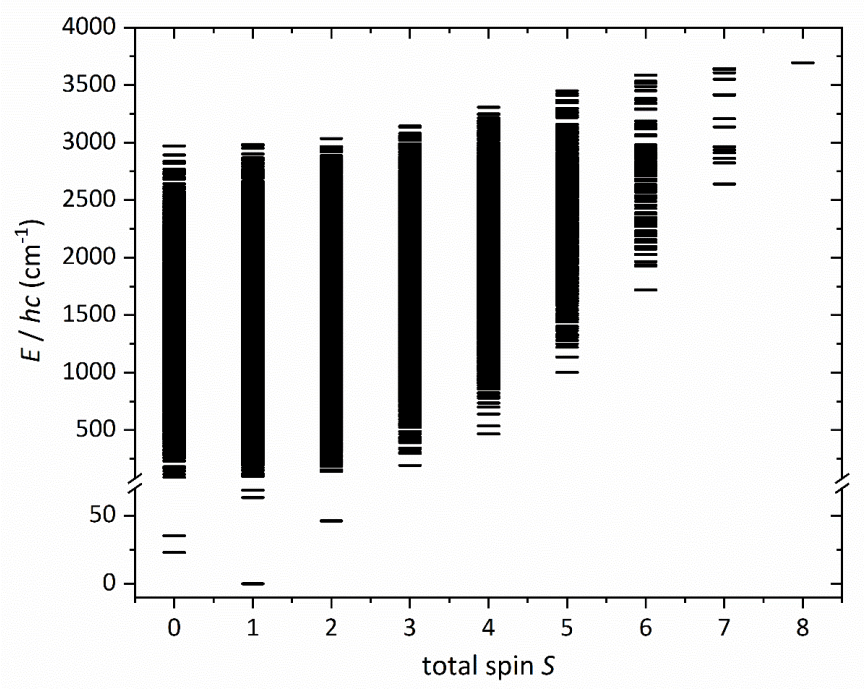

Figure 2.21 Energy spectrum of **25** calculated from the fit of the susceptibility data, as described in text. The spin ground state of **25** is an S = 1 spin-state, with excited S = 0, 0 and 2 states lying 23, 35 and 46 cm^{-1} above the ground state.

Given the relatively well-isolated S = 1 ground state evidenced by the magnetic data and modelling, we attempted to probe this state by EPR spectroscopy at low temperatures. Spectra measured at 10 K and over the 0 - 1.8 T magnetic field range, at both X- and Q-band frequencies, only gave weak signals that could be attributed to small amounts of monomeric Cu^{II} species. This indicates that the zero-field splitting (ZFS) of the S = 1 state is significantly larger than the microwave frequencies applied. In order to estimate the ZFS, attempts were made to fit the VTVB magnetisation data to an isolated S = 1 model: while these fits were not entirely satisfactory (Figure S2.21), they indicate an axial ZFS parameter (D) of several cm^{-1}. This would be consistent with **25** being EPR silent under the measurement conditions. Given the lack of single-ion ZFS for Cu^{II}, the origin of such a ZFS must lie in anisotropic components of the exchange interaction.[53-58] Although a ZFS in the region of several cm^{-1} would be unusual for a Cu cluster, the projection coefficients of anisotropic exchange are larger for lower total

spins,[59] which may provide an explanation given that the ground state of **25** is the lowest possible total spin. It is more usual for Cu clusters to either give rise to a diamagnetic ground state or a high-spin state, so there are few data to compare this against.

In order to analyse the sign and magnitude of the exchange interactions in more detail we have constructed three pentametallic models (**25A**, **25B**, **25C**) and one bimetallic model (**25D**) based on the X-ray structure of **25** to determine twelve exchange interactions (Figure 2.22). These are given in Table S2.9 and consist of ten antiferromagnetic interactions in the range $-3.9 < J < -55.7$ cm^{-1}, and two weakly ferromagnetic interactions in the range $+2.6 < J < +6.9$ cm^{-1}. The strongest antiferromagnetic exchange occurs between Cu2 (face-cap) and Cu4 (vertex) mediated by a single μ-OR$_L$ bridge with a Cu-O-Cu angle of ~131°. The second

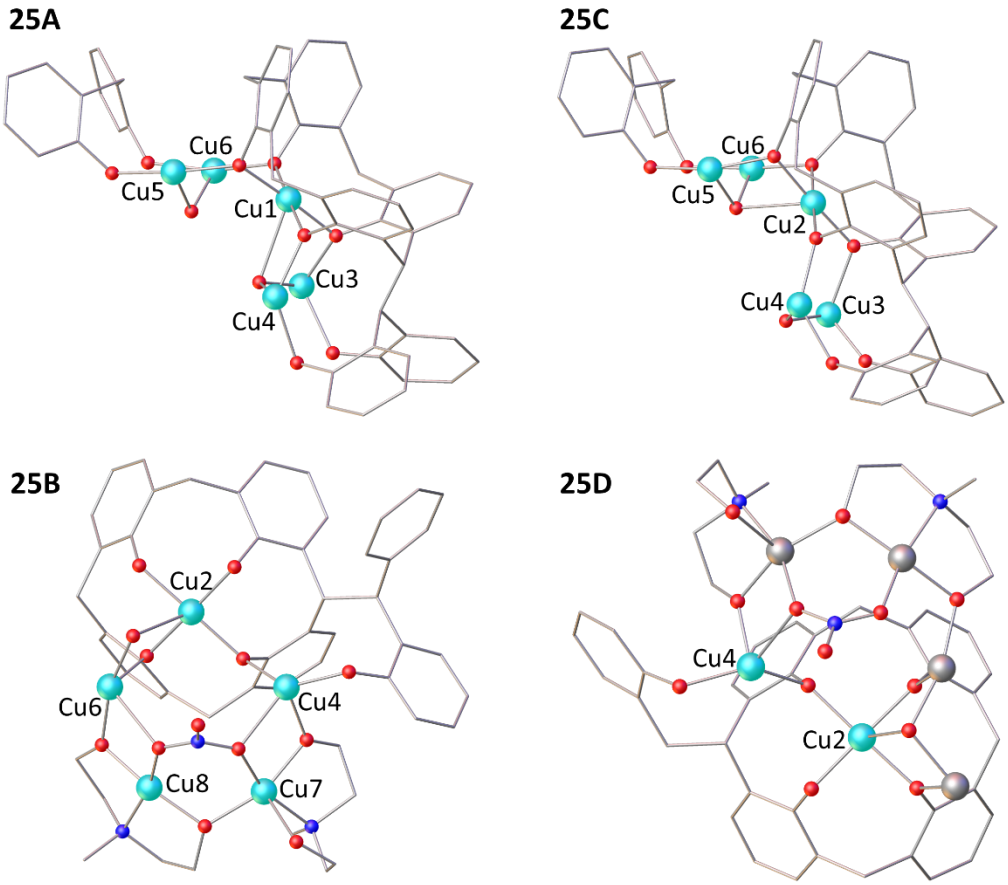

Figure 2.22 The three pentametallic models (**25A-C**) and the bimetallic model (**25D**) employed to calculate the magnetic exchange interactions in **25**. Ligated solvent molecules removed for clarity; full coordination of each metal centre given in Figure S2.22.

strongest antiferromagnetic exchange interaction is between Cu3 (vertex) and Cu4 (vertex) mediated *via* a single μ-OH bridge with a Cu-O-Cu angle of ~126°. The two ferromagnetic exchange interactions occur between Cu1 (face-cap) and Cu3 (vertex) mediated by μ-OH/μ-OR_L bridges with an average Cu-O-Cu angle of ~96° and a Cu-O-Cu-O dihedral angle of ~24°, and between Cu6 (vertex) and Cu8 (edge-cap) mediated by μ-O(NO_2)/$OR_{Me\text{-}dea}$ groups with an average Cu-O-Cu angle of ~98° and a Cu-O-Cu-O dihedral angle of ~17°.

A detailed examination of the structure reveals that the sign and magnitude of *J* strongly depends on both the Cu-O-Cu angle and the Cu-O-Cu-O dihedral angle.[59] Large Cu-O-Cu angles lead to strong antiferromagnetic exchange whose magnitude decreases with decreasing angle (Figure S2.23). The switch to ferromagnetic occurs at a Cu-O-Cu angle of ~97-99°.[46–51] A large Cu-O-Cu-O dihedral angle in conjunction with a small Cu-O-Cu angle results in accidental orbital orthogonality (a counter complementary effect arising from the presence of two different bridging ligands) which leads to a weak ferromagnetic interaction. DFT calculated spin density analysis (Figure S2.24-S2.25) suggests strong spin delocalisation with spin densities on the Cu^{II} ions of between 0.391-0.673. The bridging hydroxides/phenolic O-atoms have the largest spin density among the coordinating atoms, consistent with the strongest antiferromagnetic exchange through these moieties. The pattern of calculated exchange interactions (Table S2.9) and the spin density analysis therefore strongly suggests the presence of spin frustration between the face-capping Cu ions housed in the calixarene polyphenolic pockets and the Cu ions at the vertices of the square prism. The small spin density of the N-atom of the nitrate points to a small, near-negligible exchange through the Cu-O-N-O-Cu pathway (Figure S2.26).

2.4 Conclusions

The successful synthesis and characterisation of five novel BisTBC[4]-supported paramagnetic complexes (doubling the existing family of BisTBC[4]-supported 3*d* clusters) corroborated the approach of directing cluster formation through the tuning of reaction conditions, stoichiometry and co-ligand incorporation. Co-ligand addition, acetate (**15**) and Me-deaH (**16**), into $Mn^{III}_2Mn^{II}_2$ butterflies upholds the preference of TBC[4] moieties to bind Mn^{III} in the phenolic cavity. Magnetic studies revealed dominant antiferromagnetic exchange interactions in **15** ($-0.80 \leq J \leq -0.22$ cm^{-1}, $-3.04 \leq J' \leq -1.69$ cm^{-1}) and **16** ($J \sim +1.29$ cm^{-1} and $J' \sim -4.64$ cm^{-1}) with respect to TBC[4] counterpart **2** ($J = +0.89$ cm^{-1}, $J' = -0.91$ cm^{-1}).

Replacement of hmpH (**18**) with $pdmH_2$ (**17**) in a $[Mn^{III}_5Mn^{II}_2]$ cluster prohibited growth of the unit into the equivalent $[Mn^{III}_5Mn^{II}_2]_2$ dimer, presumably due to the increased bulk of the co-ligand. Magnetic studies revealed antiferromagnetic behaviour and a fit of the inverse susceptibility data afforded CW parameters $\theta = -10.96$ K and $C = 24.6$ cm^3 K mol^{-1}.

Altering reaction stoichiometry results in a change in oxidation state distribution in bis-calix[4]arene supported $[Mn_{10}]$ cages, without significantly altering structural topology. The shift in oxidation state from $[Mn^{III}_6Mn^{II}_4]$ (**20**) to $[Mn^{III}_4Mn^{II}_6]$ (**19**) results in increased antiferromagnetic contributions, as qualitatively observed in susceptibility and magnetisation measurements. DFT calculations revealed the change in oxidation state in the central J_1 interaction causes a 10-fold change in the magnitude of the exchange interaction.

Introducing $Me\text{-}deaH_2$ into the reaction of H_8L with $Cu(NO_3)_2{\cdot}3H_2O$ expands the $[Cu_{13}]$ cluster (**24**) to a novel $[Cu_{16}]$ cluster (**25**). In **25**, the tetra-capped square prism of **24** is upheld, but with the addition of two edge-capping $\{Cu^{II}_2(Me\text{-}dea)_2\}$ units on the remaining faces. Magnetic susceptibility measurements reveal strong antiferromagnetic exchange interactions between neighbouring Cu^{II} ions within the central $[Cu_{12}]$ tetra-capped square prism and between the Cu^{II} ions in the prism and the caps ($J = -122$ cm^{-1}) and strong ferromagnetic exchange between the Cu^{II} ions in the caps ($J' = +22$ cm^{-1}), leading to a ground state of $S = 1$. DFT calculations reveal of strong dependence of J on both the Cu-O-Cu and O-Cu-O-Cu angles and suggest significant spin frustration in the central $[Cu_{12}]$ prism. Magnetisation and EPR data suggest the presence of significant ZFS in the $S = 1$ ground state, originating from anisotropic components of the exchange interaction.

2.5 References

(1) L. T. Carroll, P. A. Hill, C. Q. Ngo, K. P. Klatt and J. L. Fantini, *Tetrahedron*, 2013, **69**, 5002–5007.

(2) P. Murphy, S. J. Dalgarno and M. J. Paterson, *J. Phys. Chem. A*, 2014, **118**, 7986–8001.

(3) C. D. Gutsche, in *Calixarenes: An Introduction*, Royal Society of Chemistry, Cambridge, 2nd edn., 2008, ch. 2, pp 27-160.

(4) G. M. Sheldrick, *Acta Crystallogr. Sect. C*, 2015, **71**, 3–8.

(5) O. V. Dolomanov, L. J. Bourhis, R. J. Gildea, J. A. K. Howard and H. Puschmann, *J. Appl. Crystallogr.*, 2009, **42**, 339–341.

(6) A. Schäfer, H. Horn and R. Ahlrichs, *J. Chem. Phys.*, 1992, **97**, 2571–2577.

(7) A. Schäfer, C. Huber and R. Ahlrichs, *J. Chem. Phys.*, 1994, **100**, 5829–5835.

(8) L. Noodleman, *J. Chem. Phys.*, 1981, **74**, 5737–5743.

(9) G. Rajaraman, J. Cano, E. K. Brechin and E. J. L. McInnes, *Chem. Commun.*, 2004, **13**, 1476–1477.

(10) P. Christian, G. Rajaraman, A. Harrison, J. J. W. McDouall, J. T. Raftery and R. E. P. Winpenny, *Dalton Trans.*, 2004, **10**, 1511–1512.

(11) P. Christian, G. Rajaraman, A. Harrison, M. Helliwell, J. J. W. McDouall, J. Raftery and R. E. P. Winpenny, *Dalton Trans.*, 2004, **16**, 2550–2555.

(12) K. R. Vignesh, S. K. Langley, B. Moubaraki, K. S. Murray and G. Rajaraman, *Chem. – Eur. J.*, 2015, **21**, 16364–16369.

(13) E. Ruiz, A. Rodríguez-Fortea, J. Cano, S. Alvarez and P. Alemany, *J. Comput. Chem.*, 2003, **24**, 982–989.

(14) T. Onishi, Y. Takano, Y. Kitagawa, T. Kawakami, Y. Yoshioka and K. Yamaguchi, *Polyhedron*, 2001, **20**, 1177–1184.

(15) M. J. Frisch, G. W. Trucks, J. R. Cheeseman *et. al., Gaussian 09, Revision E.01,* Wallingford CT, 2013.

(16) C. Lee, W. Yang and R. G. Parr, *Phys. Rev. B*, 1988, **37**, 785–789.

(17) A. D. Becke, *J. Chem. Phys.*, 1993, **98**, 5648–5652.

(18) A. D. Becke, *J. Chem. Phys.*, 1993, **98**, 1372–1377.

(19) P. J. Stephens, F. J. Devlin, C. F. Chabalowski and M. J. Frisch, *J. Phys. Chem.*, 1994, **98**, 11623–11627.

(20) G. E. Scuseria and H. F. Schaefer III, *J. Chem. Phys.*, 1989, **90**, 3700–3703.

(21) G. Karotsis, S. J. Teat, W. Wernsdorfer, S. Piligkos, S. J. Dalgarno and E. K. Brechin, *Angew. Chem. Int. Ed.*, 2009, **48**, 8285–8288.

(22) M. Coletta, S. Sanz, E. K. Brechin and S. J. Dalgarno, *Dalton Trans.*, 2020, **49**, 9882–9887.

(23) M. Coletta, R. McLellan, A. Waddington, S. Sanz, K. J. Gagnon, S. J. Teat, E. K. Brechin and S. J. Dalgarno, *Chem. Commun.*, 2016, **52**, 14246–14249.

(24) L. R. B. Wilson, M. Coletta, R. Jose, G. Rajaraman, S. J. Dalgarno and E. K. Brechin, *Dalton Trans.*, 2021, **50**, 17566–17572.

(25) R. McLellan, M. A. Palacios, C. M. Beavers, S. J. Teat, S. Piligkos, E. K. Brechin and S. J. Dalgarno, *Chem. – Eur. J.*, 2015, **21**, 2804–2812.

(26) M. A. Palacios, R. McLellan, C. M. Beavers, S. J. Teat, H. Weihe, S. Piligkos, S. J. Dalgarno and E. K. Brechin, *Chem. – Eur. J.*, 2015, **21**, 11212–11218.

(27) L. R. B. Wilson, M. Coletta, M. K. Singh, S. J. Teat, A. Brookfield, M. Shanmugam, E. J. L. McInnes, S. Piligkos, S. J. Dalgarno and E. K. Brechin, *Dalton Trans.*, 2023, **52**, 8956–8963.

(28) S. Shinkai, K. Araki, P. D. J. Grootenhuis and D. N. Reinhoudt, *J. Chem. Soc. Perkin Trans. 2*, 1991, **12,** 1883–1886.

(29) L. N. Dawe and L. K. Thompson, *Angew. Chem. Int. Ed.*, 2007, **46**, 7440–7444.

(30) Y.-W. Li, D.-C. Li, J. Xu, H.-G. Hao, S.-N. Wang, J.-M. Dou, T.-L. Hu and X.-H. Bu, *Dalton Trans.*, 2014, **43**, 15708–15712.

(31) A. Adhikary, S. Goswami, J. A. Sheikh and S. Konar, *Eur. J. Inorg. Chem.*, 2014, 963-967.

(32) T.-F. Liu, T. C. Stamatatos, K. A. Abboud and G. Christou, *Dalton Trans.*, 2010, **39**, 3554–3556.

(33) V. Chandrasekhar and L. Nagarajan, *Dalton Trans.*, 2009, **34**, 6712–6714.

(34) G. A. Craig, M. Schütze, D. Aguilà, O. Roubeau, J. Ribas-Ariño, S. Vela, S. J. Teat and G. Aromí, *Inorg. Chem.*, 2014, **53**, 3290–3297.

(35) A. K. Kostopoulos, A. D. Katsenis, J. M. Frost, V. G. Kessler, E. K. Brechin and G. S. Papaefstathiou, *Chem. Commun.*, 2014, **50**, 15002–15005.

(36) T. Zhao, X. Jing, J. Wang, D. Wang, G. Li, Q. Huo and Y. Liu, *Cryst. Growth Des.*, 2012, **12**, 5456–5461.

(37) Y.-L. Bai, V. Tangoulis, R.-B. Huang, L.-S. Zheng and J. Tao, *Chem. – Eur. J.*, 2009, **15**, 2377–2383.

(38) X. Zhang, T. Han, Q. Zou, R.-Y. Zhu, J.-J. Wang and Z.-X. Li, *Z. Für Anorg. Allg. Chem.*, 2016, **642**, 4–7.

(39) P. Klüfers and J. Schuhmacher, *Angew. Chem. Int. Ed.*, 1995, **34**, 2119–2121.

(40) N. Berg, T. Rajeshkumar, S. M. Taylor, E. K. Brechin, G. Rajaraman and L. F. Jones, *Chem. – Eur. J.*, 2012, **18**, 5906–5918.

(41) K. R. Vignesh, S. K. Langley, C. J. Gartshore, B. Moubaraki, K. S. Murray and G. Rajaraman, *Inorg. Chem.*, 2017, **56**, 1932–1949.

(42) C. J. Milios, R. Inglis, A. Vinslava, R. Bagai, W. Wernsdorfer, S. Parsons, S. P. Perlepes, G. Christou and E. K. Brechin, *J. Am. Chem. Soc.*, 2007, **129**, 12505–12511.

(43) C. J. Milios, M. Manoli, G. Rajaraman, A. Mishra, L. E. Budd, F. White, S. Parsons, W. Wernsdorfer, G. Christou and E. K. Brechin, *Inorg. Chem.*, 2006, **45**, 6782–6793.

(44) K. R. Vignesh, S. K. Langley, K. S. Murray and G. Rajaraman, *Chem. – Eur. J.*, 2015, **21**, 2881–2892.

(45) T. Gupta and G. Rajaraman, *Chem. Commun.*, 2016, **52**, 8972–9008.

(46) B. Bleaney and K. D. Bowers, *Proc. R. Soc. Lond. Ser. Math. Phys. Sci.*, 1952, **214**, 451–465.

(47) V. H. Crawford, H. Wayne. Richardson, J. R. Wasson, D. J. Hodgson and W. E. Hatfield, *Inorg. Chem.*, 1976, **15**, 2107–2110.

(48) W. E. Hatfield, *Comments Inorg. Chem.*, 1981, **1**, 105–121.

(49) W. E. Marsh, K. C. Patel, W. E. Hatfield and D. J. Hodgson, *Inorg. Chem.*, 1983, **22**, 511–515.

(50) C. P. Landee and R. E. Greeney, *Inorg. Chem.*, 1986, **25**, 3771–3775.

(51) S. S. Tandon, L. K. Thompson, M. E. Manuel and J. N. Bridson, *Inorg. Chem.*, 1994, **33**, 5555–5570.

(52) A. Bencini and D. Gatteschi, in *Electron Paramagnetic Resonance of Exchange Coupled Systems*, Springer-Verlag, 1990.

(53) I. Dzyaloshinsky, *J. Phys. Chem. Solids*, 1958, **4**, 241–255.

(54) T. Moriya, *Phys. Rev.*, 1960, **120**, 91–98.

(55) S. Ferrer, F. Lloret, E. Pardo, J. M. Clemente-Juan, M. Liu-González and S. García-Granda, *Inorg. Chem.*, 2012, **51**, 985–1001.

(56) M.-A. Bouammali, N. Suaud, N. Guihéry and R. Maurice, *Inorg. Chem.*, 2022, **61**, 12138–12148.

(57) J. Yoon and E. I. Solomon, *Coord. Chem. Rev.*, 2007, **251**, 379–400.

(58) E. J. L. McInnes and D. Collison, in *eMagRes*, 2016, pp. 1445–1458.

(59) E. Ruiz, P. Alemany, S. Alvarez and J. Cano, *J. Am. Chem. Soc.*, 1997, **119**, 1297–1303.

Chapter 3

Magneto-structural correlations of thiacalix[4]arene-supported clusters

3.1 Introduction

Polymetallic complexes of Cu^{II} represented the gateway to the field of molecular magnetism, beginning with studies of copper acetate[1] in the 1950s through to the development of magneto-structural correlations in hydroxide- and halide-bridged dimers in the 1970s and 80s.[2,3] Later research revealed the presence of spin frustration in equilateral Cu^{II} triangles and prompted detailed studies into the mechanisms of magnetic exchange.[4,5] The synthesis of such building blocks, and their successive combination into higher nuclearity complexes, requires a suitable organic ligand, and an excellent candidate is *p-tert*-butylthiacalix[4]arene.

p-tert-butylthiacalix[4]arene (H_4TC[4]A, Figure 3.1) was first synthesised in 1997 and has since proved to be a highly successful platform for a breadth of supramolecular and coordination chemistry.[6–12] In the latter area, the [S_4O_4] donor atom set typically leads to the formation of square [M_4] building blocks that can self-assemble to form aesthetically pleasing molecular cages exhibiting a variety of nuclearities and topologies.[13,14] This versatility is particularly appealing to chemists interested in constructing high nuclearity cages of paramagnetic metal ions with a view to developing magneto-structural correlations and/or uncovering novel magnetic phenomena. Surprisingly, however, a search of the Cambridge Structural Database (CSD) for TC[4]A-supported Cu^{II} cages reveals just five hits, four of which are [Cu^{II}_4] squares[15–17] and the last a [Cu^{II}_{13}] cluster.[18] Herein, we outline the synthesis, structure and magnetic behaviour of a [Cu^{II}_{24}] cage (**26**) and its [Cu^{II}_8] building block (**27**) both supported by TC[4]A (described in section A).

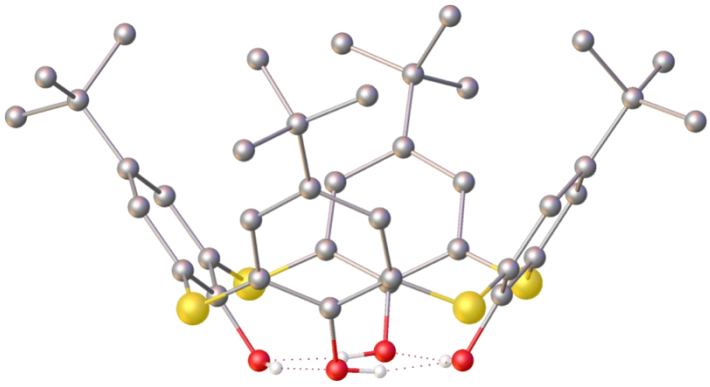

Figure 3.1 The single crystal X-ray structure of H_4TC[4]A, where the dotted lines represent hydrogen bonding.[9] For clarity, only the phenolic H atoms are shown. Colour code: S - yellow, C - grey, O - red, H - white.

The proclivity of H_4TC[4]A to form the [M^{II}_4] square motif inspired successive investigation into its coordination behaviour in the presence of other calix[*n*]arenes (*e.g.* H_4TBC[4]) which form different motifs (*e.g.* [$M^{II/III}_3$] triangles), with the intention of investigating the targeting of specific topologies and/or specific oxidation state distributions based on known building blocks. It is interesting to note that all calix[*n*]arene-supported clusters in the CSD contain just one type of C[*n*]. Herein we report the first known mixed-calix[*n*]arene-supported clusters: [$Mn^{III}_2Mn^{II}_4$] (**28**) supported by TC[4]A and TBC[4], [$Mn^{III}_6Mn^{II}_4Cu^{II}_4$] (**29**) supported by TC[4]A and TBC[4], and its TC[4]A-supported counterpart [$Mn^{II}_3Cu^{II}_2$] (**30**), and [Co^{II}_4] (**31**) supported by TC[4]A and TBC[8], where H_8TBC[8] is *p-tert*-butylcalix[8]arene (described in section B).

3.2 Experimental

Materials and Syntheses

All chemicals were procured from commercial suppliers and used as received (reagent grade). Elemental analyses were performed on a Thermo Fisher Scientific Flash SMART instrument.

Synthesis of $[Cu^{II}_{24}(TC[4]A)_6(\mu_4\text{-}Cl)_6(\mu_6\text{-}CO_3)_6(\mu\text{-}OH)_6(dmf)_6]\cdot 21dmf$ (26)

$H_4TC[4]A$ (225 mg, 0.312 mmol) and $CuCl_2\cdot 2H_2O$ (213 mg, 1.248 mmol) were dissolved in dmf/MeOH (1:1 v/v, 24 mL) and stirred for 10 minutes. NEt_3 (0.2 mL, 1.43 mmol) was added and the resultant brown solution stirred for 2 hours. After filtration, the solution was allowed to evaporate slowly to afford crystals of **26** in 17% yield after 3 days. Elemental analysis (%) calculated for **26** without any solvent molecules of crystallisation: C, 46.33; H, 4.59; N, 1.23. Found: C, 46.32; H, 4.44; N, 0.92.

Synthesis of $[Cu^{II}_8(TC[4]A)_2(\mu_4\text{-}CO_3)(\mu\text{-}OH)(Br)_5(dmf)_3(H_2O)]\cdot 2dmf$ (27)

$H_4TC[4]A$ (225 mg, 0.312 mmol) and $CuBr_2$ (279 mg, 1.248 mmol) were dissolved in dmf/MeOH (1:1 v/v, 24 mL) and stirred for 10 minutes. NEt_3 (0.2 mL, 1.43 mmol) was added and the resultant brown solution stirred for 2 hours. After filtration, the solution was allowed to evaporate slowly to afford crystals of **27** in 15% yield after 3 days. Elemental analysis (%) calculated for **27** without any solvent molecules of crystallisation: C, 40.69; H, 4.25; N, 1.58. Found: C, 40.43; H, 4.46; N, 2.04.

Synthesis of $[Mn^{III}_2Mn^{II}_4(TBC[4])_2(TC[4]A)(\mu_4\text{-}CO_3)(dmf)_6]\cdot 5MeCN$ (28)

$H_4TC[4]A$ (100 mg, 0.139 mmol), $H_4TBC[4]$ (180 mg, 0.278 mmol) and $MnCl_2\cdot 4H_2O$ (110 mg, 0.556 mmol) were dissolved in dmf/MeOH (1:1 v/v, 24 mL) and stirred for 10 minutes. NEt_3 (0.2 mL, 1.43 mmol) was added and the resultant dark purple solution stirred for 2 hours. After filtration, MeCN was diffused slowly into the mother liquor affording dark purple crystals of **28** in 14% after 7 days. Elemental analysis (%) calculated for **28** without any solvent molecules of crystallisation: C, 62.10; H, 7.02; N, 2.96. Found: C, 61.78; H, 6.98; N, 2.48.

Synthesis of $[Mn^{III}_6Mn^{II}_4Cu^{II}_4(TBC[4])_2(TC[4]A)_2(\mu_4\text{-}O)_4(\mu_3\text{-}OH)_4(\mu\text{-}OMe)_6(Cl)_2(H_2O)_2(dmf)_2(MeCN)_2]\cdot 1.5MeOH\cdot 1dmf\cdot 0.5H_2O$ (29)

$H_4TC[4]A$ (100 mg, 0.139 mmol), $H_4TBC[4]$ (100 mg, 0.154 mmol), $MnCl_2\cdot 4H_2O$ (83 mg, 0.417 mmol), $CuCl_2\cdot 2H_2O$ (71 mg, 0.417 mmol) and Na(acac) (20 mg, 0.164 mmol) were dissolved in dmf/MeOH (1:1 v/v, 24 mL) and stirred for 10 minutes. NEt_3 (0.2 mL, 1.43 mmol) was added and the resultant dark brown solution stirred for 2 hours. After filtration, MeCN was diffused slowly into the mother liquor affording dark brown crystals of **29** in 20% after 7 days. Elemental analysis (%) calculated for **29** without any solvent molecules of crystallisation: C, 52.75; H, 5.70; N, 1.31. Found: C, 52.81; H, 5.33; N, below limit of detection.

Synthesis of $[Mn^{II}_3Cu^{II}_2(TC[4]A)_2(acac)_2]\cdot 1.7MeCN\cdot 1.25dmf\cdot 0.85MeOH\cdot 0.4H_2O$ (30)

$H_4TC[4]A$ (100 mg, 0.139 mmol), $MnCl_2\cdot 4H_2O$ (83 mg, 0.417 mmol), $CuCl_2\cdot 2H_2O$ (71 mg, 0.417 mmol) and Na(acac) (122 mg, 1 mmol) were dissolved in dmf/MeOH (1:1 v/v, 24 mL) and stirred for 10 minutes. NEt_3 (0.2 mL, 1.43 mmol) was added and the resultant dark brown solution stirred for 2 hours. After filtration, MeCN was diffused slowly into the mother liquor affording dark brown crystals of **30** in 21% after 7 days. Elemental analysis (%) calculated for **30**: C, 55.19; H, 5.78; N, 1.94. Found: C, 55.47; H, 5.70; N, 1.42.

Synthesis of $[Co^{II}_4(H_3TBC[8])(TC[4]A)Cl]\cdot 3dmf$ (31)

$H_8TBC[8]$ (39 mg, 0.030 mmol), $CoCl_2\cdot 6H_2O$ (48 mg, 0.200 mmol) and isonicotinic acid (25 mg, 0.200 mmol) were dissolved in dmf/MeOH (1:1 v/v, 12 mL) and stirred for 5 minutes. $H_4TC[4]A$ (21 mg, 0.030 mmol) and NEt_3 (0.1 mL, 0.715 mmol) were added and the resultant solution stirred for 80 minutes. After filtration, an 8 mL aliquot of the solution was placed in an autoclave at 120 °C for 24 hours. Upon cooling, the solution was filtered and allowed to evaporate slowly to afford pink crystals of **31** in 24% after 7 days. Elemental analysis (%) calculated for **31**: C, 65.81; H, 6.93; N, 1.68. Found: C, 65.41; H, 7.09; N, 1.22.

X-ray crystallography

Single crystal X-ray diffraction data for **26**, **28** and **31** were collected on a Bruker Kappa APEXII DUO CCD diffractometer operating with CuK_α radiation (1.54178 Å, **26**, **31**) / MoK_α radiation (0.7288 Å, **28**). Diffraction data for **27** were collected on a Rigaku Oxford Diffraction SuperNova equipped with an Oxford Cryosystems Cryostream and operating with CuK_α radiation (1.54184 Å). Diffraction data for **29** were collected on a Rigaku FRE+ equipped with

VHF Varimax confocal mirrors, a UG2 goniometer and HyPix 6000HE detector and operating with MoK_α radiation (0.71073 Å). Diffraction data for **30** were collected on a Rigaku 007HF equipped with Varimax confocal mirrors, a UG2 goniometer and HyPix 6000 detector and operating with CuK_α radiation (1.54184 Å). Crystal data for **26**-**31** are given in Tables S3.1-S3.3. Structures were solved using ShelXT/ShelXL and refined with version 2018/3 of ShelXL interfaced through Olex2.[19,20] All non-hydrogen atoms were refined anisotropically. Most hydrogen atom positions were calculated geometrically and refined using the riding model, but some hydrogen atoms were refined freely.

Powder X-ray diffraction data for **26**-**31** were collected on polycrystalline powders using a Bruker D8 ADVANCE with Cu radiation at 40 kV, 40mA and a Johansson monochromator, 2mm divergence slit and 2.5 degree Soller slits on the incident beam side, LynxEye detector and Bruker DIFFRAC software. Data were measured from 2θ = 2 - 30°; step size, 0.0101°. Freshly prepared crystalline powders were loaded into borosilicate capillaries with a 0.7 mm inside diameter and measured while spinning (Figure S3.1).

Magnetic data

Magnetic susceptibility and magnetisation data were collected on powdered microcrystalline samples of **26**-**31** using a Quantum Design PPMS DynaCool magnetometer equipped with a 9 T dc magnet. Susceptibility data were collected in the T = 300 - 2 K range under an applied magnetic field, B = 0.1 T. Magnetisation data were collected in the ranges T = 2 - 10 K and B = 0 - 9 T. Data were modelled using PHI v3 software (**26**-**27, 31**) – see Format of Thesis.

3.3 Results and Discussion

Structure descriptions

A. TC[4]A-supported clusters

Reaction of H_4TC[4]A with $CuCl_2 \cdot 2H_2O$ in a basic dmf/MeOH mixture affords single crystals of $[Cu^{II}_{24}(TC[4]A)_6(\mu_4\text{-}Cl)_6(\mu_6\text{-}CO_3)_6(\mu\text{-}OH)_6(dmf)_6] \cdot 21dmf$ (**26**, Figure 3.2), following slow evaporation of the mother liquor. The crystals were found to be in a triclinic cell and structure solution was carried out in space group *P*-1. The asymmetric unit (ASU) contains two distinct half clusters (*i.e.* the unit cell contains two $[Cu_{24}]$ clusters) and symmetry expansion affords the cage shown in Figure 3.2. Pertinent bond lengths and bond angles are given in Table S3.4.

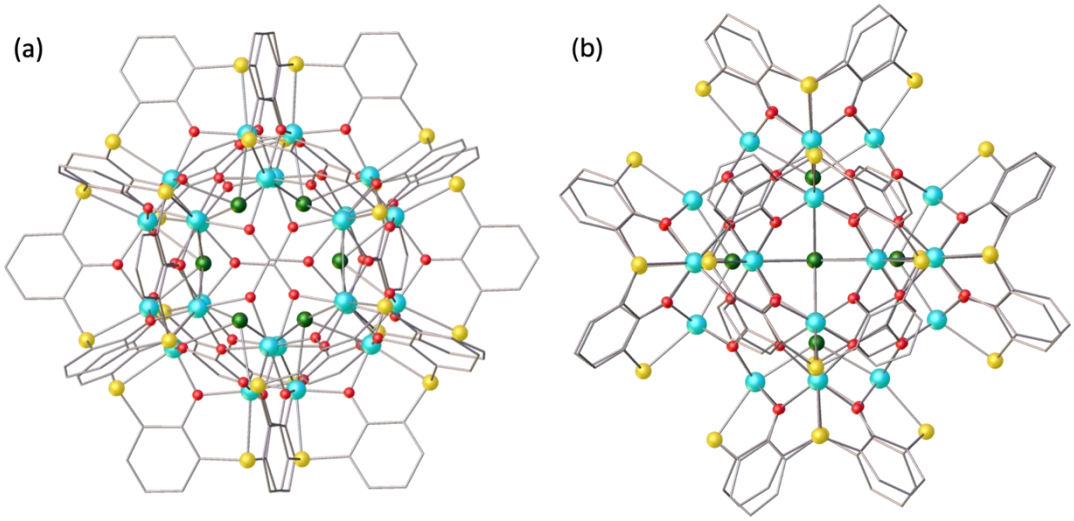

Figure 3.2 Single crystal X-ray structure of **26** shown from two different perspectives. Colour code: Cu^{II} - turquoise, Cl - dark green, S - yellow, C - grey, O - red. H atoms, ^{t}Bu groups of TC[4]A and co-crystallised solvent molecules omitted for clarity.

The metallic skeleton of **26** (Figure 3.3a) describes a $[Cu^{II}_{24}]$ truncated octahedron. The fully deprotonated TC[4]A ligands sit atop the six square faces, bonded to the four Cu ions through four μ-O atoms and four terminal S atoms, as expected. Below the square lies a μ_4-Cl ion, creating the $[Cu_4(TC[4]A)Cl]$ building block (Figure 3.3b). Six of these building blocks are self-assembled into the $[Cu_{24}]$ unit by a disordered combination of six $\mu_6\text{-}CO_3^{2-}$ ions and six $\mu\text{-}OH^-$ ions which lie in the hexagonal faces of the truncated octahedron. The carbonate anions

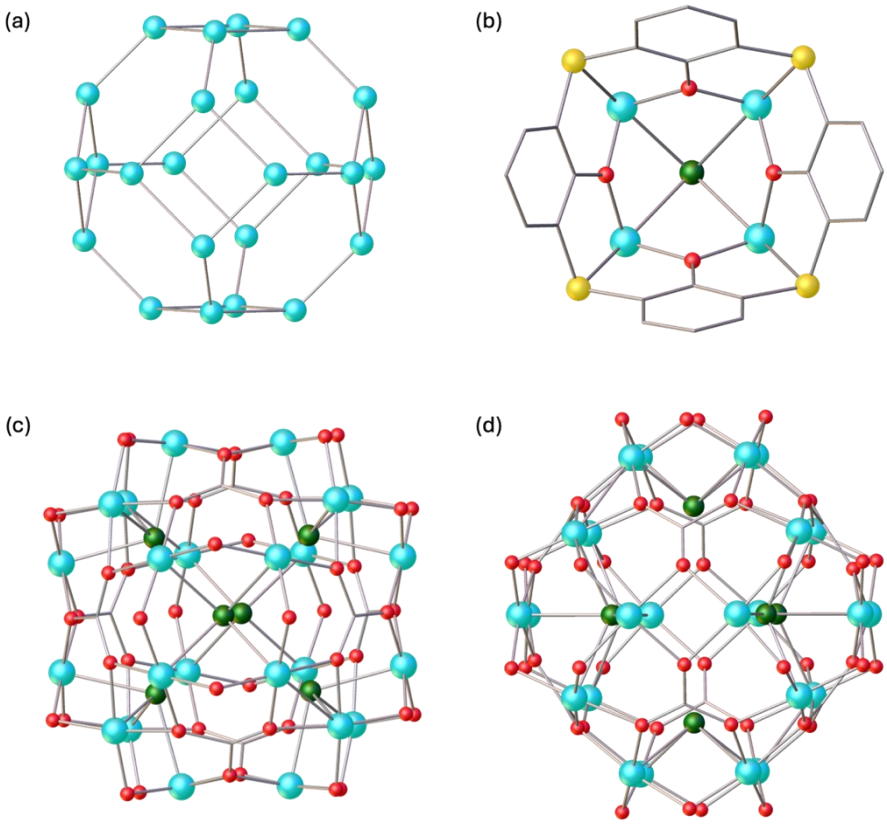

Figure 3.3 The metallic skeleton highlighting the truncated octahedron topology (a), TC[4]A bonding mode (b), and different views of the magnetic core (c-d) of **26**. Colour code: Cu^{II} - turquoise, Cl - dark green, S - yellow, C - grey, O - red.

originate from CO_2 fixation and/or MeOH oxidation. Interestingly the deliberate addition of CO_3^{2-} ions to the reaction mixture, in the form of Na_2CO_3/$NaHCO_3$, prevents crystal formation.

The Cu ions are all six-coordinate and in Jahn-Teller (JT) distorted {CuO_4SCl} environments with the JT axis directed along the S-Cu-Cl vector (Cu-O, ~1.60-2.10 Å; Cu-S, ~2.59-2.63 Å; Cu-Cl, ~2.65-2.67 Å). A disordered dmf molecule sits in each of the calixarene cavities. The self-assembly of the six [Cu_4(TC[4]A)Cl] moieties gives rise to an encapsulated space at the centre of the [Cu_{24}] cluster with a volume of ~381 $Å^3$ that is occupied by three disordered H_2O molecules. These are H-bonded to both the μ_4-Cl and the O-atoms of the μ_6-CO_3 / μ-OH ions (O···O/Cl $\leq$ 3 Å) that line the interior wall of the cage. The extended structure of **26** reveals brickwork-like packing of the clusters down the *a*- and *b*-axes (Figures S3.2-S3.3), with closest

intermolecular interactions occurring between the ^{t}Bu groups of the TC[4]A ligands (C···C ≥ 3.5 Å) and between the ^{t}Bu groups and the dmf solvate (C···O ≥ 3.7 Å).

We note that TC[4]A-stabilised truncated octahedra are known for Co^{II}, Ni^{II} and Mn^{II},[21–24] but **26** represents the first example with Cu^{II}. Interestingly, a [Cu^{I}_{24}] cage was recently synthesised using tetramercaptotetrathiacalix[4]arene,[25] which suggests that control over metal oxidation state can be achieved through choice/variation of lower rim substituent, or through the use of different calix[*n*]arenes within the same reaction, routes not yet exploited.

Interestingly, a [Cu^{II}_{8}] cluster similar to one third of the structure of **26** can be isolated be replacing $CuCl_2{\cdot}2H_2O$ with $CuBr_2$ in an otherwise identical reaction. Crystals of [Cu^{II}_{8}(TC[4]A)$_2$(μ_4-CO_3)(μ-OH)$(Br)_5$$(dmf)_3$$(H_2O)$]·2dmf (**27**, Figure 3.4) were found to be in an orthorhombic cell with structure solution performed in the space group *Pbca*; the ASU contains the whole formula. Pertinent bond lengths and bond angles are given in Table S3.5.

The structure of **27** describes two [Cu_4(TC[4]A)Br] metalloligands bridged by one μ_4-CO_3 ligand and one μ-OH ion. Here, each of the [Cu_4] squares is rather asymmetric, with one Cu-Br bond length of ~2.43-2.44 Å and three being in the range, ~2.98-3.09 Å. As a result, the Cu···Cu distances are also asymmetric, and in the range ~3.21-3.45 Å. The CO_3^{2-} ion, originating from CO_2 fixation and/or MeOH oxidation as with **26**, acts as a μ_4-bridge between the two [Cu_4] squares, linking Cu1 and Cu4 on one square with Cu6 and Cu7 on the second square. Cu4 and Cu7 are also bridged by the sole μ-OH (Cu4-O12-Cu7, ~105°) which itself is H-bonded to the terminal Br ion (Br6) attached to Cu8 with 50% occupancy (O(H)···Br, ~3.15 Å). Charge-balance is afforded through the 50% occupancy of another terminal Br ion (Br5) attached to Cu3, but at an angle that does not allow for H-bonding with the OH ion. The remaining coordination sites on the Cu ions are filled with a dmf molecule (Cu1, Cu3, Cu6), a H_2O molecule (Cu8), and a terminal Br ion with full occupancy (Cu2, Cu5).

The Cu ions adopt four different geometries/coordination spheres. Cu3 and Cu8 are either five- or six-coordinate as the Br ion is disordered across the two positions, thus have distorted square pyramidal/octahedral {$CuO_3Br_{1.5}S$} geometries. Cu2 and Cu5 are five-coordinate and in distorted square pyramidal {CuO_2Br_2S} geometries and Cu1/Cu4/Cu6/Cu7 are all six-coordinate and in distorted octahedral {CuO_4BrS} geometries. In each case the JT axis of the Cu^{II} ion lies along the S-Cu-Br vector. A molecule of dmf occupies each TC[4]A

cavity. Examination of the extended structure of **27** reveals that the closest intermolecular interactions occur between the ^{t}Bu groups on one TC[4]A and the phenyl rings on neighbouring TC[4]A units (C···C, > 3.5 Å). The clusters pack into ladder-like chains along the *b*-axis of the cell in which the [Cu^{II}_4] squares of neighbouring clusters face each other (Figure S3.4).

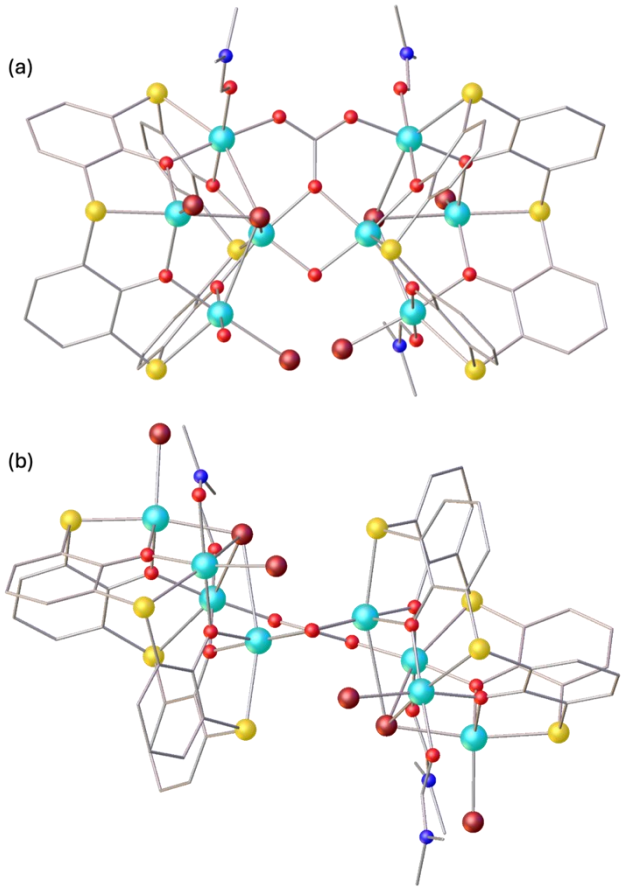

Figure 3.4 Single crystal X-ray structure of **27** shown from orthogonal perspectives. Colour code: Cu^{II} - turquoise, Br – dark red, S - yellow, N - blue, C - grey, O - red. H atoms, ^{t}Bu groups of TC[4]A and co-crystallised solvent molecules omitted for clarity.

B. Mixed-calix-supported clusters

Reaction of H_4TC[4]A and H_4TBC[4] with $MnCl_2{\cdot}4H_2O$ in a basic dmf/MeOH solution affords crystals of formula [$Mn^{III}_2Mn^{II}_4$(TBC[4])$_2$(TC[4]A)(μ_4-CO_3)(dmf)$_6$]·5MeCN (**28**, Figure 3.5), upon diffusion of MeCN into the mother liquor. The crystals were found to be in an orthorhombic

cell and structure solution was carried out in the space group *Pnma*. The ASU comprises half of the formula. Pertinent bond parameters and BVS calculations are given in Table S3.6.

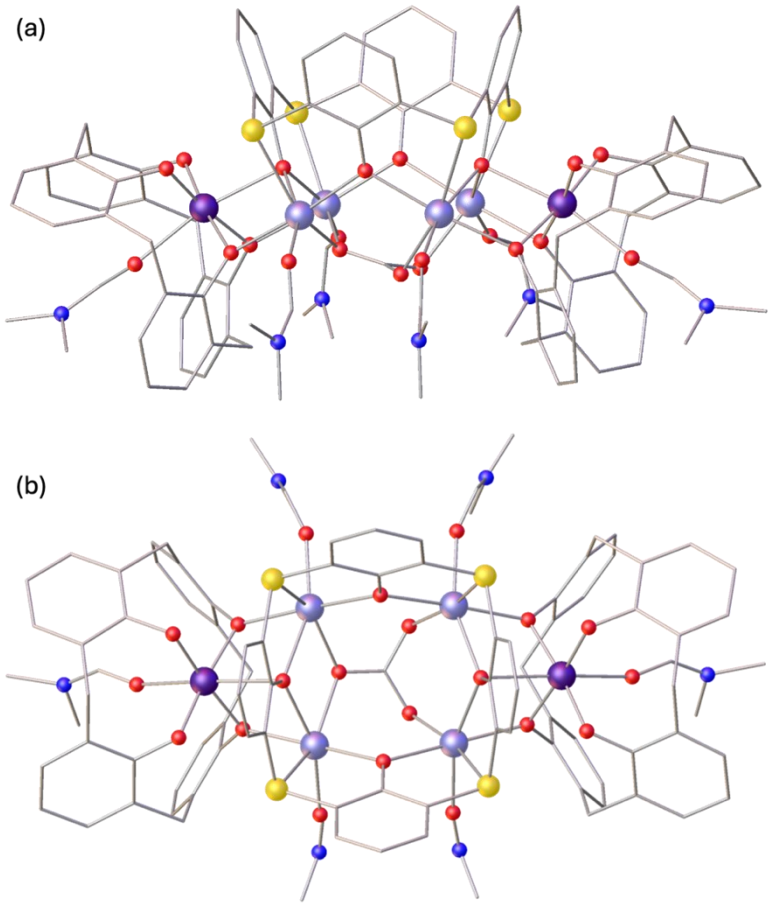

Figure 3.5 Single crystal X-ray structure of **28** shown from orthogonal perspectives. Colour code: Mn^{III} - dark purple, Mn^{II} - light purple, S - yellow, N - blue, C - grey, O - red. H atoms, ^{t}Bu groups of TC[4]A/TBC[4] and co-crystallised solvent molecules omitted for clarity.

The metallic skeleton of **28** (Figure 3.6) describes a near-planar array of six Mn ions, with the fully deprotonated TC[4]A ligand face-capping the central $[Mn^{II}_4]$ square, with each S-atom (S1, S2 and symmetry equivalent (s.e.)) bonded to a single Mn^{II} ion (Mn2, Mn3). Each of the four phenolic $\mu_{2/3}$-$OR_{TC[4]A}$ atoms bridge one edge of the square, with O12 (and s.e.) further bridging to the outer Mn^{III} ions (Mn1). The $Mn^{III}1$ ions are housed within the pocket of the fully deprotonated TBC[4] ligands, with two μ-O-atoms (O1, O4) also bridging to the Mn^{II} ions (Mn2, Mn3) in the central square. The two non-bridging O-atoms (O2, O3) are oriented towards the S-atoms of the TC[4]A ligands (O···S, ~3.1-3.2 Å). The coordination sphere of the distorted octahedral Mn^{III} ion, $\{MnO_6\}$, is completed by a terminally bonded dmf molecule,

with the O_{dmf}-Mn1-$O_{TC[4]A}$ vector defining the JT axis. A disordered CO_3^{2-} ion sits below the [Mn^{II}_4] square, opposite the TC[4]A ligand, bonding to all four Mn^{II} ions; the distorted {MnO_5S} coordination sphere of the Mn^{II} ions being completed with a molecule of dmf.

There are five MeCN molecules of crystallisation, one of which is housed in the TC[4]A cavity whilst the other four reside within the lattice space. Examination of the extended structure reveals the clusters pack in opposite layers as viewed down the *ab* plane (Figure S3.5). Closest intermolecular interactions are between the aromatic H-atoms of groups of the TC[4]A moieties and the dmf molecules in the lattice space ((C)H···N, ~2.7 Å).

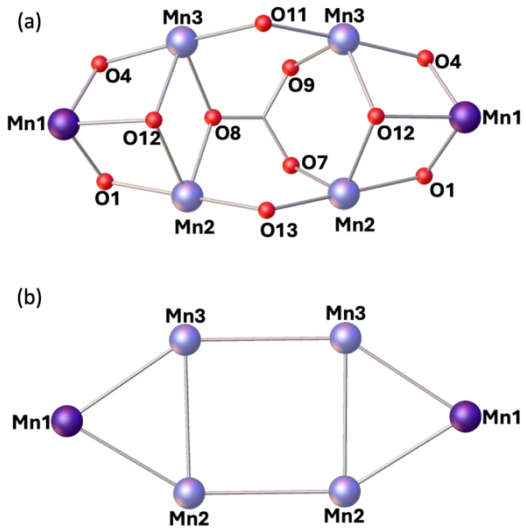

Figure 3.6 The cluster core (a) and metallic skeleton (b) of **28**. Colour code: Mn^{III} - dark purple, Mn^{II} - light purple, O - red.

Reaction of H_4TC[4]A and H_4TBC[4] with $MnCl_2{\cdot}4H_2O$, $CuCl_2{\cdot}2H_2O$ and Na(acac) in a basic dmf/MeOH mixture affords single crystals of [$Mn^{III}_6Mn^{II}_4Cu^{II}_4$(TBC[4])$_2$(TC[4]A)$_2$($\mu_4$-O)$_4$($\mu_3$-OH)$_4$($\mu$-OMe)$_6(Cl)_2$($H_2O$)$_2(dmf)_2$(MeCN)$_2$]·1.5MeOH·1dmf·0.5$H_2O$ (**29**, Figure 3.7), following vapour diffusion of MeCN into the mother liquor. The crystals were found to be in a monoclinic cell and structure solution was carried out in the space group *C2/c*. The ASU comprises half of the formula. Pertinent bond parameters and BVS calculations are provided in Table S3.7.

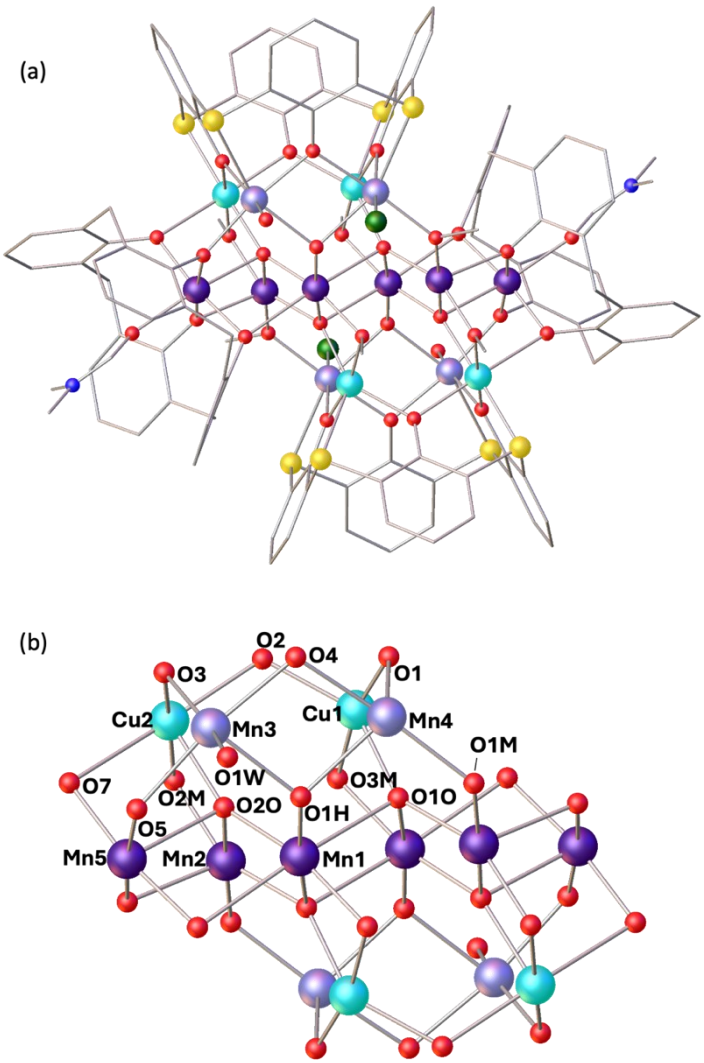

Figure 3.7 Single crystal X-ray structure (a) and cluster core (b) of **29.** Colour code: Mn^{III} - dark purple, Mn^{II} - light purple, Cu^{II} - turquoise, Cl - dark green, S - yellow, N - blue, C - grey, O - red. H atoms, ^{t}Bu groups of TC[4]A/TBC[4] and co-crystallised solvent molecules omitted for clarity.

The metallic skeleton of **29** (Figure 3.8a) describes a central, near planar, ladder-like $[Mn^{III}_6]$ unit (Mn1, Mn2, Mn5 and symmetry equivalent (s.e.)) flanked on either side by a $[Cu^{II}_2Mn^{II}_2]$ square (Cu1, Cu2, Mn3, Mn4 and s.e.). The central $[Mn^{III}_6]$ unit can alternatively be described as two edge-sharing $[Mn^{III}_4]$ butterflies. The Mn^{III} ions are connected to each other and to the Cu^{II} ions by four μ_4-O bridges (O1O, O2O and s.e.). Four of the six μ-OMe ions also bridge between the Mn^{III} and Cu^{II} ions (Mn1-O3M-Cu1, Mn2-O2M-Cu2 and s.e.) with the remaining two bridging between the Mn^{III} and Mn^{II} ions (Mn2-O1M-Mn4 and s.e.). The two μ_3-OH ions (O1H and s.e.) bridge between a Mn^{III} and two Mn^{II} ions (Mn1-O1H-Mn3/4 and s.e.).

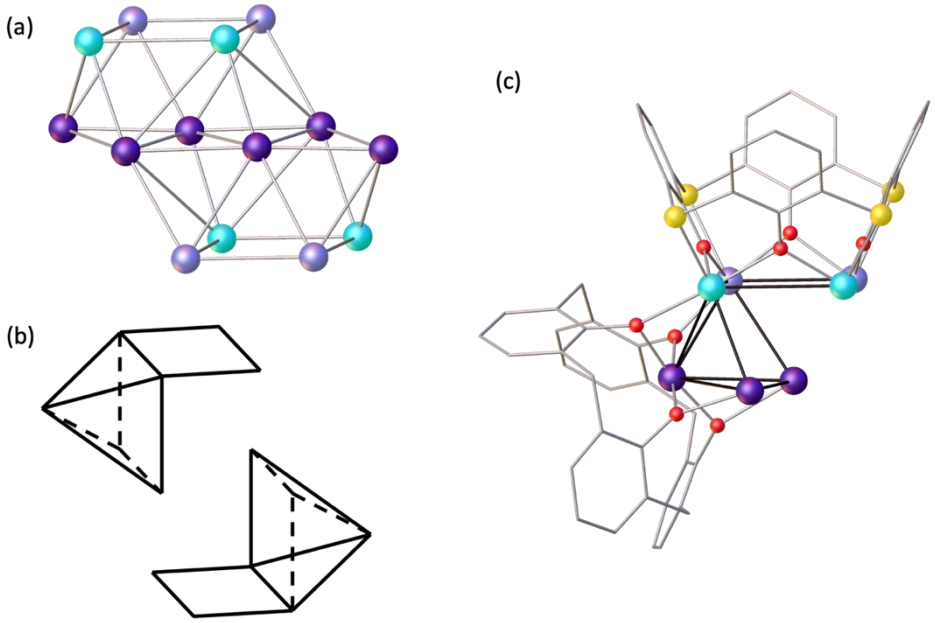

Figure 3.8 The metallic skeleton of **29** (a), with schematics showing the edge-sharing [M_5] square pyramid and [M_4] square moieties supported by perpendicular TBC[4]/TC[4]A ligands (b-c). Colour code: Mn^{III} - dark purple, Mn^{II} - light purple, Cu^{II} - turquoise, S - yellow, C - grey, O - red. H atoms and ^{t}Bu groups of TC[4]A/TBC[4] omitted for clarity.

The two fully deprotonated TC[4]A ligands each face-cap a [$Mn^{II}_2Cu^{II}_2$] square, with each S-atom (S1-S4 and s.e.) bonded to a single M^{II} ion and the four μ-$OR_{TC[4]A}$ atoms (O1-O4 and s.e.) bridging between neighbouring metal ions (Figure S3.6). The metal ions are arranged with the same metal sharing an edge (*i.e.* -Mn-Mn-Cu-Cu-) rather than alternating around the square. The two fully deprotonated TBC[4] ligands each house one Mn^{III} ion (Mn5 and s.e.) in their polyphenolic pocket with each μ-$OR_{TBC[4]}$ atom further bridging to another metal ion to form a [M_5] square pyramid (Figure S3.6). These additional metal ions are two Mn^{III} ions (Mn1, Mn2 and s.e.), one Cu^{II} ion (Cu2 and s.e.) and one Mn^{II} ion (Mn3 and s.e.). The latter also form one edge of the [$Mn^{II}_2Cu^{II}_2$] square and thus the TC[4]A and TBC[4] ligands lie perpendicular to one another (Figures 3.8). The presence of the TC[4]A-based [M_4] square and TBC[4]-based [M_5] pyramid are expected based on previously established metal ion binding rules, and preference for softer and harder M^{II} and M^{III} ions, respectively. A molecule of dmf lies in the TBC[4] cavity completing the six-coordination sphere of Mn5 (and s.e.) with the JT elongated axis defined by the O1D(dmf)-Mn5-O2O vector. The JT axes of Mn1 and Mn2 lie approximately co-parallel to this, given by the O5(TBC[4])-Mn1-O1O and O8(TBC[4])-

Mn2-O3M vectors, although Mn2 is perhaps better described as five-coordinate and square-pyramidal in geometry given the Mn2-O3M distance measures ~2.7 Å. The Mn^{II} ions (Mn3/Mn4) are six-coordinate and in distorted octahedral {MnO_4SX} coordination spheres with the sixth site (X) occupied by either a H_2O molecule (Mn3) or a Cl ion (Mn4). The Cu^{II} ions are five- (Cu1) and six- (Cu2) coordinate with distorted square pyramidal {CuO_4S} and octahedral {CuO_5S} geometries, respectively. A MeCN molecule of crystallisation occupies the TC[4]A cavity, with disordered solvent molecules of MeOH, dmf and H_2O residing throughout the lattice (1.5, 1 and 0.5 molar equivalents respectively). These form an intricate set of H-bonding interactions with each other and the [$Mn_{10}Cu_4$] cluster. For example, the Cl ions attached to Mn4 and the H_2O molecule attached to Mn4 are H-bonded to each other (Cl···(H)O, ~3.0 Å), the latter also H-bonding to a S-atom of the TC[4]A ligand (O(H)···S, ~3.3 Å). Together, these interactions serve to link individual [$Mn_{10}Cu_4$] clusters in the *ac* plane of the unit cell. Observation of the extended structure reveals that this leads to the cluster molecules packing in a columnar fashion down the *a*- and *c*-axes, whilst the *b*-axis shows the clusters orienting such that the tetraphenolic cavities of neighbouring clusters facing each other are of the same C[4] type (Figure S3.7).

It is worth nothing that whilst the presence of Na(acac) in the reaction mixture is essential for the formation of **29**, it does not appear in the structure. As part of efforts to incorporate acac into the cluster, we repeated the reaction for **29** without including H_4TBC[4] which afforded crystals of formula [$Mn^{II}_3Cu^{II}_2$(TC[4]A)$_2$(acac)$_2$]·1.7MeCN·1.25dmf·0.85MeOH·0.4H_2O (**30**, Figure 3.9) upon diffusion of MeCN into the mother liquor. We include it here to allow a comparison of the coordination in a Mn/Cu-TC[4]A-supported cluster (**30**) with respect to Mn/Cu-TC[4]A-TBC[4]-supported cluster (**29**). The crystals of **30** were found to be in a triclinic cell and structure solution was carried out in the space group *P*-1. The ASU comprises two distinct [$Mn^{II}_3Cu^{II}_2$] molecules of the same formula and structure, with similar bond distances and angles. Pertinent bond parameters and BVS calculations are given in Table S3.8.

The metallic skeleton of **30** is a near planar array of two Cu^{II} ions and three Mn^{II} ions with a [Mn^{II}_3] triangle in the centre, edge-capped on two sides by a Cu^{II} ion (Figure 3.9c). The [Mn^{II}_3] triangle is asymmetric (isosceles) with one edge being bridged by two μ-O atoms from two different TC[4]A ligands, one above the [M_5] plane and one below the [M_5] plane. The remaining two edges are bridged by just one μ_3-O atom from two different TC[4]A ligands, again originating from one ligand above and one below the [M_5] plane. These O-atoms

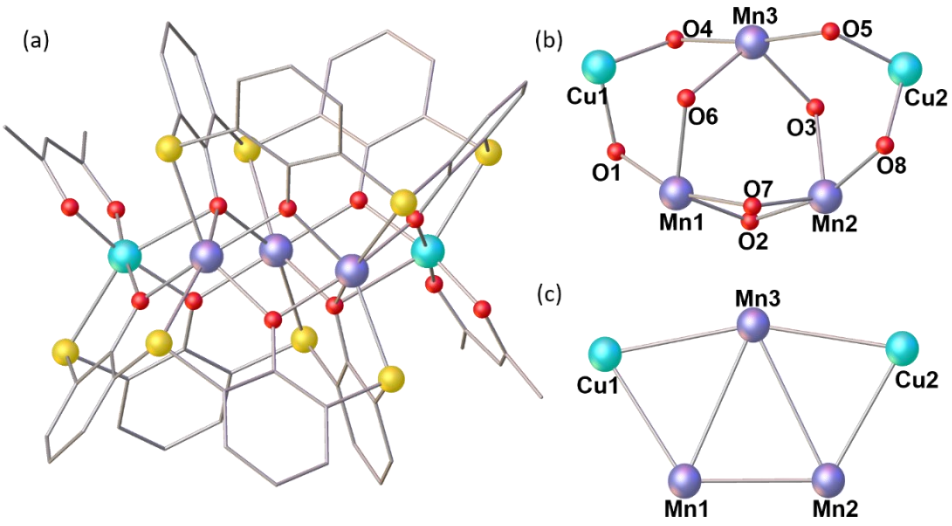

Figure 3.9 Single crystal X-ray structure (a) and cluster core (b) and metallic skeleton (c) of **30.** Colour code: Mn^{III} - dark purple, Mn^{II} - light purple, Cu^{II} - turquoise, S - yellow, C - grey, O - red. H atoms, ^{t}Bu groups of TC[4]A and co-crystallised solvent molecules omitted for clarity.

further bridge to the edge-capping Cu^{II} ions, although one of the bond distances is quite distinct (~2.44-2.49 Å *versus* ~2.64 Å). Each Cu ion is further bridged to the $[Mn^{II}_3]$ triangle through two O-atoms from the same TC[4]A ligand, thus affording a $[Mn^{II}_3Cu^{II}_2O_8]^{2+}$ magnetic core. As expected the S-atoms are coordinated terminally, with each acac chelating to a Cu ion. The latter are six-coordinate and in distorted $\{CuO_5S\}$ geometries with the JT axis directed by the S-atom (S-Cu-O). The Mn^{II} ions are also six-coordinate and in distorted octahedral $\{MnO_4S_2\}$ geometries, with two S-atoms being *cis* to each other. As with **29**, the two fully deprotonated TC[4]A ligands each face-cap a $[Mn^{II}_2Cu^{II}_2]$ square with each S-atom bonded to a single M^{II} ion and the four μ-O atoms bridging between neighbouring metal ions. However, in this case one of four O-atoms further bridges to a Cu ion, affording the unusual μ_5-bridging mode.

The cavities of the TC[4]A ligands are occupied by a disordered MeCN molecule of crystallisation in three out of four cases (across the two clusters in the ASU) with the last being occupied by a disordered combination of MeCN, dmf and MeOH. Numerous other solvent molecules are disordered throughout the lattice, with occupancies modelled to the nearest reasonable fraction making total solvent occupation hard to determine with

certainty (MeCN, ~1.7; dmf, ~1.25; MeOH, ~0.85; H_2O, ~0.4). Packing in the extended structure occurs in a columnar arrangement as viewed down the *b*-axis, with closest cluster-cluster interactions between the acac ligands on one molecule and the TC[4]A ligands on the neighbour (C···C/S distances in the range ~3.26-3.37 Å).

Comparison of the reaction mixtures and crystals structures of **29** and **30** allows us to make two observations; (a) the presence of a second calix[4]arene ligand in **29** allows us to access higher nuclearity (repeating the reaction for **30** using equimolar equivalents of calix[*n*]arene ligand as in **29** has no tangible effect on the reaction), and (b) the presence/absence of H_4TBC[4] in the reaction mixture leads to the presence/absence of Mn^{III} ions in the crystal structure.

Having started to explore the synchronous coordination behaviours of H_4TC[4]A and H_4TBC[4], successive investigation into the behaviours of H_4TC[4]A and H_8TBC[8] upon mutual (partial) deprotonation and coordination were examined. *p-tert*-butylcalix[8]arene (H_8TBC[8]) is a larger and more flexible alternative to H_4TBC[4], comprising double the phenolic rings, multiple conformations and as such, disparate coordination capacity. The solvothermal reaction of H_8TBC[8], H_4TC[4]A, $CoCl_2{\cdot}6H_2O$ and isonicotinic acid in a basic dmf/MeOH solution affords single crystals of formula $[Co^{II}_4(H_3TBC[8])(TC[4]A)Cl]{\cdot}3dmf$ (**31**, Figure 3.10) upon slow evaporation of the mother liquor. The crystals were found to be in a triclinic cell and structure solution was carried out in the space group *P*-1. The ASU comprises the whole cluster and pertinent bond parameters and BVS calculations are provided in Table S3.9. The H_3TBC[8] ligand in **31** displays the common 'pleated-loop' conformation, where the partial deprotonation (three phenolic H atoms disordered over four positions) provides charge balance and is supported *via* a network of H-bonding with OH···O distances consistent with previously reported examples (Figure S3.9).[26]

The metallic skeleton of **31** describes a $[Co^{II}_4]$ square, one face of which is capped by the deprotonated TC[4]A ligand and the other by the H_3TBC[8] ligand. As anticipated, the S-atoms of TC[4]A coordinate terminally to each Co^{II} ion, with the deprotonated μ-$O_{TC[4]A}$ atoms each bridging between two Co^{II} ions to form the edges of the square. The H_3TBC[8] ligates differently, offering each Co^{II} ion two terminal O-atoms. Each Co^{II} ion displays a distorted octahedral geometry and ligation is completed *via* a μ_4-Cl ion residing centrally within the square (Co-Cl, ~2.69-2.83 Å). One MeCN molecule sits within the TC[4]A cavity, with two further MeCN molecules residing in two of the partial cavities of the TBC[8] 'pleated-loop'.

These latter solvates form CH···π interactions with the H_3TBC[8] aromatic rings (~2.86 Å). Examination of the extended structure of **31** reveals the remaining partial cavities are blocked by the *tert*-butyl groups of the neighbouring clusters (closest cluster-cluster interaction, (C)H···H ~2.47 Å), which are closely packed and oriented alternately down the *a*-axis (Figure S3.10).

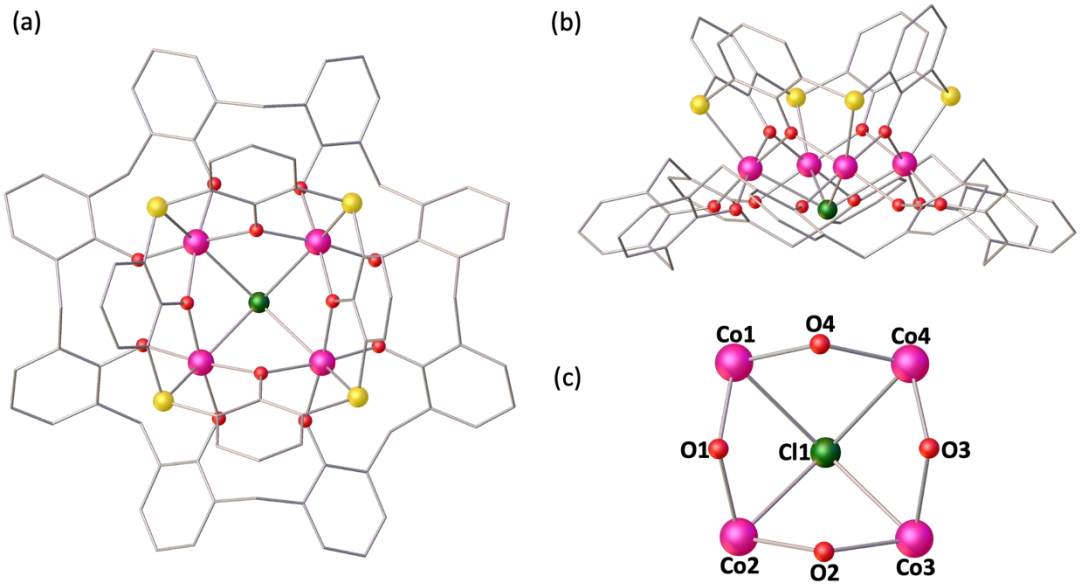

Figure 3.10 Single crystal X-ray structure shown from orthogonal perspectives (a-b) and the cluster core (c) of **31.** Colour code: Co^{II} - pink, Cl - dark green, S - yellow, C - grey, O - red. H atoms, ^{t}Bu groups of TC[4]A/TBC[8] and co-crystallised solvent molecules omitted for clarity.

It is worth nothing that this [M_4] square topology is reminiscent of multiple TC[4]A-supported [Co^{II}]$_4$ clusters in literature,[27–31] whereby one face of the square is capped by TC[4]A as in **31**, but the other face left uncapped and ligation of the Co^{II} ions completed by various small ligand/solvent molecules. This suggests that in the example of **31**, addition of H_8TBC[8] into the reaction mixture has not afforded a new cluster topology but rather obliged by the coordination behaviour of TC[4]A (*i.e.* the coordination of TC[4]A dominates). Given that TBC[8] has 16 unique conformations,[32] further exploration into the H_4TC[4]A/H_8TBC[8] reaction space seems likely to afford numerous novel topologies.

Magnetic measurements

A. TC[4]A-supported clusters

Direct current (dc) magnetic susceptibility data were measured on powdered polycrystalline samples of **26**-**27** in the T = 300 – 2 K temperature range, in a field of B = 0.1 T (Figure 3.11), where $\chi_M = M/B$ and M is the magnetisation. The $\chi_M T$ values of **26**/**27** at 300 K are 4.29/2.49 cm^3 K mol^{-1}, both well below the Curie constant expected for 24/8 uncoupled Cu^{II} (S = ½) ions (9/3 cm^3 K mol^{-1} for g = 2.00). As the temperature is decreased, the value of $\chi_M T$ decreases rapidly in both cases and reaches a value of 0 cm^3 K mol^{-1} at T = 15/5 K. This behaviour is clearly indicative of very strong antiferromagnetic exchange between neighbouring Cu^{II} ions in both **26** and **27**, and the presence of well isolated diamagnetic ground states.

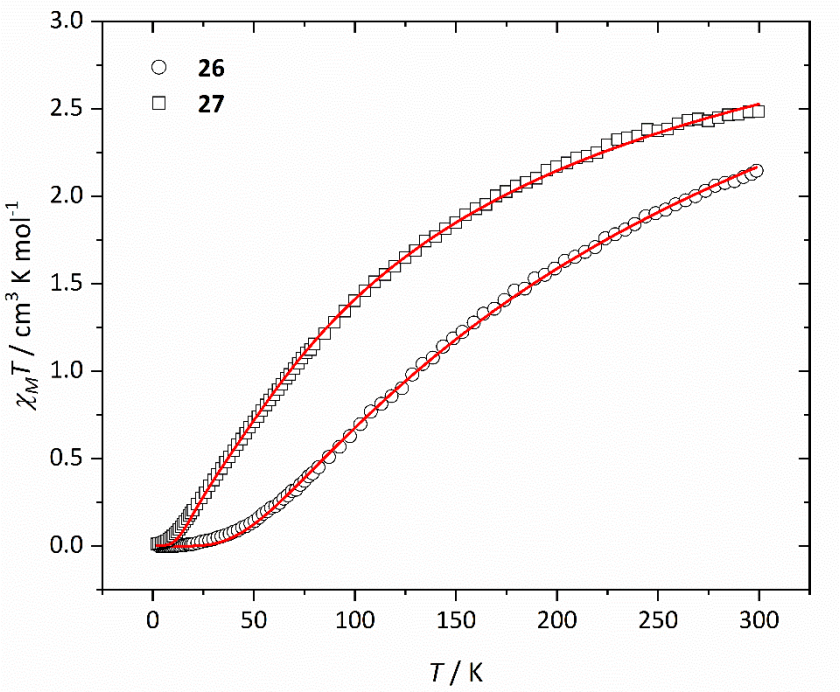

Figure 3.11 Experimental $\chi_M T$ *vs* T data for **26** (circles) and **27** (squares) measured in the T = 300 – 2 K temperature range in an applied field, B = 0.1 T. The solid red lines are the best fits modelled using spin-Hamiltonian (3.1). Data for **26** shown halved due to fitting using [Cu_{12}] models (see text).

The presence of two different clusters of **26** in the unit cell, the disordered CO_3^{2-}/OH^- and a total of 24 Cu^{II} ions per cluster poses some issues when it comes to modelling the magnetic behaviour. To overcome these issues, we have constructed a series of [Cu_{12}] model compounds (Models 1-3, Figure 3.12) that describe half the cluster, and assume the presence of not more than three distinct exchange interactions based on the different bridging atoms and angles present. These are J_1 = Cu-O/Cl-Cu along the sides of the square faces (Cu-O-Cu = ~109-112°, Cu-Cl-Cu = ~75°); J_2 = Cu-Cl-Cu across the diagonal of the square faces (Cu-Cl-Cu = ~118°); and J_3 = Cu-O-Cu along the shared edges of the hexagonal faces (Cu-O_{OH}-Cu = ~94°; Cu-O_{CO3}-Cu = ~120°) through the disordered OH/CO_3 bridges. We ignore any diagonal interactions across the face of the hexagon through the three atom Cu-O-C-O-Cu carbonate bridges. These models could then be applied to the experimental data along with spin-Hamiltonian (3.1) where the summation indices *i, j* run though the constituent metal ions, $\hat{S}$ is a spin operator, *S* is the total spin, μ_B is the Bohr magneton, *g* is the g-factor (*g* = 2.00), and J_{ij} is the bilinear pairwise isotropic exchange interaction parameter.

$$\hat{H} = \mu_B B \sum_i g_i \hat{S}_i - 2 \sum_{i,j<1} J_{i,j} \hat{S}_i \cdot \hat{S}_j \qquad (3.1)$$

Best-fit parameters for each calculation are given Table 3.1. What is clear is that each model matches the experimental data very well (Figure 3.11, S3.11) but does so with different sets of *J* values. In other words, there is no unique fit of the data and we can only conclude that the *J* values range between -115 < *J* < -139 cm^{-1}. Note, we disregard Model 2 on account of the erroneously large J_2 value.

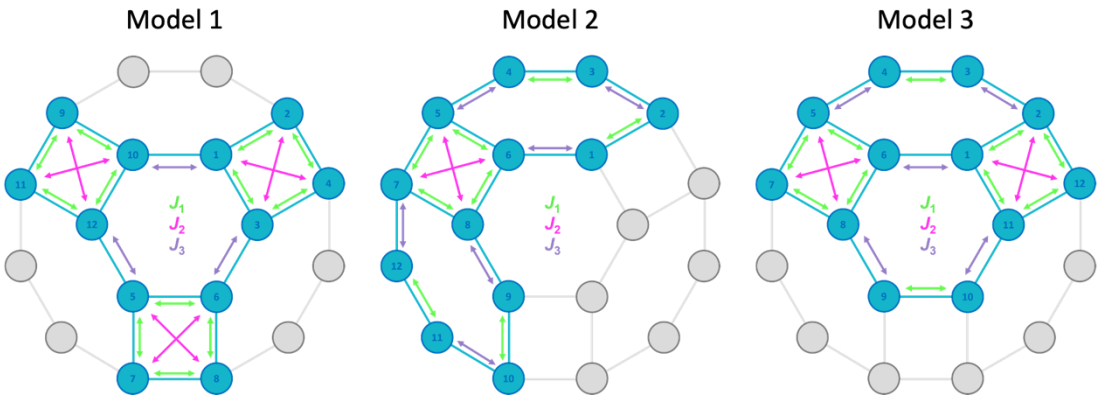

Figure 3.12 Schematic representation of the [Cu_{12}] 3*J* models (Models 1-3) used to fit the experimental susceptibility data of **26**, as discussed in text.

Table 3.1 The best-fit parameters found from fitting the magnetic susceptibility data of **26** for each [Cu_{12}] model constructed. Models 1-3 and *J* assignments are shown in Figure 3.12.

	J_1 / cm^{-1}	J_2 / cm^{-1}	J_3 / cm^{-1}
Model 1	-101.29	-56.40	-115.81
Model 2	-98.00	-295.55	-80.65
Model 3	-70.43	-138.70	-115.51

The data for **27** can be fitted in a similar fashion using spin-Hamiltonian (3.1) and the model shown in Figure 3.13, which contains two *J* values, one within the [Cu_4] squares (J_1) and one between them (J_2). The best fit parameters are J_1 = -40.56 cm^{-1} and J_2 = -98.62 cm^{-1} (g = 2.00) and give excellent agreement to the experimental data (Figure 3.11). The *J* values obtained for **26** and **27** are in accordance with previous magneto-structural correlations developed for O-/Cl-bridged Cu^{II} dimers with similar Cu-O/Cl-Cu angles.[1–3]

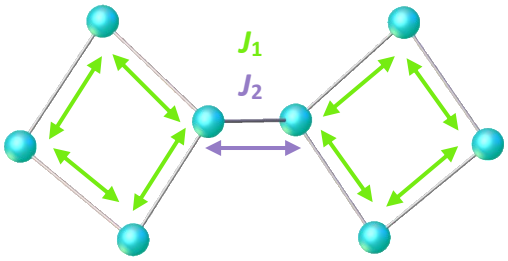

Figure 3.13 Schematic representation of the 2*J* model used to fit the experimental susceptibility data of **27,** as discussed in text.

B. Mixed-calix-supported clusters

Dc magnetic susceptibility studies were performed on a polycrystalline sample of **28** in an applied magnetic field B = 0.1 T, over the temperature range T = 300 - 2 K (Figure 3.14). At 300 K, the $\chi_M T$ value of 23.45 cm^3 K mol^{-1} is in agreement with the expected spin-only contributions to the susceptibility of a [$Mn^{III}_2Mn^{II}_4$] cluster (23.5 cm^3 K mol^{-1}, g = 2.00). Upon

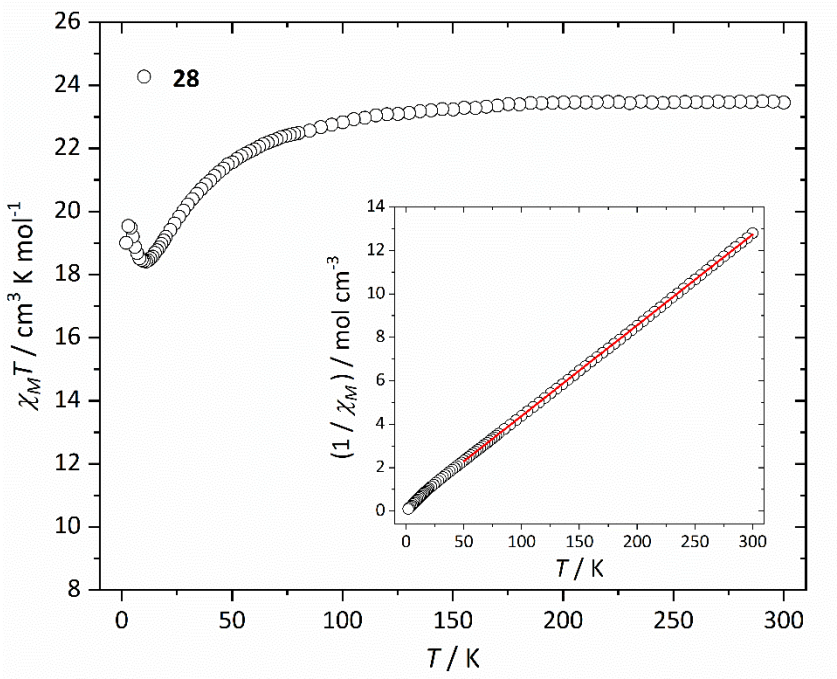

Figure 3.14 Experimental $\chi_M T$ *vs* T data for **28** measured in the T = 300 – 2 K temperature range in an applied field, B = 0.1 T. Inset: Plot of $1/\chi_M$ *vs* T data in the same T range. The solid red line is a fit of the experimental data to the Curie-Weiss law in the range T = 300 - 50 K.

cooling, the $\chi_M T$ product decreases slowly until approaching approximately T = 80 K, where it decreases more rapidly to a value of 18.43 cm^3 K mol^{-1} at T = 10 K. Upon further cooling, $\chi_M T$ increases reaching a value of 19.54 cm^3 K mol^{-1} at T = 3 K, followed by a decrease to 19.01 cm^3 K mol^{-1} at T = 2 K. Variable-temperature-variable-field (VTVB) magnetisation data measured in the temperature range T = 2 - 10 K and field range B = 0 - 9 T shows M rising steadily with increasing B, reaching a maximum value of M = 16.60 μ_B at 9 T without reaching saturation (Figure S3.12). This behaviour is indicative of the presence of weak, competing ferro- and antiferromagnetic exchange interactions. The structural complexity of **28** prevents a full quantitative analysis of the data, however a fit of the inverse susceptibility data to the Curie-Weiss law, in the range T = 300 - 50 K, affords θ = -4.90 K and C = 23.94 cm^3 K mol^{-1} (inset of Figure 3.14), suggestive of weak, dominant antiferromagnetic exchange.

Dc magnetic susceptibility studies were also performed on a polycrystalline sample of **29** in an applied magnetic field B = 0.1 T, over the temperature range T = 300 - 2 K (Figure 3.15). At 300 K, the $\chi_M T$ value of 21.82 cm^3 K mol^{-1} is well below the expected spin-only contributions to the susceptibility of a [$Mn^{III}_6Mn^{II}_4Cu^{II}_4$] cluster (37 cm^3 K mol^{-1}, g = 2.00). Upon cooling, the $\chi_M T$ product decreases consistently, reaching a value of 2.93 cm^3 K mol^{-1} at T = 2 K. Magnetisation data measured in the temperature range T = 2 - 10 K and field range B = 0 - 9 T shows M rising steadily with increasing B, reaching a maximum value of M = 5.87 μ_B at 9 T without reaching saturation (Figure S3.13). This behaviour is indicative of the presence of strong antiferromagnetic exchange interactions. The large nuclearity and structural complexity of **29** prevents any quantitative analysis of the data. The non-linearity of the inverse susceptibility also prevents a simple CW fit.

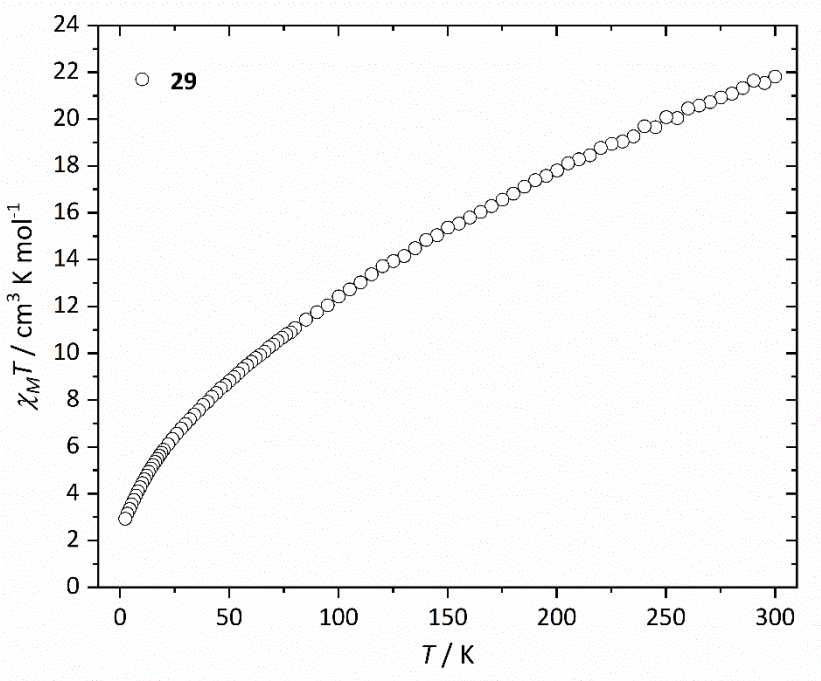

Figure 3.15 Experimental $\chi_M T$ *vs* T data for **29** measured in the T = 300 – 2 K temperature range in an applied field, B = 0.1 T.

Dc magnetic susceptibility studies were performed on a polycrystalline sample of **30** in an applied magnetic field B = 0.1 T, over the temperature range T = 300 – 2 K (Figure 3.16). At 300 K, the $\chi_M T$ value of 13.31 cm^3 K mol^{-1} is slightly below the expected spin-only contributions to the susceptibility of a [$Mn^{II}_3Cu^{II}_2$] cluster (14.03 cm^3 K mol^{-1}, $g_{Mn(II)}$ = 2.00, $g_{Cu(II)}$ = 2.20). As the temperature decreases, the $\chi_M T$ product decreases steadily until

approximately T = 100 K, where it decreases more rapidly reaching a value of 1.29 cm^3 K mol^{-1} at T = 2 K. VTVB magnetisation data (inset of Figure 3.16) shows M increasing with B, reaching a maximum value of M = 4.38 μ_B at 9 T without reaching saturation. This behaviour is suggestive of weak antiferromagnetic exchange interactions. A simultaneous fit of the susceptibility and magnetisation data was performed using spin-Hamiltonian (3.1) and the 3J model in Figure 3.17, where J_1 is the interaction between Cu^{II}-Mn^{II} ions (Cu1-Mn1, Cu1-Mn3, Cu2-Mn2, Cu2-Mn3), J_2 is the interaction between the Mn^{II} ions along the legs of the isosceles triangle (Mn1-Mn3, Mn2-Mn3) and J_3 is the interaction between the Mn^{II} ions along the base of the isosceles triangle (Mn1-Mn2). This resulted in excellent agreement with the experimental data with best-fit parameters J_1 = -2.27 cm^{-1}, J_2 = -1.47 cm^{-1} and J_3 = -3.31 cm^{-1} ($g_{Mn(II)}$ = 2.00, $g_{Cu(II)}$ = 2.20).

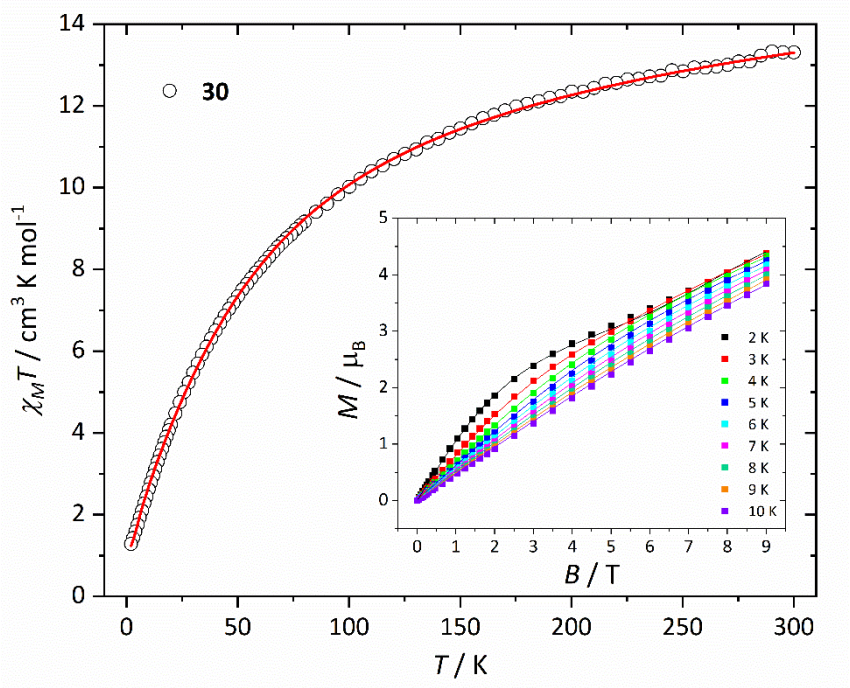

Figure 3.16 Experimental $\chi_M T$ *vs* T data for **30** measured in the T = 300 – 2 K temperature range in an applied field, B = 0.1 T. Inset: Variable-temperature-variable-field (VTVB) magnetisation data of **30** at T = 2 - 10 K and B = 0 - 9 T. The solid lines are the best fit of the data modelled using spin-Hamiltonian (3.1).

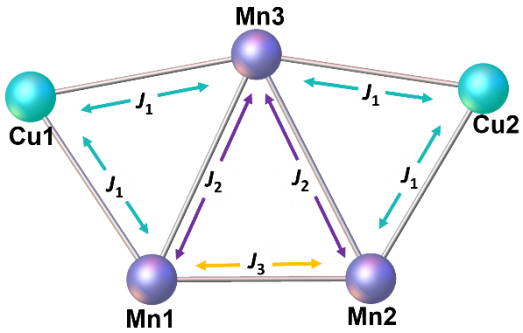

Figure 3.17 Schematic representation of the 3*J* model used to fit the experimental susceptibility and magnetisation data of **30,** as discussed in text.

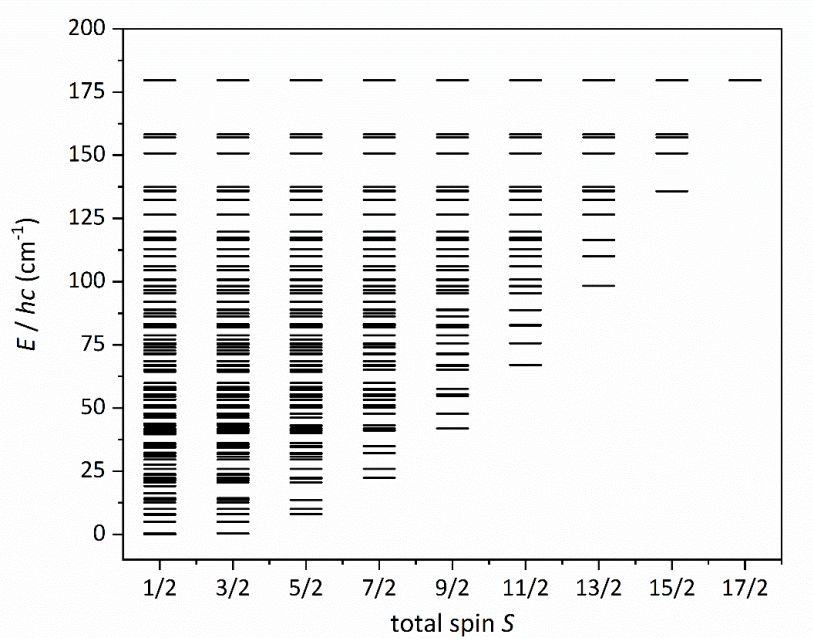

Figure 3.18 Energy spectrum of **30** calculated from the fit of the susceptibility data, as described in text. The spin ground state of **30** is an S = 1/2 spin-state, with excited S = 1/2 and S = 3/2 states lying 0.36 cm^{-1} above the ground state.

These values result in the stabilisation of an S = 1/2 spin ground state, separated by several low-lying excited S = 1/2 and S = 3/2 states by 0.36 cm^{-1}, as shown in the Energy *vs* Spin-State diagram in Figure 3.18. The *J* values are in accordance with previously reported O-bridged Mn^{II}/Cu^{II} complexes with similar M-X-M angles.[33,34]

Dc magnetic susceptibility studies were performed on a polycrystalline sample of **31** in an applied field B = 0.1 T, over the temperature range T = 300 - 2 K (Figure 3.19). At 300 K, the $\chi_M T$ value of 7.01 cm^3 K mol^{-1} is just below the expected spin-only contributions to the susceptibility of a [Co^{II}_4] cluster (7.5 cm^3 K mol^{-1}, g = 2.00). As the temperature decreases, the $\chi_M T$ product decreases steadily until approximately T = 75 K, at which point further cooling decreases it more rapidly to reach a $\chi_M T$ value of 0.25 cm^3 K mol^{-1} at T = 2 K. The magnetisation data (inset Figure 3.19) remains close to zero in fields up to B = 9 T and T = 10 K. The high temperature decrease in the susceptibility data can be assigned to a combination of the orbital contributions of the octahedral Co^{II} ion,[35,36] and/or weak antiferromagnetic exchange interactions.

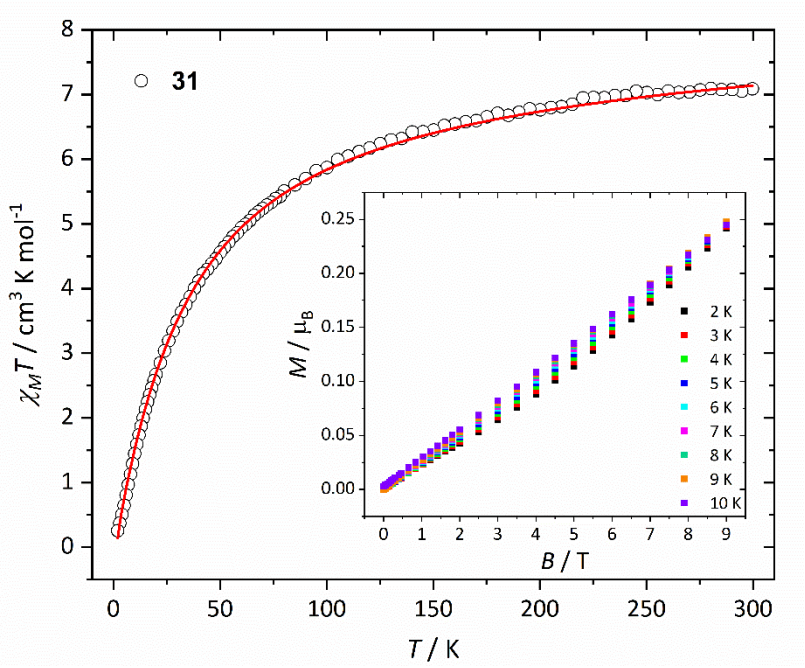

Figure 3.19 Experimental $\chi_M T$ *vs* T data for **31** measured in the T = 300 – 2 K temperature range in an applied field, B = 0.1 T. The solid red line is the best fit of the susceptibility data using spin-Hamiltonian (3.1). Inset: Variable-temperature-variable-field (VTVB) magnetisation data of **31** at T = 2 - 10 K and B = 0 - 9 T.

The susceptibility data can be fitted using a spin-only Hamiltonian (3.1) and the simple 1J model shown in Figure S3.14, affording the best-fit parameter J = -2.60 cm^{-1} with g = 2.00. Note, however, that the magnetisation data cannot be fitted with this simple model, and that the values above should be taken with a pinch of salt. Several of the aforementioned

TC[4]A-supported [Co^{II}_4] squares in literature report magnetic data with antiferromagnetic behaviour, though none provide a quantitative fit of the susceptibility/magnetisation data.[27,29,31]

3.4 Conclusions

The successful synthesis and characterisation of [Cu^{II}_{24}] (**26**) and its [Cu^{II}_{8}] building block (**27**) represent novel additions to the TC[4]A family, the former truncated octahedron joining the family of known TC[4]A-supported [M_{24}] cages of Ni^{II}, Co^{II} and Mn^{II}. Surprisingly, **26** and **27** are just the sixth and seventh known polymetallic Cu-TC[4]A clusters, with **26** being by far the largest yet reported. Given the clear affinity between M^{II} ions and TC[4]A, one would expect many more such compounds await discovery. Magnetic susceptibility measurements reveal the presence of very strong antiferromagnetic interaction between neighbouring Cu^{II} ions in **26** and **27**, resulting in well isolated S = 0 ground states in both cases.

Given the proclivity of TC[4]A to form [M^{II}_4] square moieties, and the notable absence of any mixed-calix[*n*]arene clusters in literature, successive investigations yielded the first reported heterocalix[*n*]arene clusters, all of which contain TC[4]A. Combining H_4TC[4]A and H_4TBC[4] in the presence of $MnCl_2{\cdot}4H_2O$ afforded a [$Mn^{III}_2Mn^{II}_4$] cluster (**28**), supporting our hypothesis that the M^{III}/triangle favouring TBC[4] and M^{II}/square favouring TC[4]A would assemble structures that maintained these topologies. Magnetic studies reveal weak antiferromagnetic exchange, with a fit of the inverse susceptibility data affording Curie-Weiss parameters θ = -4.90 K and C = 23.94 cm^3 K mol^{-1}.

Introducing $CuCl_2{\cdot}2H_2O$ into this reaction space, as well as the addition of Na(acac) yielded the [$Mn^{III}_6Mn^{II}_4Cu^{II}_4$] cluster (**29**), where the TBC[4] and TC[4]A oxidation state/building block preferences are again upheld. Magnetic measurements revealed strong antiferromagnetic exchange interactions, but the high nuclearity and structural complexity of the cluster prevent quantitative analysis. Interestingly, whilst Na(acac) is necessary for the formation of **29**, it does not appear in the structure. Efforts to explore this yielded a [$Mn^{II}_3Cu^{II}_2$] cluster (**30**) supported by just TC[4]A, included to highlight the absence of Mn^{III} ions when TBC[4] is not present, and the formation of squares even in a [M_5] nuclearity. Magnetic studies revealed competing antiferromagnetic exchange interactions (J_1 = -2.27 cm^{-1}, J_2 = -1.47 cm^{-1} and J_3 = -3.31 cm^{-1}).

Having seen the success of combining H_4TBC[4] and H_4TC[4]A in affording novel topologies with unique oxidation state distributions, we began investigating the octa-phenolic H_8TBC[8]. Reaction of H_8TBC[8] and H_4TC[4]A in the presence of $CoCl_2{\cdot}6H_2O$ and isonicotinic acid yielded a [Co^{II}_4] cluster (**31**). TC[4]A acted as expected by face-capping the square moiety,

whilst H_3TBC[8] adopted the pleated-loop conformation and face-capped the other face of the $[Co^{II}]_4$ square. Magnetic measurements revealed weak antiferromagnetic exchange. We postulate that since H_8TBC[8] can exist in 16 different conformations, further exploration here is likely to yield more novel mixed-calix[*n*]arene clusters.

3.5 References

(1) B. Bleaney and K. D. Bowers, *Proc. R. Soc. Lond. Ser. Math. Phys. Sci.*, 1952, **214**, 451–465.

(2) V. H. Crawford, H. Wayne. Richardson, J. R. Wasson, D. J. Hodgson and W. E. Hatfield, *Inorg. Chem.*, 1976, **15**, 2107–2110.

(3) W. E. Marsh, K. C. Patel, W. E. Hatfield and D. J. Hodgson, *Inorg. Chem.*, 1983, **22**, 511–515.

(4) S. Ferrer, F. Lloret, E. Pardo, J. M. Clemente-Juan, M. Liu-González and S. García-Granda, *Inorg. Chem.*, 2012, **51**, 985–1001.

(5) M.-A. Bouammali, N. Suaud, N. Guihéry and R. Maurice, *Inorg. Chem.*, 2022, **61**, 12138–12148.

(6) N. Iki, in *Calixarenes and Beyond*, eds. P. Neri, J. L. Sessler and M.-X. Wang, Springer International Publishing, Cham, 2016, pp. 335–362.

(7) T. Sone, Y. Ohba, K. Moriya, H. Kumada and K. Ito, *Tetrahedron*, 1997, **53**, 10689–10698.

(8) Kumagai, M. Hasegawa, S. Miyanari, Y. Sugawa, Y. Sato, T. Hori, S. Ueda, H. Kamiyama and S. Miyano, *Tetrahedron Lett.*, 1997, **38**, 3971–3972.

(9) Morohashi, F. Narumi, N. Iki, T. Hattori and S. Miyano, *Chem. Rev.*, 2006, **106**, 5291–5316.

(10) R. Kumar, Y. O. Lee, V. Bhalla, M. Kumar and J. S. Kim, *Chem. Soc. Rev.*, 2014, **43**, 4824–4870.

(11) M. Yamada, M. Rajiv Gandhi, U. M. R. Kunda and F. Hamada, *J. Incl. Phenom. Macrocycl. Chem.*, 2016, **85**, 1–18.

(12) Y. Bi, S. Du and W. Liao, *Coord. Chem. Rev.*, 2014, **276**, 61–72.

(13) A. Bilyk, A. K. Hall, J. M. Harrowfield, M. W. Hosseini, B. W. Skelton and A. H. White, *Inorg. Chem.*, 2001, **40**, 672–686.

(14) A. Bilyk, J. W. Dunlop, A. K. Hall, J. M. Harrowfield, M. W. Hosseini, G. A. Koutsantonis, B. W. Skelton and A. H. White, *Eur. J. Inorg. Chem.*, 2010, **14**, 2089–2105.

(15) A. Bilyk, J. W. Dunlop, R. O. Fuller, A. K. Hall, J. M. Harrowfield, M. W. Hosseini, G. A. Koutsantonis, I. W. Murray, B. W. Skelton, R. L. Stamps and A. H. White, *Eur. J. Inorg. Chem.*, 2010, **14**, 2106–2126.

(16) G. Mislin, E. Graf, M. Hosseini, A. Hall, J. Harrowfield, B. Skelton, A. White, and others, *Chem. Commun.*, 1999, **4**, 373–374.

(17) Y. Bi, W. Liao, X. Wang, R. Deng and H. Zhang, *Eur. J. Inorg. Chem.*, 2009, **33**, 4989–4994.

(18) C. Zhang, Z. Wang, W.-D. Si, L. Wang, J.-M. Dou, Z.-Y. Gao, C.-H. Tung and D. Sun, *ACS Nano*, 2022, **16**, 9598–9607.

(19) G. M. Sheldrick, *Acta Crystallogr. Sect. C*, 2015, **71**, 3–8.

(20) O. V. Dolomanov, L. J. Bourhis, R. J. Gildea, J. A. K. Howard and H. Puschmann, *J. Appl. Crystallogr.*, 2009, **42**, 339–341.

(21) M. Liu, W. Liao, C. Hu, S. Du and H. Zhang, *Angew. Chem. Int. Ed.*, 2012, **51**, 1585–1588.

(22) K. Xiong, F. Jiang, Y. Gai, D. Yuan, L. Chen, M. Wu, K. Su and M. Hong, *Chem Sci*, 2012, **3**, 2321–2325.

(23) K. Su, F. Jiang, J. Qian, Y. Gai, M. Wu, S. M. Bawaked, M. Mokhtar, S. A. AL-Thabaiti and M. Hong, *Cryst. Growth Des.*, 2014, **14**, 3116–3123.

(24) K.-C. Xiong, F.-L. Jiang, Y.-L. Gai, D.-Q. Yuan, D. Han, J. Ma, S.-Q. Zhang and M.-C. Hong, *Chem. – Eur. J.*, 2012, **18**, 5536–5540.

(25) N. Frank, A. Dallmann, B. Braun-Cula, C. Herwig and C. Limberg, *Angew. Chem. Int. Ed.*, 2020, **59**, 6735–6739.

(26) R. McLellan, S. M. Taylor, R. D. McIntosh, E. K. Brechin and S. J. Dalgarno, *Dalton Trans*, 2013, **42**, 6697–6700.

(27) X. Hang, S. Du, S. Wang and W. Liao, *Inorg. Chem. Commun.*, 2014, **47**, 152–154.

(28) D. Geng, M. Zhang, X. Hang, W. Xie, Y. Qin, Q. Li, Y. Bi and Z. Zheng, *Dalton Trans*, 2018, **47**, 9008–9013.

(29) K. Li, H. Han, G. Zhang, X. Zhu and W. Liao, *J. Solid State Chem.*, 2022, **308**, 122908.

(30) C. Liu, W.-Y. Pei, J.-F. Li, J. Yang and J.-F. Ma, *Sens. Actuators B Chem.*, 2020, **308**, 127677.

(31) X. Zhu, S. Wang, H. Han and W. Liao, *RSC Adv*, 2018, **8**, 39208–39213.

(32) C. D. Gutsche, *Calixarenes: An Introduction*, Royal Society of Chemistry, Cambridge, 2008.

(33) T. Shiga, K. Maruyama, G. N. Newton, R. Inglis, E. K. Brechin and H. Oshio, *Inorg. Chem.*, 2014, **53**, 4272–4274.

(34) Y.-Q. Sun, Y.-Y. Xu, L. Wu, Y.-F. Zheng, D.-Z. Gao and G.-Y. Zhang, *Polyhedron*, 2015, **91**, 1–9.

(35) M. Murrie, *Chem. Soc. Rev.*, 2010, **39**, 1986–1995.

(36) G. A. Craig and M. Murrie, *Chem. Soc. Rev.*, 2015, **44**, 2135–2147.

Chapter 4

Exploring spin frustration in TBC[4]-supported clusters

4.1 Introduction

The first use of the term spin frustration can be traced back to Anderson, Toulouse and Kirkpatrick when discussing exchange interactions in spin glasses[1,2] and has subsequently been employed to describe the magnetic behaviour observed in specific 2-3D lattices, such as those of the Kagome and pyrochlore structures.[3–6] The advent of novel 0D structures containing paramagnetic 3*d* metal ions saw the definition of geometric spin frustration in molecular systems evolve from initial descriptions requiring a degenerate ground state,[7] which was overly prohibitive, to the presence of competing antiferromagnetic exchange interactions,[8] which was overly permissive. More modern interpretations invoke scenarios which, in essence, describe the opposite of bipartiteness[9] and/or systems where the magnetic behaviour cannot be represented by classical spins.[10] Regardless of ones preferred rubric, the effects of spin frustration on the energy spectrum and magnetic properties of molecular coordination compounds are fascinating and include enhanced ground state degeneracy, low-lying singlet states, non-collinear ground states, unusual magnetisation plateaus and jumps, and attractive magnetocaloric properties.[9] This makes them both academically interesting and potentially useful for applications in, for example, cryogenic refrigeration.[11]

From a synthetic perspective designing spin frustrated molecules is not trivial. One option is to construct odd-numbered wheels[12] such as $[Cr^{III}_8Ni^{II}]$[13] and $[Cr^{III}_9]$.[14] The former is best described as a magnetic Möbius strip that contains an even number of electrons and has a singly degenerate spin ground state, while the latter has either a S = 1/2 or S = 3/2 ground state depending on the exact structure type. A second option is to construct high symmetry polyhedra (*e.g.* Archimedean, Platonic solids / Keplerates) which primarily possess odd numbered faces, *i.e.* triangles, pentagons, heptagons, *etc*. While the latter are known in polyoxometalate chemistry, the $[Mo_{72}Fe_{30}]$ icosidodecahedron being a pertinent example,[15] they are less common in magnetic materials containing only 3*d* metals. Examples are also often restricted to relatively small molecules such as triangles, which are perhaps not as interesting or as potentially useful as larger species since they have a rather simple energy spectrum consisting of one band of energy levels.[16,17]

In attempts to construct large, high symmetry cages that may display spin frustration effects we turn to the use of *p-tert*-butylcalix[4]arene (H_4TBC[4], Chapter 1),[18] whose predisposition

for metal binding in its maximal μ_5-bridging mode presents a square-pyramidal [M_5] building block (Figure 4.1).[19]

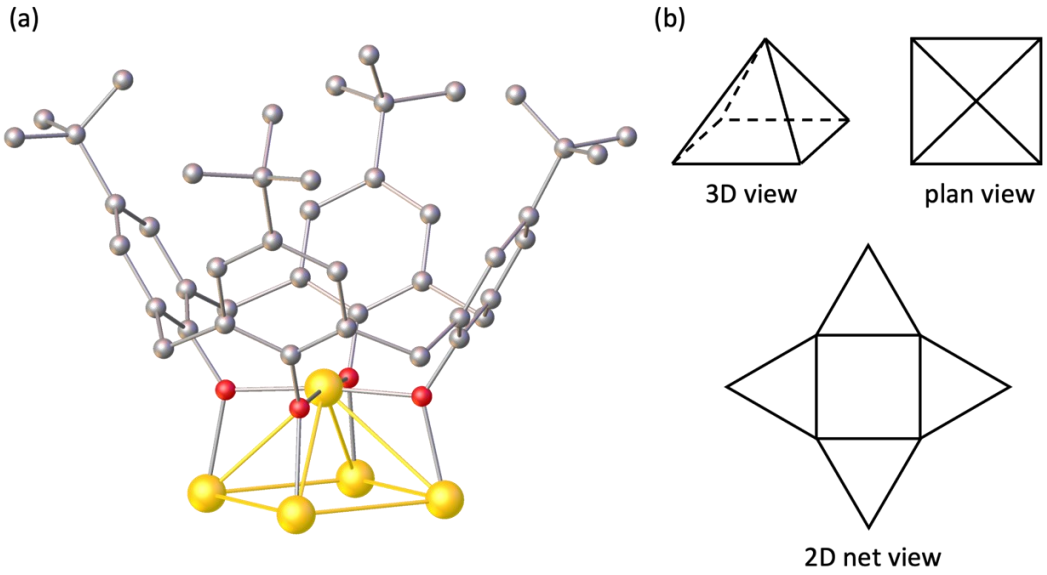

Figure 4.1 (a) The [M_5] square pyramidal building block constructed from TBC[4] in its maximal μ_5-coordination. H atoms are omitted for clarity. Colour code: M - yellow, C - grey, O - red. (b)-(d) Representations of (a) in 3D, plan and 2D net views, respectively.

We note the established binding rules of TBC[4], that in all known complexes to date the TBC[4] cavity will preferentially bind: (1) TM^{III} ions, (2) TM^{II} in the absence of TM^{III} ions, and (3) LnM^{III} ions in the absence of $TM^{II/III}$ ions. Efforts made to access high symmetry cages were initiated by examination of the previously published TBC[4]-supported [Cu^{II}_9] (**11**, Chapter 1), an enneanuclear tricapped trigonal prism. Reported in this chapter are the variations made to the reaction yielding **11**, switching halide salts to afford a Br capped [Cu^{II}_9] cluster (**32**) and introducing a lanthanide salt to give a [$Cu^{II}_7Gd^{III}_2$] cluster (**33**), the latter of which breaks the established empirical binding rules for the first time. Efforts to access the same topology using Mn salts produces a [$Mn^{III}_3Na_6$] cluster (**34**), and switching H_4TBC[4] for 2,2'-bis-*p*-*tert*-butylcalix[4]arene (BisTBC[4]/H_8L, Chapter 2) results in a [$Mn^{III}_4Mn^{II}_2Na_6$] cluster (**35**). The self-assembly of the TBC[4]-supported [M_5] building blocks shown in Figure 4.1 under high pressures and high temperatures should lead to the formation of stellated polyhedra supported by an internal core of oxides and hydroxides, and solvothermal techniques afford the stellated cuboctahedron [Fe^{III}_{18}] (**36**) and the highly symmetric [Fe^{III}_{28}] (**37**).

4.2 Experimental

Materials and Syntheses

All chemicals were procured from commercial suppliers and used as received (reagent grade). Elemental analyses (CHN) were performed on a Thermo Fisher Scientific Flash SMART instrument and (Cl) performed by Medac Ltd.

Synthesis of $[Cu^{II}_9(TBC[4])_3(\mu\text{-}OH)_3(Br)_2(dmso)_6][Cu^{I}Br_2]\cdot 7MeCN$ (32)

$H_4TBC[4]$ (112 mg, 0.173 mmol), $CuBr_2$ (309 mg, 1.384 mmol) and NH_4ClO_4 (117 mg, 1 mmol) were dissolved in dmso/EtOH (1:1 v/v, 24 mL) and stirred for 10 minutes. NEt_3 (0.3 mL, 2.152 mmol) was added and the resultant solution stirred for 2 hours. After filtration, MeCN was diffused slowly into the mother liquor affording black crystals of **32** in 27% yield after 7 days. Elemental analysis (%) calculated for **32** without any solvent molecules of crystallisation: C, 50.73; H, 5.76; N, 0.00. Found: C, 49.69; H, 5.90; N, 0.33.

Synthesis of $[Cu^{II}_7Gd^{III}_2(TBC[4])_3(\mu_3\text{-}OH)_4(dmso)_6(MeCN)_2(H_2O)]Cl_4\cdot 3MeCN$ (33)

$H_4TBC[4]$ (112 mg, 0.173 mmol), $CuCl_2\cdot 2H_2O$ (59 mg, 0.346 mmol) and $GdCl_3\cdot 6H_2O$ (97 mg, 0.260 mmol) were dissolved in dmso/MeOH (1:1 v/v, 24 mL) and stirred for 10 minutes. NEt_3 (0.3 mL, 2.152 mmol) was added and the resultant solution stirred for 2 hours. After filtration, MeCN was diffused slowly into the mother liquor affording black crystals of **33** in 16% yield after 7 days. Elemental analysis (%) calculated for **33** without any solvent molecules of crystallisation: C, 51.19; H, 5.92; N, 0.81. Found: C, 51.27; H, 5.79; N, 0.47.

Synthesis of $[Mn^{III}_3Na_6(TBC[4])_3(\mu_9\text{-}CO_3)(Cl)(dmso)_7]\cdot 5MeCN$ (34)

$H_4TBC[4]$ (200 mg, 0.308 mmol) and $MnCl_2\cdot 4H_2O$ (61 mg, 0.308 mmol) were dissolved in dmso/MeOH (1:1 v/v, 20 mL) and stirred for 10 minutes. NaOH (0.025 g, 0.616 mmol) was added and the resultant solution stirred for 3 hours. After filtration, MeCN was diffused slowly into the mother liquor affording black crystals of **34** in 15% yield after 7 days. Elemental analysis (%) calculated for **34** without any solvent molecules of crystallisation: C, 61.31; H, 6.93; N, 0.00. Found: C, 61.03; H, 6.81; N, 0.08.

Synthesis of $[Mn^{III}_4Mn^{II}_2Na_6(L)_2(\mu\text{-}OH)(\mu_8\text{-}CO_3)_{1.5}(Cl)_2(dmf)_8(MeOH)_{1.2}(H_2O)_{0.8}]\cdot 6MeCN$ (35)

H_8L (100 mg, 0.077 mmol), $MnCl_2\cdot 4H_2O$ (91 mg, 0.462 mmol) and NaOPh (54 mg, 0.462 mmol) were dissolved in dmf/MeOH (1:1 v/v, 20 mL) and stirred for 10 minutes. NEt_3 (0.4 mL, 2.87 mmol) was added and the resultant solution stirred for 2 hours. After filtration, MeCN was diffused slowly into the mother liquor affording black crystals of **35** in 12% yield after 7 days. Elemental analysis (%) calculated for **35** without any solvent molecules of crystallisation: C, 63.58; H, 6.93; N, 2.95. Found: C, 63.21; H, 6.84; N, 2.57.

Synthesis of $[Fe^{III}_{18}(TBC[4])_4(\mu_5\text{-}O)_6(\mu_3\text{-}O)_8(\mu\text{-}OH)_8(dmf)_4(H_2O)_2]Cl_2$ (36)

$H_4TBC[4]$ (200 mg, 0.308 mmol) and $FeCl_2\cdot 4H_2O$ (61 mg, 0.308 mmol) were dissolved in dmf/EtOH (1:1 v/v, 20 mL) and stirred for 10 minutes. NEt_3 (0.1 mL, 0.717 mmol) was added and the resulting solution stirred for 2 hours. After filtration, 8 mL aliquots of the solution were placed in Teflon-lined autoclaves at 120 °C for 12 hours, affording black crystals of **36** in 6% yield upon cooling. Elemental analysis (%) calculated for **36**: C, 51.98; H, 5.75; N, 1.29. Found: C, 51.70; H, 5.68; N, 1.47.

Synthesis of $[Fe^{III}_{28}(TBC[4])_4(\mu_5\text{-}O)_4(\mu_4\text{-}O)_6(\mu_3\text{-}O)_{16}(\mu\text{-}OEt)_{10}(\mu\text{-}O_2CNMe_2)_{1.5}(\mu\text{-}O_2CH)_{0.5}(Cl)_4(MeCN)_4]$ (37)

$H_4TBC[4]$ (200 mg, 0.308 mmol), $FeCl_2\cdot 4H_2O$ (30 mg, 0.154 mmol) and $(NH_4)_2[FeCl_4]$ (36 mg, 0.154 mmol) were dissolved in dmf/EtOH (1:1 v/v, 20 mL) and stirred for 10 minutes. NEt_3 (0.1 mL, 0.717 mmol) was added and the resulting solution stirred for 2 hours. After filtration, 8 mL aliquots of the solution were placed in Teflon-lined autoclaves at 120 °C for 24 hours. Upon cooling and filtration, MeCN was diffused slowly into the mother liquor affording black crystals of **37** in 5% yield after 21 days. Elemental analysis (%) calculated for **37**: C, 45.93; H, 5.18; N, 1.53. Found: C, 45.49; H, 5.04; N, 1.39.

X-ray crystallography

Single crystal X-ray diffraction data for **32** were collected on a Rigaku Oxford Diffraction SuperNova diffractometer equipped with an Oxford Cryosystems Cryostream and operating with CuK_a radiation (1.54184 Å). Diffraction data for **33**-**35** were collected on a Bruker Kappa APEXII DUO CCD diffractometer operating with CuK_a radiation (1.54178 Å, **34**, **35**) / synchrotron radiation (1.0402 Å, **33**). Diffraction data for **36** were collected on a Rigaku 007HF equipped with Varimax confocal mirrors, a UG2 goniometer and HyPix 6000HE detector and

operating with CuK_a radiation (1.54184 Å). Diffraction data for **37** were collected on a Rigaku FRE+ equipped with VHF Varimax confocal mirrors, a UG2 goniometer and HyPix 6000 detector and operating with MoK_a radiation (0.71073 Å). Crystal data for **32**-**37** are given in Tables S4.1-S4.3. Structures were solved using ShelXT/ShelXL and refined with version 2018/3 of ShelXL interfaces through Olex2.[20,21] All non-hydrogen atoms were refined anisotropically. Most hydrogen atom positions were calculated geometrically and refined using the riding model, but some hydrogen atoms were refined freely.

Powder X-ray diffraction data for **32-36** were collected on polycrystalline powders using a Bruker D8 ADVANCE with Cu radiation at 40 kV, 40mA and a Johansson monochromator, 2mm divergence slit and 2.5 degree Soller slits on the incident beam side, LynxEye detector and Bruker DIFFRAC software. Data were measured from 2θ = 2 - 30°; step size, 0.0101°. Freshly prepared crystalline powders were loaded into borosilicate capillaries with a 0.7 mm inside diameter and measured while spinning (Figure S4.1).

Magnetic data

Magnetic susceptibility and magnetisation data were collected on powdered microcrystalline samples using a Quantum Design PPMS DynaCool magnetometer equipped with a 9 T dc magnet (**32**, **34**-**37)** and a Quantum Design MPMS XL SQUID magnetometer equipped with a 7 T dc magnet (**33**). Susceptibility data were collected in the T = 300 – 2 K range under an applied magnetic field, B = 0.1 T. Magnetisation data were collected in the range T = 2 - 10 K and B = 0 – 9 T (**32**, **34**-**37**) / B = 0 – 7 T (**33**). Data were modelled using PHI v3 software (**32**-**35**) and bespoke collaborator software (**36**, JS) – see Format of Thesis.

Low-temperature, high field magnetisation data were measured for **36** using a conventional inductive probe in pulsed magnetic fields, where the temperature reached as low as 0.4 K. The maximum field reached was 32.5 T. Polycrystalline samples with a typical mass of 10 mg were mounted in a capillary tube made of polyimide. The sample, which was not fixed within the sample tube, was aligned along the magnetic field direction. Magnetisation curves were found to be identical after the magnetic field was applied several times due to the saturation of the orientation effect.

4.3 Results and Discussion

Structure descriptions

Reaction of H_4TBC[4] with $CuBr_2$ and NH_4ClO_4 in a basic dmso/EtOH mixture affords single crystals of $[Cu^{II}_9(TBC[4])_3(\mu\text{-}OH)_3(Br)_2(dmso)_6][Cu^{I}Br_2]\cdot 7MeCN$ (**32**, Figure 4.2) following diffusion of MeCN into the mother liquor. The crystals were found to be in an orthorhombic cell and the structure solution was carried out in space group *Pnma*. The asymmetric unit (ASU) comprises half of the formula. Pertinent bond parameters for **32** are given in Table S4.4. The metallic skeleton of **32** describes a tricapped trigonal prism in which three $[Cu(TBC[4])]^{2-}$ metalloligands (Cu2, Cu4 and symmetry equivalent (s.e.)) cap the square faces of a $[Cu^{II}_6(\mu\text{-}OH)_3(dmso)_6]^{9+}$ trigonal prism (Cu1, Cu3 (and s.e.), Cu5, Cu6) (Figure 4.3). The 'upper' and 'lower' triangular faces are each capped by a Br ion (Br1/Br2) with long contacts in the range ~2.84-2.99 Å. The two triangular faces are linked *via* three μ-OH ligands along each vertical edge of the prism.

The ions at the vertices of the prism (Cu1, Cu3 (and s.e.), Cu5, Cu6) are all 5-coordinate and display square pyramidal geometries when considering the Br contacts, with the coordination spheres completed by two $\mu\text{-}O_{TBC[4]}$ atoms, a μ-OH bridge and a terminally

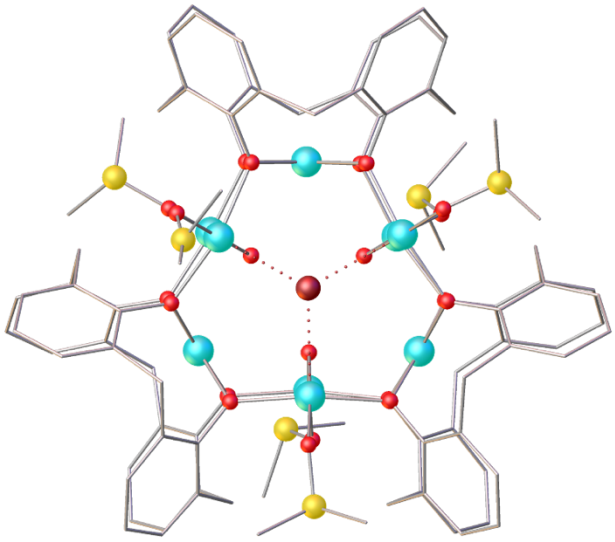

Figure 4.2 Single crystal X-ray structure of **32.** Colour code: Cu^{II} - turquoise, Br – dark red, S - yellow, C - grey, O - red. H atoms, ^{t}Bu groups of TBC[4] and co-crystallised solvent molecules omitted for clarity.

bonded dmso molecule. The Cu^{II} ion caps (Cu2, Cu4 and s.e.) are all 4-coordinate and display square planar geometries, being bonded to each of the four μ-$O_{TBC[4]}$ atoms in the TBC[4] pocket. A MeCN molecule of crystallisation resides in each TBC[4] cavity, with long contact Cu···C(CN) distances in the range ~3.91-4.04 Å. Charge-balance is afforded by a linear $[Cu^{I}Br_2]$ anion that resides within the lattice along with four further MeCN molecules per formula unit. Observation of the extended structure of **32** down the *c*-axis displays the familiar bilayer packing arrangement seen for H_4TBC[4],[22,23] where each TBC[4] cavity lies opposite the ^{t}Bu groups from a neighbouring bi-layer and are occupied by MeCN molecules with $[Cu^{I}Br_2]$ anions occupying the interstitial spaces (Figure S4.2). Closest cluster-cluster interactions are between neighbouring ^{t}Bu groups of TBC[4] ligands (C···C $\geq$ 3.8 Å) and the closest M···M distance is between the Cu^{I} in the $[Cu^{I}Br_2]$ anion and $Cu^{II}1$ in the main cluster (~6.60 Å). The closest M···M distance between the cationic clusters is ~8.65 Å between Cu1···Cu3.

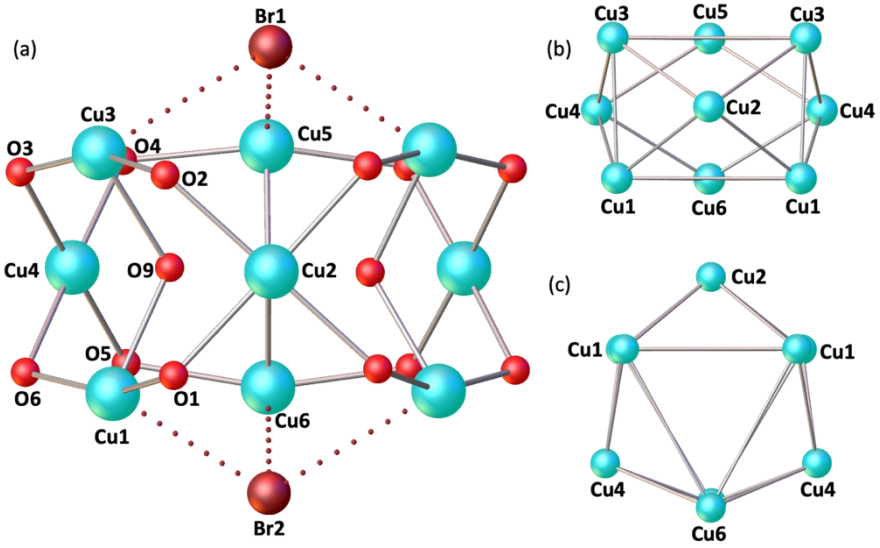

Figure 4.3 Cluster core (a) and metallic skeleton (b)-(c) of **32**. Colour code: Cu^{II} - turquoise, Br – dark red, O - red.

Complex **32** is structurally analogous to **11** (*vide supra*, Chapter 1) which were made in a similar reaction but replacing the $CuBr_2$ with $CuCl_2{\cdot}2H_2O$ and $Cu(NO_3)_2{\cdot}3H_2O$, and crystallised in *C2/c* and *P*-1 space groups, respectively.[24] The former replaces the Br triangular face-capping anions with Cl^- and the latter with NO_3^- anions, whilst the cationic clusters vary only in the solvent molecules of crystallisation.

Reaction of H_4TBC[4] with $CuCl_2 \cdot 2H_2O$ and $GdCl_3 \cdot 6H_2O$ in a basic dmso/MeOH solution affords single crystals of $[Cu^{II}_7Gd^{III}_2(TBC[4])_3(\mu_3\text{-}OH)_4(dmso)_6(MeCN)_2(H_2O)]Cl_4 \cdot 3MeCN$ (**33**, Figure 4.4) following diffusion of MeCN into the mother liquor. As with **32**, the crystals were found to be in an orthorhombic cell and the structure solution was carried out in space group *Pnma*. Pertinent bond parameters for **33** are given in Table S4.5.

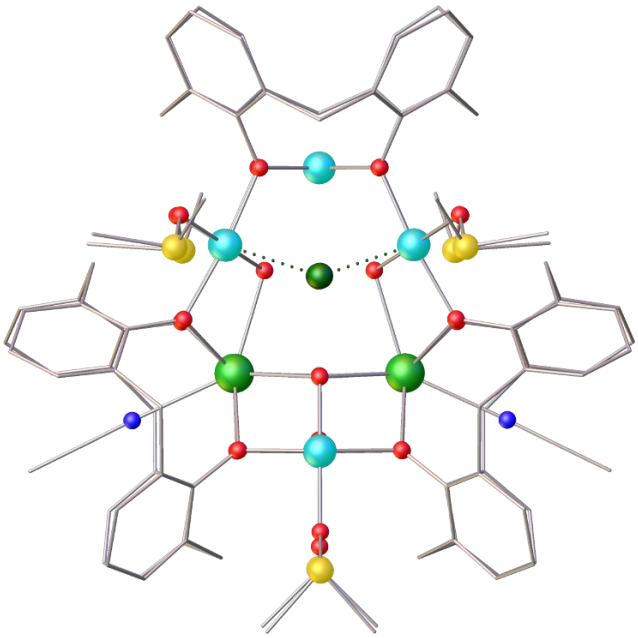

Figure 4.4 Single crystal X-ray structure of **33.** Colour code: Cu^{II} - turquoise, Gd^{III} - bright green, Cl - dark green, S - yellow, N - dark blue, C - grey, O - red. H atoms, ^{t}Bu groups of TBC[4] and co-crystallised solvent molecules omitted for clarity.

The metallic skeleton again describes a tricapped trigonal prism, but in this case two of the three capping moieties are $[Gd^{III}(TBC[4])]^{1-}$ metalloligands. The $[Cu^{II}_6]$ trigonal prism is maintained but is now more 'isosceles' in nature (Figure 4.5). The 'upper' half (as drawn in Figures 4.4 - 4.5) is similar to that in **32**, with two OH ions (O9 and s.e.) bridging between two Cu ions (Cu3, Cu5 and s.e.). However, these OH ions now further bridge to a Gd^{III} ion (Gd1 and s.e.), converting from a μ-bridging mode in **32** (Cu-O, ~1.92-1.95 Å) to a μ_3-bridging mode in **33** (Cu-O, ~1.94-1.96 Å; Gd-O, ~2.44 Å). The 'bottom' half now contains two μ_3-OH ions (O7, O8) that bridge between the two Gd^{III} ions (Gd1 and s.e.) and Cu1 and Cu2 respectively (Cu-O, ~1.89-1.90 Å; Gd-O, ~2.36-2.40 Å). Thus, the prism unit is now $[Cu^{II}_6(\mu_3\text{-}OH)_4(dmso)_6(H_2O)]^{8+}$ rather than the $[Cu^{II}_6(\mu\text{-}OH)_3(dmso)_6]^{9+}$ seen in **32**. As with **32**, halide ions (Cl1, Cl2) cap the 'upper' and 'lower' triangular faces of the prism with long contacts in

the range ~2.86-2.88 Å. Contacts between the Cl ions and Cu1/Cu2 in the lower half of the prism are no longer viable due to their increased length (~4.16-4.18 Å). The Cu^{II} ions in the prism are of three types. Cu3/Cu5 (and s.e.) are five-coordinate and square pyramidal when considering the Cl long contacts, with the remainder of their coordination spheres completed by the aforementioned μ_3-OH, two μ-$O_{TBC[4]}$ atoms and a ligated dmso molecule. Cu2 is also five-coordinate and displays a very distorted square pyramidal geometry, made up of a μ_3-OH ion, two μ-$O_{TBC[4]}$ atoms, a ligated dmso molecule and a ligated H_2O molecule. Cu1 is 4-coordinate and distorted square planar; it displays a similar coordination sphere to Cu2 but without the additionally ligated H_2O molecule. The sole Cu^{II} ion (Cu4) located in the tetraphenolic cavity of TBC[4] is 4-coordinate and square planar. The Gd1 ions are 8-coordinate and in square antiprismatic geometry, being bonded to four μ-$O_{TBC[4]}$ atoms, three μ_3-OH ions and a MeCN molecule located in the TBC[4] pocket. Two further Cl^- anions per formula reside in the lattice, providing charge-balance. These form H-bonds to the same terminal H_2O molecule, whilst the former Cl ions form H-bonds with the μ_3-OH bridges (Figure S4.3). Examination of the extended structure of **33** down the *a*-axis reveals a columnar arrangement of clusters organised to mimic the bi-layer arrangement seen in TBC[4] solvates (Figure S4.4).[22,23] In contrast to **32**, each cluster is oriented opposite to its neighbour down the column. The data was modelled by removing the equivalent of 3 MeCN molecules which

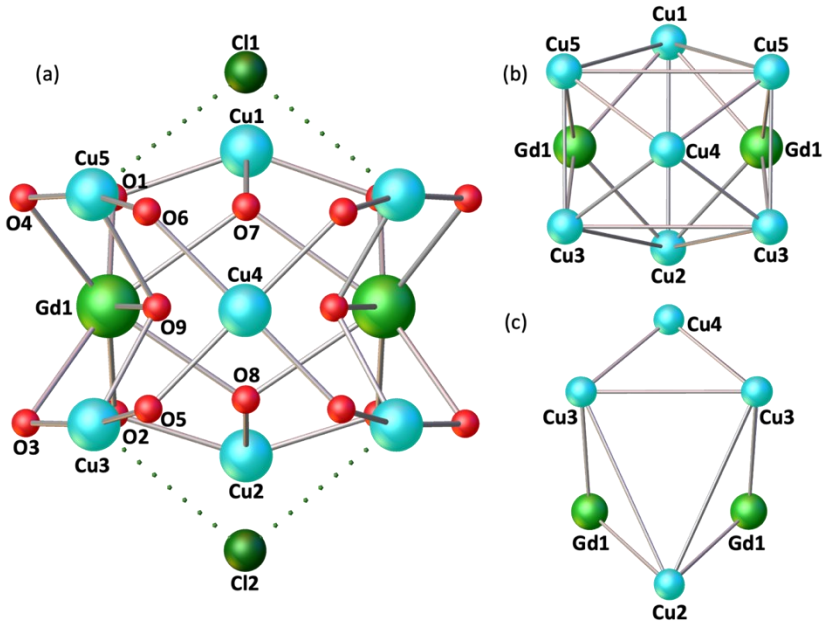

Figure 4.5 Cluster core (a) and metallic skeleton (b)-(c) of **33**. Colour code: Cu^{II} - turquoise, Gd^{III} - bright green, Cl - dark green, O - red.

also reside throughout the lattice. Clusters appear quite isolated, with closest intermolecular interactions between the ^{t}Bu groups of neighbouring TBC[4] ligands (~4.06 Å) and between dmso ligands and ^{t}Bu groups (~4.09 Å). The closest M···M distance is ~8.65 Å between Cu2···Cu5, exactly equal to the closest M···M distance between the cationic clusters in **32**.

Having seen the proclivity of the TBC[4] ligand in supporting Cu-based tricapped trigonal prisms, accessing analogous Mn-based topologies was attempted. Using identical reactions to **11**/**32** yielded the cluster $[Mn^{III}_2Mn^{II}_2]$ (**2**, Chapter 1), as did many permutations of these experimental procedures. Only upon the introduction of Na into the reaction space were we able to yield a Mn-based tricapped trigonal prism. Reaction of H_4TBC[4] with $MnCl_2{\cdot}4H_2O$ in a basic (NaOH) dmso/MeOH mixture affords single crystals of formula $[Mn^{III}_3Na_6(TBC[4])_3(\mu_9\text{-}CO_3)(Cl)(dmso)_7]{\cdot}5MeCN$ (**34**, Figure 4.6) following diffusion of MeCN into the mother liquor. The crystals were found to be in a monoclinic cell and structure solution was carried out in the space group *C*2/c. The ASU comprises half of the formula. Pertinent bond parameters and BVS calculations for **34** are provided in Table S4.6.

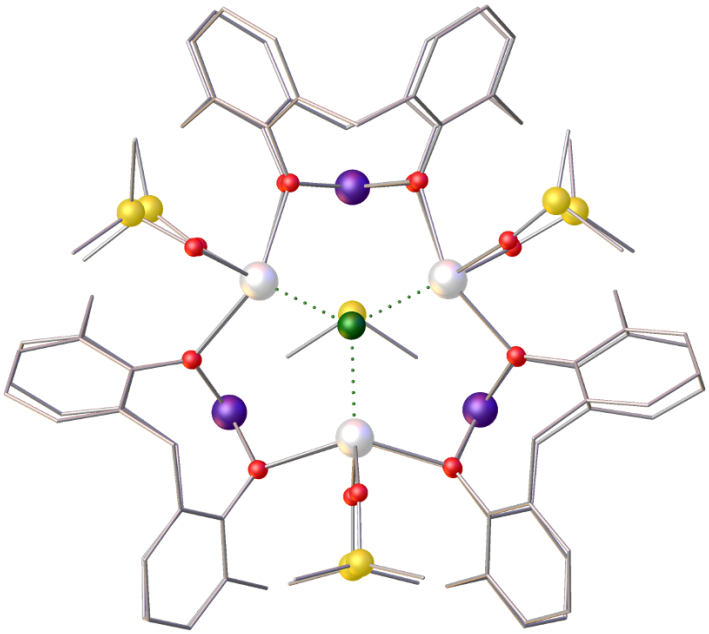

Figure 4.6 Single crystal X-ray structure of **34.** Colour code: Mn^{III} - dark purple, Na - white, Cl - dark green, S - yellow, C - grey, O - red. H atoms, ^{t}Bu groups of TBC[4], the disordered $[CO_3]^{2-}$ ligand and co-crystallised solvent molecules omitted for clarity.

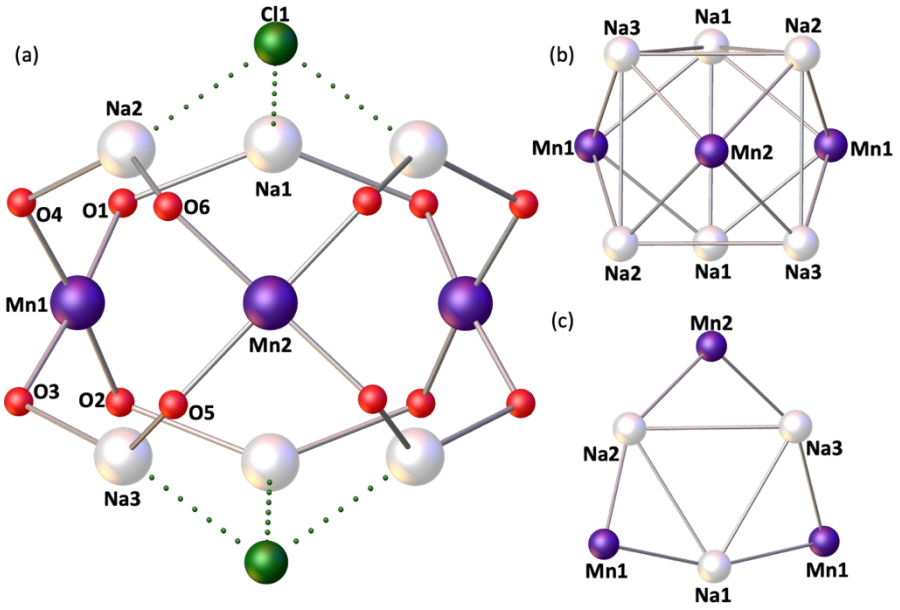

Figure 4.7 Cluster core (a) and metallic skeleton (b)-(c) of **34**. Colour code: Mn^{III} - dark purple, Na - white, Cl - dark green, O - red.

The metallic skeleton describes a $[Mn^{III}_3Na_6]$ tricapped trigonal prism with the Na ions sitting on the vertices and the Mn ions capping the square faces (Figure 4.7). A disordered $[CO_3]^{2-}$ ion sits in the centre of the cage, bonding to all nine metal ions (Mn-O, ~2.14-2.21 Å; Na-O, ~2.42-2.49 Å). The Mn ions are all square pyramidal and sit in the phenolic TBC[4] pockets, having $\{MnO_5\}$ coordination geometries with a sixth, longer contact to a MeCN molecule of crystallisation that sits in the TBC[4] cavity (~4.1 Å). The Mn-O(carbonate) bond (~2.14-2.21 Å) is significantly longer than the four Mn-O(phenoxide) bonds (~1.92-1.93 Å). The TBC[4] ions are all in their maximal μ_5-bridging mode, each O-arm bonded to a Mn ion and further bridging to a Na ion, thus directing the formation of square pyramidal $[MnNa_3(TBC[4])]$ building blocks. The triangular $[Na_3]$ faces of the prism are capped by a disordered mixture of one Cl ion (Na···Cl, ~2.6-2.7 Å) and one dmso molecule (Na···O, ~2.4-2.6 Å). The latter is asymmetrically situated with two Na-O distance of ~2.58 Å and two Na-O distances in the range ~2.43-2.45 Å. The remaining site on each 5-coordinate, distorted square pyramidal Na ion is occupied by a dmso molecule. The Na ion in **34** originates from the NaOH base employed to deprotonate the H_4TBC[4] ligands, and the $[CO_3]^{2-}$ ion from the fixation of atmospheric CO_2 and/or the oxidation of MeOH.

Examination of the extended structure of **34** reveals columnar packing down the *c*-axis in a manner analogous to **33** (Figure S4.5). Closest contacts/intermolecular interactions exist between the dmso ligands of neighbouring clusters ((S)C···C(S), ~3.82 Å), and the dmso ligands and the MeCN molecules of crystallisation ((S)C···N(C)), ~ 3.68 Å). The closest M···M distance in **34** is between the Na1···Na1 ions (~8.11 Å), slightly shorter than the closest M···M distances in **32**/**33**.

Comparing complex **34** with complex **32**, it is noted that the [Cu_9] cage does not contain an encapsulated $[CO_3]^{2-}$ and neighbouring vertex Cu ions are connected to each other with a μ-OH ion. Alongside the larger anionic radius of Na^{I}, the result is that the dimensions of the prisms are rather different, with [Mn_3Na_6] being 'taller and thinner' than the 'shorter and fatter' [Cu_9] (Figure 4.8). Figure 4.8 also gives the comparative dimensions of the tricapped trigonal prism in **33,** signifying the robust nature of the topology when dimensionally modified to accommodate various metal ions.

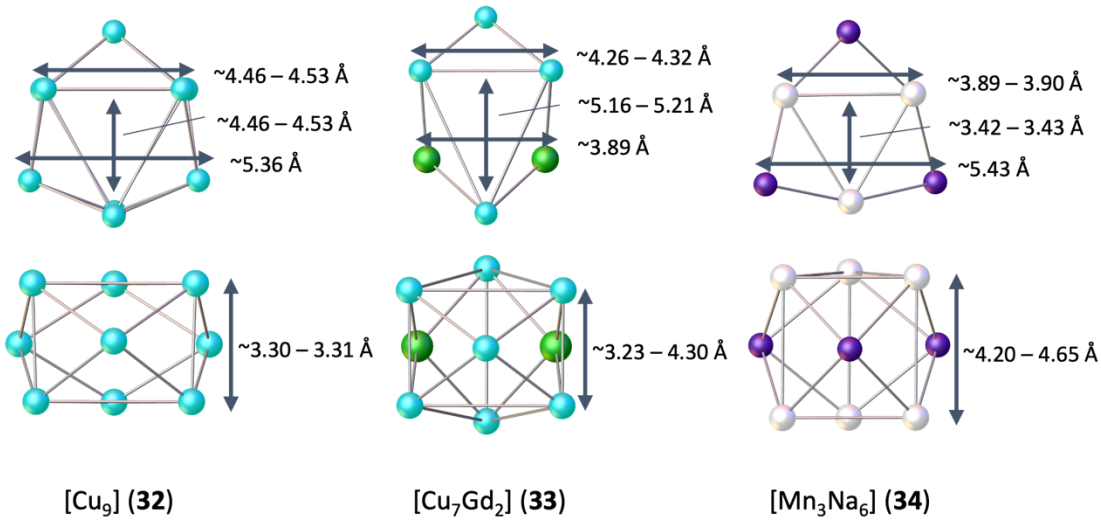

Figure 4.8 Comparison of the metallic skeletons in **32** (left), **33** (middle) and **34** (right). Colour code: Cu^{II} - turquoise, Gd^{III} - bright green, Mn^{III} - dark purple, Na - white.

Further efforts to investigate the Mn/calix[*n*]arene relationship included reactions with 2,2'-bis-*p*-^{t}Bu-calix[4]arene (BisTBC[4]/H_8L, Chapter 2). Reaction of $MnCl_2{\cdot}4H_2O$ with BisTBC[4] and NaOPh in a basic dmf/MeOH mixture affords single crystals of formula $[Mn^{III}_4Mn^{II}_2Na_6(L)_2(\mu\text{-}OH)(\mu_8\text{-}CO_3)_{1.5}(Cl)_2(dmf)_8(MeOH)_{1.2}(H_2O)_{0.8}]{\cdot}6MeCN$ (**35**, Figure 4.9) following diffusion of MeCN into the mother liquor. The crystals were found to be in a triclinic

cell and structure solution was carried out in the space group *P*-1. The ASU comprises half of the formula. Pertinent bond parameters and BVS calculations for **35** are given in Table S4.7. We include this cluster here to allow a comparison of Mn/Na coordination with both TBC[4] (**34**) and BisTBC[4] (**35**) ligation.

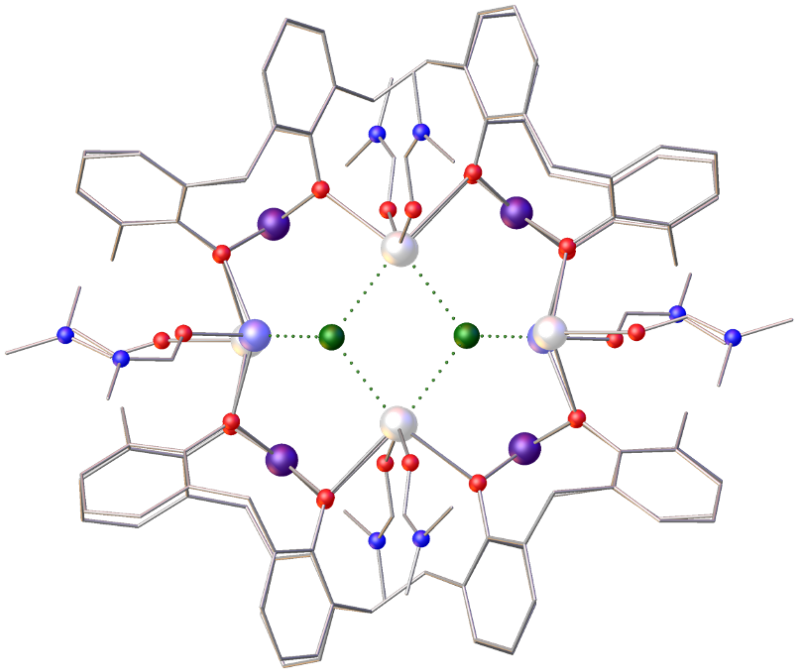

Figure 4.9 Single crystal X-ray structure of **35.** Colour code: Mn^{III} - dark purple, Mn^{II} - light purple, Na - white, Cl - dark green, N - dark blue, C - grey, O - red. H atoms, ^{t}Bu groups of TBC[4], the disordered $[CO_3]^{2-}$, OH^-, MeOH and H_2O ligands, and co-crystallised solvent molecules omitted for clarity.

The metallic skeleton of **35** describes a $[Mn^{III}_4Mn^{II}_2Na_6]$ tetracapped square prism with the Mn^{II}/Na^{I} ions sitting on the vertices and the Mn^{III} ions capping the square faces (Figure 4.10). A disordered combination of μ_8-CO_3 and μ-OH ions occupy the inside of the cage, positioned to bridge between four vertex metal ions (Na1-3, Mn3) and two capping metal ions (Mn1-2). As with **34**, the $[CO_3]^{2-}$ ions come from the fixation of atmospheric CO_2 and/or the oxidation of MeOH. Note that deliberate addition of carbonate in the form of Na_2CO_3 or $NaHCO_3$ worked to produce **34** and **35** in both cases, increasing the yield approximately two-fold for **34** and four-fold for **35**. The four face-capping Mn^{III} ions are housed in the polyphenolic pockets of the two fully deprotonated BisTBC[4] ligands whose O-atoms further bridge to the

Mn^{II}/Na^{I} ions in the square prism. The L^{8-} ligands adopt the maximal μ_8-bridging mode and thus wrap around the four square faces of the prism, completely encapsulating the $[Mn^{III}_4Mn^{II}Na_6(CO_3)_{1.5}(OH)]$ moiety. The 'upper' and 'lower' square faces of the prism (as drawn in Figures 4.9 - 4.10) are each asymmetrically capped by a Cl anion (Mn···Cl, ~2.38 Å; Na···Cl, ~2.94-3.03 Å). The Mn^{III} ions in the calix[4]arene pockets have square pyramidal $\{MnO_5\}$ coordination spheres, with the bonds to the four phenolic O-atoms (~1.91-2.00 Å) significantly shorter than that to the carbonate/hydroxide O-atom (2.07-2.32 Å), with a sixth, longer contact to a MeCN molecule of crystallisation that sits in the TBC[4] cavity (~4 Å). The coordination spheres of the distorted square pyramidal Mn^{II} ions, $\{MnO_5\}$, and distorted 'pentagonal bipyramidal' Na ions are completed by dmf, H_2O and MeOH molecules.

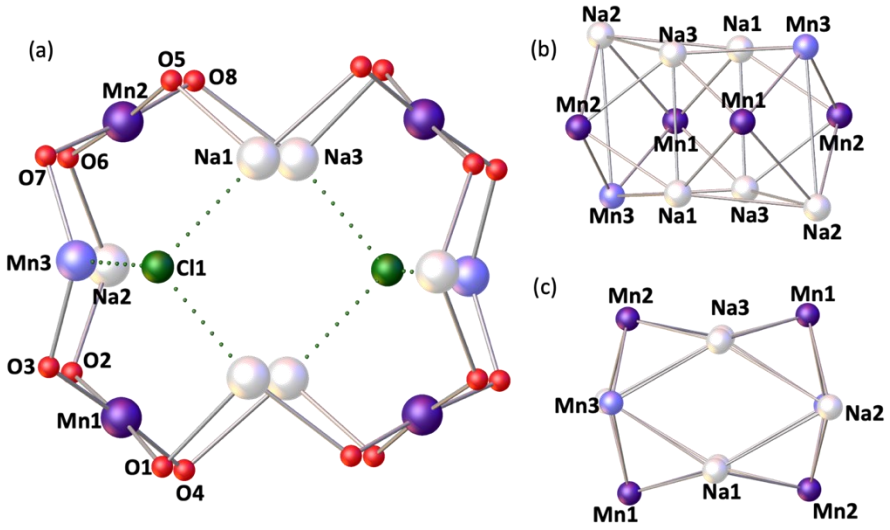

Figure 4.10 Cluster core (a) and metallic skeleton (b)-(c) of **35.** Colour code: Mn^{III} - dark purple, Mn^{II} - light purple, Na - white, Cl - dark green, O - red.

Examination of the extended structure of **35** reveals columnar packing as viewed down the *a*-axis, with two MeCN per formula unit occupying the spaces between clusters (Figure S4.6). Closest intermolecular contacts are between the ^{t}Bu groups of neighbouring BisTBC[4] ligands (C···C, ~3.86 Å), between ligated dmf molecules of neighbouring clusters ((C)N···N(C), ~3.72 Å), and between MeCN molecules within the BisTBC[4] cavity and the MeCN molecules of crystallisation ((NC)C···NC(C), ~3.48 Å). The clusters are isolated from nearest neighbours with closest M···M distances surpassing 12 Å.

The structure of **35** is reminiscent of the BisTBC[4]-supported [Cu^{II}_{13}] cluster (**24**, Chapter 2), whose metallic skeleton also describes a (centred) tetracapped square prism.[25] Interestingly, the latter contains an encapsulated and disordered Cu^{II} ion at its centre. Like the [Cu_9] cages, neighbouring vertices in [Cu_{13}] are linked to each other through μ-OH bridges, making [Mn_6Na_6] (**35**) 'taller and thinner' than the 'shorter and fatter' [Cu_{13}] (Figure 4.11).

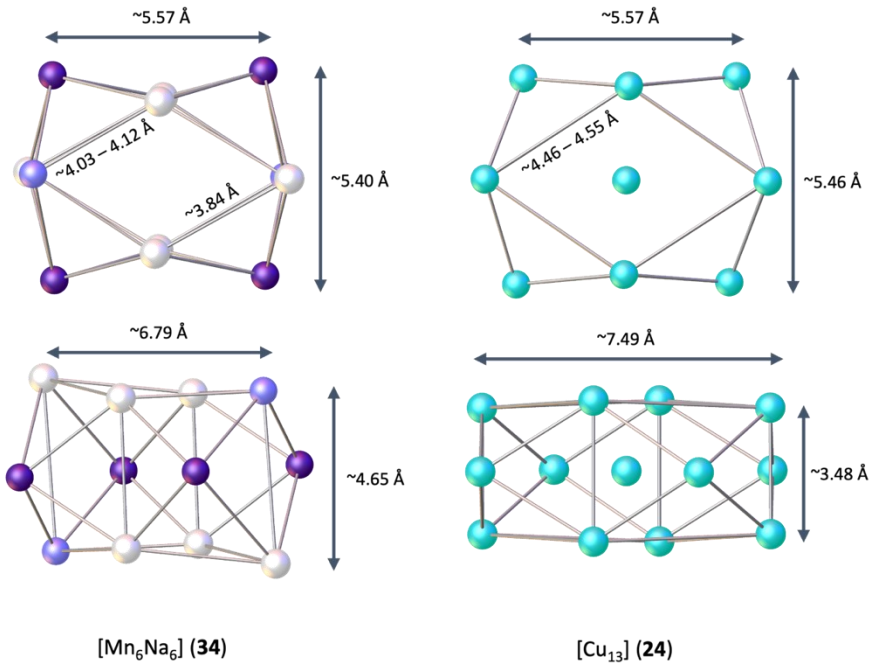

Figure 4.11 Comparison of the metallic skeletons in **35** (left) and **24** (right). Colour code: Mn^{III} - dark purple, Mn^{II} - light purple, Cu^{II} - turquoise.

The differences in the reactions that produced **34** and **35** are twofold. (A) The addition of NaOH (**34**) / NaOPh (**35**); clearly both are the source of Na ions and base to deprotonate the calix[*n*]arene. (B) Changing H_4TBC[4] in **34** to H_8L in **35**; full deprotonation in both cases allows expansion of an organic ligand framework containing three Mn^{III}-TBC[4] metalloligands encapsulating a trigonal prism, to four Mn^{III}-TBC[4] metalloligands encapsulating a square prism.

Solvothermal techniques were then employed in an effort to access larger nuclearity, high symmetry clusters with TBC[4], with a view to building magnetically frustrated complexes. The solvothermal reaction between H_4TBC[4] and $FeCl_2{\cdot}4H_2O$ in a basic dmf/EtOH solution affords single crystals of $[Fe^{III}_{18}(TBC[4])_4(\mu_5\text{-}O)_6(\mu_3\text{-}O)_8(\mu\text{-}OH)_8(dmf)_4(H_2O)_2]Cl_2$ (**36**, Figure 4.12) upon cooling of the mother liquor. The crystals were found in a cubic cell and structure solution was performed in the *Fm*-3*c* space group. The ASU contains one eighth of the formula and pertinent bond parameters and BVS calculations for **36** are provided in Table S4.8.

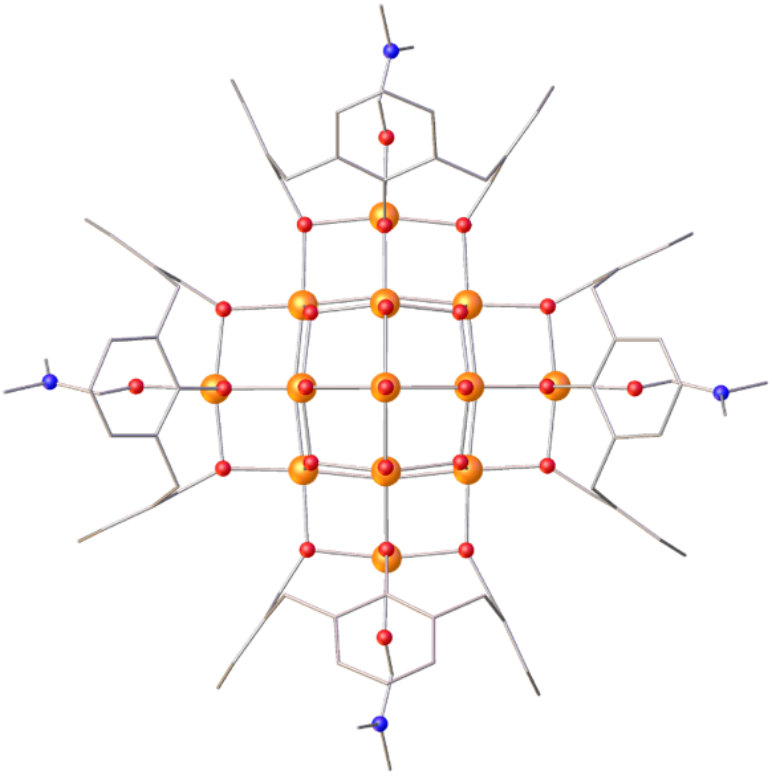

Figure 4.12 Single crystal X-ray structure of **36.** Colour code: Fe^{III} - orange, N - dark blue, C - grey, O - red. H atoms, ^{t}Bu groups of TBC[4] and co-crystallised solvent molecules omitted for clarity.

The metallic skeleton of **36** describes a stellated cuboctahedron, *i.e.* a cuboctahedron (Fe2-3 and s.e.) in which each of the square faces is capped (Fe1, Fe4 and s.e.), the caps themselves forming an octahedron (Figure 4.13). The stellated cuboctahedron is a class of Archimedean solid. All Fe ions are six-coordinate and display octahedral geometries. The six μ_5-O ions (O1O, O2O and s.e.) connect the four Fe ions in the square faces of the cuboctahedron (Fe2-3 and

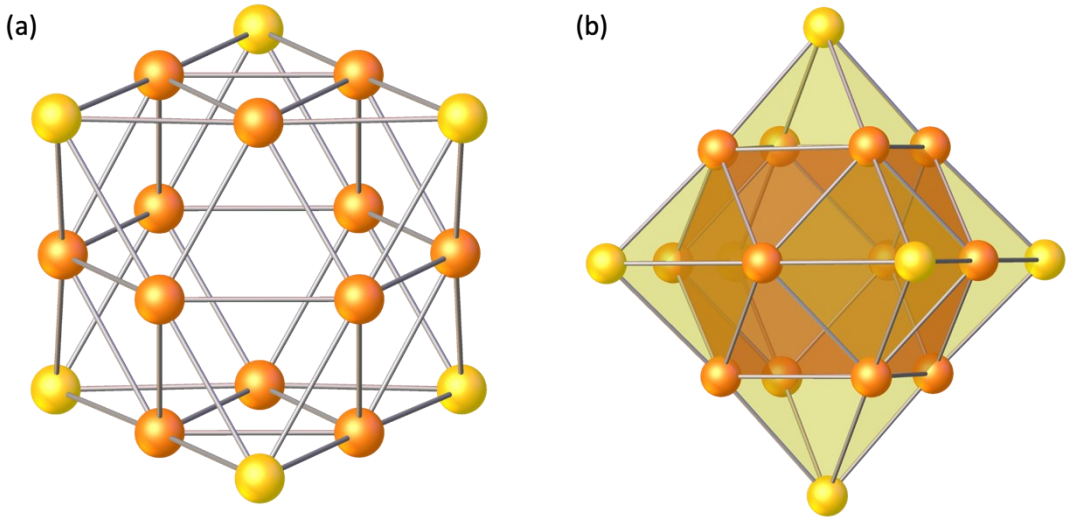

Figure 4.13 Metallic skeleton of **36** shown from different perspectives (a)-(b). Colour code: orange - Fe^{III} ions in the cuboctahedron, yellow - Fe^{III} ions capping the squares faces to form an octahedron.

s.e.) and further bridge to an Fe ion in the octahedron (Fe1) (Figure 4.14). The eight μ_3-O ions (O3O and s.e.) bond between the three Fe ions (Fe2, Fe3 and s.e.) in the triangular faces of the cuboctahedron. The eight μ-O ions (O1H and s.e.) bridge between an Fe ion in the octahedron (Fe4 and s.e.) and an Fe ion in the cuboctahedron (Fe3 and s.e.). The sixth coordination site on Fe4 (and s.e.) is occupied by a H_2O molecule. The four, fully deprotonated μ_5-TBC[4] ligands (O1-3 and s.e.) chelate to Fe1 (and s.e.) and further bridge to the square faces of the cuboctahedron (Fe2-3 and s.e.). The sixth coordination site on Fe1 (and s.e.) is occupied by a dmf molecule. *Cis* and *trans* Fe-O-Fe bond angles fall in the range ~89.18-104.70° and ~166.3-170.7°, respectively.

Examination of the extended structure of **36** reveals that six symmetry equivalent clusters pack such that they are at the vertices of an octahedron (Figure S4.7) forming a capsule-like arrangement. This provides a closed shell environment and expansion around a triangular face of this octahedron reveals six s.e. clusters arranged in a hexagon. Subsequent expansion around the latter affords a s.e. octahedron and doing so generates a cuboctahedral assembly (Figures S4.8). Each cuboctahedron presents a second closed shell environment and together, these environments constitute ~31% (48,027 $Å^3$) of the unit cell volume (155,525 $Å^3$) if one employs a 1.5 Å probe radius in contact surface calculations. Closest intermolecular Fe···Fe

distance is ~12.6 Å, the large TBC[4] ligands provide an encapsulating organic shell around the Fe-oxide core, inducing inherent structural/magnetic dilution in the solid state.

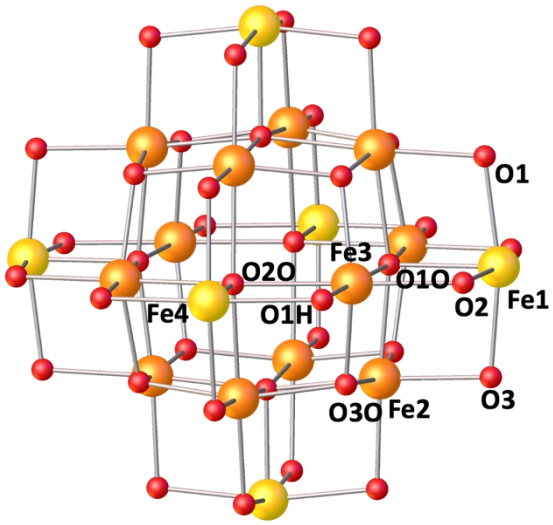

Figure 4.14 Cluster core of **36.** Colour code: orange – Fe^{III} ions in the cuboctahedron, yellow – Fe^{III} ions capping the squares faces to form an octahedron, O – red.

Perhaps surprisingly, compound **36** is the first structurally characterised homometallic cluster of Fe^{III} built using H_4TBC[4], the only previous examples being heterometallic [Fe_2Ln_2] cages (**14**).[26] The metal-oxygen core of **36** is similar to the "Super Lindqvist" complex [$HFe^{III}_{19}O_{14}(OEt)_3$] which has an additional Fe^{III} ion at its centre.[27] There are just two other stellated cuboctahedra reported: the first is a supramolecular [$Pd_{18}L_{24}$] cage constructed with a polypyridine ligand,[28] and the second a [Mn^{III}_{18}] 'superoctahedron' built with an aminoalcohol.[29]

The solvothermal reaction of H_4TBC[4] with $FeCl_2{\cdot}4H_2O$ and $(NH_4)_2[FeCl_4]$ in a basic dmf/EtOH solution affords single crystals of $[Fe^{III}_{28}(TBC[4])_4(\mu_5\text{-}O)_4(\mu_4\text{-}O)_6(\mu_3\text{-}O)_{16}(\mu\text{-}OEt)_{10}(\mu\text{-}O_2CNMe_2)_{1.5}(\mu\text{-}O_2CH)_{0.5}(Cl)_4(MeCN)_4]$ (**37**, Figure 4.15) following diffusion of MeCN into the cooled mother liquor. The crystals were found to be in a monoclinic cell and the structure solution was carried out in the space group *I*2/*m*. The ASU comprises one quarter of the formula. Pertinent bond parameters and BVS calculations for **37** are given in Table S4.9.

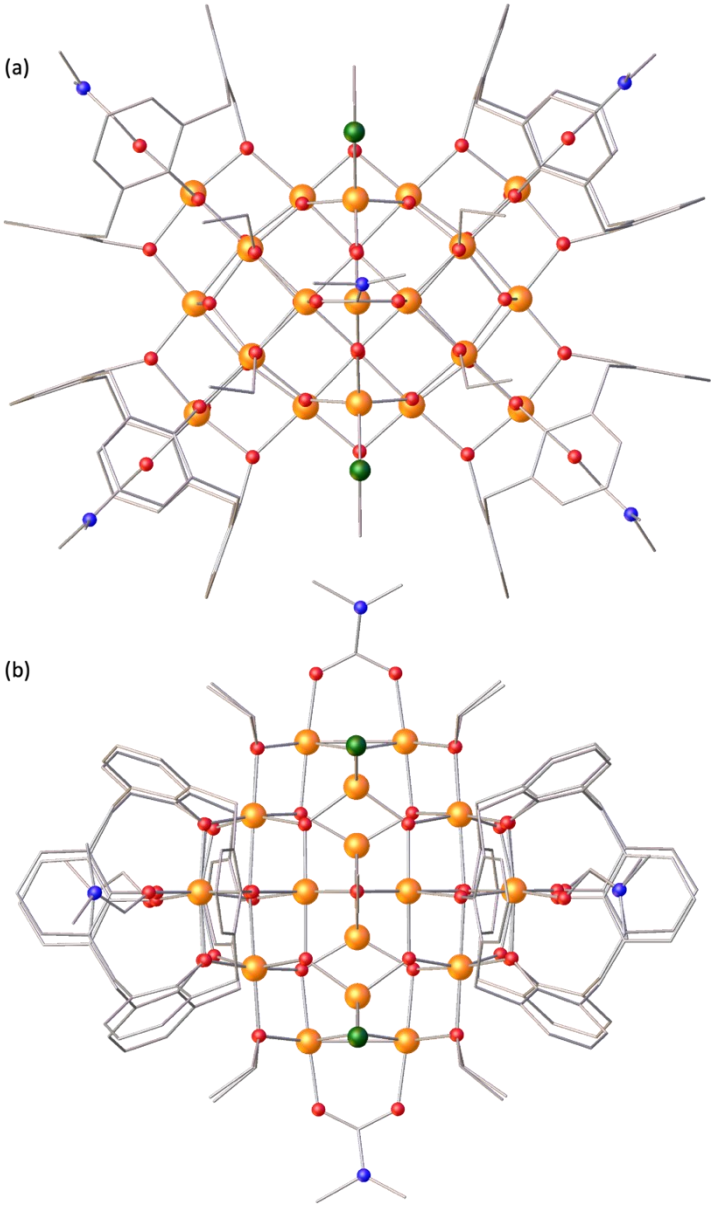

Figure 4.15 Single crystal X-ray structure of **37.** Colour code: Fe^{III} - orange, Cl - dark green, N - blue, C - grey, O - red. H atoms, ^{t}Bu groups of TBC[4] and co-crystallised solvent molecules omitted for clarity.

The metallic skeleton of **37** is best described by its central $\{Fe_{20}\}$ unit comprising four edge-sharing hexagonal faces (Figure 4.16, shown in yellow) which in turn edge-share with four squares (shown in blue); two vertex-sharing squares on each side. The remaining edges make up the eight triangular faces (shown in green), which themselves arrange in a 'pair of pairs'; two edge-sharing pairs coupled *via* a vertex on each side. This unit is reminiscent of Archimedean/Johnson type solids in its assembly of regular polyhedra but cannot be defined by any of the distinct solids.

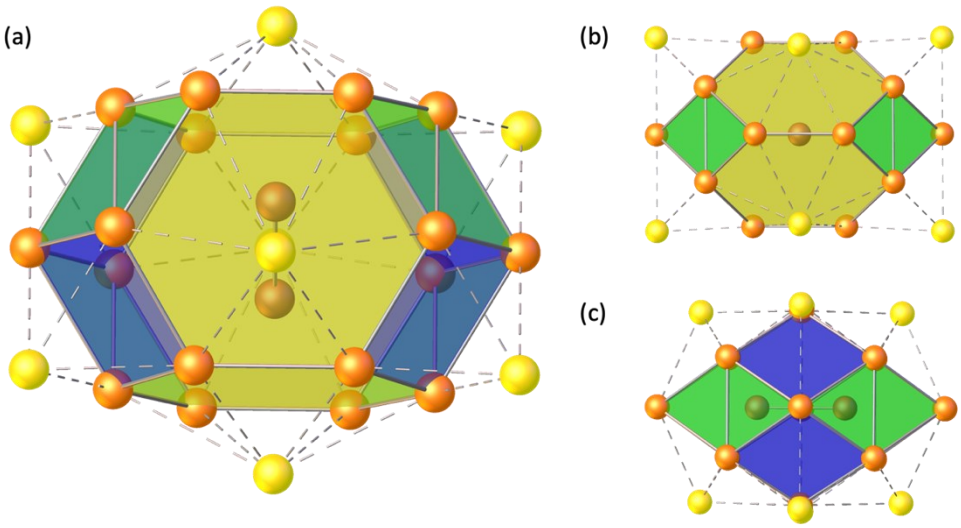

Figure 4.16 Metallic skeleton of **37** shown at various orientations. The hexagonal faces are shown in yellow, square in blue and triangular in green. Colour code: orange - Fe^{III} ions in the main unit, yellow - Fe^{III} ions capping the hexagonal/squares, brown - Fe^{III} ions in central dimer.

The shape is supported by a network of $\mu_{3\text{-}5}$-O/μ-OEt bridges (Figure 4.17), the former of which also support the {Fe_2} dimer centred within the unit (Fe10 and s.e.). Twenty-two of the Fe^{III} ions are six-coordinate and octahedral (Fe1-8), while six are four-coordinate and tetrahedral (Fe9-10). The tetrahedral geometry of Fe10 is supported by four μ_4-O ions. Each hexagonal face is capped by one Fe ion (Fe9) *via* three μ_3-O bridges and the tetrahedral geometry of Fe9 is completed by a terminal Cl. Each square face is capped by a TBC[4]-supported Fe ion (Fe6, Fe8) creating the familiar square pyramidal unit upheld by a μ_5-O bridge. The distorted octahedral geometries of Fe6/Fe8 are completed by a dmf molecule residing in the TBC[4] cavity. The Fe ions at the vertices of the hexagonal faces (Fe1-Fe5) all display distorted octahedral {FeO_6} geometries but these are of two types. Fe1 is supported by a disordered combination of dimethyl carbamate, μ-O_2CNMe_2, and formate, μ-O_2C, which are fixed at 75% and 25% occupancy respectively, and form *in situ* from the decomposition of dmf. The coordination sphere of Fe1 therefore comprises μ_4-O (O10), two μ_3-O (O8 and s.e.), two μ-OEt (O1E, O2E) and μ-O_2CNMe_2/μ-O_2C (O101). Fe2-Fe5 are all bridged in part by the TBC[4] ligand, with coordination spheres comprising μ_5-O (O14-O15), μ_4-O (O10, O13), two μ_3-O (O9, O11-O12), μ-OEt (O1E-O3E) and μ-$O_{TBC[4]}$ (O1-O2, O4, O6-O7) bridges. As such, Fe2-Fe5 also make up the Fe ions at the vertices of the square faces with the addition of Fe7 which occupies the vertex-sharing site of the two squares. Fe7 displays a distorted octahedral geometry containing two μ_5-O, two μ_3-O and two μ-$O_{TBC[4]}$ bridges.

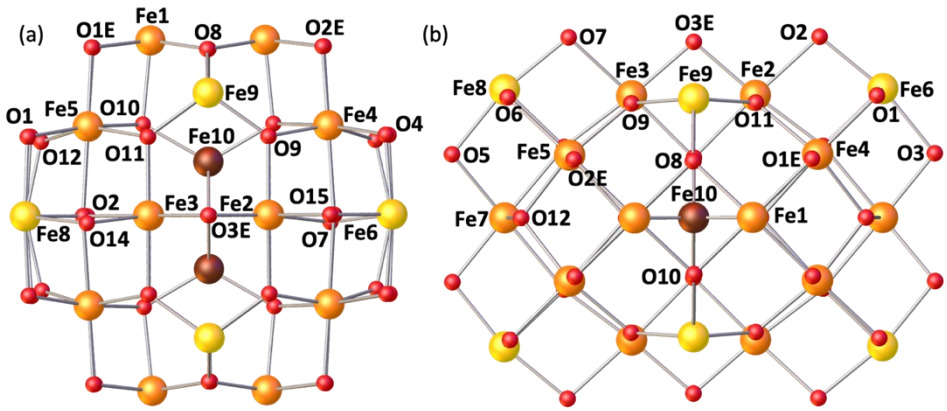

Figure 4.17 Cluster core of **37.** Colour code: orange - Fe^{III} ions in the main unit, yellow - Fe^{III} ions capping the hexagonal/squares faces, brown - Fe^{III} ions in the dimer, O - red.

Examination of the extended structure of **37** shows that clusters pack in an aesthetically pleasing brickwork-like motif when viewed down the *a*-axis (Figure S4.9). Closest intermolecular interactions are between the ^{t}Bu groups of neighbouring TBC[4] ligands at distances > 4 Å.

A search of the CSD reveals just one other cluster-type with a nuclearity of [Fe_{28}], which is arranged as a wheel of four {Fe_7} units tethered together *via* chiral tartrate ligands.[30,31] The {Fe_{28}} clusters then assemble in a similar fashion to afford "{Fe_{168}}".[32] Magnetic data for the latter was not provided but with each {Fe_7} unit being separated by a lengthy three-atom bridge, one would expect the cluster to exhibit magnetic behaviour markedly different to the {Fe_{28}} magnetic core in **37**.

Magnetic measurements

Direct current (dc) magnetic susceptibility (χ_M) and magnetisation data were measured on a polycrystalline sample of **32** in the T = 2 – 300 K temperature range, in a field of B = 0.1 T (Figure 4.18), where $\chi_M = M/B$ and M is the magnetisation. At 300 K, the $\chi_M T$ product of **32** is 3.18 cm^3 K mol^{-1}, slightly lower than the value expected for nine non-interacting Cu^{II} ions (3.38 cm^3 K mol^{-1}, g = 2.00; 4.08 cm^3 K mol^{-1}, g = 2.20). Upon cooling, $\chi_M T$ decreases rapidly until approximately 75 K, where it decreases extremely slowly to a plateau between 40 – 15 K of ~1.30 cm^3 K mol^{-1}. Cooling below 15 K decreases the $\chi_M T$ product rapidly, reaching a value of 0.84 cm^3 K mol^{-1} at T = 2 K. This behaviour is indicative of relatively strong competing antiferromagnetic exchange interactions. Magnetisation data was measured in the ranges T = 2 - 10 K and B = 0 - 9 T with M rising with increasing B but not reaching saturation; the maximum value being M = 2.3 μ_B at T = 2 K and B = 9 T.

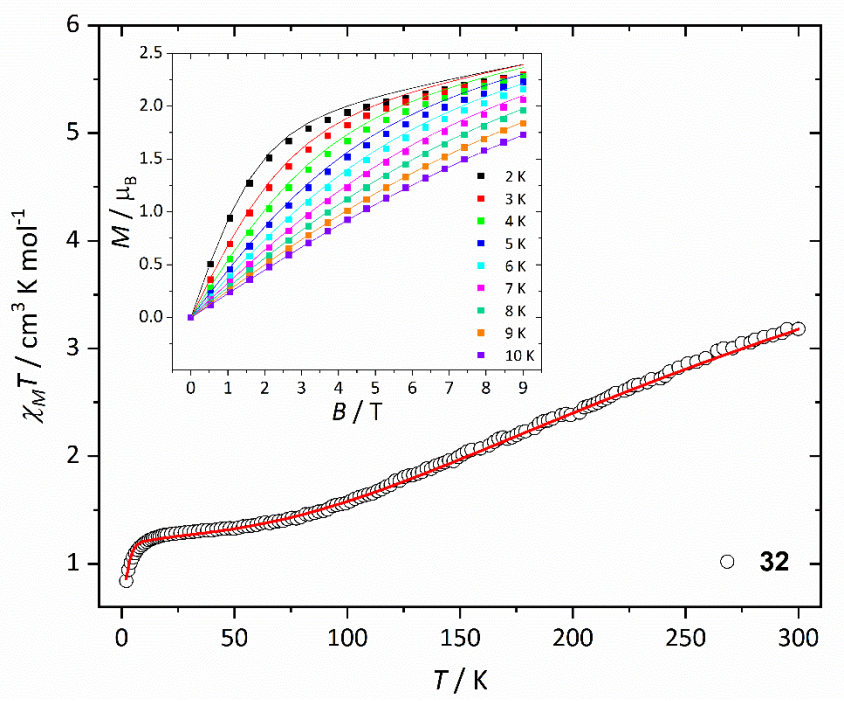

Figure 4.18 Experimental $\chi_M T$ *vs* T data for **32** measured in the T = 2 - 300 K temperature range in an applied field, B = 0.1 T. Inset: Variable-temperature-variable-field (VTVB) magnetisation data of **32** at T = 2 - 10 K and B = 0 - 9 T. The solid lines are the best fit of the data modelled using spin-Hamiltonian (4.1).

Inspection of the magnetic [Cu_9O_{15}] core of **32** reveals that the Cu-O-Cu angle subtended by the phenolic O-atoms of the TBC[4] ligands fall in the range 112.2-116.9°, while those mediated by the OH ions are in the range 116.7-117.8°. This suggests the latter should be more strongly antiferromagnetic.

The plateau of the $\chi_M T$ is not surprising, being an archetypal feature of {Cu_3} triangles in the literature and symptomatic of spin frustration. Thus we expect significant antisymmetric exchange (ASE) in the excited states of **32** with substantial second-order effects that should contribute to the magnetisation.[33] A quantitative interpretation of the data of **32** was obtained using a spin-Hamiltonian (4.1), where the summation indices *i, j* run though the constituent metal ions, $\hat{S}$ is a spin operator, *S* is the total spin, μ_B is the Bohr magneton, *g* is the g-factor, J_{ij} is the bilinear pairwise isotropic exchange interaction parameter and G_{ij} is the antisymmetric exchange parameter.

$$\hat{H} = \mu_B B \sum_i g_i \hat{S}_i - 2 \sum_{i,j<1} J_{i,j} \hat{S}_i \cdot \hat{S}_j + \sum_{i,j<1} G_{i,j} \hat{S}_i \cdot \hat{S}_j \qquad (4.1)$$

The antisymmetric exchange (ASE) term in Hamiltonian (4.1) must be included to allow for the presence of the non-zero ASE vector brought about by the lack of an inversion centre in trigonal trinuclear units (*i.e.* the Dzyaloshinsky-Moriya antisymmetric interaction).[34–37] Due to the similar Cu^{II} environments and symmetry in **32**, we assume that G_{ij} is equal between all neighbouring Cu^{II} ions and only consider G_z (based on G_x, G_y << G_z) to avoid over-parameterisation. We also adopt a 2*J* model which defines *J* as the interactions between Cu^{II} ions at the equivalent vertices of the 'upper' and 'lower' triangular faces of the prism and *J'* as the interactions between the Cu^{II} capping ions and the Cu^{II} ions at the vertices of the square faces of the triangular prism (Figure 4.19). The model gives good agreement with the experimental data (Figure 4.18), with best-fit parameters *J* = -141.55 cm^{-1}, *J'* = -53.19 cm^{-1} and *G* = 39.70 cm^{-1} (*g* = 2.20), values concurrent with previous magneto-structural parameters of {Cu_3}-containing clusters.[33,37–39] We note here that inclusion of the Cu-Br-Cu interactions decreased the quality of fit in all cases and was therefore not included. The values obtained are indicative of antiferromagnetic exchange interactions and support our quantitative hypothesis that the exchange interactions within the triangular prism are more antiferromagnetic than between the prism and the caps. The experimental data is also in line

with that shown for the analogous [Cu^{II}_9] cluster **11**, which did not provide a quantitative analysis.[24]

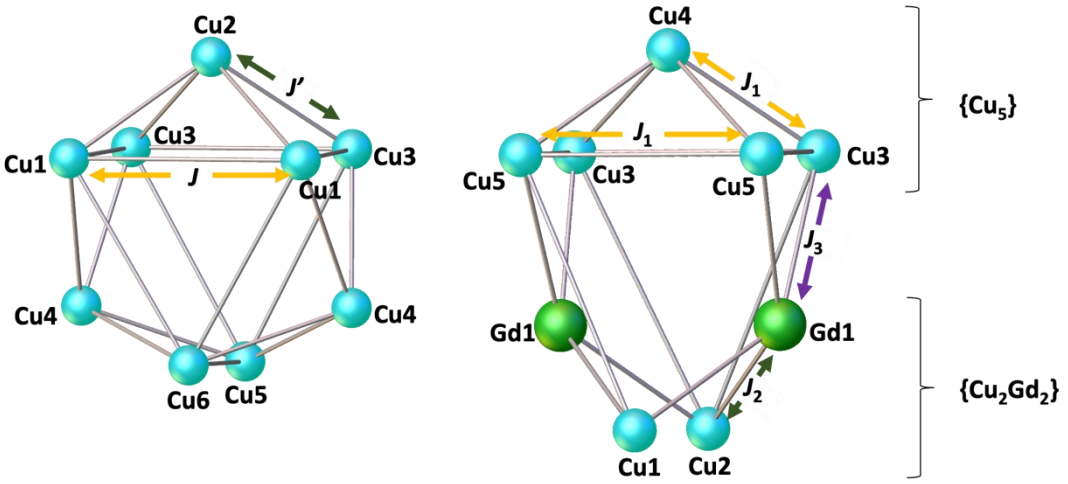

Figure 4.19 Schematic representation of the two different exchange pathways used to fit the experimental susceptibility and magnetisation data of **32** (left) and the three exchange pathways used to fit the equivalent data of **33** (right).

Equivalent dc magnetic susceptibility measurements were also performed on complex **33** and show that the introduction of Gd^{III} ions into the [Cu^{II}_9] framework has a marked effect upon the magnetic properties (Figure 4.20). At 300 K, the $\chi_M T$ product of **33** ~18.02 cm^3 K mol^{-1} matches the expected value for spin-only contributions to the susceptibility assuming $g_{Cu(II)}$ = 2.20, $g_{Gd(III)}$ = 2.00. Upon cooling, the $\chi_M T$ product decreases very slowly reaching a value of 17.65 cm^3 K mol^{-1} at approximately T = 100 K. This is indicative of antiferromagnetic exchange interactions between the Cu^{II} ions. Further cooling gives an increase in $\chi_M T$ to reach a maximum value of 33.51 cm^3 K mol^{-1} at T = 2 K, a behaviour suggestive of ferromagnetic exchange between the Cu^{II} and Gd^{III} ions. Magnetisation data measured between T = 2 - 10 K and B = 0 - 7 T shows a saturation value of M_{sat} = 15 μ_B suggesting the presence of an S = 15/2 ground state.

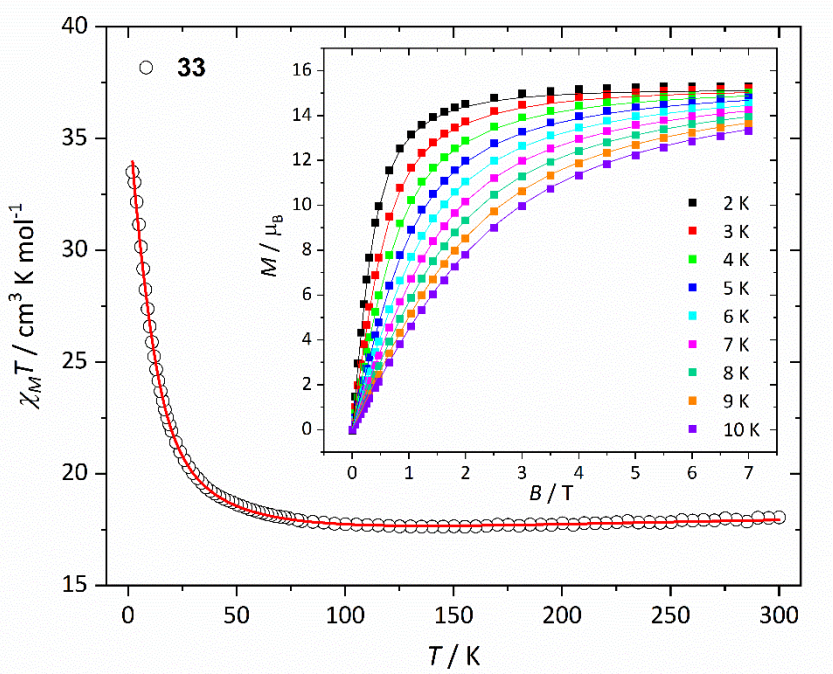

Figure 4.20 Experimental $\chi_M T$ *vs* T data for **33** measured in the T = 2 - 300 K temperature range in an applied field, B = 0.1 T. Inset: Variable-temperature-variable-field (VTVB) magnetisation data of **33** at T = 2 - 10 K and B = 0 - 9 T. The solid lines are the best fit of the data modelled using the isotropic part of spin-Hamiltonian (4.1).

For the quantitative interpretation of the magnetic properties of **33** we used the isotropic part of spin-Hamiltonian (4.1) and the 3J model shown in Figure 4.19 which splits the magnetic core of **33** into two parts – a $\{Cu_5\}$ and a $\{Cu_2Gd_2\}$ unit. J_1 represents the exchange between Cu^{II}-Cu^{II} ions in the $\{Cu_5\}$ part of the molecule, J_2 represents the exchange between Cu^{II}-Gd^{III} ions in the $\{Cu_2Gd_2\}$ part of the molecule and J_3 represents the interactions between the Cu^{II}-Gd^{III} ions that link the two parts together. We also assume a negligible Gd^{III}-Gd^{III} interaction and note that the two Cu ions in $\{Cu_2Gd_2\}$ are not connected. This model gives excellent agreement with the experimental data of **33** and affords best-fit parameters J_1 = -88.14 cm^{-1}, J_2 = +2.03 cm $^{-1}$ and J_3 = -3.92 cm^{-1} ($g_{Cu(II)}$ = 2.20, $g_{Gd(III)}$ = 2.00). These values corroborate our qualitative analysis, indicating relatively strong antiferromagnetic exchange between Cu^{II}-Cu^{II} ions in $\{Cu_5\}$, weak ferromagnetic exchange between Cu^{II}-Gd^{III} ions in $\{Cu_2Gd_2\}$ and weak antiferromagnetic exchange between the Cu^{II}-Gd^{III} ions that link the units together.

To understand the influence of the Gd^{III} ions in this cluster, we can compare the Energy *vs* Spin State diagrams of **32** and **33** (Figures 4.21). For **32**, the best-fit parameters calculated give a spin ground state of $S = 1/2$ (Figure 4.22) with $S = 1/2$ and $S = 3/2$ states lying 11.43 cm^{-1} and 13.16 cm^{-1} above the ground state, respectively. For **33**, however, the best-fit parameters calculated give a spin ground state of $S = 15/2$, with numerous excited states lying close the ground state, the lowest being $S = 15/2$ (2.20 cm^{-1}) and $S = 13/2$ (4.29 cm^{-1}).

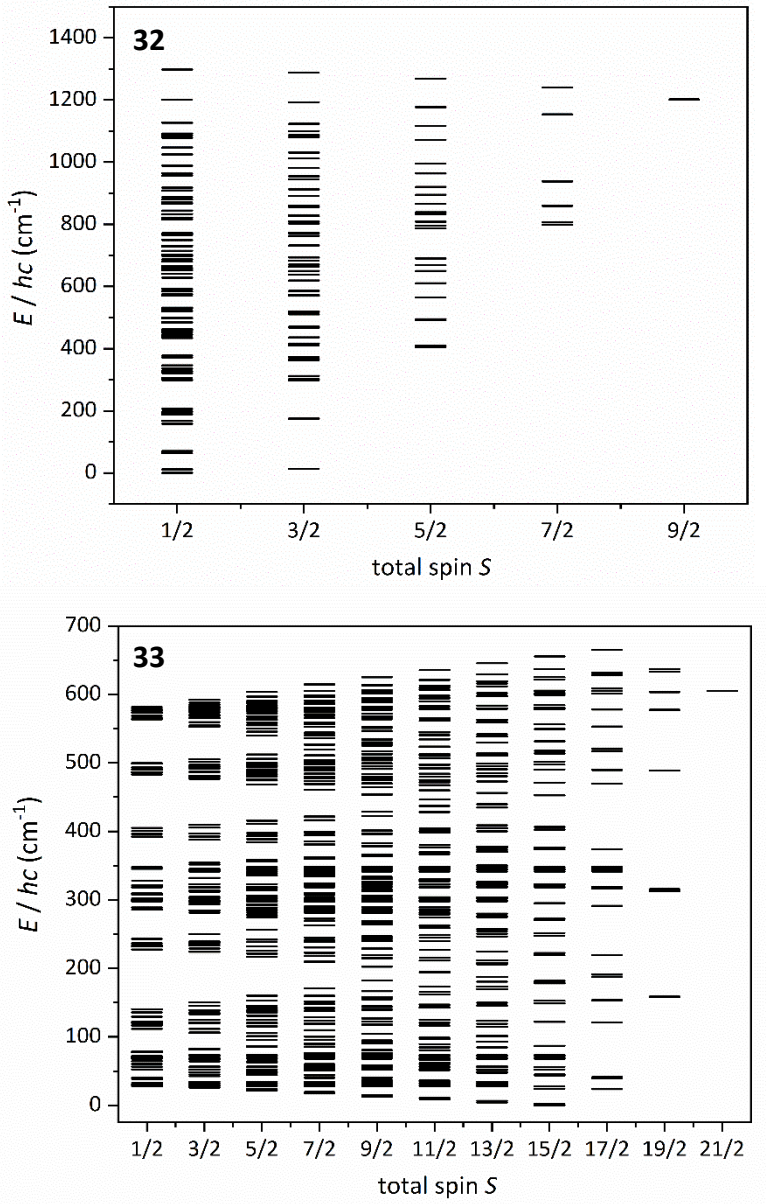

Figure 4.21 Energy spectrum of **32** (top) and **33** (bottom) calculated from the fit of the experimental data, as described in text. The spin ground states are $S = 1/2$ and $S = 15/2$ respectively.

Consideration of the exchange parameters allows us to visualise the nature of this S = 15/2 spin ground state. Strong antiferromagnetic exchange in the $\{Cu_5\}$ unit of **33** would result in an S = 1/2 ground state, while weak ferromagnetic exchange in $\{Cu_2Gd_2\}$ would result in an S = 16/2 ground state. Weak antiferromagnetic exchange between the two would therefore result in an S = 15/2 ground state (Figure 4.22).

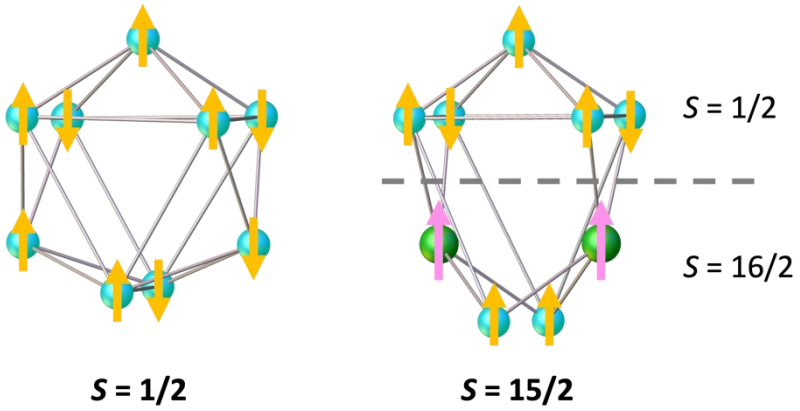

Figure 4.22- Schematic representation of nature of the spin ground states in **32** (left) and **33** (right). The yellow arrows represent S = 1/2 and the pink arrows S = 7/2. The dashed line separates the $\{Cu_5\}$ and $\{Cu_2Gd_2\}$ units in **33**, as discussed in text .

Dc magnetic susceptibility and magnetisation studies were also performed on polycrystalline samples of **34** and **35** in the temperature and field ranges T = 300 - 2 K, B = 0.1 T, and T = 3 - 10 K, B = 0 - 9 T, respectively (Figures 4.23-4.24). At 300 K, the $\chi_M T$ value of ~9.0 cm^3 K mol^{-1} for **34** matches the Curie constant expected for three uncorrelated Mn^{III} ions with g = 2.00 (Figure 4.23). Upon cooling, the $\chi_M T$ product is invariant with temperature until approximately T = 8 K where it rapidly decreases to a minimum value of 5.66 cm^3 K mol^{-1} at T = 2 K. The high temperature data are therefore suggestive of paramagnetism, with the low temperature decline assigned to a combination of zero-field splitting effects and/or intra- and inter-molecular antiferromagnetic exchange interactions. Note that at these temperatures the three are likely to be correlated. The magnetisation data rise rapidly with increasing field, reaching a value of 10.4 μ_B at T = 3 K and B = 9 T. The zero, or very weak, exchange is not surprising given that the three Mn ions are only connected to each other *via* the single, disordered $[CO_3]^{2-}$ ion lying in the centre of the cage (Mn···Mn ~5.30-5.43 Å). A simultaneous fit of the susceptibility and magnetisation data using spin-Hamiltonian (4.1) afforded the

best-fit parameters $|D_{Mn(III)}|$ = 3.7 cm^{-1} and zJ = +0.01 cm^{-1} (where zJ denotes the intermolecular contribution). The value of D is in line with that expected for a Jahn-Teller (JT) distorted Mn^{III} ions with a {MnO_5} coordination sphere.[40]

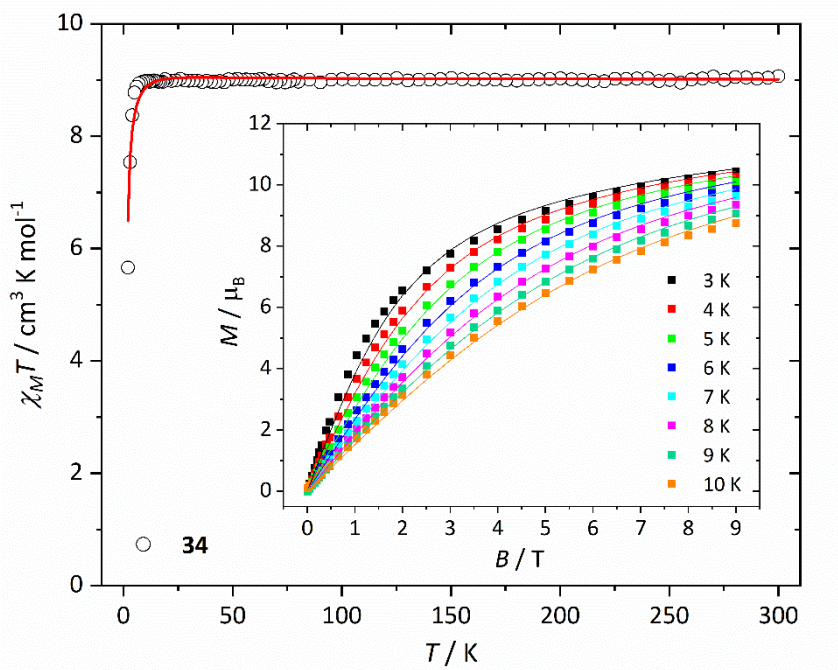

Figure 4.23 Experimental $\chi_M T$ *vs* T data for **34** measured in the T = 300-2 K temperature range in an applied field, B = 0.1 T. Inset: Variable-temperature-variable-field (VTVB) magnetisation data of **34** at T = 3-10 K and B = 0-9 T. The solid lines are the best fit of the data modelled using the isotropic part of spin-Hamiltonian (4.1).

At 300 K, $\chi_M T$ value of 19.81 cm^3 K mol^{-1} for **35** is slightly below the value expected for four Mn^{III} ions and two Mn^{II} ions (20.75 cm^3 K mol^{-1}) with g = 2.00 (Figure 4.24). Upon cooling, the $\chi_M T$ product is invariant until approximately T = 200 K wherefrom it slowly decreases to a value of 17.40 cm^3 K mol^{-1} at T = 75 K, before decreasing more rapidly below this temperature to a value of 6.34 cm^3 K mol^{-1} at T = 2 K. Magnetisation data rise in a near linear-like fashion without saturating; the maximum value being M = 11.7 μ_B at T = 3 K and B = 9 T. These data are indicative of weak antiferromagnetic exchange between neighbouring metal ions. An examination of the magnetic core of **35** reveals two 'linear' and asymmetric [Mn^{III}-Mn^{II}-Mn^{III}] trimers that are not connected to each other. Thus, we simultaneously fitted the susceptibility and magnetisation data to a model containing three metal ions and two distinct J values (Figure S4.10). This in conjunction with the isotropic part of spin-Hamiltonian (4.1)

afforded the best fit values J = +0.10 cm^{-1}, J' = -2.52 cm^{-1}, $|D_{Mn(III)}|$ = 3.75 cm^{-1}. The larger (and negative) J' value reflects the larger Mn-$O_{TBC[4]}$-Mn (~118° *vs* ~109°) angles present. The magnitude of the exchange is in agreement with that found in calix[4]arene-supported Mn clusters with similar Mn^{III}-O-Mn^{II} motifs.[41]

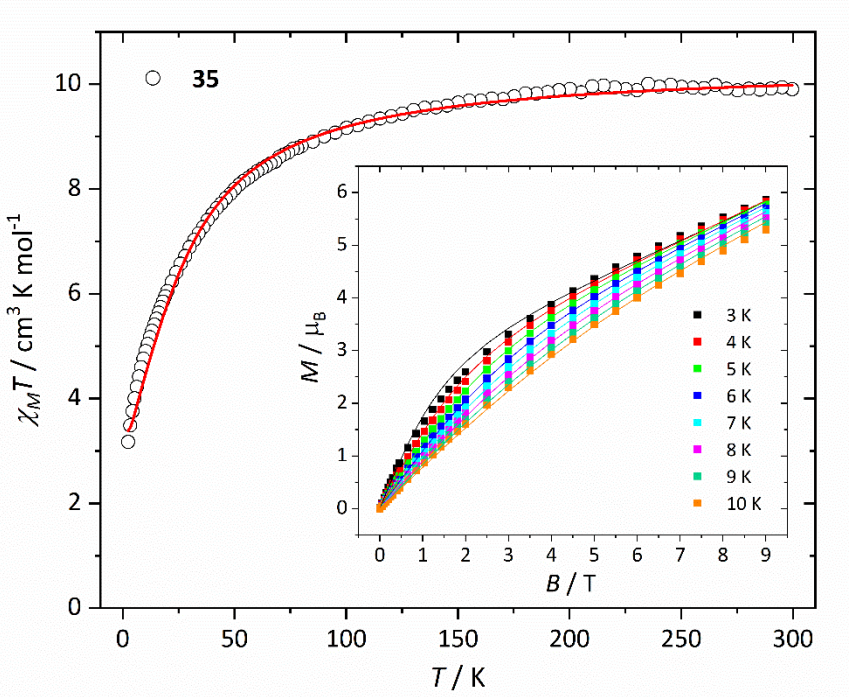

Figure 4.24 Experimental $\chi_M T$ *vs* T data for **35** measured in the T = 300 - 2 K temperature range in an applied field, B = 0.1 T. Inset: Variable-temperature-variable-field (VTVB) magnetisation data of **35** at T = 3 - 10 K and B = 0 - 9 T. The solid lines are the best fit of the data modelled using the isotropic part of spin-Hamiltonian (4.1).

Dc magnetic susceptibility and magnetisation data were measured on a polycrystalline sample of **36** in the T = 300 - 2 K, B = 0.1 T and T = 2 - 10 K, B = 0 - 9 T temperature and field ranges respectively (Figure 4.25, Figure S4.11). At 300 K the value of $\chi_M T$ is well below that expected for eighteen non-interacting S = 5/2 ions (78.75 cm^3 K mol^{-1}) assuming g = 2.00. As the temperature is lowered the $\chi_M T$ product decreases rapidly to a value 9.2 cm^3 K mol^{-1} at T = 2 K. The magnetisation data at T = 2 K rise rapidly up to B = 2.0 T before increasing in a more linear fashion between B = 2 - 9 T, reaching a maximum value of M = 12.3 μ_B but without saturating (Figure S4.11). This behaviour is indicative of strong, competing antiferromagnetic exchange interactions. Low-temperature high-field magnetisation measurements were also

performed up to fields of 32.5 T at T = 0.4 K (Figure 4.25 and Figure S4.12). The magnetisation reaches a maximum value of 7.6 μ_B at B = 32.5 T and a minimum value of -8.1 μ_B at B = -20 T (where the negative denotes the field being oriented in the opposite direction).

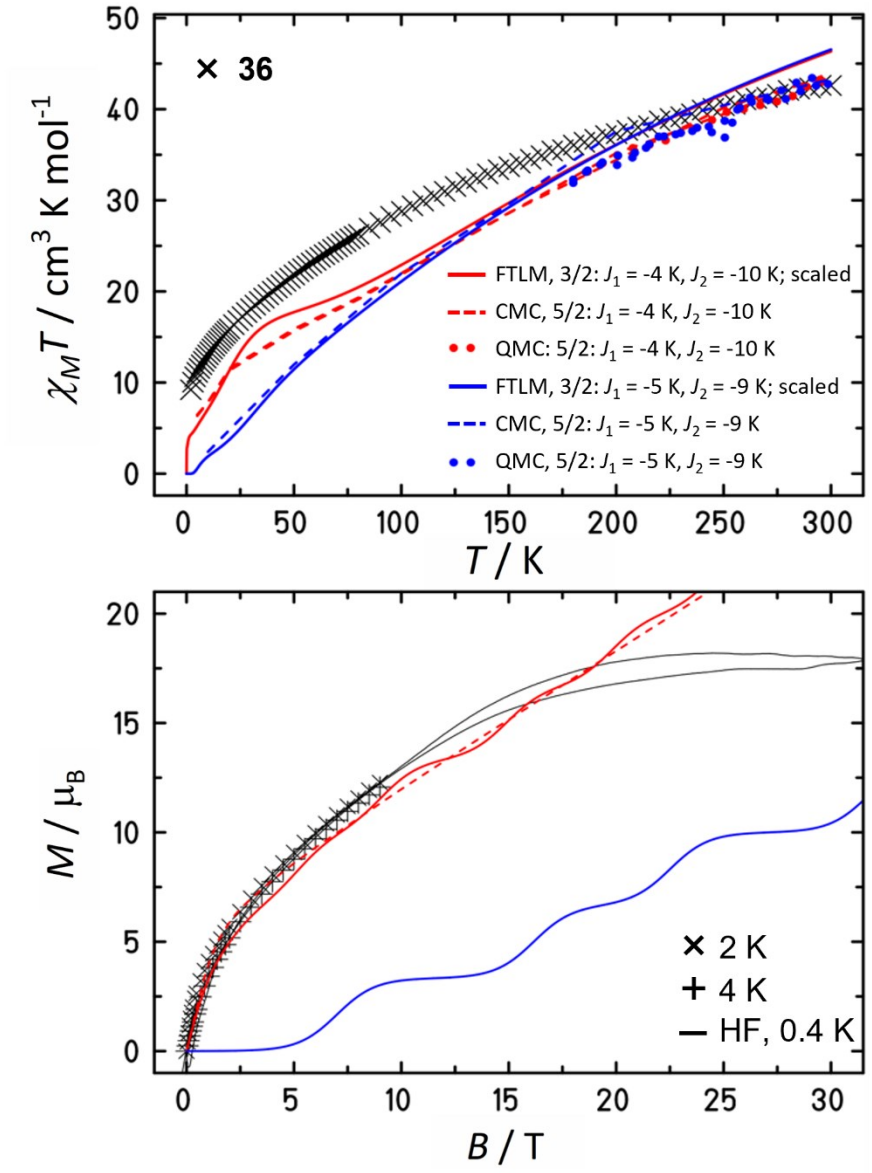

Figure 4.25 Top: Experimental $\chi_M T$ *vs* T data (x) for **36** measured in the T = 2 - 300 K temperature range in an applied field, B = 0.1 T. Bottom: Magnetisation data of **36** measured at B = 0 - 9 T for T = 2 K (x) and 4 K (+). High-field magnetisation data shown from B = 0 - 32.5 T at T = 0.4 K. The solid and dashed blue/red lines are the best fits of the data modelled using the isotropic part of spin-Hamiltonian (4.1) and various calculation techniques (see text).

The magnetic susceptibility and magnetisation data of **36** could in principle be simulated using the isotropic part of spin-Hamiltonian (4.1). However, due to the large dimension (1.02 x 10^{14}) of the related Hilbert space an exact[42] or approximate[43–45] diagonalisation of the Hamiltonian and a subsequent calculation is virtually impossible. We thus resort to more drastic approximations to at least obtain order of magnitude estimates for the exchange couplings present. A reasonable reduction of parameters is given by assuming just two exchange interactions, J_1 along the edges of the cuboctahedron and J_2 along the edges of the square pyramids to the respective tip (Figure S4.13). As Figure 4.25 shows, large scale classical Monte-Carlo (CMC) calculations agree well with scaled-up finite-temperature Lanczos calculations,[43,44] performed with fictitious spins S = 3/2 and J_1 = -4 K / -2.78 cm^{-1} and J_2 = -10 K / -6.95 cm^{-1} with $g_{Fe(III)}$ = 2.00 (red curves). The magnetisation is particularly well simulated up to 10 T. However, simulations are rough and the assumption of just two parameters oversimplifies the situation. The plateau-like flattening of *M vs B* is thus not modelled. Nevertheless, the result shows that rather strong antiferromagnetic exchange interactions characterise the cluster. It is highly frustrated and situated in a parameter space close to scenarios with gapped singlet ground states as demonstrated by the blue curves.

Dc magnetic susceptibility measurements were performed on a polycrystalline sample of **37** in the temperature range T = 2 - 300 K and under an applied field, B = 0.1 T (Figure 4.26). At 300 K, the $\chi_M T$ product is 106.44 cm^3 K mol^{-1}, somewhat lower than the expected value for 28 non-interacting Fe^{III} spins (122.5 cm^3 K mol^{-1}, g = 2.00). Upon cooling, the $\chi_M T$ product decreases steadily until approximately 80 K, where it decreases more rapidly to reach a value of 1.75 cm^3 K mol^{-1} at T = 2 K. Magnetisation measurements performed in the ranges T = 2 - 10 K and B = 0 - 9 T show the magnetisation increasing with increasing field, with a maximum value of 7.3 μ_B as saturation is reached (Figure S4.14). This behaviour is indicative of competing antiferromagnetic exchange interactions. The complicated magnetic core and the huge dimension (6.14 x 10^{21}) of the related Hilbert space prevents even an order of magnitude estimation from being possible. However, a fit of the inverse susceptibility data to the Curie-Weiss law, in the range T = 300 - 50 K, affords θ = -40.66 K and C = 121.65 cm^3 K mol^{-1} (inset of Figure 4.26). We surmise, therefore, that **37** is highly frustrated with relatively strong, competing antiferromagnetic exchange interactions likely in the same order of magnitude as **36**.

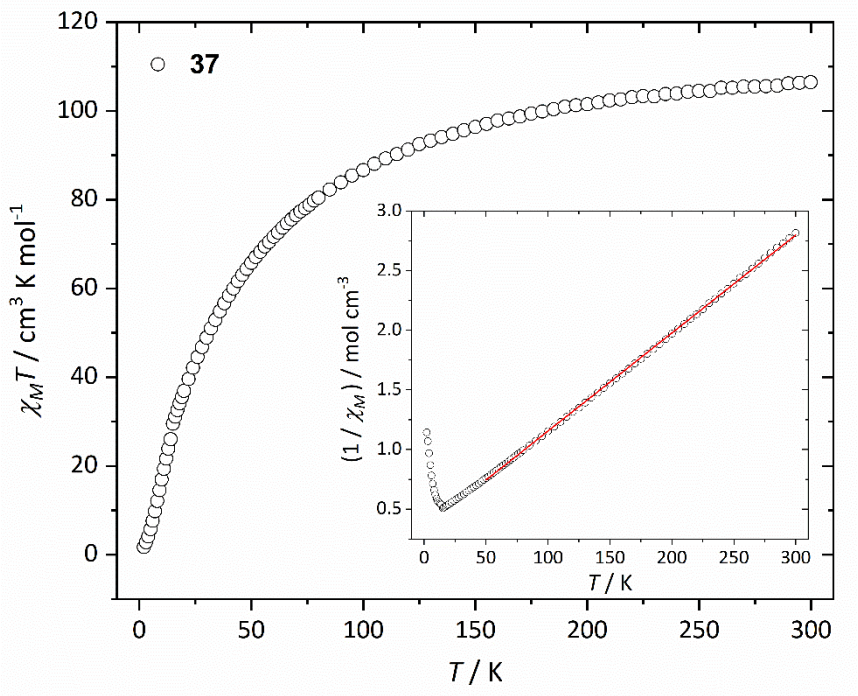

Figure 4.26 Experimental $\chi_M T$ *vs* T data for **37** measured in the T = 2 - 300 K temperature range in an applied field, B = 0.1 T. Inset: Plot of $1/\chi_M$ *vs* T data in the same T range. The solid red line is a fit of the experimental data to the Curie-Weiss law in the range T = 300 - 50 K.

4.4 Conclusions

Employment of H_4TBC[4] in exploration of the tricapped trigonal prism topology yields three novel polymetallic clusters, [Cu^{II}_9] (**32**), [$Cu^{II}_7Gd^{III}_2$] (**33**) and [$Mn^{III}_3Na_6$] (**34**). Magnetic studies of **32** reveal dominant antiferromagnetic exchange interactions and significant antisymmetric exchange brought about by the repeating {Cu_3} triangle geometries (J = -141.55 cm^{-1}, J' = -53.19 cm^{-1} and G = 39.70 cm^{-1}). Introduction of Gd^{III} into the framework gives the first example of LnM^{III} > TM^{III} preference in the TBC[4] pocket, altering the equilateral trigonal prism in **32** to an isosceles trigonal prism in **33**. This has a marked effect on the magnetic properties, revealing competing antiferromagnetic (Cu^{II}-Cu^{II}, Cu^{II}-Gd^{III}) and ferromagnetic (Cu^{II}-Gd^{III}) exchange interactions (J_1 = -88.14 cm^{-1}, J_2 = 2.03 cm^{-1} and J_3 = -3.92 cm^{-1}).

Investigation of this framework with Mn salts afforded [$Mn^{III}_3Na_6$] (**34**) of the same topology, highlighting the dominant structure-directing effect of the TBC[4] ligand and the relative stability of the [M_9] tricapped trigonal prismatic moiety. Switching H_4TBC[4] for BisTBC[4] (H_8L) in an otherwise analogous reaction affords the tetracapped square prism [$Mn^{III}_4Mn^{II}_2Na_6$] (**35**), following the same prismatic expansion as the TBC[4]-supported [Cu_9] (**11**) to the BisTBC[4]-supported [Cu^{II}_{13}] (**24**) in the literature. Magnetic studies of **34** reveal paramagnetism ($|D_{Mn(III)}|$ = 3.7 cm^{-1} and zJ = 0.01 cm^{-1}) due to the separation of the Mn^{III} ions in the cluster, whilst **35** exhibits competing ferrimagnetic exchange interactions (J = +0.10 cm^{-1}, J' = -2.52 cm^{-1}, $|D_{Mn(III)}|$ = 3.75 cm^{-1}).

Employing solvothermal techniques afforded the highly-symmetric [Fe^{III}_{18}] (**36**) and [Fe^{III}_{28}] (**37**). These are the first homometallic Fe-TBC[4] clusters reported and exhibit geometries reminiscent of Archimedean-type solids, the former displaying a stellated cuboctahedron and the latter a regular arrangement of hexagonal, square and triangular polyhedra. The magnetic properties of **36** reveal antiferromagnetic behaviour approximated using both Monte-Carlo and finite-temperature Lanczos calculations (J_1 = -4 K / -2.78 cm^{-1} and J_2 = -10 K / -6.95 cm^{-1}). The magnetic properties of **37** are also dominated by competing antiferromagnetic exchange interactions but the high nuclearity and structural complexity of the cluster prevents even approximate quantitative analysis. Both **36** and **37** are highly frustrated, demonstrating the success of solvothermal technique in affording highly symmetric species with significant geometric spin frustration.

4.5 References

(1) G. Toulouse, *Comm. Phys.*, 1977, **2**, 115–119.

(2) S. Kirkpatrick, *Phys. Rev. B*, 1977, **16**, 4630–4641.

(3) A. P. Ramirez, *Annu. Rev. Mater. Sci.*, 1994, **24**, 453–480.

(4) J. E. Greedan, *J. Mater. Chem.*, 2001, **11**, 37–53.

(5) R. Moessner, *Can. J. Phys.*, 2001, **79**, 1283–1294.

(6) S. T. Bramwell and M. J. Gingras, *Science*, 2001, **294**, 1495–1501.

(7) O. Kahn, *Chem. Phys. Lett.*, 1997, **265**, 109–114.

(8) J. K. McCusker, E. A. Schmitt and D. N. Hendrickson, in *Magnetic Molecular Materials*, eds. D. Gatteschi, O. Kahn, J. S. Miller and F. Palacio, Springer Netherlands, Dordrecht, 1991, pp. 297–319.

(9) J. Schnack, *Dalton Trans.*, 2010, **39**, 4677–4686.

(10) M. L. Baker, G. A. Timco, S. Piligkos, J. S. Mathieson, H. Mutka, F. Tuna, P. Kozłowski, M. Antkowiak, T. Guidi, T. Gupta, H. Rath, R. J. Woolfson, G. Kamieniarz, R. G. Pritchard, H. Weihe, L. Cronin, G. Rajaraman, D. Collison, E. J. L. McInnes and R. E. P. Winpenny, *Proc. Natl. Acad. Sci.*, 2012, **109**, 19113–19118.

(11) M. Evangelisti and E. K. Brechin, *Dalton Trans.*, 2010, **39**, 4672–4676.

(12) N. Hoshino, M. Nakano, H. Nojiri, W. Wernsdorfer and H. Oshio, *J. Am. Chem. Soc.*, 2009, **131**, 15100–15101.

(13) O. Cador, D. Gatteschi, R. Sessoli, F. K. Larsen, J. Overgaard, A.-L. Barra, S. J. Teat, G. A. Timco and R. E. P. Winpenny, *Angew. Chem. Int. Ed.*, 2004, **43**, 5196–5200.

(14) R. J. Woolfson, G. A. Timco, A. Chiesa, I. J. Vitorica-Yrezabal, F. Tuna, T. Guidi, E. Pavarini, P. Santini, S. Carretta and R. E. P. Winpenny, *Angew. Chem. Int. Ed.*, 2016, **55**, 8856–8859.

(15) V. O. Garlea, S. E. Nagler, J. L. Zarestky, C. Stassis, D. Vaknin, P. Kögerler, D. F. McMorrow, C. Niedermayer, D. A. Tennant, B. Lake, Y. Qiu, M. Exler, J. Schnack and M. Luban, *Phys. Rev. B*, 2006, **73**, 024414.

(16) B. Cage, F. A. Cotton, N. S. Dalal, E. A. Hillard, B. Rakvin and C. M. Ramsey, *J. Am. Chem. Soc.*, 2003, **125**, 5270–5271.

(17) D. Dai and M.-H. Whangbo, *J. Chem. Phys.*, 2004, **121**, 672–680.

(18) C. D. Gutsche, *Calixarenes : an Introduction*, RSC Publishing, Cambridge, 2nd ed., 2008.

(19) L. R. B. Wilson, M. Coletta, M. Evangelisiti, S. Piligkos, S. J. Dalgarno and E. K. Brechin, *Dalton Trans.*, 2022, **51**, 4213–4226.

(20) G. M. Sheldrick, *Acta Crystallogr. Sect. C*, 2015, **71**, 3–8.

(21) O. V. Dolomanov, L. J. Bourhis, R. J. Gildea, J. A. K. Howard and H. Puschmann, *J. Appl. Crystallogr.*, 2009, **42**, 339–341.

(22) J. A. Ripmeester, G. D. Enright, C. I. Ratcliffe, K. A. Udachin and I. L. Moudrakovski, *Chem. Commun.*, **48**, 2006, 4986–4996.

(23) S. J. Dalgarno, P. K. Thallapally, L. J. Barbour and J. L. Atwood, *Chem. Soc. Rev.*, 2007, **36**, 236–245.

(24) G. Karotsis, S. Kennedy, S. J. Dalgarno and E. K. Brechin, *Chem. Commun.*, 2010, **46**, 3884–3886.

(25) R. McLellan, M. A. Palacios, C. M. Beavers, S. J. Teat, S. Piligkos, E. K. Brechin and S. J. Dalgarno, *Chem. – Eur. J.*, 2015, **21**, 2804–2812.

(26) S. Sanz, K. Ferreira, R. D. McIntosh, S. J. Dalgarno and E. K. Brechin, *Chem. Commun.*, 2011, **47**, 9042–9044.

(27) O. Nachtigall, M. Kusserow, R. Clérac, W. Wernsdorfer, M. Menzel, F. Renz, J. Mrozinski and J. Spandl, *Angew. Chem. Int. Ed.*, 2015, **54**, 10361–10364.

(28) Q.-F. Sun, S. Sato and M. Fujita, *Nat. Chem.*, 2012, **4**, 330–333.

(29) A.-J. Zhou, J.-D. Leng, J.-S. Hu and M.-L. Tong, *Dalton Trans.*, 2013, **42**, 9428–9431.

(30) Z.-M. Zhang, Y.-G. Li, S. Yao, E.-B. Wang, Y.-H. Wang and R. Clérac, *Angew. Chem. Int. Ed.*, 2009, **48**, 1581–1584.

(31) P. Yin, Z.-M. Zhang, H. Lv, T. Li, F. Haso, L. Hu, B. Zhang, J. Bacsa, Y. Wei, Y. Gao, Y. Hou, Y.-G. Li, C. L. Hill, E.-B. Wang and T. Liu, *Nat. Commun.*, 2015, **6**, 6475.

(32) Z.-M. Zhang, S. Yao, Y.-G. Li, R. Clérac, Y. Lu, Z.-M. Su and E.-B. Wang, *J. Am. Chem. Soc.*, 2009, **131**, 14600–14601.

(33) J. Yoon and E. I. Solomon, *Coord. Chem. Rev.*, 2007, **251**, 379–400.

(34) I. Dzyaloshinsky, *J. Phys. Chem. Solids*, 1958, **4**, 241–255.

(35) T. Moriya, *Phys. Rev. Lett.*, 1960, **4**, 228–230.

(36) T. Moriya, *Phys. Rev.*, 1960, **120**, 91–98.

(37) S. Ferrer, F. Lloret, E. Pardo, J. M. Clemente-Juan, M. Liu-González and S. García-Granda, *Inorg. Chem.*, 2012, **51**, 985–1001.

(38) C. G. Efthymiou, C. P. Raptopoulou, V. Psycharis, A. J. Tasiopoulos, A. Escuer, S. P. Perlepes and C. Papatriantafyllopoulou, *Polyhedron*, 2013, **64**, 30–37.

(39) N. Zamstein, A. Tarantul and B. Tsukerblat, *Inorg. Chem.*, 2007, **46**, 8851–8858.

(40) A. Abragam and B. Bleaney, *Electron Paramagnetic Resonance of Transition Ions*, Clarendon Press, Oxford, 1970.

(41) G. Karotsis, S. J. Teat, W. Wernsdorfer, S. Piligkos, S. J. Dalgarno and E. K. Brechin, *Angew. Chem. Int. Ed.*, 2009, **48**, 8285–8288.

(42) R. Schnalle and J. Schnack, *Int. Rev. Phys. Chem.*, 2010, **29**, 403–452.

(43) J. Jaklic and P. Prelovsek, *Phys. Rev. B*, 1994, **49**, 5065–5068.

(44) J. Schnack, J. Richter and R. Steinigeweg, *Phys. Rev. Res.*, 2020, **2**, 013186.

(45) N. A. G. Bandeira, O. Sadeghi, T. J. Woods, Y.-Z. Zhang, J. Schnack, K. Dunbar, M. Nyman and C. Bo, *J. Phys. Chem. A*, 2017, **121**, 1310–1318.

Chapter 5

Conclusions and future perspectives

5.1 Conclusions

The aim of this thesis was to synthesise novel polymetallic complexes supported by calix[*n*]arenes and explore their magnetic properties. A comprehensive study of the synthesis and characterisation of smaller 'building block' clusters with calix[*n*]arenes would then allow systematic understanding of their coordination requirements/behaviour, permitting modification of reaction conditions to access specific topologies.

Chapter 1 provided a mini-review of the TBC[4]-supported polymetallic clusters of paramagnetic ions known to date. Inspection of the metallic skeletons of these structures revealed common building blocks, the geometries of which were dependent on the identity of the metal ion. Hierarchal metal ion bonding preferences when in competitive reaction media were identified, as well as the current gaps in the TBC[4]/3*d* coordination literature (*viz.* Cr^{III}, $Fe^{II/III}$, Co^{II} or Ni^{II}).

Chapter 2 employed 2,2'-bis-*p*-*tert*-butylcalix[4]arene (BisTBC[4], H_8L), in which two TBC[4] moieties are tethered together directly *via* the methylene bridge, to build polymetallic clusters of 3*d* transition metal ions. This yielded five novel clusters containing Mn^{III}, Mn^{II} or Cu^{II} ions, doubling the existing 3*d* family of BisTBC[4]-supported clusters. Structure comparison allowed us to conclude that BisTBC[4] maintains the empirical binding preferences of the TBC[4] cavity - given access to both M^{III} and M^{II} ions, the cavity will favour M^{III} ions, coordinating M^{II} ions only in the absence of the former. Addition of co-ligands, adjustment of reaction conditions and variation of oxidation state sees the coordination of BisTBC[4] upheld, revealing the structure-directing nature of the ligand. This family of compounds displays dominant antiferromagnetic behaviour across all complexes, with DFT calculations used to explore the relationship between M-O-M/O-M-O-M angles and their respective magnetic exchange interactions.

Chapter 3 explored the coordination chemistry of *p*-*tert*-butylthiacalix[4]arene (H_4TC[4]A), whereby the sulfur atoms situated between the phenol groups provide double the number of coordination sites compared to the methylene-bridged counterpart, *p*-*tert*-butylcalix[4]arene (H_4TBC[4]). This afforded two novel Cu^{II} TC[4]A-supported complexes, including the highest nuclearity Cu^{II} TC[4]A-supported cluster to date. Combination of H_4TC[4]A with H_4TBC[4] and H_8TBC[8] afforded the first four hetero-calix clusters reported in literature, and gave rise to unique topologies not yet observed in homo-calix coordination chemistry. Magnetic measurements revealed antiferromagnetic exchange interactions across

the family, strong in the homo-calix Cu^{II} clusters and weaker in the hetero-calix clusters as a result of increased competitive exchange.

Chapter 4 focussed on H_4TBC[4], exploring the tendency for TBC[4]-supported clusters to exhibit significant spin-frustration. This led to the formation of six novel complexes. The prevalence of the tricapped trigonal prismatic topology across Cu^{II}, Mn^{III}, Gd^{III} and Na^{I} chemistry highlights the dominant structure directing effects of the ligand, and suggests that many more homo- and heterometallic complexes conforming to this shape may await discovery. Introducing Gd^{III} saw breaking of the established TBC[4] binding rules for the first time. The magnetic exchange interactions across the complexes, whilst all ferrimagnetic in nature, were markedly different as a result of the structural changes observed. Employing solvothermal techniques gave rise to two novel, high-symmetry Fe^{III} complexes. These represent the first homometallic Fe complexes with TBC[4] and the highest nuclearity of any 3*d* TBC[4] complexes to date. The magnetic skeletons of both resemble Archimedean/Keplerate solids resulting in strong antiferromagnetic exchange interactions and significant spin frustration.

5.2 Future perspectives

Archimedean polyhedra offer potentially exciting magnetic properties through their high degree of spin frustration. For example, such frustrated molecule-based materials may possess an enhanced magnetocaloric effect, thus have potential application in cryogenic refrigeration as a replacement for helium (both ^{3}He and ^{4}He), a finite, non-renewable resource.[1] Given the formation of several Archimedean polyhedra presented in this work, the high temperature and pressure synthesis and characterisation of further members of this family should be targeted.

The formation of the stellated [M_{18}] cuboctahedron with octahedral Fe^{III} suggests that analogous structures with V^{III} and Cr^{III} may be accessible, as seen in the {$Mo_{72}M_{30}$} family of POMs[2], alongside diamagnetic Sc^{III}, Al^{III} and Ga^{III} versions. If the [V^{III}_{18}] cage is accessible, this further suggests that partial/full oxidation of that cage may give rise to V^{IV} or V^{V} containing family members with different structure types. This, in turn, points towards the synthesis of an almost unprecedented number of heterometallic and heterovalent 3*d* clusters. These would represent core-shell type molecules in which the different metals/valencies and the

interactions between them would proffer multifunctionality and access to applications beyond magnetism.

The ability of TBC[4] to form the square pyramidal [M_5TBC[4]] metalloligand also permits targeting of other Archimedean solids containing square faces (Figure 5.1). These include, for example, the truncated octahedron, truncated cuboctahedron, rhombicuboctahedron and snub cube. Synthesis of these clusters will be highly dependent on metal:ligand ratios and "control" over the internal oxide/hydroxide core. Thus, they will require methodical investigation of reaction conditions (solution basicity, metal oxidation state, temperature, pressure and solvent). Extension of the same chemistry to bis-*p*-*tert*-butylcalix[4]arenes should therefore also be possible. The ability to covalently link calix[4]arenes allows the introduction of two square pyramidal [M_5TBC[4]] units in one ligand, *i.e.* a [M_{10}(TBC[4])$_2$] moiety, whose spatial orientation is controlled by the length and rigidity of the spacer.

For example, use of H_8L in which the H_4TBC[4] moieties are directly linked at the methylene bridge will produce a [M_8(TBC[4])$_2$] building block which will self-assemble polyhedra containing edge-sharing square faces, an example of which is the rhombicuboctahedron. Introducing a longer spacer will self-assemble polyhedra in which the square faces are linked by a linear bridge, for example a truncated octahedron.

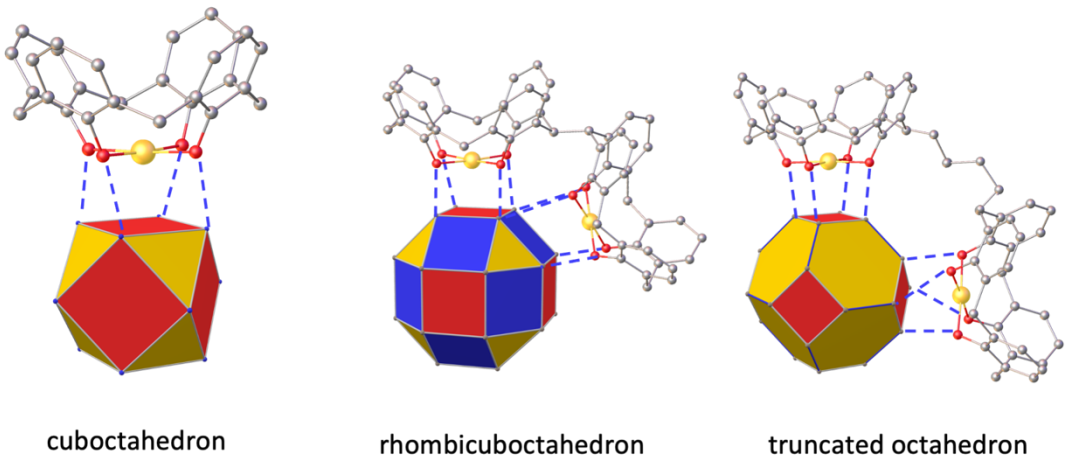

Figure 5.1 Representation of TBC[4] (left), L (middle) and butyl-tethered L (right) bonding to square faces of cuboctahedron, rhombicuboctahedron and truncated octahedron geometries.

This work details the synthesis of numerous calix[*n*]arene-supported molecular magnets, but it is clear the field is far from saturated. Beyond solvothermal and solvochemical employment which is still in its early stages of exploration, further probing of mixed-calix assemblies or else synthetic modification of the 'basic' calix[*n*]arene units at the 'upper' rim, 'lower' rim and/or methylene bridge offers vast opportunities to study the magneto-structural relationship of calix[*n*]arene-based systems. Rigorous understanding and control of such systems promises a breadth of novel complexes with fascinating magnetic properties.

5.3 References

(1) J.-L. Liu, Y.-C. Chen, F.-S. Guo and M.-L. Tong, *Coord. Chem. Rev.,* 2014, **281**, 26-49.

(2) T. Kihara, H. Nojiri, Y. Narumi, Y. Oshima, K. Kindo, C. Heesing, J. Schnack and A. Müller, *Phys. Rev. B,* 2019, **99**, 064430.

Supplementary Information

Table S2.1- Crystallographic information for **15** and **16**.

Compound	**15**	**16**
Formula	$C_{104.5}H_{146.62}Mn_4N_{4.25}O_{19.28}$	$C_{108}H_{147}Mn_4N_7O_{15}$
$D_{calc.}$/ g cm^{-3}	1.247	1.241
μ / mm^{-1}	4.327	0.657
Formula Weight	1986.48	2003.08
Colour	dark violet	purple
Shape	plate	plate
Size / mm^3	0.17x0.13x0.08	0.1x0.05x0.01
T / K	100(2)	100(2)
Crystal System	triclinic	monoclinic
Space Group	P-1	$P2_1/m$
a / Å	13.5024(3)	13.8645(6)
b / Å	16.4838(3)	23.1636(9)
c / Å	25.1040(4)	1748.75(7)
α / °	78.2540(10)	90
β / °	76.246(2)	107.315(2)
γ / °	82.127(2)	90
V / Å^3	5290.46(18)	5361.6(4)
Z	2	2
Z'	1	0.5
Wavelength / Å	1.54184	0.7749
Radiation type	Cu K_α	Synchrotron
θ_{min} / °	2.750	2.333
θ_{max} / °	70.915	25.516
Measured Refl's.	196638	7904
Indep't Refl's	35325	7904
Refl's used I≥2σ(I)	15957	6691
R_{int}	0.0706	0.0476
Parameters	1396	593
Restraints	29	11
Largest Peak	1.105	1.242
Deepest Hole	-0.939	-1.065
GooF	1.029	1.038
wR_2 (all data) (wR_2)	0.2330	0.2279
wR_2	0.2186	0.2131
R_1 (all data)	0.0878	0.0973
R_1	0.0755	0.0820

Table S2.2- Crystallographic information for **17** and **19**.

Compound	**17**	**19**
Formula	$C_{220.50}H_{298.50}Mn_7N_{11.50}O_{34.50}$	$C_{200}H_{270}Mn_{10}N_8O_{32}$
$D_{calc.}$/ g cm^{-3}	1.237	1.151
μ / mm^{-1}	0.429	4.960
Formula Weight	4046.77	3847.62
Colour	black	blue
Shape	block	block
Size / mm^3	0.046x0.046x0.03	0.24x0.2x0.12
T / K	100.0	100.0
Crystal System	triclinic	monoclinic
Space Group	P-1	$P2_1/n$
a / Å	21.3557(15)	22.322(6)
b / Å	22.1933(16)	18.903(5)
c / Å	23.1371(17)	27.502(7)
α / °	97.5670(10)	90
β / °	90.1080(10)	106.948(16)
γ / °	91.1710(10)	90
V / Å^3	10868.0(14)	11100.6
Z	2	2
Z'	1	0.5
Wavelength / Å	0.6889	1.54178
Radiation type	Synchrotron	CuK_α
θ_{min} / °	0.861	2.253
θ_{max} / °	15.364	73.163
Measured Refl's.	47550	157579
Indep't Refl's	10327	21932
Refl's used I≥2σ(I)	7818	14106
R_{int}	0.0668	0.1384
Parameters	1937	990
Restraints	4622	19
Largest Peak	1.161	1.869
Deepest Hole	-0.380	-1.343
GooF	1.044	1.406
wR_2 (all data) (wR_2)	0.2914	0.3958
wR_2	0.2713	0.3624
R_1 (all data)	0.1119	0.1627
R_1	0.0955	0.1275

Table S2.3- Crystallographic information for **25**.

Compound	**25**
Formula	$C_{343}H_{510.50}Cu_{16}N_{25.50}O_{68}$
$D_{calc.}$/ g cm^{-3}	1.300
μ / mm^{-1}	1.251
Formula Weight	7095.88
Colour	black
Shape	rod
Size / mm^3	0.19x0.03x0.03
T / K	100(2)
Crystal System	triclinic
Space Group	*P*-1
a / Å	21.4369(9)
b / Å	21.9078(9)
c / Å	22.0660(9)
α / °	105.596(3)
β / °	111.468(2)
γ / °	95.527(3)
V / Å^3	9067.1(7)
Z	1
Z'	0.5
Wavelength / Å	0.7749
Radiation type	Synchrotron
θ_{min} / °	2.156
θ_{max} / °	23.892
Measured Refl's.	56519
Indep't Refl's	21580
Refl's used I≥2σ(I)	14859
R_{int}	0.0705
Parameters	1988
Restraints	512
Largest Peak	1.691
Deepest Hole	-0.626
GooF	1.052
wR_2 (all data) (wR_2)	0.1551
wR_2	0.1416
R_1 (all data)	0.0857
R_1	0.0566

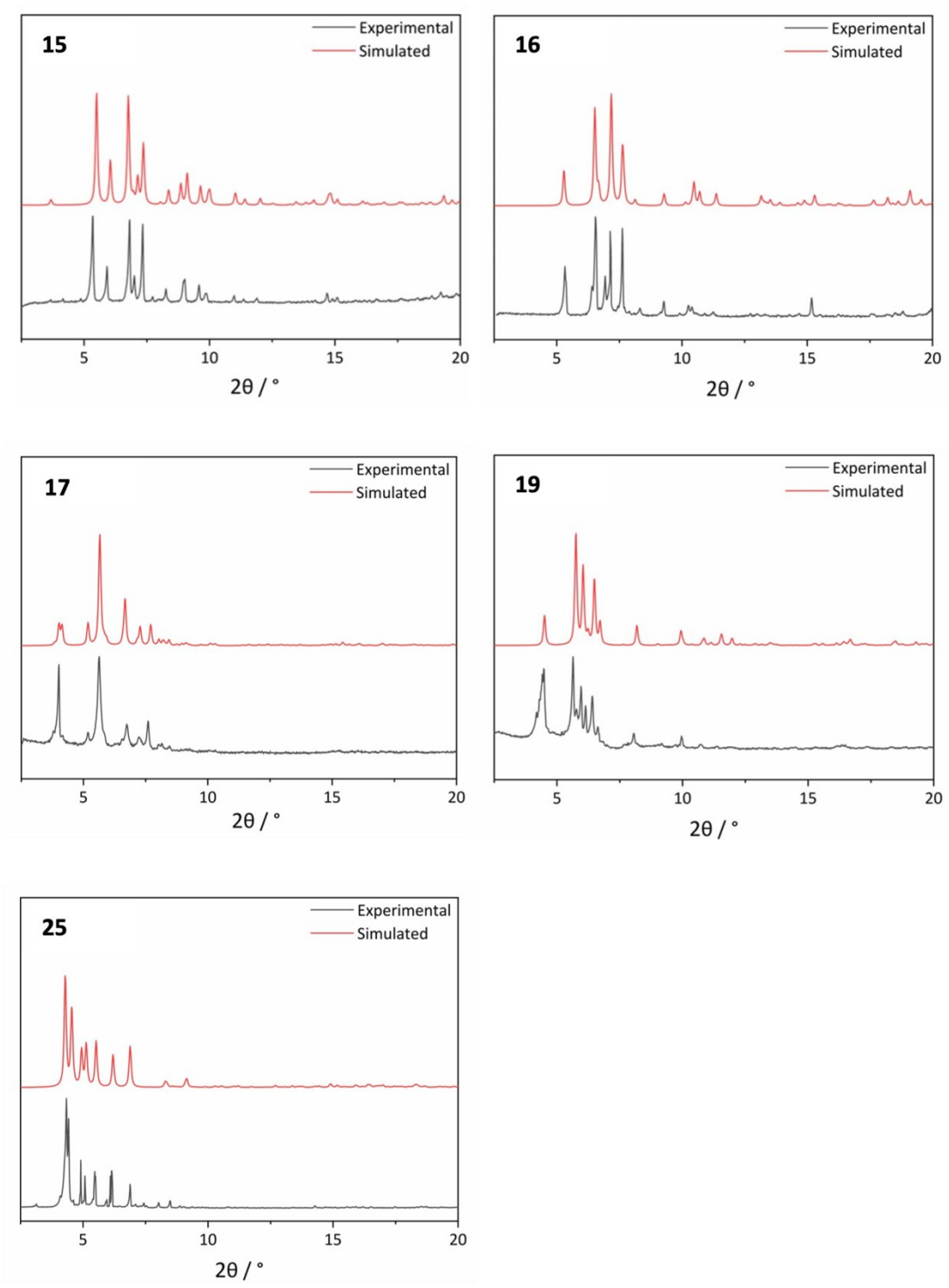

Figure S2.1- Powder diffraction data (black) shown against simulated data (red) for **15**-**17**, **19** and **25**.

Table S2.4- Pertinent bond lengths and bond angles and calculated metal BVS values for **15**.

Mn1 / Å		**Mn2 / Å**	
Mn1-O1 (OR_L)	1.956(3)	Mn2-O1 ($OR_{L)}$	2.163(2)
Mn1-O2 (OR_L)	1.916(3)	Mn2-O5 ($OR_{L)}$	2.251(2)
Mn1-O3 (OR_L)	1.901(3)	Mn2-O2A ($O_{acetate}$)	2.166(3)
Mn1-O4 (OR_L)	1.994(3)	Mn2-O1H (OH)	2.149(3)
Mn1-O1A ($O_{acetate}$)	2.094(3)	Mn2-O1D (O_{dmf})	2.160(3)
-	-	Mn2-O1M (O_{MeOH})	2.256(3)
BVS(Mn1) = 2.865		BVS(Mn2) = 2.045	
Mn3 / Å		**Mn4 / Å**	
Mn3-O4 (OR_L)	2.193(3)	Mn4-O5 (OR_L)	1.978(2)
Mn3-O8 (OR_L)	2.215(2)	Mn4-O6 (OR_L)	1.935(2)
Mn3-O1H (OH)	2.156(2)	Mn4-O7 (OR_L)	1.940(3)
Mn3-O2D (O_{dmf})	2.138(3)	Mn4-O8 (OR_L)	1.960(2)
Mn3-O2M (O_{MeOH})	2.264(3)	Mn4-O1H (OH)	2.205(2)
Mn3-O3M (O_{MeOH})	2.248(3)	Mn4-O3D (O_{dmf})	2.272(3)
BVS(Mn3) = 1.984		BVS(Mn4) = 2.923	
(Mn-O-Mn) bond angles / °			
Mn1-O1-Mn2	117.21(13)	Mn2-O1H-Mn4	98.13(10)
Mn1-O4-Mn3	120.87(12)	Mn3-O8-Mn4	103.76(10)
Mn2-O5-Mn4	101.95(10)	Mn3-O1H-Mn4	97.89(9)

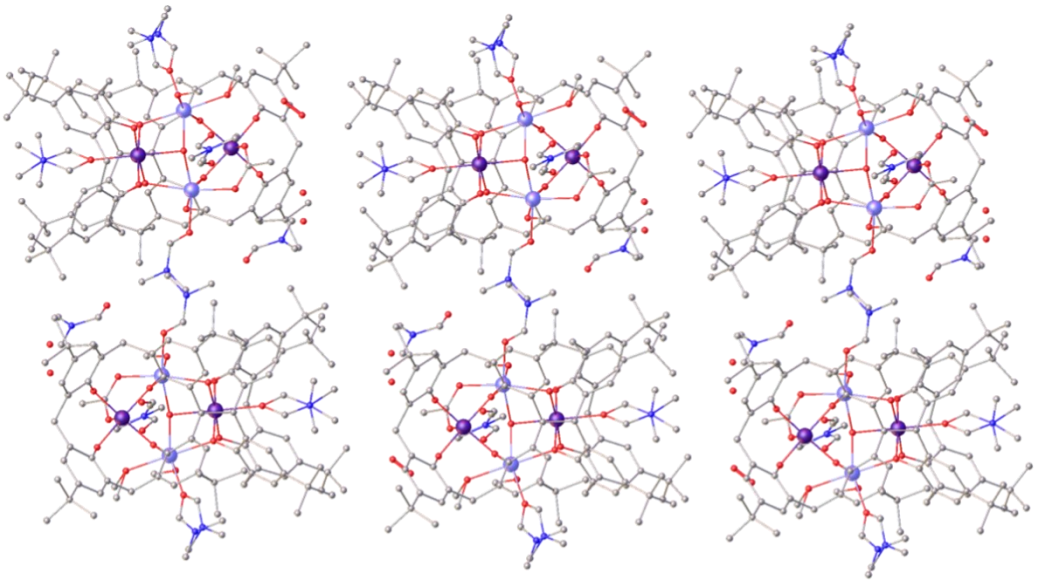

Figure S2.2- Extended structure of **15** shown down the *a*-axis. Colour code: Mn^{III} – dark purple, Mn^{II} – light purple, N – dark blue, C – grey, O – red. H atoms omitted for clarity.

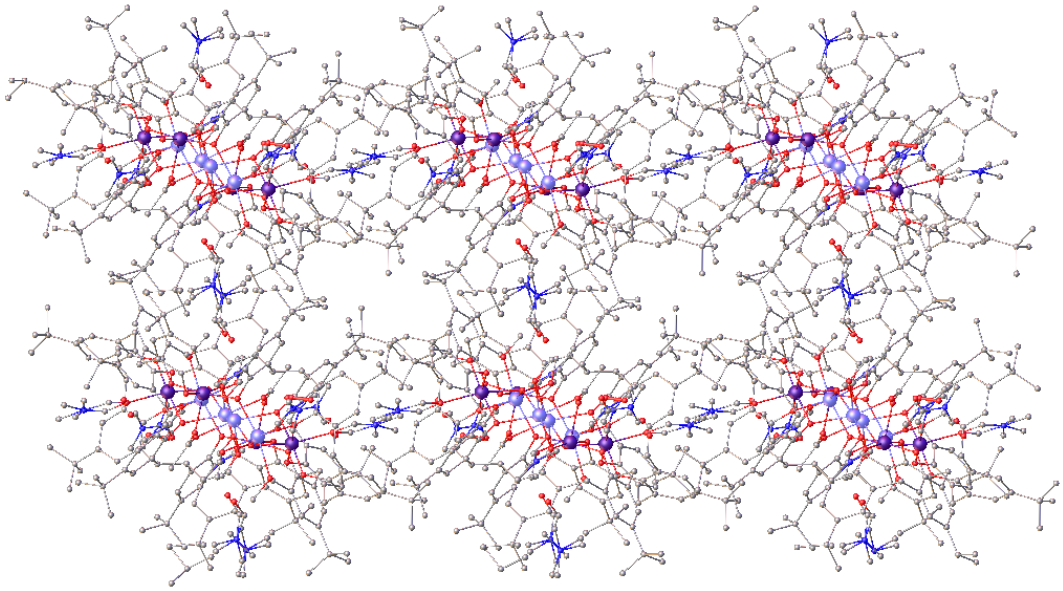

Figure S2.3- Extended structure of **15** shown down the *c*-axis. Colour code: Mn^{III} – dark purple, Mn^{II} – light purple, N – dark blue, C – grey, O – red. H atoms omitted for clarity.

Table S2.5- Pertinent bond lengths and bond angles and calculated metal BVS values for **16**.

Mn1 / Å		**Mn2 / Å**	
Mn1-O1 (OR_L)	1.978(5)	Mn2-O3 (OR_L)	1.949(5)
Mn1-O1' (OR_L)	1.978(5)	Mn2-O3' (OR_L)	1.949(5)
Mn1-O2 (OR_L)	1.898(5)	Mn2-O4 (OR_L)	1.912(5)
Mn1-O2' (OR_L)	1.898(5)	Mn2-O4' (OR_L)	1.912(5)
Mn1-O6 ($O_{Me\text{-}deaH}$)	2.095(10)	Mn2-O5 (OMe)	2.050(8)
BVS(Mn1) = 2.891		BVS(Mn2) = 2.983	
Mn3 / Å			
Mn3-O1 (OR_L)	2.171(4)	Mn3-O8* (H_2O)	2.251(10)
Mn3-O3 (OR_L)	2.406(5)	Mn3-O9* (H_2O)	2.226(11)
Mn3-O5 (OMe)	2.241(5)	Mn3-O10 (O_{dmf})	2.202(5)
Mn3-O6* ($O_{Me\text{-}deaH}$)	2.349(10)	-	-
Mn3-O7* ($O_{Me\text{-}deaH}$)	2.234(11)	-	-
Mn3-N1* ($N_{Me\text{-}deaH}$)	2.534(13)	BVS(Mn3) = 1.766 – 1.849	
(Mn-O-Mn) bond angles / °			
Mn1-O1-Mn3	109.8(2)	Mn2-O5-Mn3	101.3(3)
Mn1-O6-Mn3	99.5(4)	Mn2-O5-Mn3'	101.3(3)
Mn2-O3-Mn3	98.8(2)	-	-

*Denotes atoms that are fixed at partial occupancy

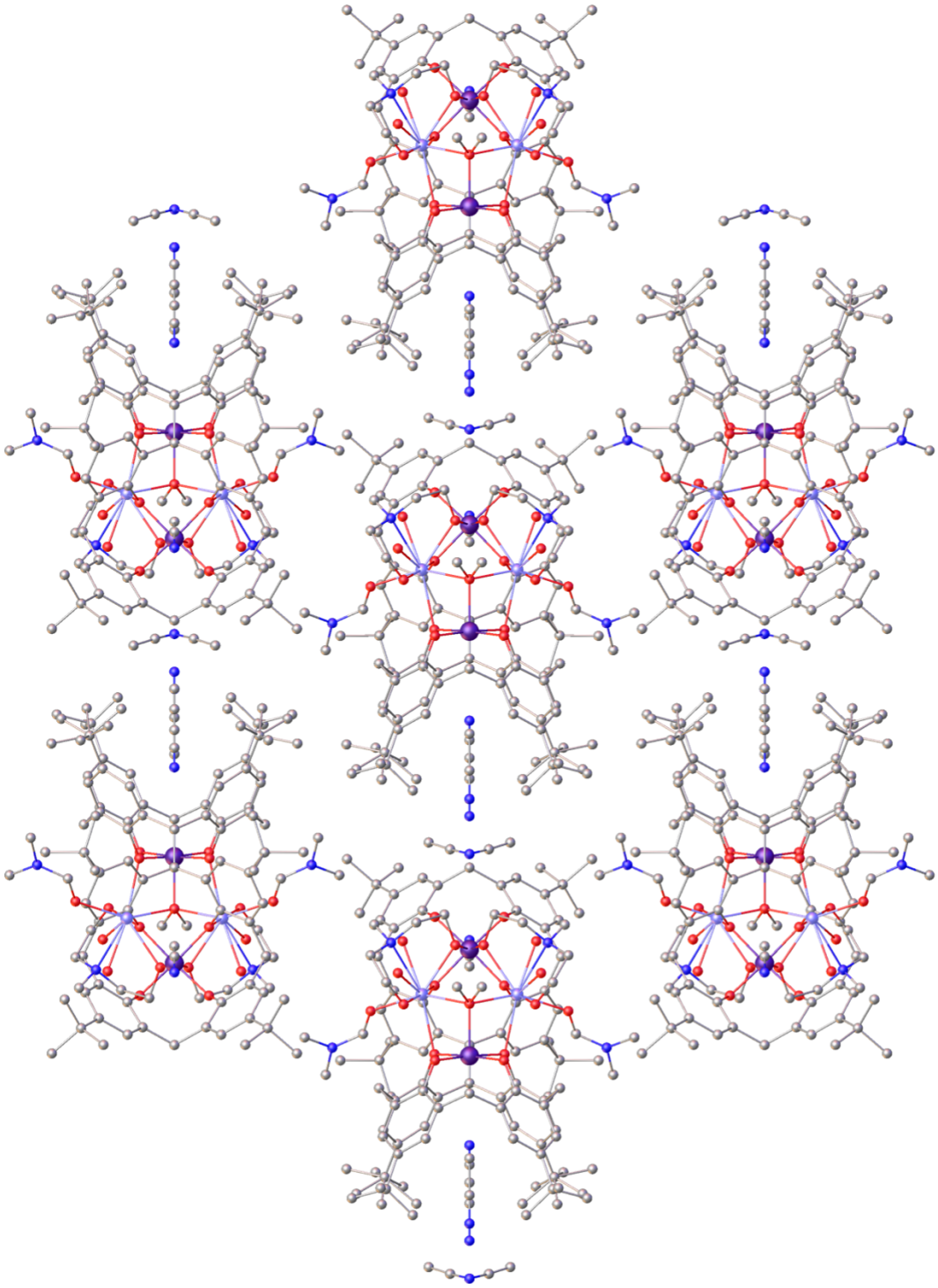

Figure S2.4- Extended structure of **16** shown down the *a*-axis. Colour code: Mn^{III} – dark purple, Mn^{II} – light purple, N – dark blue, C – grey, O – red. H atoms omitted for clarity.

Table S2.6- Pertinent bond lengths and bond angles and calculated metal BVS values for **17**.

Mn1 / Å		**Mn2 / Å**	
Mn1-O1 (OR_L)	1.944(10)	Mn2-O2 (OR_L)	2.327(9)
Mn1-O2 (OR_L)	1.972(10)	Mn2-O7 (OR_L)	2.158(10)
Mn1-O3 (OR_L)	1.965(10)	Mn2-O17 (OH)	2.169(9)
Mn1-O4 (OR_L)	1.935(11)	Mn2-O20 (O_{pdmH})	2.178(9)
Mn1-O17 (OH)	2.172(8)	Mn2-O25 (O_{MeOH})	2.275(12)
-	-	Mn2-O1B (O_{dmf})	2.156(12)
BVS(Mn1) = 2.926		BVS(Mn2) = 1.955	
Mn3 / Å		**Mn4 / Å**	
Mn3-O8 (OR_L)	2.097(11)	Mn4-O5 (OR_L)	1.931(9)
Mn3-O17 (OH)	2.142(9)	Mn4-O6 (OR_L)	1.931(9)
Mn3-O22 (O_{pdmH})	2.188(9)	Mn4-O7 (OR_L)	1.939(9)
Mn3-O24 (O_{MeOH})	2.206(12)	Mn4-O8 (OR_L)	1.962(9)
Mn3-O1A (O_{dmf})	2.246(11)	Mn4-O18 (O)	2.175(10)
BVS(Mn3) = 1.780		BVS(Mn4) = 3.016	
Mn5 / Å		**Mn6 / Å**	
Mn5-O6 (OR_L)	2.295(11)	Mn6-O5 (OR_L)	2.281(11)
Mn5-O11 (OR_L)	2.257(11)	Mn6-O12 (OR_L)	2.179(12)
Mn5-O18 (O)	1.895(8)	Mn6-O18 (O)	1.889(8)
Mn5-O19 (O)	1.912(9)	Mn6-O19 (O)	1.928(9)
Mn5-O20 (O_{pdmH})	1.899(9)	Mn6-O22 (O_{pdmH})	1.943(9)
Mn5-N1 (N_{pdmH})	2.137(13)	Mn6-N2 (N_{pdmH})	2.108(13)
BVS(Mn5) = 2.985		BVS(Mn6) = 2.998	
Mn7 / Å		-	
Mn7-O9 (OR_L)	1.935(9)	-	-
Mn7-O10 (OR_L)	1.896(9)	-	-
Mn7-O11 (OR_L)	1.965(8)	-	-
Mn7-O12 (OR_L)	1.969(9)	-	-
Mn7-O19 (O)	2.10(1)	-	-
BVS(Mn7) = 2.858		-	-
(Mn-O-Mn) bond angles / °			
Mn1-O2-Mn2	101.2(4)	Mn4-O18-Mn5	98.6(4)

Mn1-O17-Mn2	100.2(4)	Mn4-O18-Mn6	100.5(4)
Mn1-O17-Mn3	105.9(4)	Mn4-O5-Mn6	95.6(4)
Mn2-O17-Mn3	124.9(5)	Mn5-O18-Mn6	96.6(4)
Mn2-O7-Mn4	121.0(5)	Mn5-O19-Mn6	94.7(4)
Mn2-O20-Mn5	121.0(5)	Mn5-O19-Mn7	101.0(4)
Mn3-O8-Mn4	113.7(5)	Mn5-O11-Mn7	94.2(4)
Mn3-O22-Mn6	112.5(5)	Mn6-O19-Mn7	101.6(5)
Mn4-O6-Mn5	93.6(4)	Mn6-O12-Mn7	97.6(5)

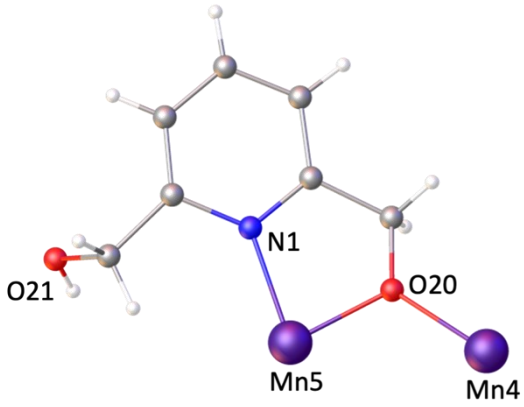

Figure S2.5- The bonding mode of pdmH in **17**. Colour code: Mn^{III} – dark purple, N – dark blue, C – grey, O – red, H – white.

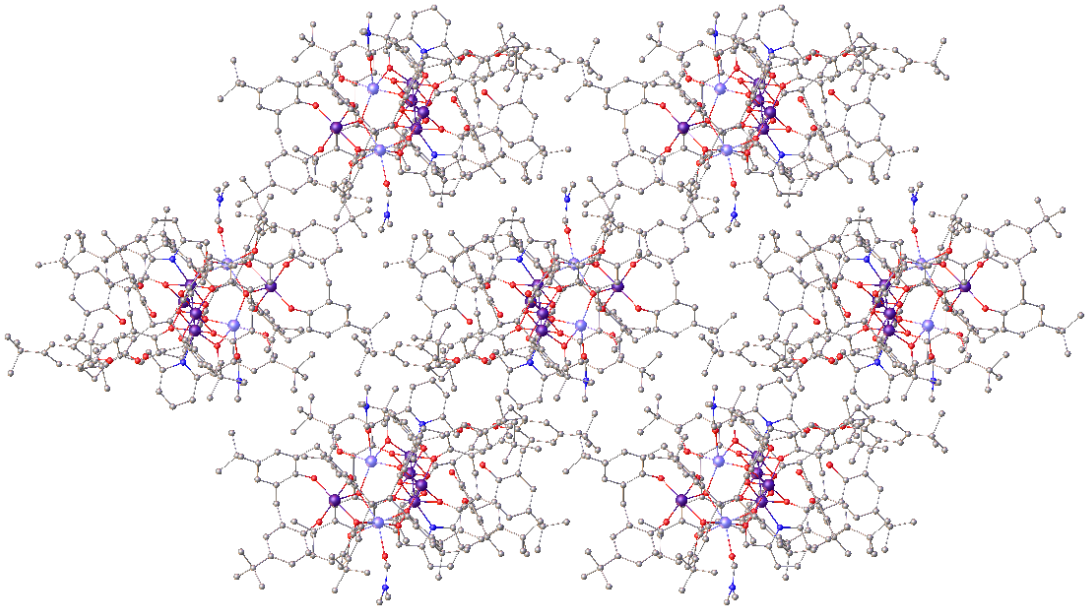

Figure S2.6- Extended structure of **17** shown down the *b*-axis. Colour code: Mn^{III} – dark purple, Mn^{II} – light purple, N – dark blue, C – grey, O – red. H atoms omitted for clarity.

Table S2.7- Pertinent bond lengths and bond angles and calculated metal BVS values for **19**.

Mn1 / Å		**Mn2 / Å**	
Mn1-O1 (OR_L)	1.928(6)	Mn2-O5 (OR_L)	1.925(5)
Mn1-O2 (OR_L)	1.910(5)	Mn2-O6 (OR_L)	1.912(4)
Mn1-O3 (OR_L)	1.925(6)	Mn2-O7 (OR_L)	1.924(5)
Mn1-O4 (OR_L)	1.943(5)	Mn2-O8 (OR_L)	1.934(4)
Mn1-O13 (OH)	2.139(6)	Mn2-O14 (OH)	2.101(4)
-	-	Mn2-N3 (N_{dmf})	2.336(8)
BVS(Mn1) = 2.911		BVS(Mn2) = 3.228	
Mn3 / Å		**Mn4 / Å**	
Mn3-O8 (OR_L)	2.104(4)	Mn4-O4 (OR_L)	2.424(7)
Mn3-O11 (O_{dmf})	2.11(1)	Mn4-O5 (OR_L)	2.114(4)
Mn3-O13 (OH)	2.213(6)	Mn4-O12 (O_{dmf})	2.16(1)
Mn3-O15 (O_{MeOH})	2.199(8)	Mn4-O13 (OH)	2.214(5)
Mn3-O16 (OH)	2.220(6)	Mn4-O17 (OH)	2.262(6)
Mn3-O1 (OR_L)	2.577(7)	Mn4-O18 (O_{MeOH})	2.219(8)
BVS(Mn3) = 1.931		BVS(Mn4) = 1.876	
Mn5 / Å		**-**	
Mn5-O6 (OR_L)	2.272(4)	-	-
Mn5-O7’ (OR_L)	2.272(4)	-	-
Mn5-O14 (OH)	1.997(5)	-	-
Mn5-O14’ (OH)	1.997(5)	-	-
Mn5-O16 (OH)	2.320(5)	-	-
Mn5-O17 (OH)	2.290(6)	-	-
BVS(Mn5) = 2.184		-	-
(Mn-O-Mn) bond angles / °			
Mn1-O1-Mn3	96.6(2)	Mn2-O7-Mn5’	97.6(2)
Mn1-O13-Mn3	102.3(2)	Mn2-O14-Mn5’	101.1(2)
Mn1-O4-Mn4	98.8(2)	Mn3-O13-Mn4	128.4(3)

Mn1-O13-Mn4	99.8(2)	Mn3-O16-Mn5’	104.0(2)
Mn2-O8-Mn3	113.5(2)	Mn4-O17-Mn5	107.5(2)
Mn2-O5-Mn4	118.6(2)	Mn5-O14-Mn5’	97.7(2)
Mn2-O6-Mn5	97.3(2)	Mn5-O14’-Mn5’	97.7(2)
Mn2-O14-Mn5	100.6(2)	-	-

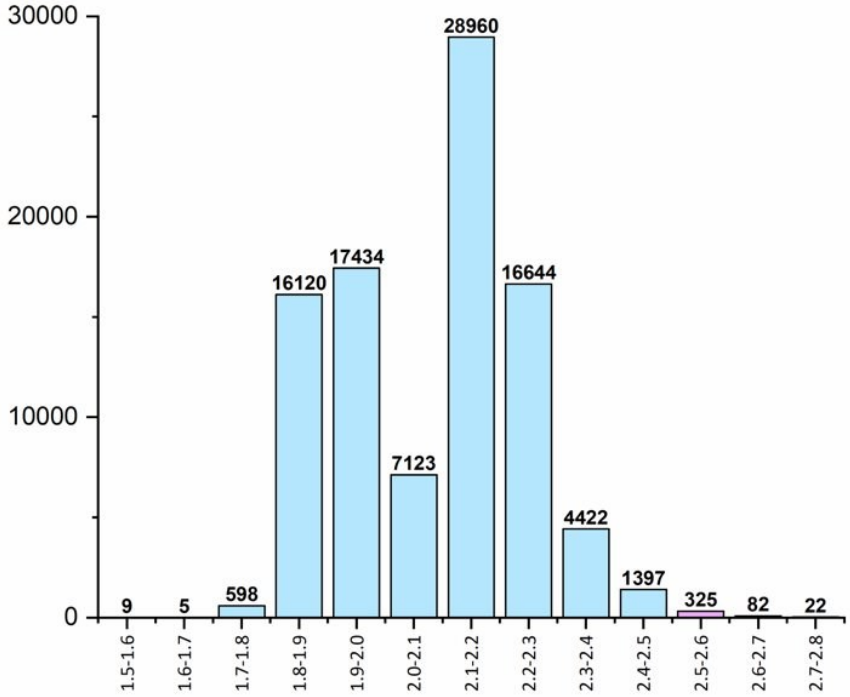

Figure S2.7- A histogram showing the variation in Mn-O bond lengths in the CSD. The purple bar denotes the range where the Mn3···O1 distance in complex **19** lies.

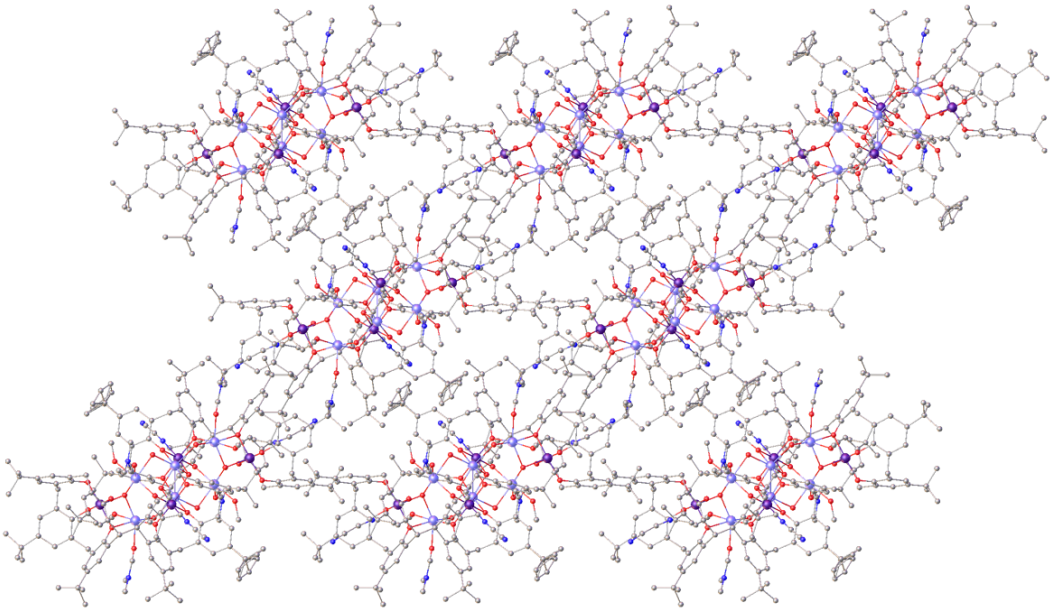

Figure S2.8- Extended structure of **19** shown down the *b*-axis. Colour code: Mn^{III} – dark purple, Mn^{II} – light purple, N – dark blue, C – grey, O – red. H atoms omitted for clarity.

Table S2.8- Pertinent bond lengths and bond angles for **25**.

Cu1 / Å		**Cu2 / Å**	
Cu1-O1 (OR_L)	1.958(3)	Cu2-O5 (OR_L)	1.979(4)
Cu1-O2 (OR_L)	1.943(4)	Cu2-O6 (OR_L)	1.952(3)
Cu1-O3 (OR_L)	1.960(3)	Cu2-O7 (OR_L)	1.971(4)
Cu1-O4 (OR_L)	1.932(4)	Cu2-O8 (OR_L)	1.907(4)
Cu3 / Å		**Cu4 / Å**	
Cu3-O1 (OR_L)	1.967(4)	Cu4-O4 (OR_L)	1.957(4)
Cu3-O8 (OR_L)	2.173(4)	Cu4-O5 (OR_L)	2.040(4)
Cu3-O9 (OH)	1.969(4)	Cu4-O9 (OH)	1.943(4)
Cu3-O12 (O_{NO3})	1.977(4)	Cu4-O11 (O_{NO3})	2.266(4)
Cu3-O18 ($O_{dmf)}$	1.970(4)	Cu4-O14 ($O_{Me\text{-}dea}$)	1.922(4)
Cu5 / Å		**Cu6 / Å**	
Cu5-O3 (OR_L)	1.979(4)	Cu6-O2 (OR_L)	1.972(4)
Cu5-O7 (OR_L)	1.964(4)	Cu6-O6 (OR_L)	1.964(4)
Cu5-O10 (OH)	1.959(4)	Cu6-O10 (OH)	1.939(3)
Cu5-O19 (O_{H2O})	2.269(4)	Cu6-O17 ($O_{Me\text{-}dea}$)	1.917(4)
Cu5-O20 (O_{dmf})	1.950(4)	-	-
Cu7 / Å		**Cu8 / Å**	
Cu7-O11 (O_{NO3})	1.953(4)	Cu8-O13 (OH)	1.895(4)
Cu7-O14 ($O_{Me\text{-}dea}$)	1.901(4)	Cu8-O16 ($O_{Me\text{-}dea}$)	1.914(4)
Cu7-O15 ($O_{Me\text{-}dea}$)	2.335(5)	Cu8-O17 ($O_{Me\text{-}dea}$)	1.897(4)
Cu7-O16 ($O_{Me\text{-}dea}$)	1.944(4)	Cu8-N2 ($N_{Me\text{-}dea}$)	1.975(5)
Cu7-N1 ($N_{Me\text{-}dea}$)	2.047(6)	-	-
(Cu-O-Cu) bond angles / °			
Cu1-O1-Cu3	105.27(16)	Cu2-O6-Cu6	108.71(18)
Cu1-O4-Cu4	112.0(2)	Cu3-O9-Cu4	125.73(19)
Cu1-O3-Cu5	120.677	Cu4-O11-Cu7	96.17(18)
Cu1-O2-Cu6	120.482	Cu4-O14-Cu7	110.8(2)
Cu2-O8-Cu3	118.74(17)	Cu5-O10-Cu6	107.12(17)
Cu2-O5-Cu4	131.5(2)	Cu6-O17-Cu8	108.02(18)
Cu2-O7-Cu5	111.47(17)	Cu7-O16-Cu8	114.80(18)

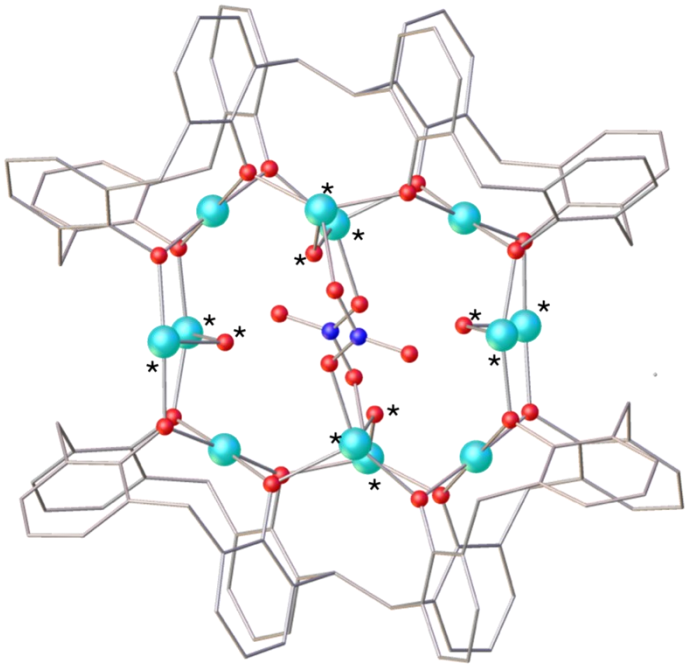

Figure S2.9- The $[Cu_{12}]$ tetracapped square prism in **25**, highlighting the coordination of the OH^-, L^{8-} and NO_3^- ions. The * denotes the atoms in the $[Cu_8(OH)_4]$ central unit, as discussed in text. Colour code: Cu^{II} – turquoise, N – dark blue, C – grey, O – red.

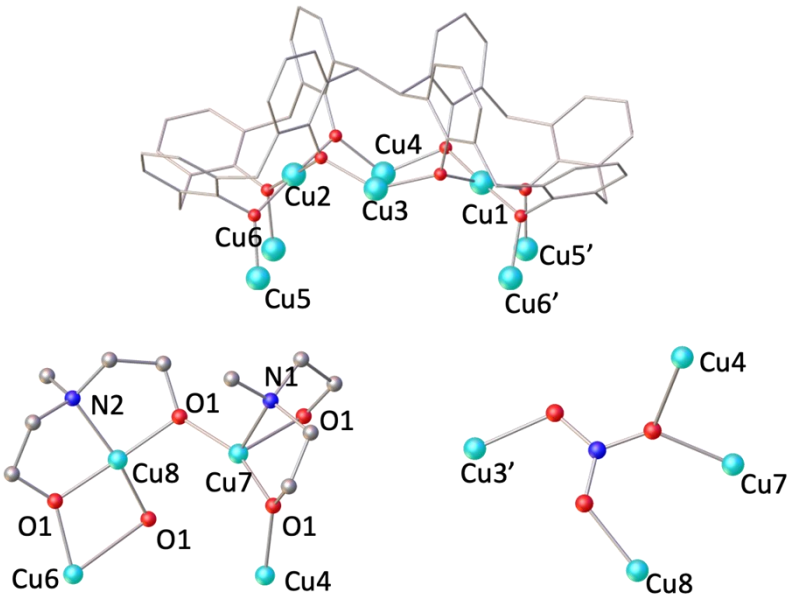

Figure S2.10- The bonding modes of L (top), Me-dea (bottom left) and NO_3 (bottom right) in **25**. Colour code: Cu^{II} – turquoise, N – dark blue, C – grey, O – red.

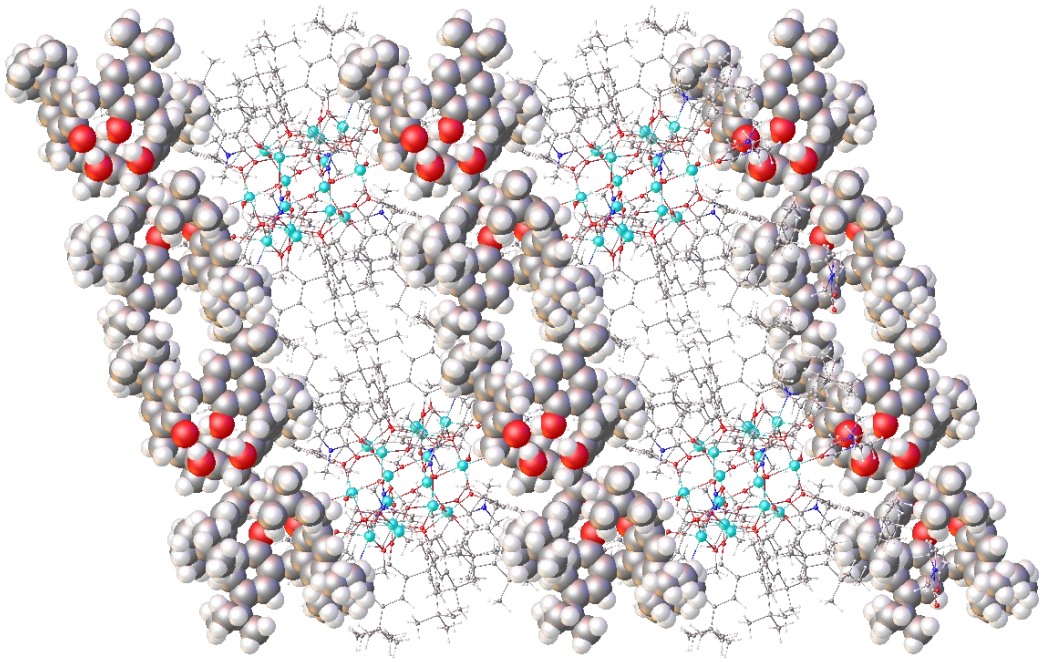

Figure S2.11- Extended structure of **25** shown down the *a*-axis, highlighting the connection between the cluster (ball and stick) and the H_6L^{2-} counter ions (space fill). Colour code: Cu^{II} – turquoise, N – dark blue, C – grey, O – red, H – white.

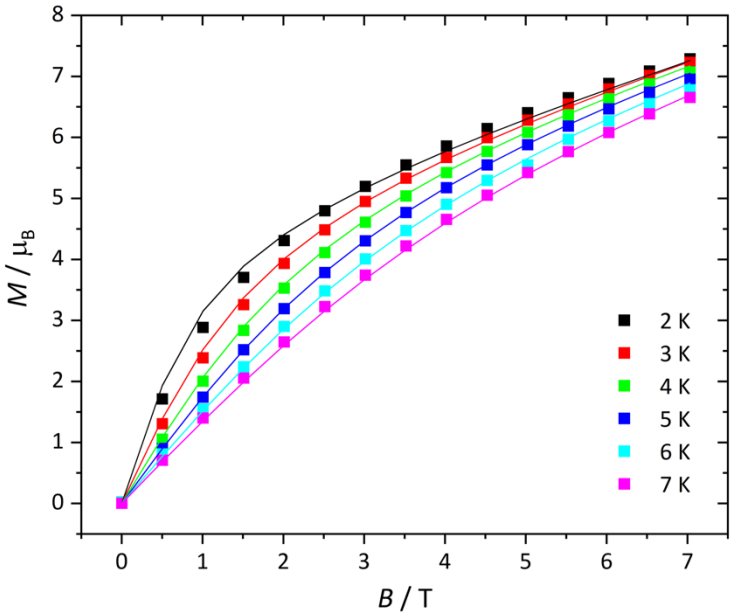

Figure S2.12- Variable-temperature-variable-field magnetisation measurements of **15** measured between *T* = 2-7 K and *B* = 0-7 T. Solids lines represent the fitting of the experimental data. See main text for details.

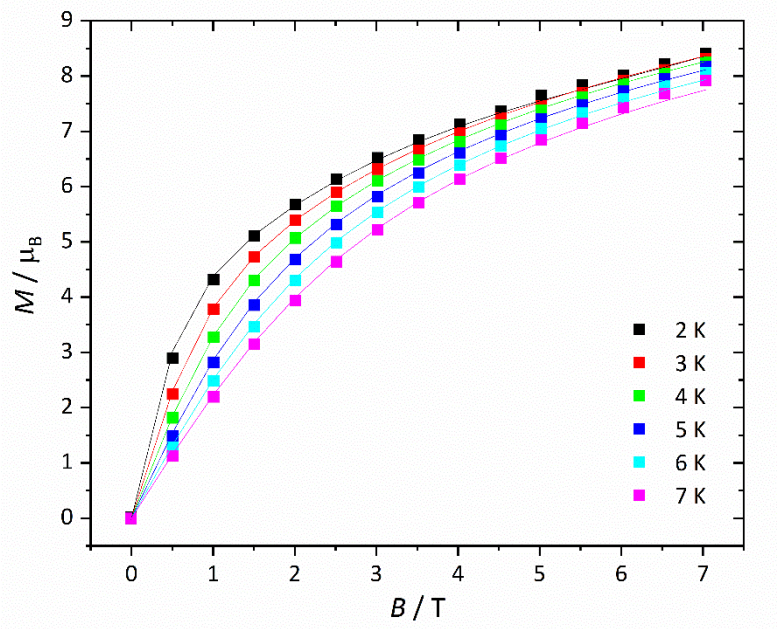

Figure S2.13- Variable-temperature-variable-field magnetisation measurements of **16** measured between *T* = 2-7 K and *B* = 0-7 T. Solids lines represent the fitting of the experimental data. See main text for details.

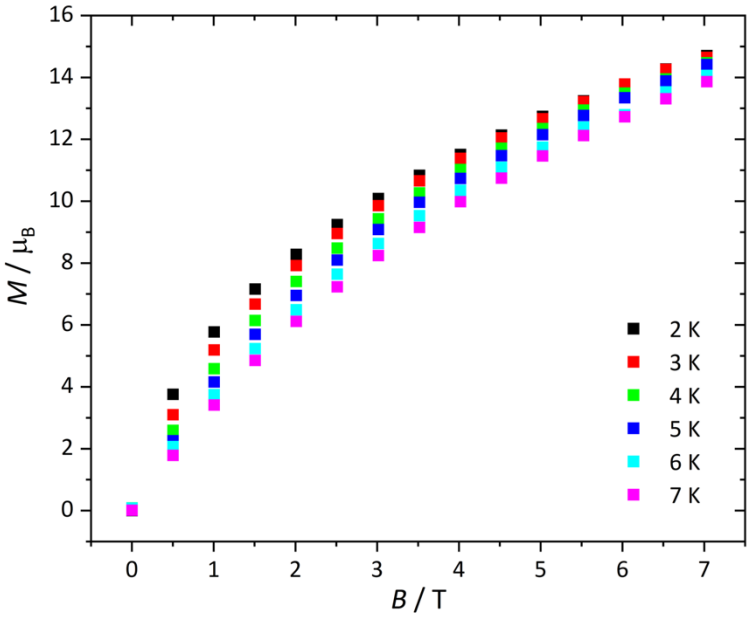

Figure S2.14- Variable-temperature-variable-field magnetisation measurements of **17** measured between T = 2-7 K and B = 0-7 T.

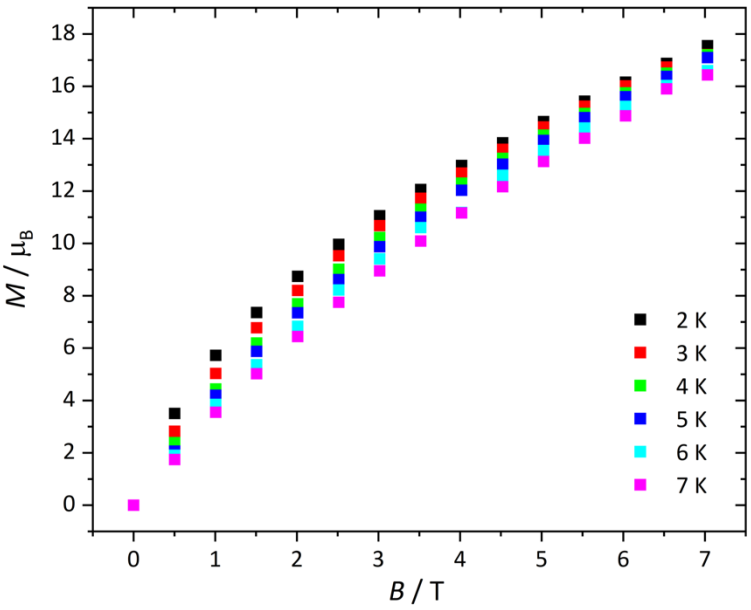

Figure S2.15- Variable-temperature-variable-field magnetisation measurements of **19** measured between T = 2-7 K and B = 0-7 T.

$$E_{HS} = -J_1[\hat{S}_1 \cdot \hat{S}_2] - J_2[\hat{S}_1 \cdot \hat{S}_3 + \hat{S}_1 \cdot \hat{S}_4 + \hat{S}_2 \cdot \hat{S}_5 + \hat{S}_2 \cdot \hat{S}_6] - J_3[\hat{S}_3 \cdot \hat{S}_5 + \hat{S}_4 \cdot \hat{S}_6] - J_4[\hat{S}_3 \cdot \hat{S}_9 + \hat{S}_5 \cdot \hat{S}_9 + \hat{S}_4 \cdot \hat{S}_{10} + \hat{S}_6 \cdot \hat{S}_{10}] - J_5[\hat{S}_1 \cdot \hat{S}_7 + \hat{S}_1 \cdot \hat{S}_8 + \hat{S}_2 \cdot \hat{S}_7 + \hat{S}_2 \cdot \hat{S}_8] - J_6[\hat{S}_3 \cdot \hat{S}_7 + \hat{S}_4 \cdot \hat{S}_8 + \hat{S}_5 \cdot \hat{S}_7 + \hat{S}_6 \cdot \hat{S}_8]$$

Equation S2.1- Spin-Hamiltonian for the six different exchange interactions present in **19** and **20**.

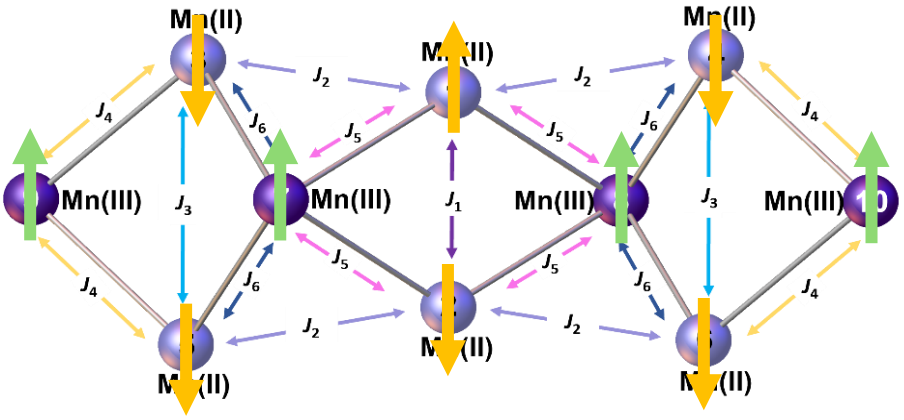

Figure S2.16- Depiction of the ground state (S = 2) of complex **19** based on the DFT calculated exchange coupling constants, $J_{1\text{-}6}$. The orange arrows represent S = 5/2 and the green arrows represent S = 2.

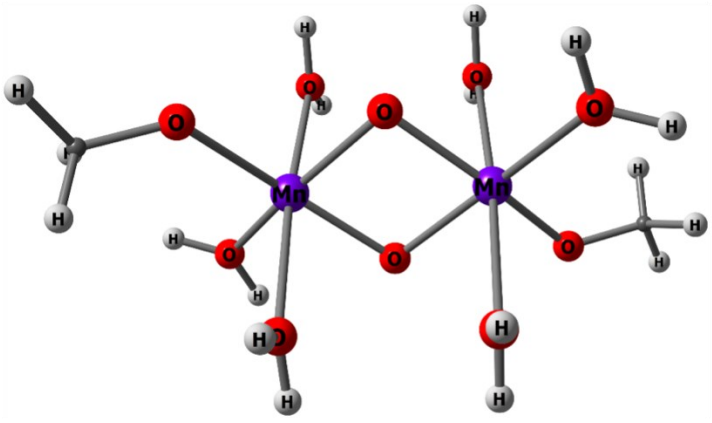

Figure S2.17- Dimeric model complex taken from the X-ray structure employed to verify the magnitude of J_1 in complex **20**. The exchange interaction obtained in the dimeric model is J = -92 cm^{-1}. We have verified the J value using the Yamaguchi model, which computes J = -115 cm^{-1}.[1]

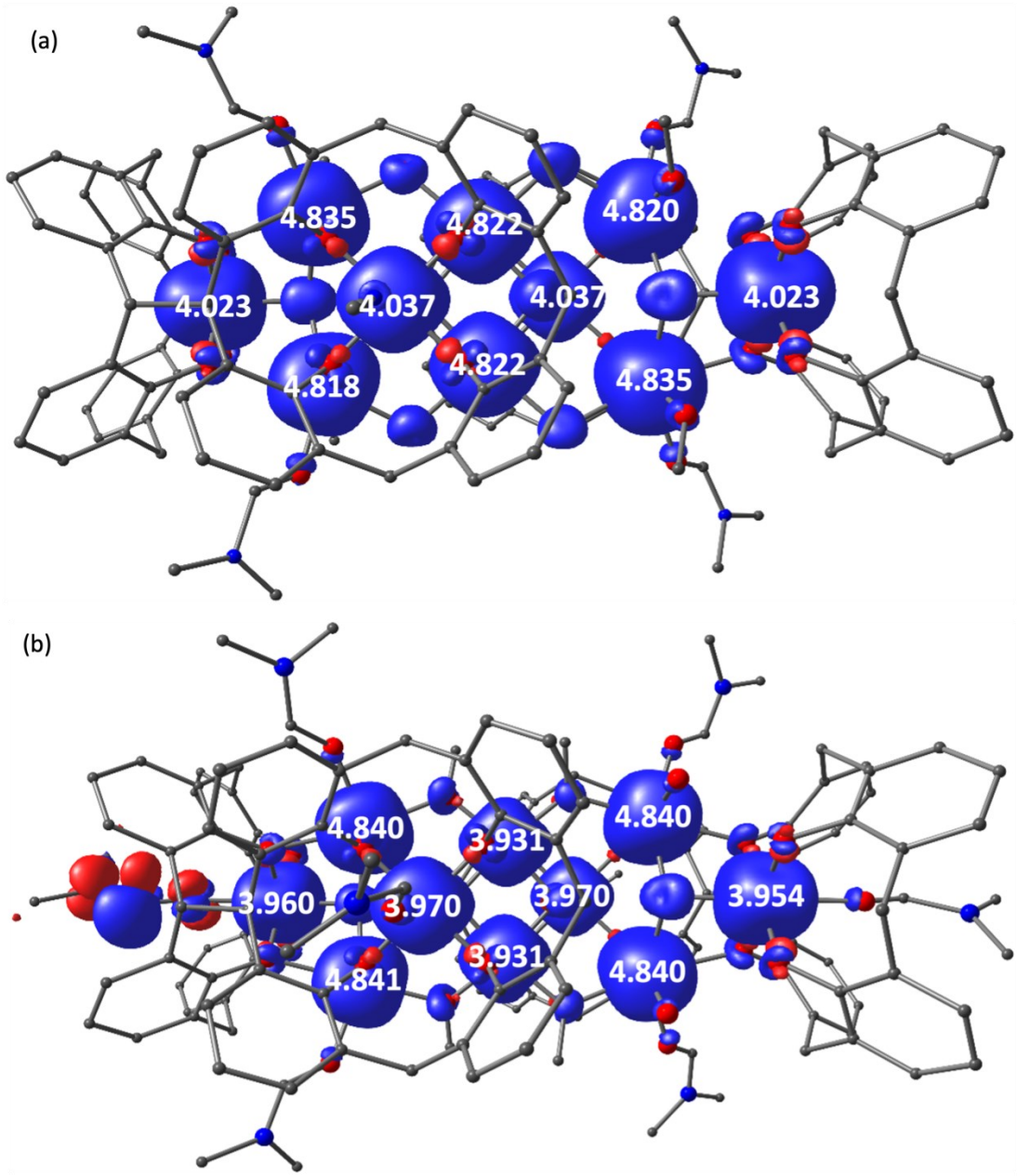

Figure S2.18- Computed spin density plots and values for the high spin state of **19** (a) and **20** (b) with a cut-off value of 0.0006 e bohr^{-3}. The blue colour represents positive spin density and the red colour negative spin density.

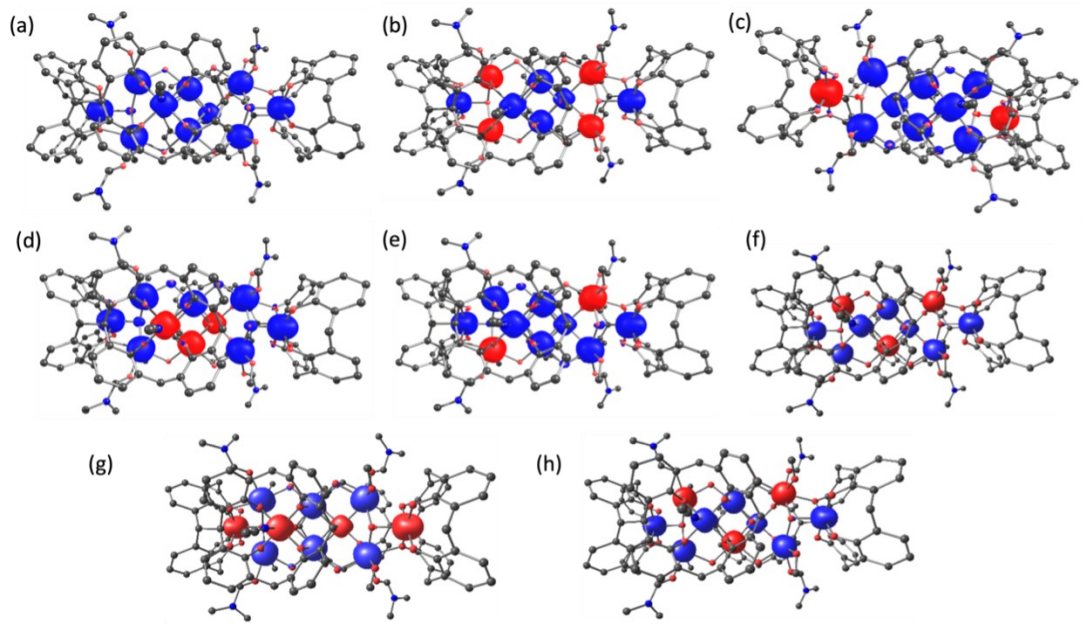

Figure S2.19- Computed spin density plots for all broken symmetries of complex **19** with a cut-off value of 0.0006 e bohr^{-3}. The blue colour represents positive spin density and the red colour negative spin density.

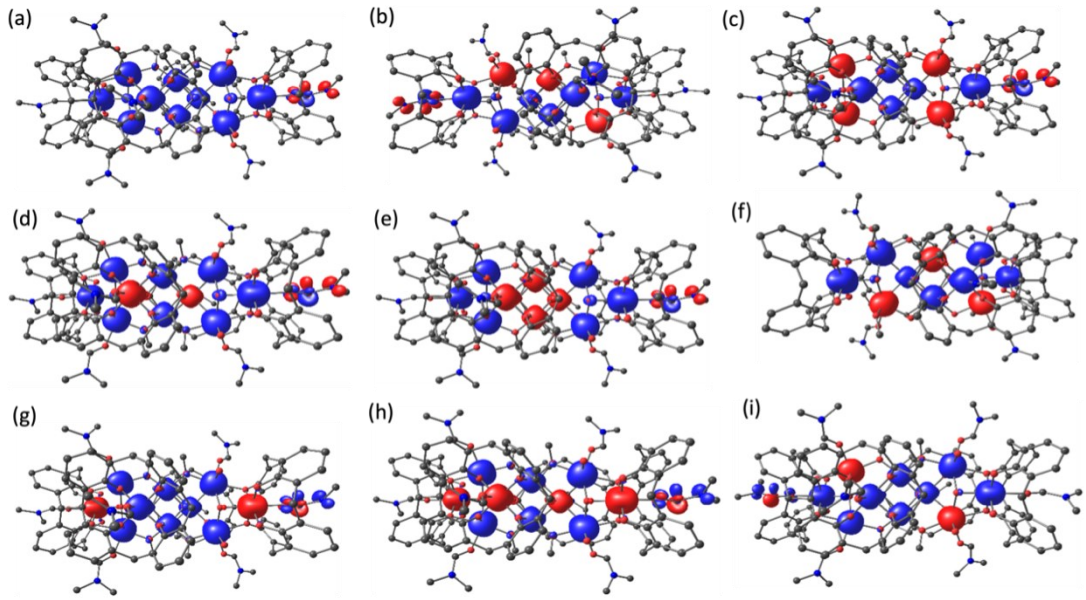

Figure S2.20- Computed spin density plots for all broken symmetries of complex **20** with a cut-off value of 0.0006 e bohr^{-3}. The blue colour represents positive spin density and the red colour negative spin density.

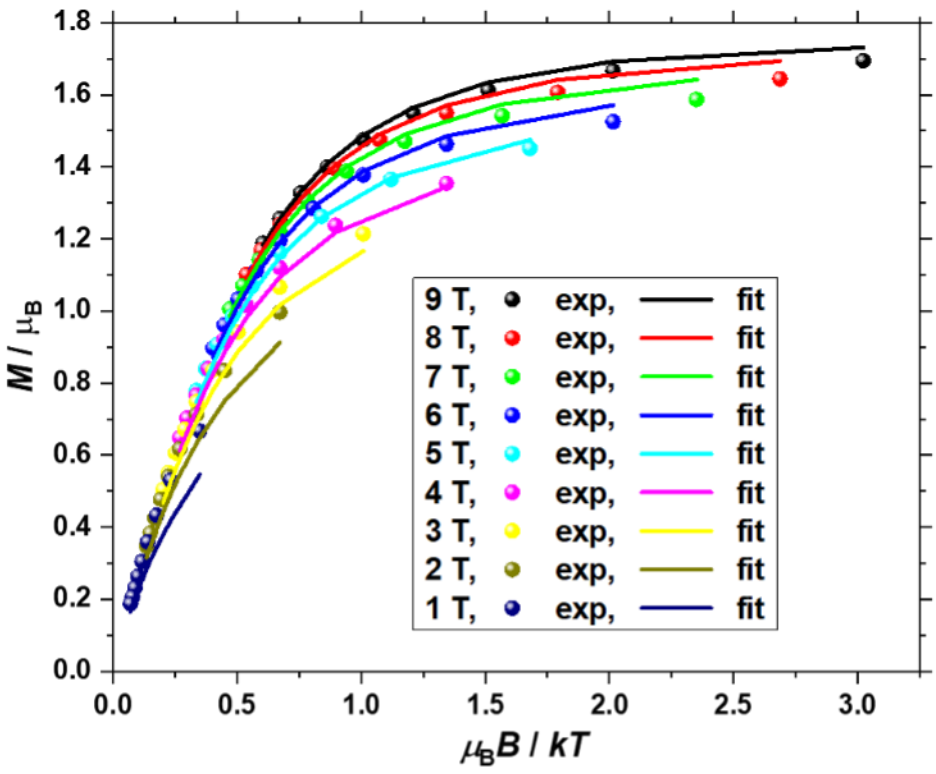

Figure S2.21- Variable-temperature-variable-field magnetisation measurements of **25** measured between T = 2-10 K and B = 0-9 T. The solid lines are a fit of the data assuming an isolated S = 1 state, affording D = -8.5 cm^{-1} with g fixed at g = 2.00 and using the spin-Hamiltonian, $\hat{H} = \sum_i D_i (\hat{S}_z{}^2 - \frac{S(S+1)}{3})$.

Table S2.9- DFT estimated magnetic exchange interactions alongside the pertinent structural parameters for complex **25**. Calculations are based on the $\widehat{H} - 2\sum_{i,j<1} J_{i,j}\widehat{S}_i \cdot \widehat{S}_j$ formalism.

J	cm^{-1}	Avg. Cu-O-Cu Angle (°)	Avg. Cu-O Distance (Å)	Cu-O-Cu-O Dihedral Angle (°)	Cu···Cu Distance (Å)	Bridging group(s)
$J_{Cu1\text{-}Cu3}$	+6.9	95.9	2.108	23.6	3.118	μ-OH, μ-OR$_L$
$J_{Cu1\text{-}Cu4}$	-16.6	101.6	2.091	10.3	3.223	μ$_3$-OH, μ-OR$_L$
$J_{Cu1\text{-}Cu5}$ / $J_{Cu1\text{-}Cu6}$	-25.3	120.0/120.6	1.962/1.971	--	3.400/3.424	μ-OR$_L$
$J_{Cu2\text{-}Cu3}$	-17.7	119.0	2.038	--	3.514	μ-OR$_L$
$J_{Cu2\text{-}Cu4}$*	-55.7	131.7	2.010	--	3.668	μ-OR$_L$
$J_{Cu2\text{-}Cu5}$	-22.0	102.8	2.087	1.1	3.251	μ-OH, μ-OR$_L$
$J_{Cu2\text{-}Cu6}$	-7.5	100.2	2.081	16.4	3.183	μ-OH, μ-OR$_L$
$J_{Cu3\text{-}Cu4}$	-30.8	125.7	1.957	--	3.482	μ-OH
$J_{Cu4\text{-}Cu7}$	-11.6	103.2	2.014	5.5	3.146	μ-O(NO$_2$), μ-OR$_{Me\text{-}dea}$
$J_{Cu5\text{-}Cu6}$	-3.9	107.2	1.947	--	3.135	μ-OH
$J_{Cu6\text{-}Cu8}$	+2.6	98.1	2.049	16.9	3.086	μ-O(NO$_2$), μ-OR$_{Me\text{-}dea}$
$J_{Cu7\text{-}Cu8}$	-9.9	114.6	1.930	--	3.249	η^1, η^1, η^2, μ$_4$-NO$_3$, μ-OR$_{Me\text{-}dea}$

*Estimated using bimetallic model **25D**.

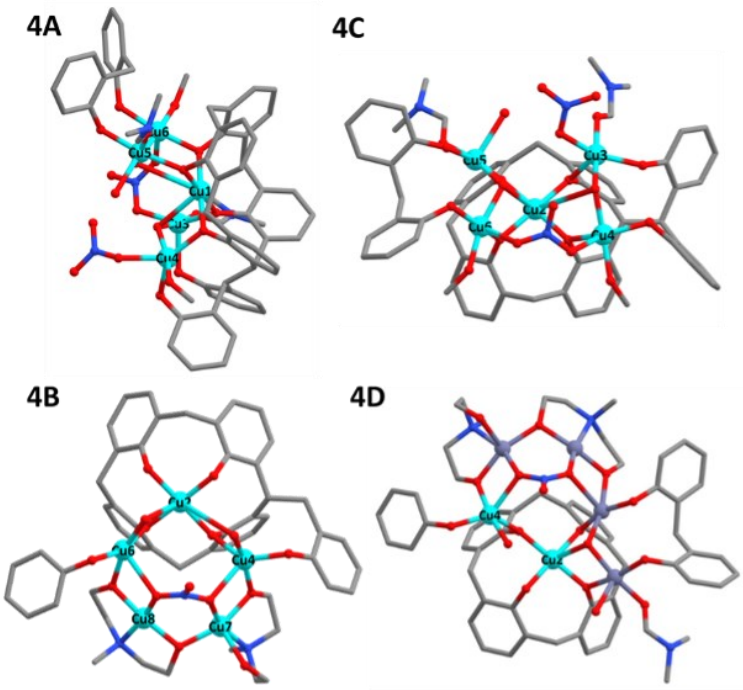

Figure S2.22- The three pentametallic models **25A**-**C** and the bimetallic model **25D** employed to calculate the magnetic exchange interactions in **25**.

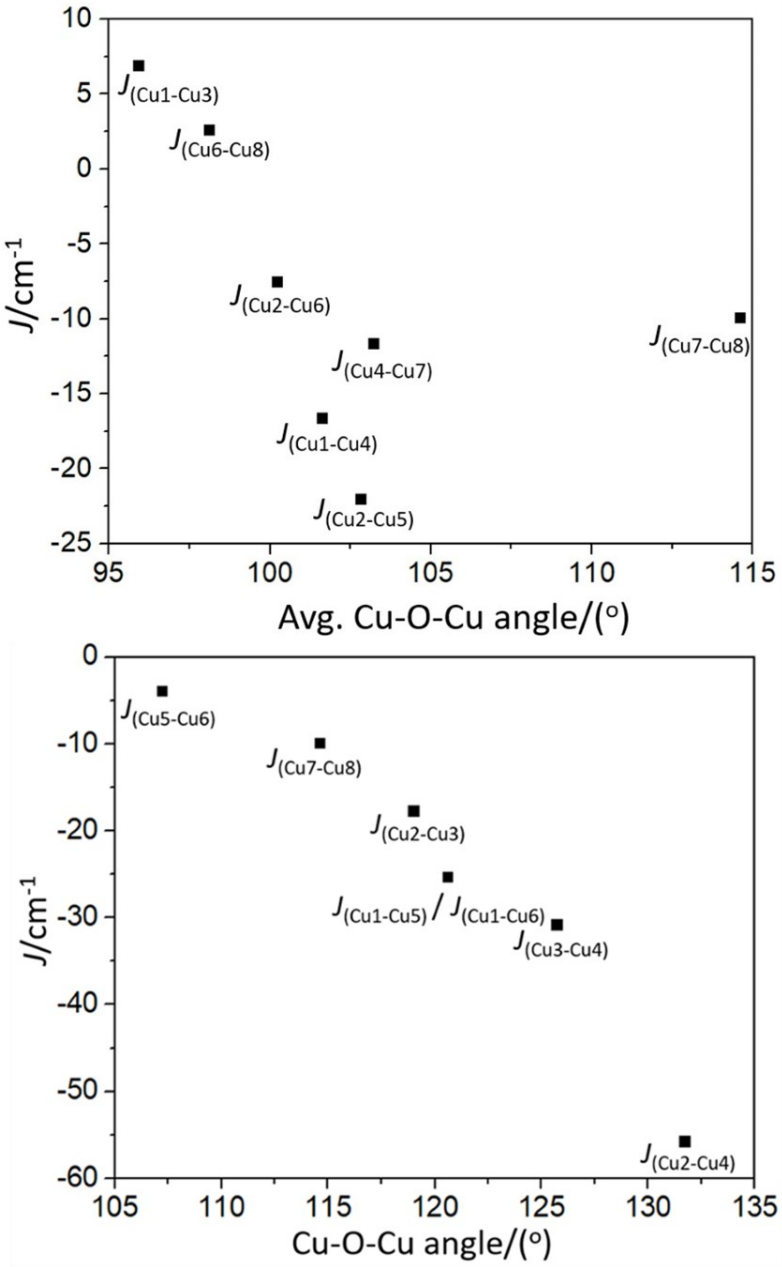

Figure S2.23- DFT estimated magnetic exchange interactions plotted *vs* the Cu-O-Cu angle (°) for pairs of nearest neighbour Cu ions in **25**. The upper graph shows Cu ions linked by two different bridging ligands; the lower graph shows Cu ions linked by one bridging ligand. $J_{(Cu7\text{-}Cu8)}$ is included on both due to the near-negligible contribution through the nitrate anion. Counter-complementary effect due to μ-$OR_{Me\text{-}dea}$/$O(NO_2)$ presence causes the small deviation seen for $J_{(Cu4\text{-}Cu7)}$. See main text for details.

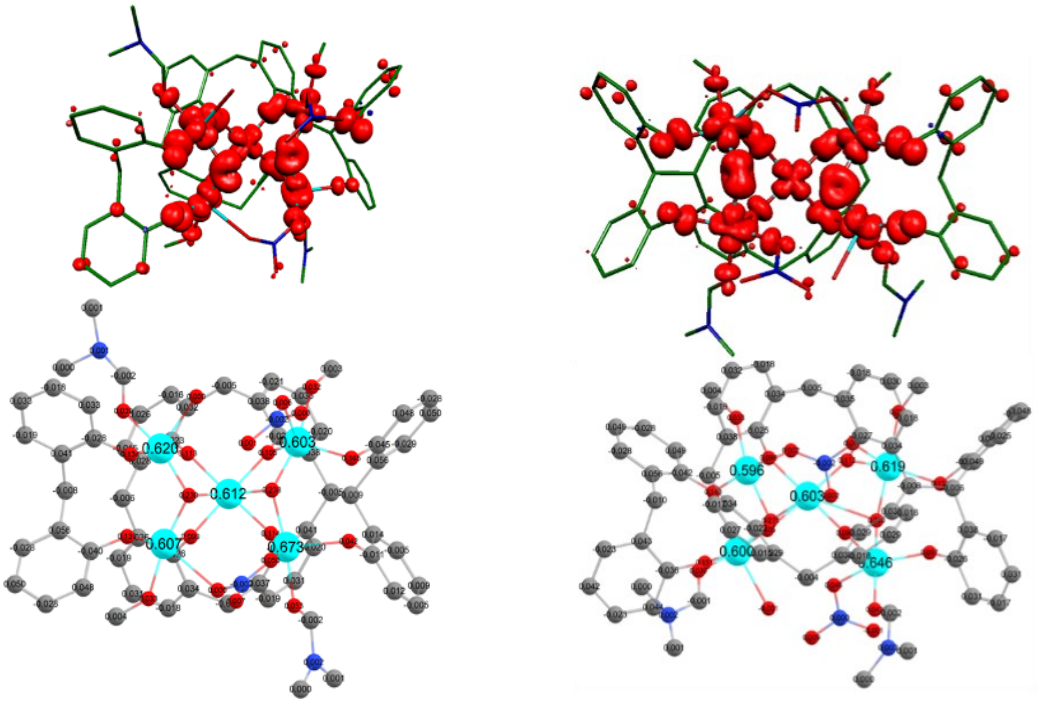

Figure S2.24- DFT estimated spin density plot (top) and values (bottom) for model **25A** (left) and **25B** (right) with the isodensity surface value 0.003 e bohr^{-3}.

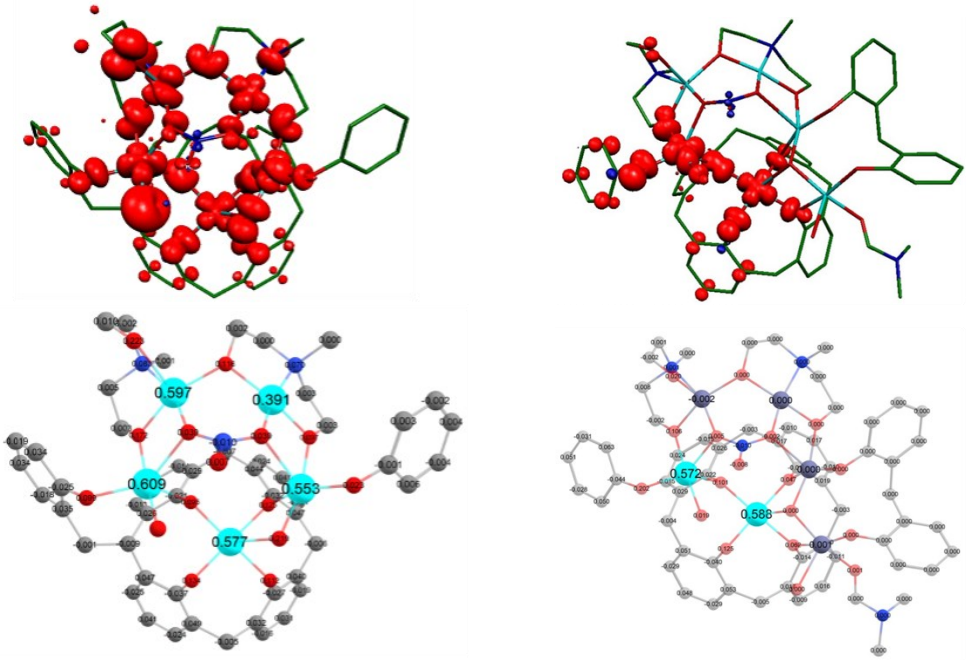

Figure S2.25- DFT estimated spin density plot (top) and values (bottom) for model **25C** (left) and **25D** (right) with the isodensity surface value 0.003 e bohr^{-3}.

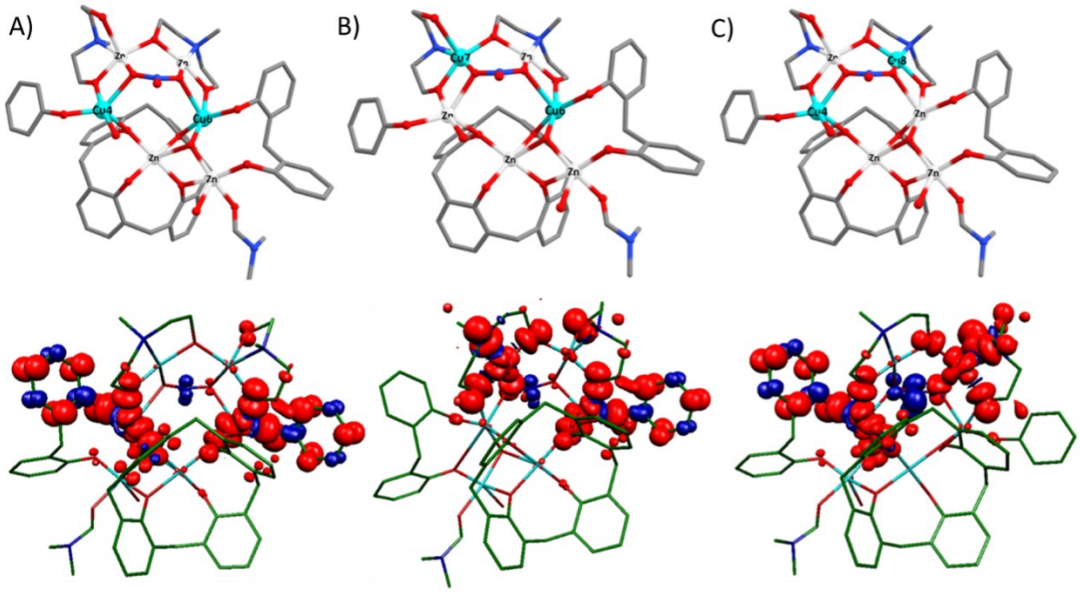

Figure S2.26- The three dimetallic complexes (top) used to calculate the magnetic exchange interactions mediated solely through the nitrate anions between A) Cu4-Cu6, B) Cu6-Cu7 and C) Cu4-Cu8. The values are J = -0.6 cm^{-1}, +0.9 cm^{-1} and +0.8 cm^{-1}, respectively. The *syn*, *syn*-coordination mode ($J_{Cu4-Cu6}$) results in a weak antiferromagnetic exchange interactions and *syn, anti*-coordination mode ($J_{Cu6-Cu7}$ and $J_{Cu4-Cu8}$) results in a weak ferromagnetic exchange interaction. The associated spin density plots are shown in the bottom half of the figure, with an isodensity surface value of 0.001 e $bohr^{-3}$. The small spin densities evident on the N, O-atoms of the nitrate are indicative of weak magnetic exchange.

References

1 T. Onishi, Y. Takano, Y. Kitagawa, T. Kawakami, Y. Yoshioka and K. Yamaguchi, *Polyhedron*, 2001, **20**, 1177.

Table S3.1- Crystallographic information for **26** and **27**.

Compound	**26**	**27**
Formula	$C_{325.50}H_{448.50}Cl_6Cu_{24}N_{27}O_{77}S_{24}$	$C_{96}H_{126}Br_5Cu_8N_5O_{18}S_8$
$D_{calc.}$/ g cm^{-3}	1.441	1.472
μ / mm^{-1}	3.538	4.984
Formula Weight	8478.69	2802.36
Colour	yellow	pale brown
Shape	block	plate
Size / mm^3	0.2x0.14x0.12	0.14x0.09x0.03
T / K	100.0	200.01(10)
Crystal System	triclinic	orthorhombic
Space Group	*P*-1	*Pbca*
a / Å	22.2855(4)	*23.4990(4)*
b / Å	2.2953(3)	25.0057(5)
c / Å	40.7937(7)	43.0467(8)
α / °	75.7320(10)	90
β / °	84.1880(10)	90
γ / °	89.7150(10)	90
V / Å^3	19538.4(6)	25294.6(8)
Z	2	8
Z'	1	1
Wavelength / Å	1.54178	1.54184
Radiation type	CuK_a	CuK_a
θ_{min} / °	1.993	3.535
θ_{max} / °	72.239	50.436
Measured Refl's.	46220	177307
Indep't Refl's	46220	13238
Refl's used I≥2σ(I)	27327	9465
R_{int}	0.0600	0.1074
Parameters	3059	1254
Restraints	1024	1390
Largest Peak	0.943	1.834
Deepest Hole	-0.887	-0.745
GooF	1.138	1.028
wR_2 (all data) (wR_2)	0.3122	0.2607
wR_2	0.2903	0.2358
R_1 (all data)	0.1439	0.1188
R_1	0.1001	0.0906

Table S3.2- Crystallographic information for **28** and **29**.

Compound	**28**	**29**
Formula	$C_{157}H_{205}Mn_6N_{11}O_{21}S_4$	$C_{188.25}H_{249}Cl_2Cu_4Mn_{10}N_5O_{34.75}S_8$
$D_{calc.}$/ g cm^{-3}	1.292	1.401
μ / mm^{-1}	0.627	1.188
Formula Weight	3040.19	4268.85
Colour	dark red	brown
Shape	block	plate
Size / mm^3	0.25x0.13x0.06	0.16x0.11x0.03
T / K	100(2)	100(2)
Crystal System	orthorhombic	monoclinic
Space Group	*Pnma*	*C*2/*c*
a / Å	29.3360(17)	40.3603(15)
b / Å	40.303(2)	12.6791(3)
c / Å	13.2234(8)	44.3016(18)
α / °	90	90
β / °	90	116.799(5)
γ / °	90	90
V / Å^3	15634.3(16)	20235.6(15)
Z	4	4
Z'	1	0.5
Wavelength / Å	0.7288	0.71073
Radiation type	MoK_α	MoK_α
θ_{min} / °	1.424	1.841
θ_{max} / °	23.921	26.373
Measured Refl's.	131634	151337
Indep't Refl's	114400	20683
Refl's used I≥2σ(I)	9564	15976
R_{int}	0.0484	0.0580
Parameters	1053	1232
Restraints	191	197
Largest Peak	1.311	1.729
Deepest Hole	-0.996	-1.464
GooF	1.039	1.080
wR_2 (all data) (wR_2)	0.1884	0.1879
wR_2	0.1808	0.1757
R_1 (all data)	0.0735	0.0904
R_1	0.0640	0.0674

Table S3.3- Crystallographic information for **30** and **31**.

Compound	**30**	**31**
Formula	$C_{195.51}H_{232.91}Cu_4Mn_6N_{6.48}O_{26.95}S_{16}$	$C_{158}H_{221}ClCo_4N_{10}O_{22}S_4$
$D_{calc.}$/ g cm^{-3}	1.313	1.214
μ / mm^{-1}	5.195	4.237
Formula Weight	4201.50	3011.84
Colour	brown	pink
Shape	plate	block
Size / mm^3	0.31x0.23x0.05	0.38x0.28x0.2
T / K	100(2)	144.00
Crystal System	triclinic	triclinic
Space Group	*P*-1	*P*-1
a / Å	18.15240(10)	18.1116(8)
b / Å	25.5200(2)	19.8540(9)
c / Å	26.85080(10)	25.0287(12)
α / °	96.5370(10)	97.736(2)
β / °	109.0670(10)	97.371(2)
γ / °	110.6260(10)	109.914(2)
V / Å^3	10627.77(14)	8237.1(7)
Z	2	2
Z'	1	1
Wavelength / Å	1.54184	1.54178
Radiation type	CuK$_a$	CuK$_a$
θ_{min} / °	1.802	2.855
θ_{max} / °	76.890	70.069
Measured Refl's.	360467	232560
Indep't Refl's	42969	31061
Refl's used I≥2σ(I)	39372	25252
R_{int}	0.330	0.0527
Parameters	2700	1700
Restraints	19	368
Largest Peak	1.393	1.850
Deepest Hole	-0.750	-1.489
GooF	1.023	1.113
wR_2 (all data) (wR_2)	0.1431	0.1933
wR_2	0.1401	0.1858
R_1 (all data)	0.0516	0.0726
R_1	0.0479	0.0627

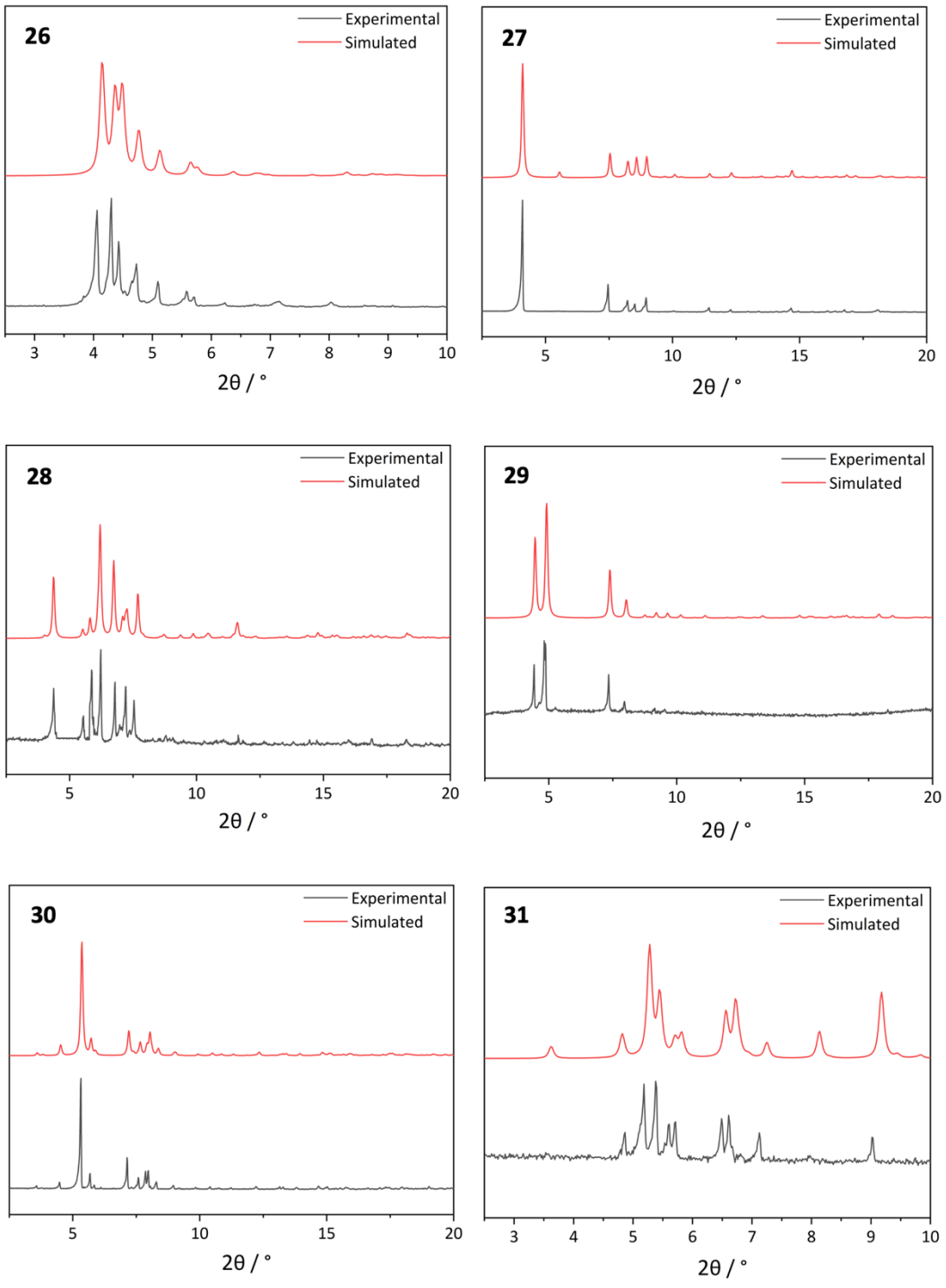

Figure S3.1- Powder diffraction data (black) shown against simulated data (red) for **26**-**31**.

Table S3.4- Pertinent bond lengths and bond angles for **26**.**

Cu1 / Å		**Cu2 / Å**	
Cu1-O1 ($OR_{TC[4]A}$)	1.985(7)	Cu2-O2 ($OR_{TC[4]A}$)	1.970(6)
Cu1-O2 ($OR_{TC[4]A}$)	1.968(7)	Cu2-O3 ($OR_{TC[4]A}$)	1.668(7)
Cu1-O13A (O)*	1.89(6)	Cu2-O18 (O_{CO3})*	2.046(11)
Cu1-O13 (O_{CO3})*	2.028(17)	Cu2-O19 (O)*	1.80(4)
Cu1-O14 (O)*	1.70(4)	Cu2-O30 (O_{CO3})*	2.081(11)
Cu1-O15 (O_{CO3})*	2.095(12)	Cu2-O31 (O)*	1.94(4)
Cu1-S1 ($S_{TC[4]A}$)	2.601(3)	Cu2-S2 ($S_{TC[4]A}$)	2.610(3)
Cu1-Cl1 (Cl)	2.681(3)	Cu2-Cl1 (Cl)	2.679(3)
Cu3 / Å		**Cu4 / Å**	
Cu3-O3 ($OR_{TC[4]A}$)	1.968(6)	Cu4-O5 ($OR_{TC[4]A}$)	1.982(6)
Cu3-O4 ($OR_{TC[4]A}$)	1.953(6)	Cu4-O8 ($OR_{TC[4]A}$)	1.975(8)
Cu3-O22 (O_{CO3})*	2.045(14)	Cu4-O13A (O_{CO3})*	1.74(5)
Cu3-O23 (O)*	1.77(5)	Cu4-O13 (O)	2.046(14)
Cu3-O28 (O_{CO3})*	2.013(14)	Cu4-O14 (O_{CO3})*	1.83(3)
Cu3-O29 (O)*	1.80(5)	Cu4-O15 (O)	2.046(14)
Cu3-S3 ($S_{TC[4]A}$)	2.588(3)	Cu4-S8 ($S_{TC[4]A}$)	2.601(3)
Cu3-Cl1 (Cl)	2.645(3)	Cu4-Cl2 (Cl)	2.688(3)
Cu5 / Å		**Cu6 / Å**	
Cu5-O5 ($OR_{TC[4]A}$)	1.958(6)	Cu6-O6 ($OR_{TC[4]A}$)	1.9752(6)
Cu5-O6 ($OR_{TC[4]A}$)	2.024(7)	Cu6-O7 ($OR_{TC[4]A}$)	1.976(7)
Cu5-O26 (O)*	1.86(4)	Cu6-O22 (O_{CO3})*	2.024(12)
Cu5-O27 (O_{CO3})	2.077(13)	Cu6-O23 (O)*	1.82(4)
Cu5-O33 (O_{CO3})	1.976(8)	Cu6-O28 (O_{CO3})*	2.070(12)
Cu5-S5 ($S_{TC[4]A}$)	2.616(2)	Cu6-O29 (O)*	1.80(4)
Cu5-Cl2 (Cl)	2.682(3)	Cu6-S6 ($S_{TC[4]A}$)	2.626(3)
-	-	Cu6-Cl2 (Cl)	2.663(3)
Cu7 / Å		**Cu8 / Å**	
Cu7-O7 ($OR_{TC[4]A}$)	1.9753(6)	Cu8-O9 ($OR_{TC[4]A}$)	1.978(7)
Cu7-O8 ($OR_{TC[4]A}$)	2.005(7)	Cu8-O12 ($OR_{TC[4]A}$)	1.986(6)
Cu7-O16 (O_{CO3})*	2.075(10)	Cu8-O16 (O_{CO3})*	2.100(13)
Cu7-O17 (O)*	1.70(3)	Cu8-O17 (O)*	1.84(4)

Cu7-O20 (O)*	1.83(3)	Cu8-O20 (O)*	1.66(3)
Cu7-O21 (O_{CO3})*	2.075(11)	Cu8-O21 (O_{CO3})*	2.075(10)
Cu7-S7 ($S_{TC[4]A}$)	2.603(3)	Cu8-S12 ($S_{TC[4]A}$)	2.603(3)
Cu7-Cl2 (Cl)	2.674(3)	Cu8-Cl3 (Cl)	2.677(3)
Cu9 / Å		**Cu10 / Å**	
Cu9-O9 ($OR_{TC[4]A}$)	1.950(6)	Cu10-O10 ($OR_{TC[4]A}$)	1.954(8)
Cu9-O10 ($OR_{TC[4]A}$)	1.978(5)	Cu10-O11 ($OR_{TC[4]A}$)	2.002(6)
Cu9-O24 (O_{CO3})*	2.077(9)	Cu10-O26 (O_{CO3})*	1.74(5)
Cu9-O25 (O)*	1.64(3)	Cu10-O27 (O_{CO3})*	2.013(15)
Cu9-O32 (O)*	2.047(11)	Cu10-O33 (O)*	2.002(8)
Cu9-O43 (O_{CO3})*	1.78(3)	Cu10-S10 ($S_{TC[4]A}$)	2.599(3)
Cu9-S9 ($S_{TC[4]A}$)	2.591(4)	Cu10-Cl3 (Cl)	2.670(2)
Cu9-Cl3 (Cl)	2.697(4)	-	
Cu11 / Å		**Cu0C / Å**	
Cu11-O11 ($OR_{TC[4]A}$)	1.970(5)	Cu0C-O1 ($OR_{TC[4]A}$)	1.994(6)
Cu11-O12 ($OR_{TC[4]A}$)	1.976(7)	Cu0C-O4 ($OR_{TC[4]A}$)	1.975(6)
Cu11-O18 (O_{CO3})*	2.061(10)	Cu0C-O24 (O_{CO3})*	2.024(11)
Cu11-O19 (O)*	1.80(3)	Cu0C-O25 (O)*	1.79(3)
Cu11-O30 (O_{CO3})*	1.997(11)	Cu0C-O32 (O_{CO3})*	2.091(12)
Cu11-O31 (O)*	1.60(4)	Cu0C-O43 (O)*	1.73(4)
Cu11-S11 ($S_{TC[4]A}$)	2.611(3)	Cu0C-S4 ($S_{TC[4]A}$)	2.609(4)
Cu11-Cl3 (Cl)	2.664(3)	Cu0C-Cl1 (Cl)	2.715(3)
Cu-O-Cu / °			
Cu1-O2-Cu2	110.6(3)	Cu5-O6-Cu6	108.9(2)
Cu1-Cl1-Cu2	74.51(8)	Cu5-Cl2-Cu6	74.52(7)
Cu1-O13A*-Cu4	112(2)	Cu5-Cl2-Cu7	117.51(8)
Cu1-O13*-Cu4	94.8(5)	Cu5-O26*-Cu10	113.3(14)
Cu1-O14*-Cu4	116.7(17)	Cu5-O27*-Cu10	94.9(5)
Cu1-O15*-Cu4	92.9(4)	Cu5-O33-Cu10	98.5(4)
Cu1-O1-Cu0C	109.8(3)	Cu6-O7-Cu7	110.1(3)
Cu1-Cl1-O3	117.43(12)	Cu6-Cl20-Cu7	74.23(9)
Cu2-O3-Cu3	109.9(3)	Cu7-O16*-Cu8	92.7(5)
Cu2-Cl1-Cu3	74.50(7)	Cu7-O17*-Cu8	117(2)
Cu2-O18*-Cu11	94.2(3)	Cu7-O20*-Cu8	120(2)

Cu2-O19*-Cu11	113.3(14)	Cu7-O21*-Cu8	93.5(4)
Cu2-O30*-Cu11	95.0(4)	Cu8-O9-Cu9	112.2(3)
Cu2-O31*-Cu11	116.0(15)	Cu8-Cl3-Cu9	74.68(9)
Cu2-Cl1-Cu0C	117.49(12)	Cu8-Cl3-Cu10	118.01(11)
Cu3-O22-Cu6	95.5(4)	Cu8-O12-Cu11	109.9(3)
Cu3-O23-Cu6	114.2(19)	Cu8-Cl3-Cu11	74.77(8)
Cu3-O28-Cu6	95.1(5)	Cu9-O10-Cu10	111.4(3)
Cu3-O29-Cu6	113.73(8)	Cu9-Cl3-Cu10	74.49(8)
Cu3-O4-Cu0C	110.86(5)	Cu9-Cl3-Cu11	117.92(1)
Cu3-Cl1-Cu0C	74.24(9)	Cu9-O24*-Cu0C	94.4(4)
Cu4-O5-Cu5	108.9(2)	Cu9-O25*-Cu0C	122.5(17)
Cu4-Cl2-Cu5	74.49(8)	Cu9-O32*-Cu0C	93.3(4)
Cu4-Cl2-Cu6	117.80(8)	Cu9-O43*-Cu0C	117.9(16)
Cu4-O8-Cu7	109.4(3)	Cu10-O11-Cu11	108.7(3)
Cu4-Cl2-Cu7	74.59(8)	Cu10-Cl3-Cu11	74.46(7)

*Denotes atoms at partial occupancy.

The ASU of **26 comprises two half clusters. Structural parameters are distinct but similar. See cif for details.

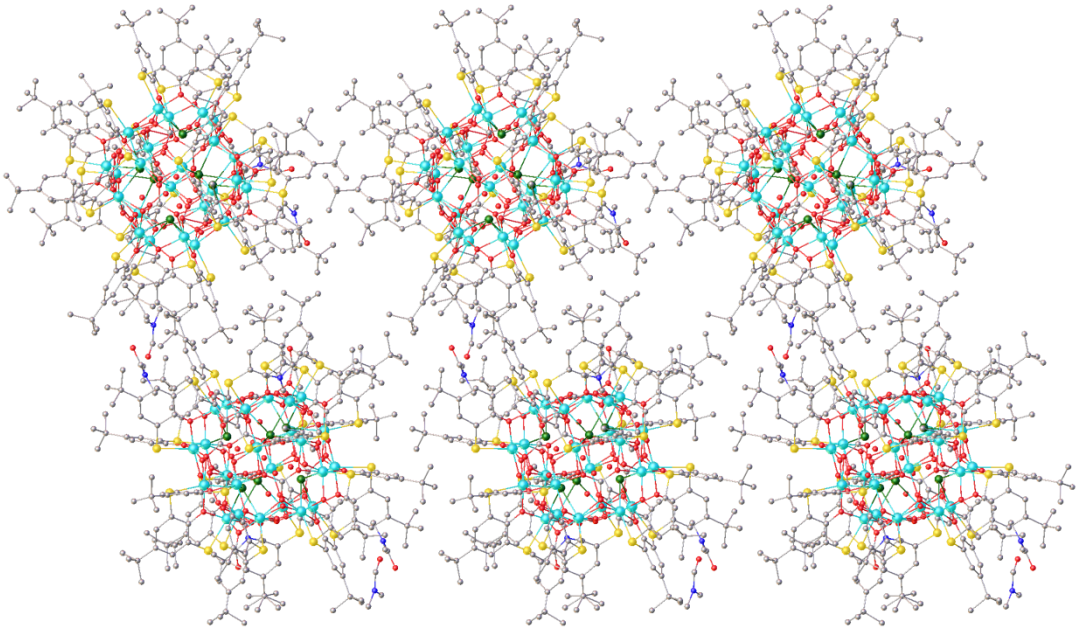

Figure S3.2- Extended structure of **26** shown down the *a*-axis. Colour code: Cu^{II} – turquoise, S – yellow, Cl – dark green, N – dark blue, C – grey, O – red. H atoms omitted for clarity.

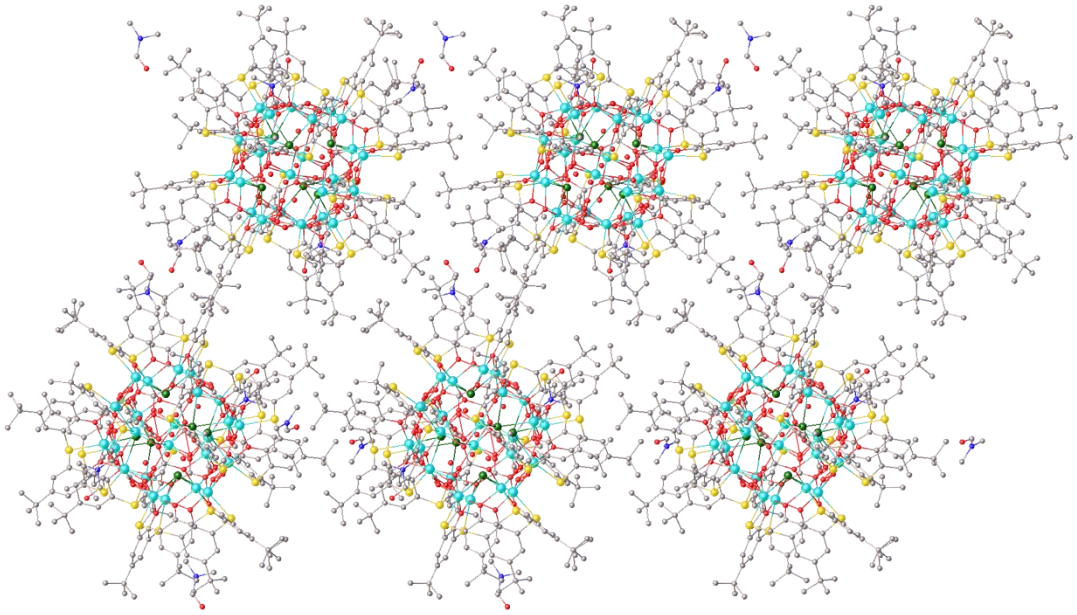

Figure S3.3- Extended structure of **26** shown down the *b*-axis. Colour code: Cu^{II} – turquoise, S – yellow, Cl – dark green, N – dark blue, C – grey, O – red. H atoms omitted for clarity.

Table S3.5- Pertinent bond lengths and bond angles for **27**.

Cu1 / Å		**Cu2 / Å**	
Cu1-O1 ($OR_{TC[4]A}$)	1.958(8)	Cu2-O1 ($OR_{TC[4]A}$)	2.066(9)
Cu1-O4 ($OR_{TC[4]A}$)	1.987(8)	Cu2-O4 ($OR_{TC[4]A}$)	2.052(9)
Cu1-O9 (O_{CO3})	1.915(8)	Cu2-S3 ($S_{TC[4]A}$)	2.347(4)
Cu1-O13 (O_{dmf})	1.985(9)	Cu2-Br1 (Br)	2.372(3)
Cu1-S1 ($S_{TC[4]A}$)	2.629(4)	Cu2-Br2 (Br)	2.440(2)
Cu3 / Å		**Cu4 / Å**	
Cu3-O2 ($OR_{TC[4]A}$)	1.966(9)	Cu4-O3 ($OR_{TC[4]A}$)	2.030(8)
Cu3-O3 ($OR_{TC[4]A}$)	1.992(9)	Cu4-O4 ($OR_{TC[4]A}$)	1.946(7)
Cu3-O14 (O_{dmf})	1.962(11)	Cu4-O10 (O_{CO3})	2.016(8)
Cu3-S3 ($S_{TC[4]A}$)	2.589(4)	Cu4-O12 (OH)	1.913(7)
Cu3-Br5* (Br)	2.260(5)	Cu4-S4 ($S_{TC[4]A}$)	2.526(4)
Cu5 / Å		**Cu6 / Å**	
Cu5-O5 ($OR_{TC[4]A}$)	2.081(9)	Cu6-O5 ($OR_{TC[4]A}$)	1.960(8)
Cu5-O8 ($OR_{TC[4]A}$)	2.053(9)	Cu6-O6 ($OR_{TC[4]A}$)	1.971(8)
Cu5-S5 ($S_{TC[4]A}$)	2.346(4)	Cu6-O11 (O_{CO3})	1.924(8)
Cu5-Br3 (Br)	2.431(2)	Cu6-O15 (O_{dmf})	2.001(9)
Cu5-Br4 (Br)	2.361(3)	Cu6-S6 ($S_{TC[4]A}$)	2.620(4)
Cu7 / Å		**Cu8 / Å**	
Cu7-O6 ($OR_{TC[4]A}$)	1.948(8)	Cu8-O7 ($OR_{TC[4]A}$)	1.992(10)
Cu7-O7 ($OR_{TC[4]A}$)	2.021(8)	Cu8-O8 ($OR_{TC[4]A}$)	1.956(9)
Cu7-O10 (O_{CO3})	2.020(7)	Cu8-O16 (O_{dmf})	2.058(13)
Cu7-O12 (OH)	1.913(7)	Cu8-S8 ($S_{TC[4]A}$)	2.565(5)
Cu7-S7 ($S_{TC[4]A}$)	2.531(4)	Cu8-Br6* (Br)	2.372(4)
Cu-O-Cu / °			
Cu1-O1-Cu2	117.7(4)	Cu4-O12-Cu7	104.5(3)
Cu1-O4-Cu4	110.6(4)	Cu5-O5-Cu6	117.2(4)
Cu2-O2-Cu3	114.6(4)	Cu5-O8-Cu8	117.8(5)
Cu3-O3-Cu4	116.2(4)	Cu6-O6-Cu7	109.7(4)
Cu4-O10-Cu7	97.1(3)	Cu7-O7-Cu8	116.9(4)

*Denotes atoms at half-occupancy.

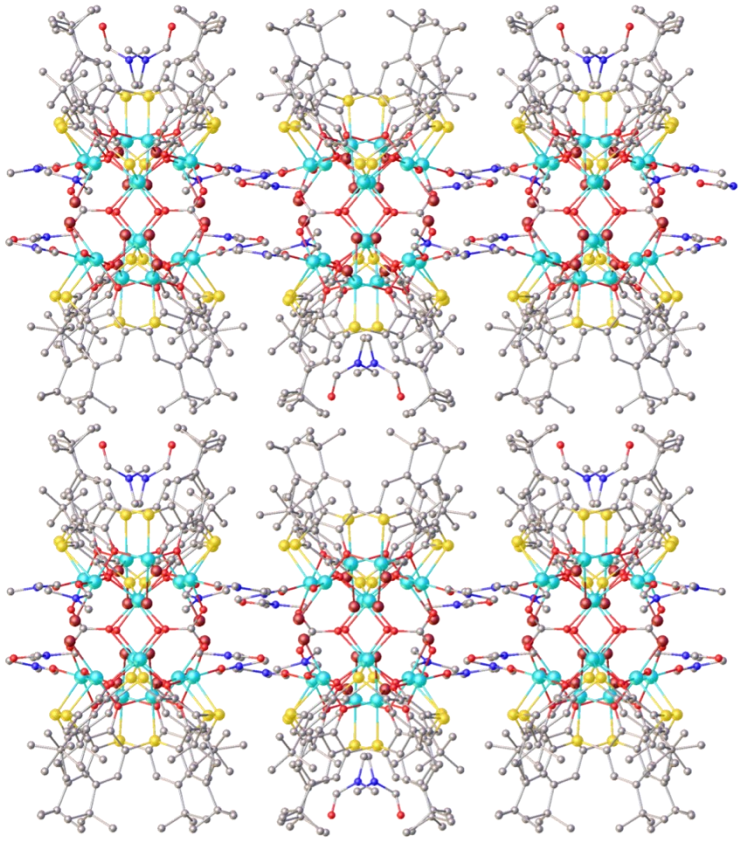

Figure S3.4- Extended structure of **27** shown down the *b*-axis. Colour code: Cu^{II} – turquoise, S – yellow, Br – dark red, N – dark blue, C – grey, O – red. H atoms omitted for clarity.

Table S3.6- Pertinent bond lengths and bond angles and calculated Mn BVS values for **28**.

Mn1		**Mn2**	
Mn1-O1 ($OR_{TBC[4]}$)	1.958(3)	Mn2-O1 ($OR_{TBC[4]}$)	2.161(3)
Mn1-O2 ($OR_{TBC[4]}$)	1.902(3)	Mn2-O6 (O_{dmf})	2.160(4)
Mn1-O3 ($OR_{TBC[4]}$)	1.911(3)	Mn2-O7* (O_{CO3})	2.101(6)
Mn1-O4 ($OR_{TBC[4]}$)	1.965(3)	Mn2-O8* (O_{CO3})	2.198(6)
Mn1-O5 (O_{dmf})	2.293(4)	Mn2-O12 ($OR_{TC[4]A}$)	2.226(3)
Mn1-O12 ($OR_{TC[4]A}$)	2.313(3)	Mn2-O13 ($OR_{TC[4]A}$)	2.186(2)
-	-	Mn2-S2 ($S_{TC[4]A}$)	2.6389(13)

BVS(Mn1) = 2.968		BVS(Mn2) = 2.139	
Mn3		-	
Mn3-O4 ($OR_{TBC[4]}$)	2.194(3)	-	-
Mn3-O8/O9 (O_{CO3})	2.159(6)/2.114(6)	-	-
Mn3-O10 (O_{dmf})	2.123(4)	-	-
Mn3-O11 ($OR_{TC[4]A}$)	2.224(2)	-	-
Mn3-O12 ($OR_{TC[4]A}$)	2.237(3)	-	-
Mn3-S1 ($S_{TC[4]A}$)	2.6278(13)	--	-
BVS(Mn3) = 2.051		-	
Mn-O-Mn / °			
Mn1-O1-Mn2	108.05(13)	Mn2-O13-Mn2’	113.01(18)
Mn1-O12-Mn2	94.58(11)	Mn2-O8-Mn3	111.6(3)
Mn1-O12-Mn3	95.26(11)	Mn2-O12-Mn3	107.69(13)
Mn1-O4-Mn3	107.75(13)	Mn3-O11-Mn3’	115.65(17)

*Denotes atoms at half-occupancy.

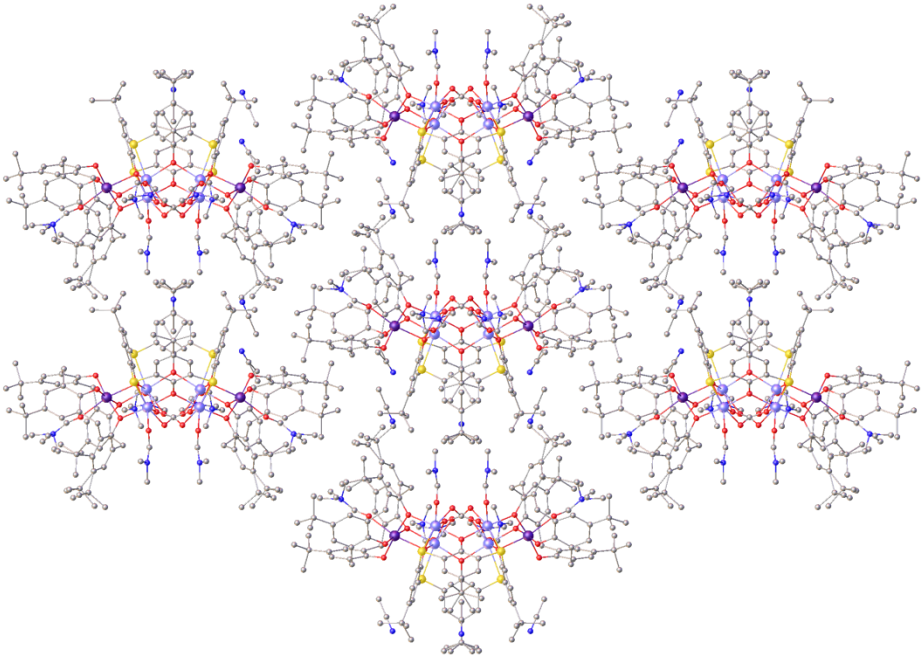

Figure S3.5- Extended structure of **28** shown down the *c*-axis. Colour code: Mn^{III} – dark purple, Mn^{II} – light purple, S – yellow, N – dark blue, C – grey, O – red. H atoms omitted for clarity.

Table S3.7- Pertinent bond lengths and bond angles and calculated Mn BVS values for **29**.

Mn1 / Å		**Mn2 / Å**	
Mn1-O5 (μ-$OR_{TBC[4]}$)	2.431(3)	Mn2-O8 (μ-OR_{TBC4})	2.164(3)
Mn1-O1O (μ_4-O)	1.903(1)	Mn2-O1O (μ_4-O)	1.923(3)
Mn1-O1O' (μ_4-O)	2.327(3)	Mn2-O2O (μ_4-O)	1.918(3)
Mn1-O2O (μ_4-O)	1.877(3)	Mn2-O1M (μ-OMe)	1.878(4)
Mn1-O1H (μ_3-OH)	1.894(3)	Mn2-O2M (μ-OMe)	1.927(3)
Mn1-O3M (μ-OMe)	1.933(3)	-	-
BVS(Mn1) = 3.110		BVS(Mn2) = 2.995	
Mn3 / Å		**Mn4 / Å**	
Mn3-O3 (μ-$OR_{TC[4]A}$)	2.167(3)	Mn4-O1 (μ-$OR_{TC[4]A}$)	2.193(3)
Mn3-O4 (μ-$OR_{TC[4]A}$)	2.079(3)	Mn4-O4 (μ-$OR_{TC[4]A}$)	2.091(3)
Mn3-O6 (μ-$OR_{TBC[4]}$)	2.067(3)	Mn4-O1H (μ_3-OH)	2.207(3)
Mn3-O1H (μ_3-OH)	2.178(3)	Mn4-O1M (μ-OMe)	2.079(4)
Mn3-O1W (O_{H2O})	2.315(5)	Mn4-S4 ($S_{TC[4]A}$)	2.6257(15)
Mn3-S3 ($S_{TC[4]A}$)	2.6765(16)	Mn4-Cl1 (Cl)	2.532(2)
BVS(Mn3) = 2.175		BVS(Mn4) = 2.236	
Mn5 / Å		**Cu1 / Å**	
Mn5-O5 (μ-$OR_{TBC[4]}$)	1.926(3)	Cu1-O1 (μ-$OR_{TC[4]A}$)	1.920(3)
Mn5-O6 (μ-$OR_{TBC[4]}$)	1.951(3)	Cu1-O2 (μ-$OR_{TC[4]A}$)	2.014(3)
Mn5-O7 (μ-$OR_{TBC[4]}$)	1.914(3)	Cu1-O1O (μ_4-O)	2.011(3)
Mn5-O8 (μ-$OR_{TBC[4]}$)	1.922(3)	Cu1-O3M (μ-OMe)	1.961(3)
Mn5-O2O (μ_4-O)	2.262(3)	Cu1-S1 ($S_{TC[4]A}$)	2.5835(14)
Mn5-O1D (O_{dmf})	2.187(3)	-	-
BVS(Mn5) = 3.135		-	
Cu2 / Å		-	
Cu2-O2 (μ-$OR_{TC[4]A}$)	2.154(3)	-	-
Cu2-O3 (μ-$OR_{TC[4]A}$)	1.996(4)	-	-
Cu2-O7 (μ-$OR_{TBC[4]}$)	2.400(3)	-	-
Cu2-O2O (μ_4-O)	2.039(3)	-	-
Cu2-O2M (μ-OMe)	1.995(4)	-	-
Cu2-S2 ($S_{TC[4]A}$)	2.4054(14)	-	-
M-O-M / °			

Mn1-O1O-Mn1’	98.46(13)	Mn2-O8-Mn5	101.39(14)
Mn1-O1O’-Mn1’	98.46(13)	Mn2-O2O-Mn5	98.14(13)
Mn1-O1O’-Mn2	94.56(14)	Mn2-O1O’-Cu1’	148.77(17)
Mn1-O2O-Mn2	95.49(14)	Mn2-O2O-Cu2	98.50(14)
Mn1-O1O-Mn2’	104.60(13)	Mn2-O2M-Cu2	99.69(16)
Mn1-O1H-Mn3	120.69(17)	Mn3-O4-Mn4	105.51(14)
Mn1-O1H-Mn4	117.71(16)	Mn3-O1H-Mn4	98.44(13)
Mn1-O5-Mn5	95.64(13)	Mn3-O6-Mn5	119.21(17)
Mn1-O2O-Mn5	102.92(13)	Mn3-O3-Cu2	117.27(15)
Mn1-O1O-Cu1	95.12(14)	Mn4-O1-Cu1	113.91(15)
Mn1-O1O’-Cu1’	95.12(14)	Mn5-O7-Cu2	93.38(13)
Mn1-O3M’-Cu1’	95.73(14)	Mn5-O2O-Cu2	94.28(12)
Mn1-O2O-Cu2	156.02(18)	Cu1-O2-Cu2	114.73(15)
Mn2-O1M’-Mn4’	120.90(18)	-	-

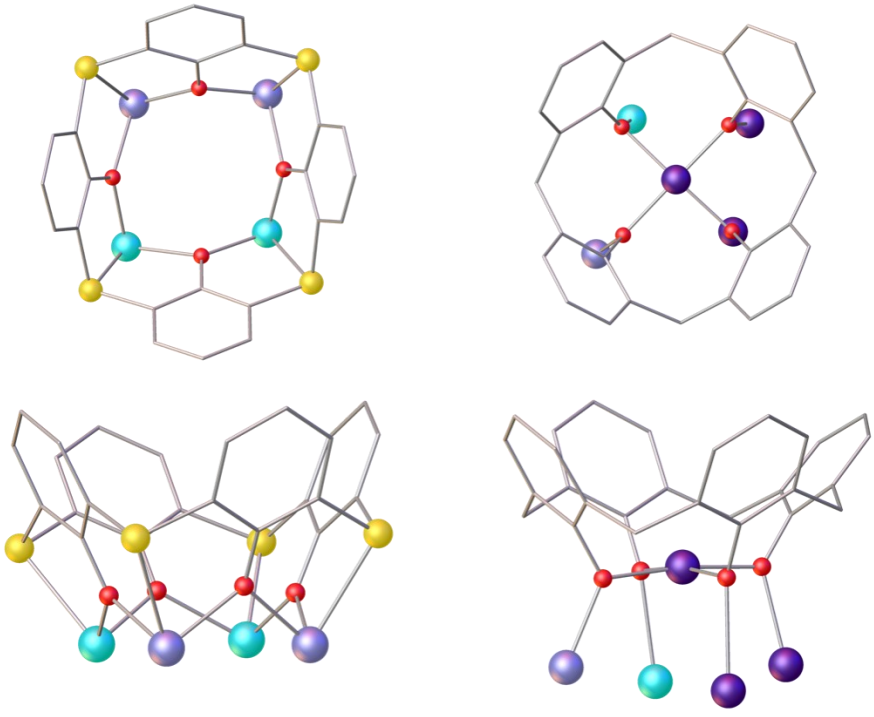

Figure S3.6- The bonding modes of TC[4]A and TBC[4] in **29**. Colour code: Mn^{III} – dark purple, Mn^{II} – light purple, Cu^{II} – turquoise, S – yellow, C – grey, O – red. H atoms and ^{t}Bu groups omitted for clarity.

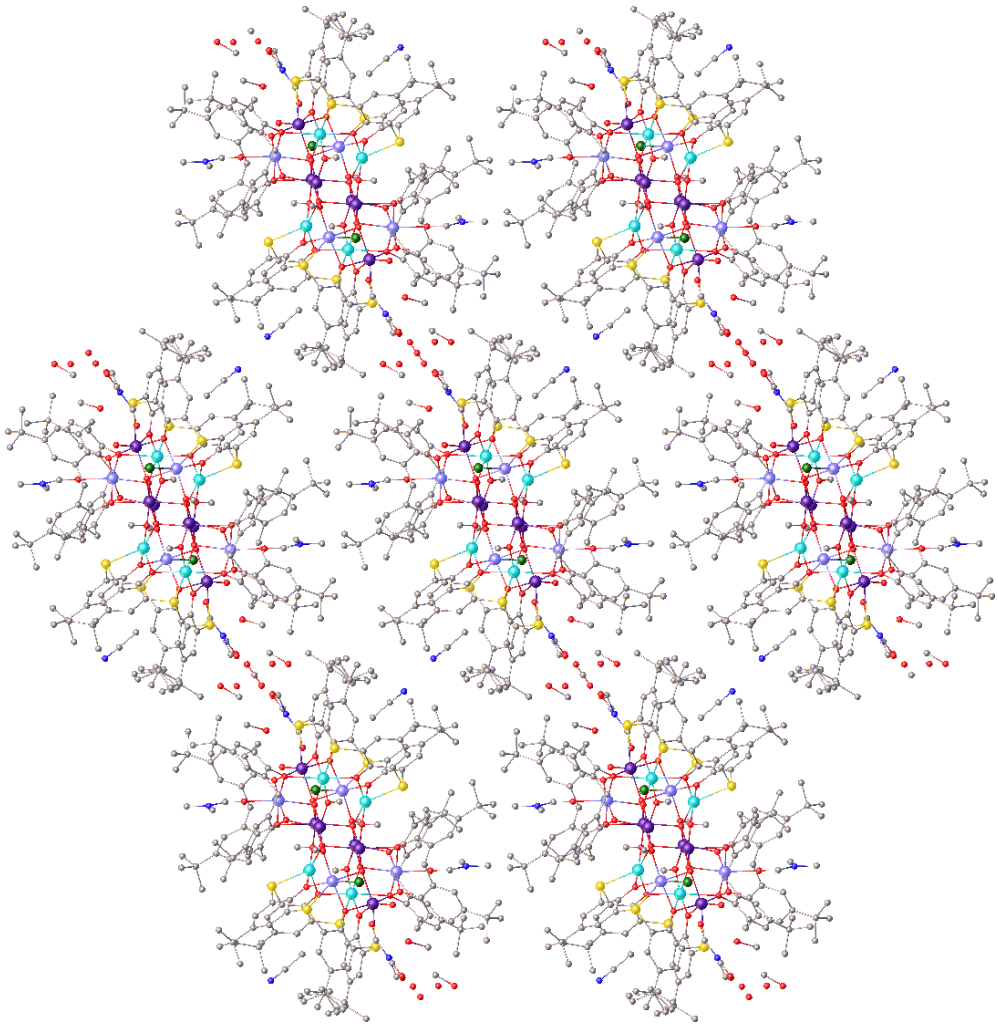

Figure S3.7- Extended structure of **29** shown down the *b*-axis. Colour code: Mn^{III} – dark purple, Mn^{II} – light purple, Cu^{II} – turquoise, S – yellow, N – dark blue, C – grey, O – red. H atoms omitted for clarity.

Table S3.8- Pertinent bond lengths and bond angles and calculated Mn BVS values for **30**.**

Mn1 / Å		**Mn2 / Å**	
Mn1-O1 ($OR_{TC[4]A}$)	2.060(2)	Mn2-O2 ($OR_{TC[4]A}$)	2.088(3)
Mn1-O2 ($OR_{TC[4]A}$)	2.058(2)	Mn2-O3 ($OR_{TC[4]A}$)	2.262(2)
Mn1-O6 ($OR_{TC[4]A}$)	2.209(2)	Mn2-O7 ($OR_{TC[4]A}$)	2.044(2)
Mn1-O7 ($OR_{TC[4]A}$)	2.130(3)	Mn2-O8 ($OR_{TC[4]A}$)	2.035(2)
Mn1-S2 ($S_{TC[4]A}$)	2.8104(9)	Mn2-S3 ($S_{TC[4]A}$)	2.5510(11)
Mn1-S7 ($S_{TC[4]A}$)	2.6137(9)	Mn2-S8 ($S_{TC[4]A}$)	2.7733(9)
BVS(Mn1) = 2.078		BVS(Mn2) = 2.242	
Mn3 / Å		**Cu1 / Å**	
Mn3-O3 ($OR_{TC[4]A}$)	2.139(2)	Cu1-O1 ($OR_{TC[4]A}$)	1.970(2)
Mn3-O4 ($OR_{TC[4]A}$)	2.1487(19)	Cu1-O4 ($OR_{TC[4]A}$)	1.9874(19)
Mn3-O5 ($OR_{TC[4]A}$)	2.1354(19)	Cu1-O6 ($OR_{TC[4]A}$)	2.490(19)
Mn3-O6 ($OR_{TC[4]A}$)	2.1577(19)	Cu1-O1L (O_{acac})	1.927(2)
Mn3-S4 ($S_{TC[4]A}$)	2.6663(8)	Cu1-O2L (O_{acac})	1.917(2)
Mn3-S6 ($S_{TC[4]A}$)	2.6519(8)	Cu1-S1 ($S_{TC[4]A}$)	2.5773(8)
BVS(Mn3) = 2.023		-	
Cu2 / Å		-	
Cu1-O5 ($OR_{TC[4]A}$)	1.987(2)	-	-
Cu1-O8 ($OR_{TC[4]A}$)	1.967(2)	-	-
Cu2-O3 ($OR_{TC[4]A}$)	2.476()	-	-
Cu1-O3L (O_{acac})	1.923(2)	-	-
Cu1-O4L (O_{acac})	1.915(2)	-	-
Cu1-S5 ($S_{TC[4]A}$)	2.5775(8)	-	-
Bond M-O-M / °			
Mn1-O2-Mn2	102.23(12)	Mn2-O3-Cu2	86.764(9)
Mn1-O7-Mn2	101.27(11)	Mn2-O8-Cu2	108.98(10)
Mn1-O6-Mn3	114.35(8)	Mn3-O6-Cu1	110.21(9)
Mn1-O1-Cu1	108.76(9)	Mn3-O4-Cu1	93.518(9)
Mn1-O6-Cu1	88.2(10)	Mn3-O5-Cu2	110.69(9)
Mn2-O3-Mn3	115.06(9)	Mn3-O3-Cu2	94.340(9)

The ASU of **30 comprises two [Mn_3Cu_2] clusters. Structural parameters are distinct but similar. See cif for details.

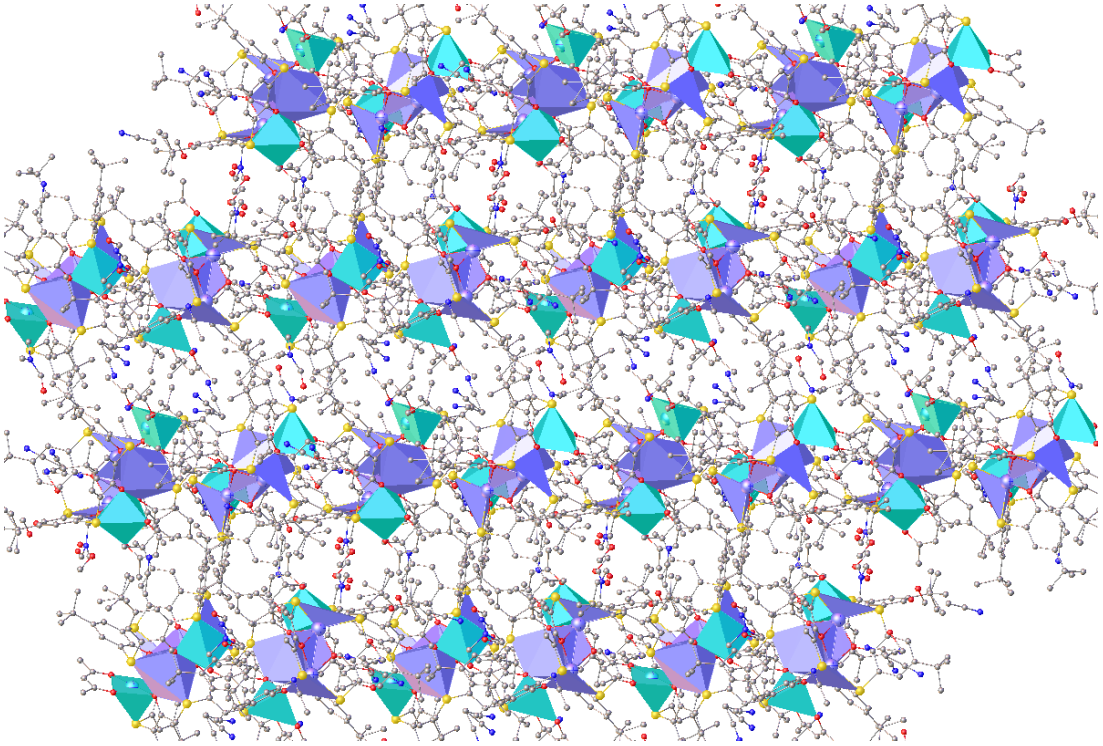

Figure S3.8- Extended structure of **30 s**hown down the *b*-axis. Colour code: Mn^{II} – light purple, Cu^{II} – turquoise, S – yellow, N – dark blue, C – grey, O – red. H atoms omitted for clarity.

Table S3.9- Pertinent bond lengths and bond angles and Co BVS values for **31**.

Co1 / Å		**Co2 / Å**	
Co1-O1 ($OR_{TC[4]A}$)	2.018(2)	Co2-O1 ($OR_{TC[4]A}$)	2.025(2)
Co1-O4 ($OR_{TC[4]A}$)	2.031(2)	Co2-O2 ($OR_{TC[4]A}$)	2.030(2)
Co1-O11 ($OR_{TBC[8]}$)	2.044(2)	Co2-O5 ($OR_{TBC[8]}$)	2.019(2)
Co1-O12 ($OR_{TBC[8]}$)	2.063(2)	Co2-O6 ($OR_{TBC[8]}$)	2.055(2)
Co1-S1 ($S_{TC[4]A}$)	2.4820(9)	Co2-S2 ($S_{TC[4]A}$)	2.4855(8)
Co1-Cl9 (Cl)	2.7327(11)	Co2-Cl9 (Cl)	2.8284(12)
BVS(Co1) = 1.940		BVS(Co2) = 1.935	
Co3 / Å		**Co4 / Å**	
Co3-O2 ($OR_{TC[4]A}$)	2.045(19)	Co4-O3 ($OR_{TC[4]A}$)	2.032(2)
Co3-O3 ($OR_{TC[4]A}$)	2.010(2)	Co4-O4 ($OR_{TC[4]A}$)	2.033(2)
Co3-O7 ($OR_{TBC[8]}$)	2.033(2)	Co4-O9 ($OR_{TBC[8]}$)	2.044(2)
Co3-O8 ($OR_{TBC[8]}$)	2.079(2)	Co4-O10 ($OR_{TBC[8]}$)	2.061(2)
Co3-S3 ($S_{TC[4]A}$)	2.4731(8)	Co4-S4 ($S_{TC[4]A}$)	2.4696(9)
Co3-Cl9 (Cl)	2.6927(11)	Co4-Cl9 (Cl)	2.7596(12)
BVS(Co3) = 1.953		BVS(Co4) = 1.906	
Co-O-Co / °			
Co1-O1-Co2	115.58(10)	Co2-O2-Co3	114.62(9)
Co1-Cl9-Co2	75.91(3)	Co2-Cl9-Co3	76.76(3)
Co1-Cl9-Co3	122.42(4)	Co2-Cl9-Co4	123.75(4)
Co1-Cl9-Co4	77.50(3)	Co3-O3-Co4	114.91(10)
Co1-O4-Co4	115.56(10)	Co3-Cl9-Co4	77.36(3)

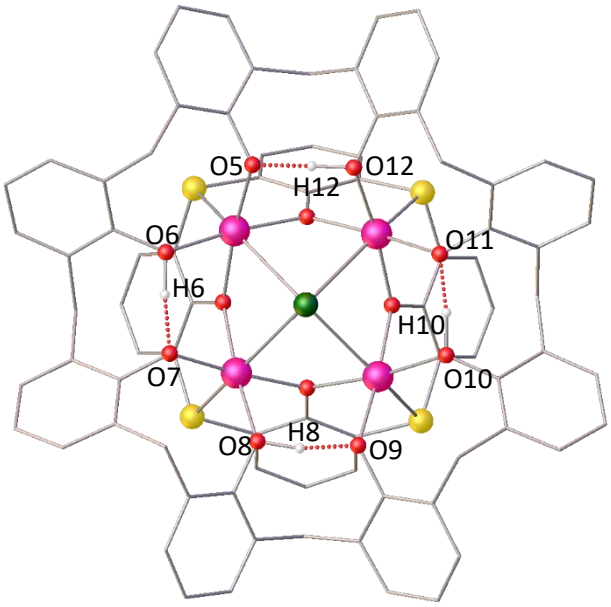

Figure S3.9- Partial structure of **31** with H_3TBC[8] H-bonding shown. Three H atoms are disordered across the four positions. Colour code: Co^{II} – pink, S – yellow, Cl – dark green, C – grey, O – red, H – white.

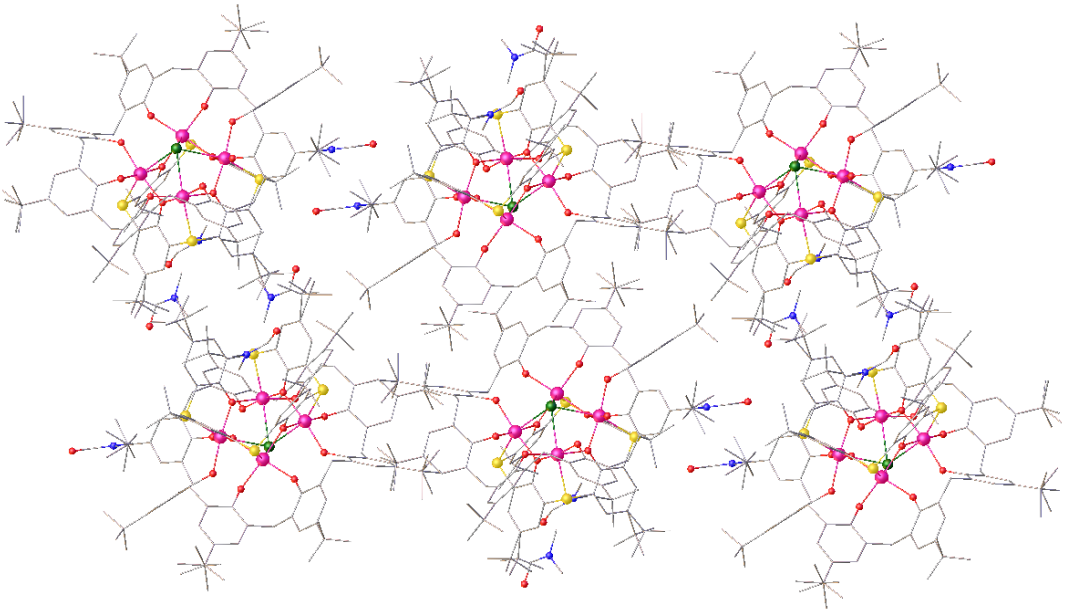

Figure S3.10- Extended structure of **31 s**hown down the *a*-axis. Colour code: Co^{II} – pink, S – yellow, Cl – dark green, N – dark blue, C – grey, O – red. H atoms omitted for clarity.

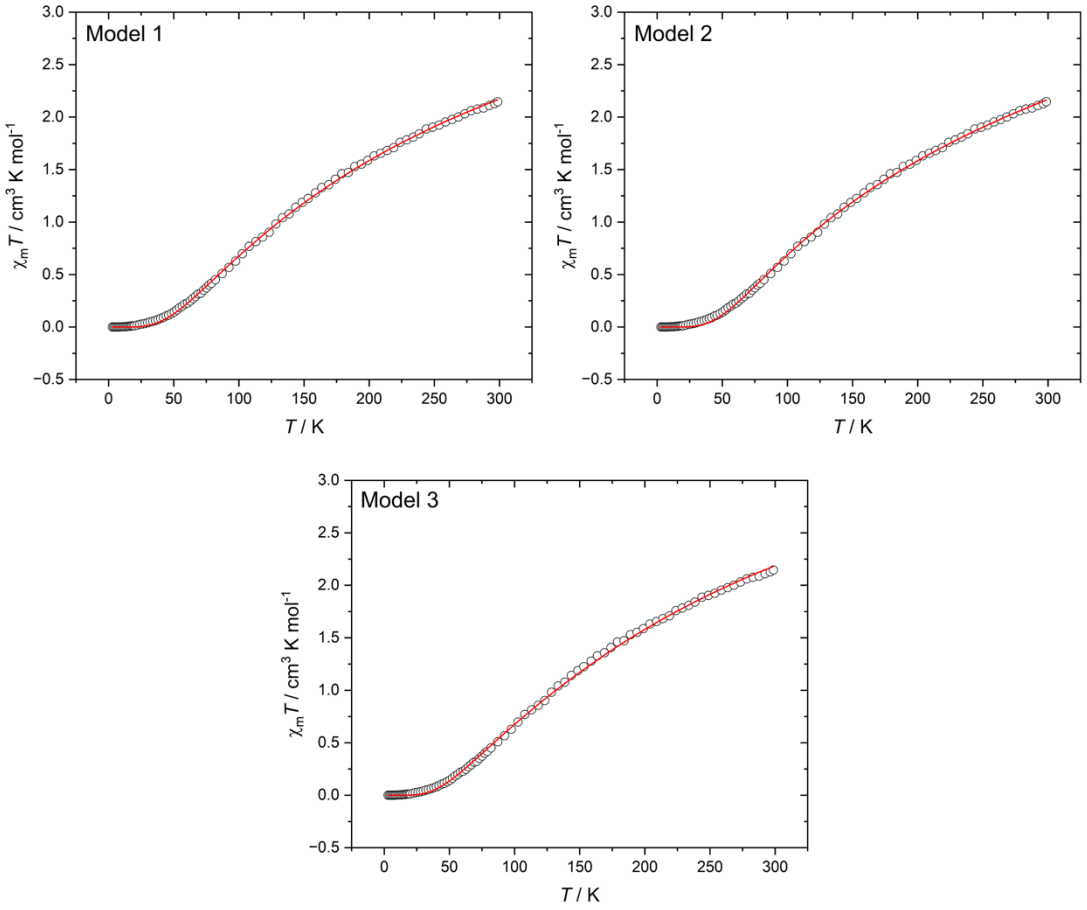

Figure S3.11- The best-fit data (solid red line) for each Model 1-3, plotted with experimental $\chi_M T$ *vs* T data for **26** (circles) measured in the T = 2-300 K temperature range in an applied field of B = 0.1 T. The experimental data for **26** is halved and modelled as discussed in main text.

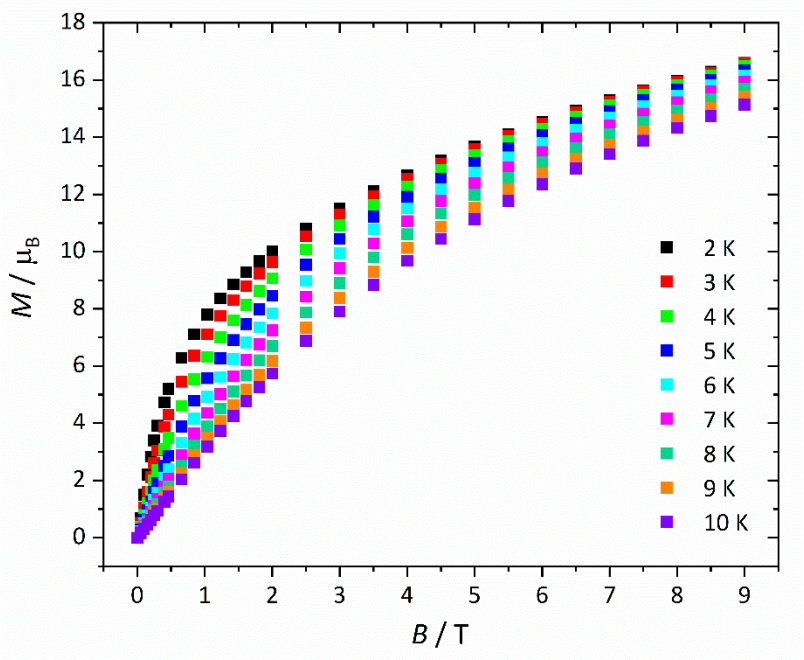

Figure S3.12- Variable-temperature-variable-field magnetisation measurements of **28** measured between *T* = 2-10 K and *B* = 0-9 T.

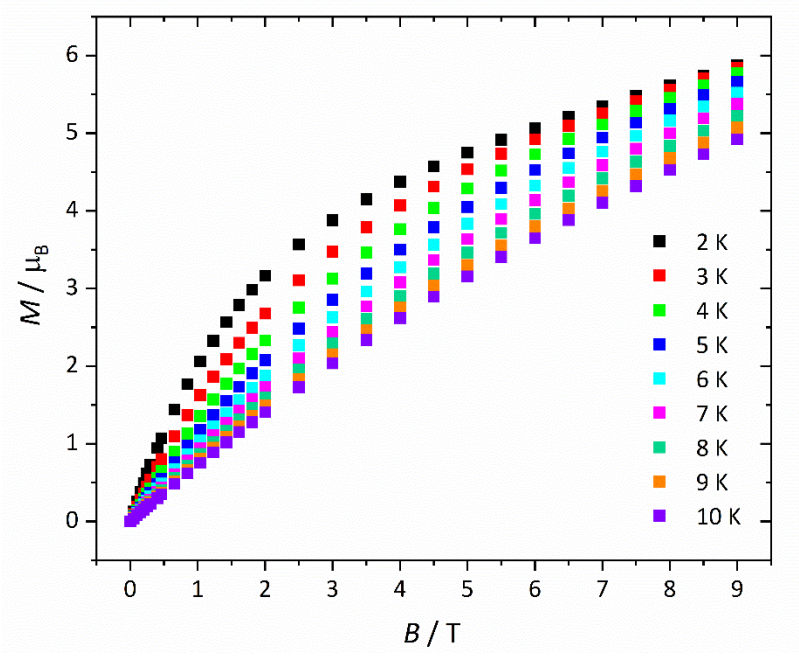

Figure S3.13- Variable-temperature-variable-field magnetisation measurements of **29** measured between *T* = 2-10 K and *B* = 0-9 T.

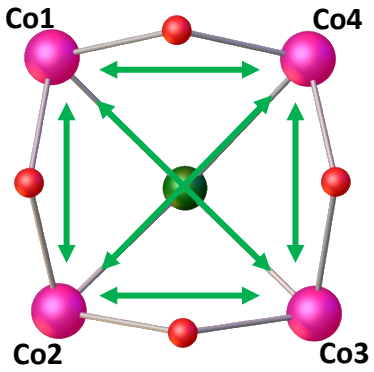

Figure S3.14- Schematic representation of the 1*J* model used to fit the experimental susceptibility data of **31.**

Table S4.1- Crystallographic information for **32** and **33**.

Compound	**32**	**33**
Formula	$Br_4C_{158}Cu_{10}H_{212}N_7O_{21}S_6$	$C_{158}H_{217}Cl_4Cu_7Gd_2N_7O_{23}S_6$
$D_{calc.}$/ g cm^{-3}	1.484	1.460
μ / mm^{-1}	3.719	5.042
Formula Weight	3692.73	3675.81
Colour	black	brown
Shape	lath-shaped	block
Size / mm^3	0.13x0.03x0.02	0.116x0.069x0.063
T / K	120.01(10)	100.00
Crystal System	orthorhombic	orthorhombic
Space Group	*Pnma*	*Pnma*
a / Å	40.0115(6)	24.4756(11)
b / Å	34.1612(5)	34.0803(7)
c / Å	12.092(2)	20.0525(5)
α / °	90	90
β / °	90	90
γ / °	90	90
V / Å^3	16528.4(4)	16726.5(9)
Z	4	4
Z'	0.5	0.5
Wavelength / Å	1.54184	1.0402
Radiation type	CuK_a	Synchrotron
θ_{min} / °	3.402	1.749
θ_{max} / °	51.112	25.683
Measured Refl's.	103483	52302
Indep't Refl's	9060	5200
Refl's used I≥2σ(I)	6522	3741
R_{int}	0.1290	0.1275
Parameters	995	916
Restraints	923	1649
Largest Peak	0.851	3.719
Deepest Hole	-0.749	-1.433
GooF	1.011	1.916
wR_2 (all data) (wR_2)	0.1684	0.4428
wR_2	0.1496	0.4166
R_1 (all data)	0.0919	0.1801
R_1	0.0615	0.1577

Table S4.2- Crystallographic information for **34** and **35**.

Compound	**34**	**35**
Formula	$C_{157.50}H_{216}ClMn_3N_5Na_6O_{22}S_7$	$C_{112.10}H_{146.30}ClMn_3N_{10}Na_3O_{15.75}$
$D_{calc.}$/ g cm^{-3}	1.204	1.262
μ / mm^{-1}	3.364	3.532
Formula Weight	3093.97	2155.12
Colour	blue	blue
Shape	block	block
Size / mm^3	0.3x0.26x0.2	0.22x0.16x0.14
T / K	100.00	100.00
Crystal System	monoclinic	triclinic
Space Group	*C*2/*c*	P-*1*
a / Å	34.6511(7)	17.5535(4)
b / Å	20.6506(5)	18.1099(4)
c / Å	24.2274(6)	20.5110(5)
α / °	90	91.090(2)
β / °	100.104(2)	110.5190(10)
γ / °	90	109.8950(10)
V / Å^3	17067.4(7)	5670.9(2)
Z	4	2
Z'	0.5	1
Wavelength / Å	1.54178	1.54178
Radiation type	CuK$_a$	CuK$_a$
θ_{min} / °	2.974	4.276
θ_{max} / °	72.511	74.488
Measured Refl's.	16571	223893
Indep't Refl's	16571	23081
Refl's used I≥2σ(I)	13077	16910
R_{int}	0.0841	0.0697
Parameters	1006	1363
Restraints	100	201
Largest Peak	0.960	2.621
Deepest Hole	-0.945	-2.069
GooF	1.023	1.667
wR_2 (all data) (wR_2)	0.2909	0.4075
wR_2	0.2768	0.3807
R_1 (all data)	0.1335	0.1399
R_1	0.1105	0.1191

Table S4.3- Crystallographic information for **36** and **37**.

Compound	**36**	**37**
Formula	$C_{188}H_{248}Cl_2Fe_{18}N_4O_{44}$	$C_{245.62}H_{371.62}Cl_4Fe_{28}N_{16.38}O_{70.88}$
$D_{calc.}$/ g cm^{-3}	1.113	1.329
μ / mm^{-1}	8.451	1.328
Formula Weight	4344.09	6393.63
Colour	black	black
Shape	caltrop-shaped	parallelepiped-shaped
Size / mm^3	0.06x0.05x0.03	0.200x0.100x0.080
T / K	100(2)	100(2)
Crystal System	cubic	monoclinic
Space Group	*Fm*-3*c*	*I*2/*m*
a / Å	53.7774(11)	23.6518(3)
b / Å	53.7774(11)	22.2726(4)
c / Å	53.7774(11)	30.5601(5)
α / °	90	90
β / °	90	97.0650(10)
γ / °	90	90
V / Å^3	155525(10)	15976.4(4)
Z	24	2
Z'	0.125	0.25
Wavelength / Å	0.154184	0.71073
Radiation type	CuK_a	MoK_a
θ_{min} / °	2.324	1.829
θ_{max} / °	38.043	29.130
Measured Refl's.	22907	373935
Indep't Refl's	1843	22006
Refl's used I≥2σ(I)	1417	16313
R_{int}	0.0686	0.0933
Parameters	197	1076
Restraints	25	563
Largest Peak	0.920	1.074
Deepest Hole	-0.573	-0.641
GooF	1.688	1.056
wR_2 (all data) (wR_2)	0.3855	0.1789
wR_2	0.3678	0.1671
R_1 (all data)	0.1513	0.0700
R_1	0.1301	0.0557

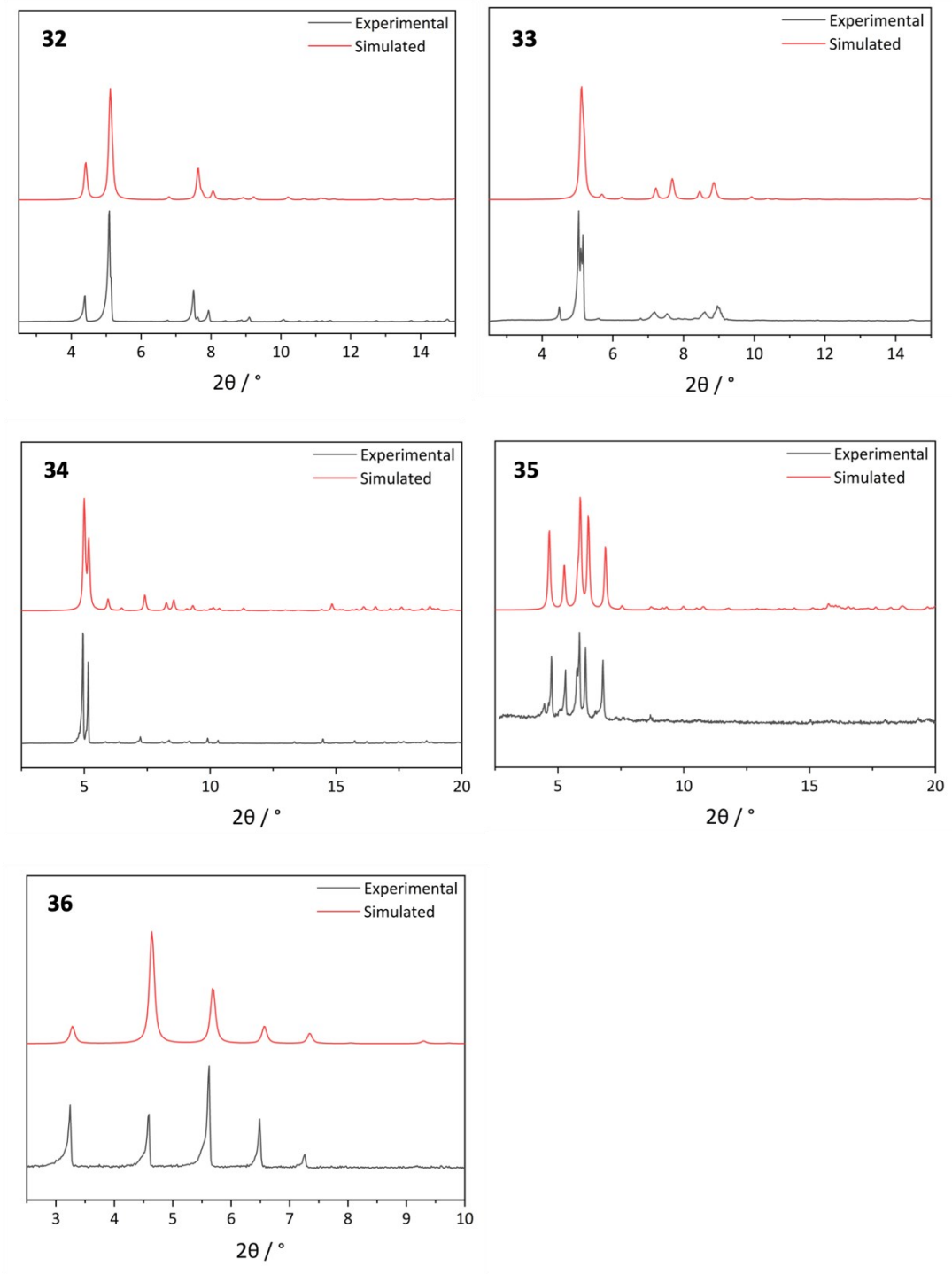

Figure S4.1- Powder diffraction data (black) shown against simulated data (red) for **32**-**36**.

Table S4.4- Pertinent bond lengths and bond angles for **32**.

Cu1 / Å		**Cu2 / Å**	
Cu1-O1 ($OR_{TBC[4]}$)	1.968(5)	Cu2-O1 ($OR_{TBC[4]}$)	1.963(5)
Cu1-O6 ($OR_{TBC[4]}$)	1.970(5)	Cu2-O2 ($OR_{TBC[4]}$)	1.957(5)
Cu1-O7 (O_{dmso})	2.001(6)	Cu2-O1' ($OR_{TBC[4]}$)	1.963(5)
Cu1-O9 (OH)	1.937(6)	Cu2-O2' ($OR_{TBC[4]}$)	1.957(5)
Cu1-Br2 (Br)	2.992*	-	-
Cu3 / Å		**Cu4 / Å**	
Cu3-O2 ($OR_{TBC[4]}$)	1.972(5)	Cu4-O3 ($OR_{TBC[4]}$)	1.960(6)
Cu3-O3 ($OR_{TBC[4]}$)	1.980(5)	Cu4-O4 ($OR_{TBC[4]}$)	1.969(5)
Cu3-O8 (O_{dmso})	1.954(5)	Cu4-O5 ($OR_{TBC[4]}$)	1.953(5)
Cu3-O9 (OH)	1.924(6)	Cu4-O6 ($OR_{TBC[4]}$)	1.974(5)
Cu3-Br1 (Br)	2.8564(14)	-	-
Cu5 / Å		**Cu6 / Å**	
Cu5-O4 ($OR_{TBC[4]}$)	1.946(5)	Cu6-O5 ($OR_{TBC[4]}$)	1.999(5)
Cu5-O4' ($OR_{TBC[4]}$)	1.946(5)	Cu6-O5' ($OR_{TBC[4]}$)	1.999(5)
Cu5-O10 (O_{dmso})	1.992(8)	Cu6-O11 (OH)	1.948(8)
Cu5-O11 (OH)	1.939(8)	Cu6-O12 (O_{dmso})	1.946(7)
Cu5-Br1 (Br)	3.091*	Cu6-Br2 (Br)	2.849(2)
Cu-O-Cu / °			
Cu1-O1-Cu2	114.7(3)	Cu3-Br1-Cu3'	98.386
Cu1-O9-Cu3	117.8(3)	Cu3-O3-Cu4	113.5(3)
Cu1-O6-Cu4	116.9(3)	Cu3-Br1-Cu5	99.011*
Cu1-Br2-Cu1'	1.937(6)	Cu4-O4-Cu5	115.2(3)
Cu1-Br2-Cu6	99.546*	Cu4-O5-Cu6	112.2(3)
Cu2-O2-Cu3	114.1(3)	Cu5-O11-Cu6	116.7(4)

*Long bonds/contacts; angles containing long bonds/contacts

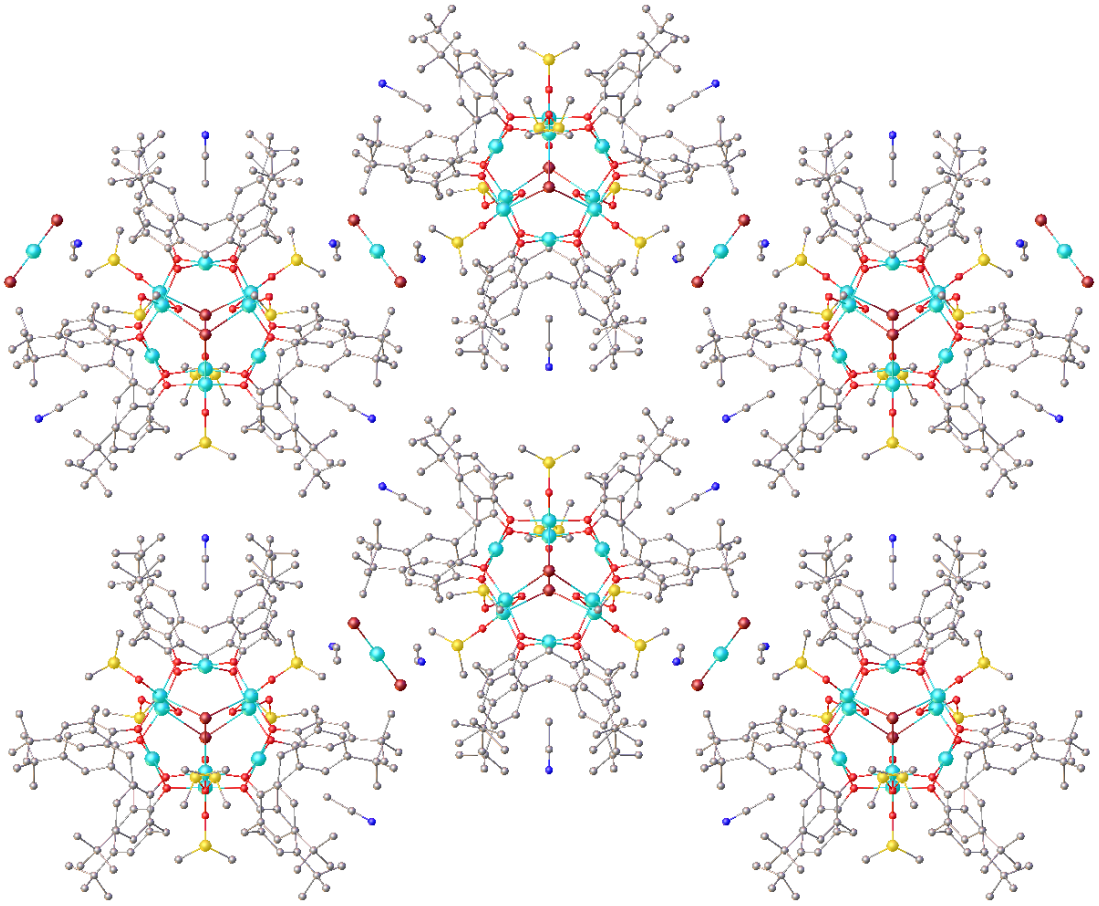

Figure S4.2- Extended structure of **32 s**hown down the *c*-axis. Colour code: Cu^{II} – turquoise, S – yellow, Br – dark red, N – dark blue, C – grey, O – red. H atoms omitted for clarity.

Table S4.5- Pertinent bond lengths and bond angles for **33**.

Cu1 / Å		**Cu2 / Å**	
Cu1-O1 ($OR_{TBC[4]}$)	1.941(15)	Cu2-O2 ($OR_{TBC[4]}$)	2.025(15)
Cu1-O1' ($OR_{TBC[4]}$)	1.941(15)	Cu2-O2' ($OR_{TBC[4]}$)	2.024(15)
Cu1-O7 (OH)	1.894(18)	Cu2-O8 (OH)	1.90(2)
Cu1-O10 (O_{dmso})	1.91(2)	Cu2-O11 (O_{dmso})	2.13(13)
-	-	Cu2-O14 (O_{H2O})	2.03(2)
Cu3 / Å		**Cu4 / Å**	
Cu3-O3 ($OR_{TBC[4]}$)	1.992(14)	Cu4-O5 ($OR_{TBC[4]}$)	1.967(15)
Cu3-O5 ($OR_{TBC[4]}$)	1.930(14)	Cu4-O5' ($OR_{TBC[4]}$)	1.967(15)
Cu3-O9 (OH)	1.957(13)	Cu4-O6 ($OR_{TBC[4]}$)	1.967(15)
Cu3-O12 (O_{dmso})	1.861(17)	Cu4-O6' ($OR_{TBC[4]}$)	1.967(15)
Cu3-Cl2 (Cl)	2.865*	-	
Cu5 / Å		**Gd1 / Å**	
Cu5-O4 ($OR_{TBC[4]}$)	1.950(14)	Gd1-O1 ($OR_{TBC[4]}$)	2.311(16)
Cu5-O6 ($OR_{TBC[4]}$)	1.934(14)	Gd1-O2 ($OR_{TBC[4]}$)	2.312(15)
Cu5-O9 (OH)	1.940(13)	Gd1-O3 ($OR_{TBC[4]}$)	2.279(15)
Cu5-O13 (O_{dmso})	1.907(16)	Gd1-O4 ($OR_{TBC[4]}$)	2.252(14)
Cu5-Cl1 (Cl)	2.883*	Gd1-O7 (OH)	2.357(9)
-	-	Gd1-O8 (OH)	2.400(12)
-	-	Gd1-O9 (OH)	2.437(14)
-	-	Gd1-N1 (N_{MeCN})	2.60(2)
Cu-O-Cu / °			
Cu1-O1-Gd1	105.0(7)	Cu3-O9-Cu5	112.2(6)
Cu1-O7-Gd1	104.9(5)	Cu3-O3-Gd1	102.9(6)
Cu1-O1'-Gd1'	105.0(7)	Cu3-O9-Gd1	98.5(5)
Cu1-O7-Gd1'	104.9(5)	Cu4-O6-Cu5	110.5(7)
Cu2-O2-Gd1	103.8(6)	Cu4-O6'-Cu5'	110.5(7)
Cu2-O8-Gd1	104.7(6)	Cu5-Cl1-Cu5	95.439*
Cu2-O2'-Gd1'	103.8(6)	Cu5-O4-Gd1	101.4(6)
Cu2-O8-Gd'	104.7(6)	Cu5-O9-Gd1	98.8(5)
Cu3-Cl2-Cu3'	97.854*	Gd1-O7-Gd1'	111.1(6)
Cu3-O5-Cu4	110.6(7)	Gd1-O8-Gd1'	108.2(8)

*Long bonds/contacts; angles containing long bonds/contacts

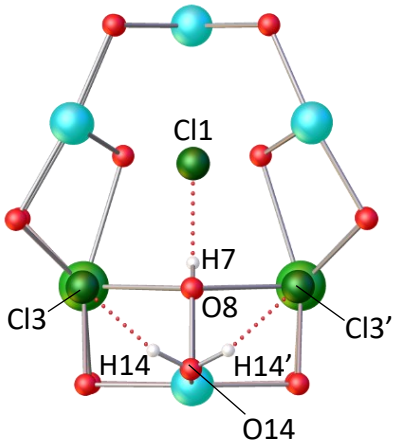

Figure S4.3- Cross-section of complex **33** with H-bonding shown between the ligated μ_3-OH/ terminal H_2O molecule and the Cl anions. Colour code: Cu^{II} – turquoise, Gd^{III} – bright green, Cl – dark green, O – red, H – white.

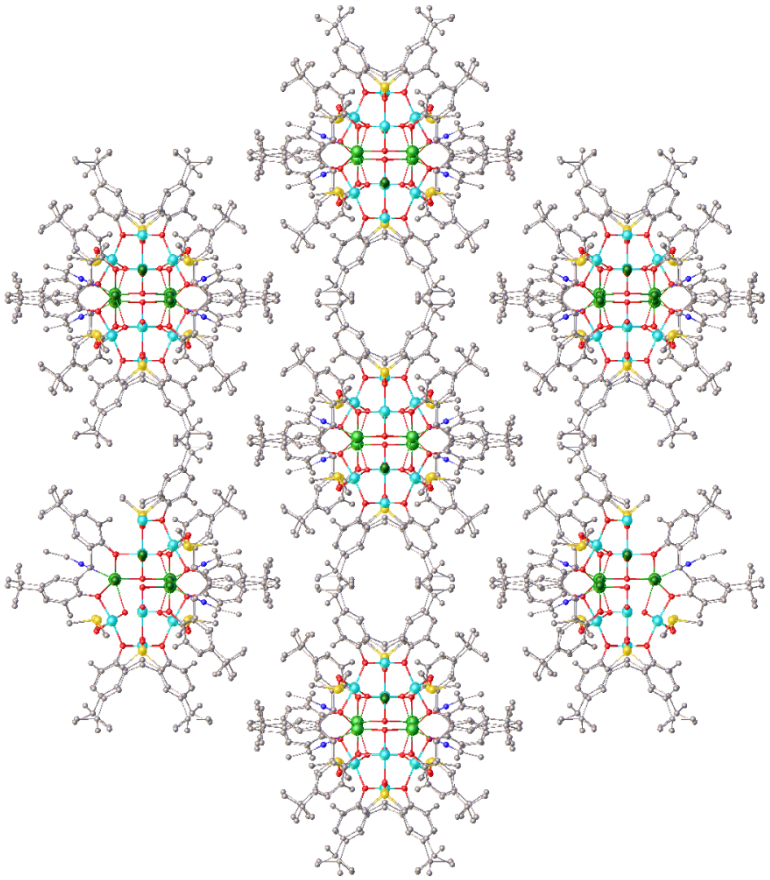

Figure S4.4- Extended structure of **33 s**hown down the *a*-axis. Colour code: Cu^{II} – turquoise, Gd^{III} – bright green, S – yellow, Cl – dark green, N – dark blue, C -grey, O – red, H atoms omitted for clarity.

Table S4.6- Pertinent bond lengths and bond angles and Mn BVS values for **34**.

Mn1 / Å		**Mn2 / Å**	
Mn1-O1 ($OR_{TBC[4]}$)	1.921(5)	Mn2-O5 ($OR_{TBC[4]}$)	1.926(4)
Mn1-O2 ($OR_{TBC[4]}$)	1.923(5)	Mn2-O5' ($OR_{TBC[4]}$)	1.926(4)
Mn1-O3 ($OR_{TBC[4]}$)	1.931(4)	Mn2-O6 ($OR_{TBC[4]}$)	1.926(4)
Mn1-O4 ($OR_{TBC[4]}$)	1.926(5)	Mn2-O6' ($OR_{TBC[4]}$)	1.926(4)
Mn1-O7 (O_{CO3})*	2.151(6)	Mn2-O9 (O_{CO3})*	2.186(6)
Mn1-O8 (O_{CO3})*	2.210(6)	Mn2-O9' (O_{CO3})*	2.186(6)
BVS(Mn1) = 3.203		BVS(Mn2) = 3.186	
Na1 / Å		**Na2 / Å**	
Na1-O1 ($OR_{TBC[4]}$)	2.310(4)	Na2-O4 ($OR_{TBC[4]}$)	2.315(4)
Na1-O2 ($OR_{TBC[4]}$)	2.298(4)	Na2-O6 ($OR_{TBC[4]}$)	2.287(4)
Na1-O7 (O_{CO3})*	2.472(7)	Na2-O8 (O_{CO3})*	2.432(7)
Na1-O7' (O_{CO3})*	2.472(7)	Na2-O9 (O_{CO3})*	2.462(7)
Na1-O10 (O_{dmso})	2.246(4)	Na2-O11 (O_{dmso})*	2.58(2)
Na1-O11 (O_{dmso})*	2.438(19)	Na2-O12 (O_{dmso})	2.220(7)
Na1-Cl1 (Cl)*	2.720(7)	Na2-Cl1 (Cl)*	2.628(9)
Na3 / Å		**-**	
Na3-O3 ($OR_{TBC[4]}$)	2.307(4)	-	-
Na3-O5 ($OR_{TBC[4]}$)	2.290(4)	-	-
Na3-O8 (O_{CO3})*	2.490(6)	-	-
Na3-O9 (O_{CO3})*	2.433(6)	-	-
Na3-O11 (O_{dmso})*	2.452(19)	-	-
Na3-O13 (O_{dmso})	2.271(5)	-	-
Na3-Cl1 (Cl)*	2.692(7)	-	-
Mn-O-Na / °			
Mn1-O1-Na1	109.8(2)	Mn1-O8*-Na3	98.1(2)
Mn1-O7*-Na1	97.8(2)	Mn2-O6-Na2	112.84(18)
Mn1-O2-Na1	111.3(2)	Mn2-O9*-Na2	97.9(2)
Mn1-O4-Na2	112.5(2)	Mn2-O5-Na3	111.32(19)
Mn1-O8*-Na2	99.0(3)	Mn2-O9*-Na3	97.9(2)

*Denotes atoms with half-occupancy.

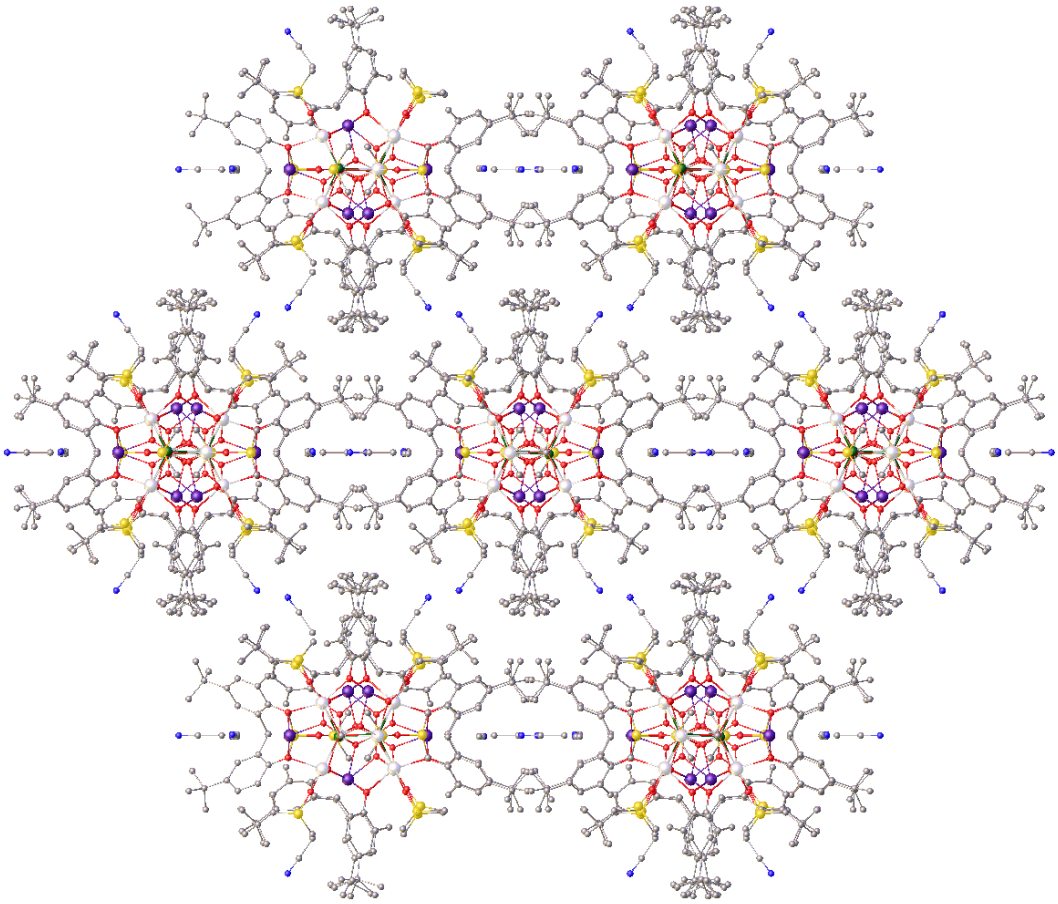

Figure S4.5- Extended structure of **34 s**hown down the *c*-axis. Colour code: Mn^{III} – dark purple, Na – white, S – yellow, Cl – dark green, N – dark blue, C – grey, O – red. H atoms omitted for clarity.

Table S4.7- Pertinent bond lengths and bond angles and Mn BVS values for **35**.

Mn1 / Å		**Mn2 / Å**	
Mn1-O1 (OR_L)	1.901(5)	Mn2-O5 (OR_L)	1.911(5)
Mn1-O2 (OR_L)	1.956(5)	Mn2-O6 (OR_L)	1.925(5)
Mn1-O3 (OR_L)	2.001(4)	Mn2-O7 (OR_L)	1.957(5)
Mn1-O4 (OR_L)	1.918(5)	Mn2-O8 (OR_L)	1.921(5)
Mn1-O11* (O_{CO3})	2.078(4)	Mn2-O9* (O)	2.071(8)
Mn1-O13* (O)	2.315(9)	Mn2-O10* (O_{CO3})	2.154(5)
BVS(Mn1) = 3.092		BVS(Mn2) = 3.316	
Mn3 / Å		**Na1 / Å**	
Mn3-O3 (OR_L)	2.138(4)	Na1-O1 (OR_L)	2.545(5)
Mn3-O7 (OR_L)	2.133(3)	Na1-O8 (OR_L)	2.325(4)
Mn3-O10* (O_{CO3})	2.154(5)	Na1-O9* (O)	2.340(5)
Mn3-O13* (O)	2.188(12)	Na1-O10* (O_{CO3})	2.977(6)
Mn3-O17 (O_{dmf})	2.130(5)	Na1-O11* (O_{CO3})	2.465(5)
-	-	Na1-O12* (O_{CO3})	2.422(4)
-	-	Na1-O19 (O_{dmf})	2.384(7)
BVS(Mn3) = 1.900		Na1-Cl1 (Cl)	3.034(3)
Na2 / Å		**Na3 / Å**	
Na2-O2 (OR_L)	2.385(5)	Na3-O4 (OR_L)	2.434(4)
Na2-O6 (OR_L)	2.386(5)	Na3-O5 (OR_L)	2.381(4)
Na2-O12* (O_{CO3})	2.409(4)	Na3-O9* (O)	2.496(11)
Na2-O14 (O_{dmf})	2.313(7)	Na3-O11* (O_{CO3})	2.374(5)
Na2-O15* (OEt)	2.38(1)	Na3-O12* (O_{CO3})	2.416(4)
Na2-O16* (OEt)	2.41(2)	Na3-O13* (O)	3.009(12)
-	-	Na3-O18 (O_{dmf})	2.389(7)
-	-	Na3-Cl1 (Cl)	2.946(2)
Mn-O-Mn / °			
Mn1-O3-Mn3	117.620	Mn2-O7-Mn3	108.67(18)
Mn1-O13*-Mn3	103.715	Mn2-O10*-Mn3	101.0(2)

*Denotes atoms with partial occupancy.

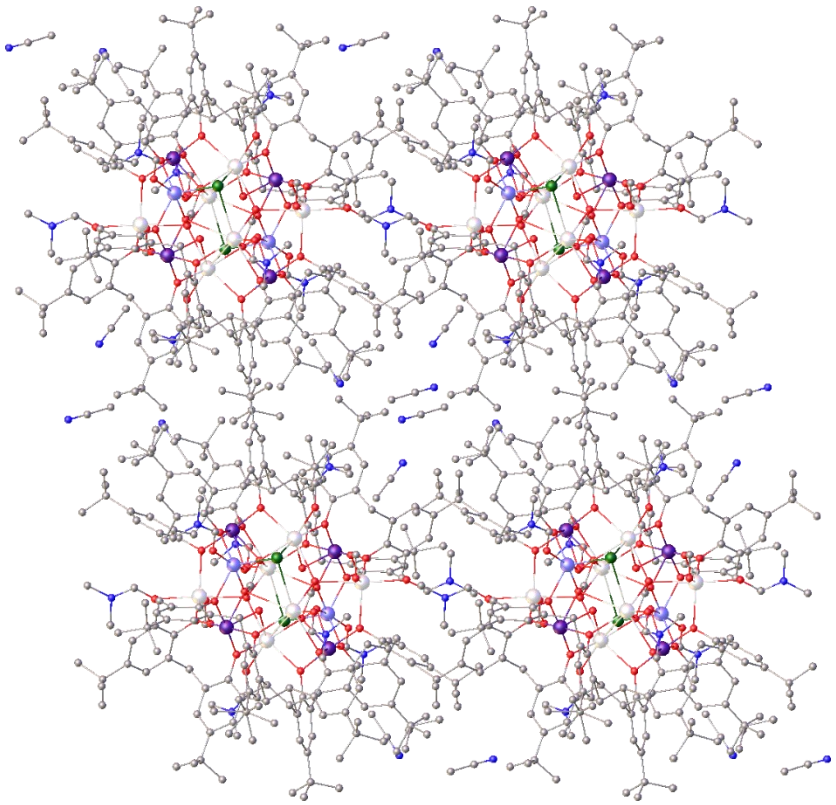

Figure S4.6- Extended structure of **35 s**hown down the *a*-axis. Colour code: Mn^{III} – dark purple, Mn^{II} – light purple, Na – white, Cl – dark green, N – dark blue, C -grey, O – red. H atoms omitted for clarity.

Table S4.8- Pertinent bond lengths and bond angles and Fe BVS values for **36**.

Fe1 / Å		**Fe2 / Å**	
Fe1-O1 ($OR_{TBC[4]}$)	2.016(18)	Fe2-O1 ($OR_{TBC[4]}$)	2.001(19)
Fe1-O2 ($OR_{TBC[4]}$)	1.988(12)	Fe2-O3 ($OR_{TBC[4]}$)	2.026(19)
Fe1-O2^{1} ($OR_{TBC[4]}$)	1.988(12)	Fe2-O1O (O)	2.088(16)
Fe1-O3 ($OR_{TBC[4]}$)	2.012(18)	Fe2-O1O^{2} (O)	2.088(16)
Fe1-O1O (O)	1.996(18)	Fe2-O3O (O)	1.951(11)
Fe1-O2D (O_{dmf})	2.00(2)	Fe2-O3O^{1} (O)	1.951(11)
BVS(Fe1) = 3.129		BVS(Fe2) = 3.018	
Fe3 / Å		**Fe4 / Å**	
Fe3-O2 ($OR_{TBC[4]}$)	1.983(14)	Fe4-O2O	2.01(2)
Fe3-O1O (O)	2.272(4)	Fe4-O1H	2.029(15)
Fe3-O2O (O)	2.125(4)	Fe4-O1H^{3}	2.029(15)
Fe3-O3O (O)	1.933(12)	Fe4-O1H^{4}	2.029(15)
Fe3-O3O’ (O)	1.933(12)	Fe4-O1H^{5}	2.029(15)
Fe3-O1H (OH)	2.023(15)	Fe4-O2W	2.321(2)
BVS(Fe3) = 2.907		BVS(Fe4) = 2.615	
Fe-O-Fe / °			
Fe1-O1-Fe2	98.9(7)	Fe3-O2O-Fe3^{4}	89.18(13)
Fe1-O3-Fe2^{3}	96.8(8)	Fe3^{4}-O2O-Fe3^{5}	89.18(13)
Fe1-O1O-Fe2	96.6(7)	Fe3^{3}-O2O-Fe3^{5}	116.3(11)
Fe1-O1O-Fe2^{3}	95.5(7)	Fe3-O2O-Fe3^{4}	116.3(11)
Fe1-O2-Fe3	104.7(6)	Fe3-O2O-Fe3^{5}	89.19(13)
Fe1-O1O-Fe3^{1}	94.7(4)	Fe3-O3O-Fe3^{5}	101.5(6)
Fe2^{3}-O1O-Fe3^{1}	89.4(4)	Fe3^{5}-O3O-Fe2	104.7(5)
Fe2-O3O-Fe3	104.7(5)	Fe3-O1H-Fe4	99.7(7)
Fe2-O1O-Fe2^{3}	167.9(10)	Fe4-O2O-Fe3^{3}	96.9(5)
Fe2-O1O-Fe3^{1}	89.6(4)	Fe4-O2O-Fe3^{4}	96.9(5)
Fe3-O1O-Fe3^{1}	170.7(9)	Fe4-O2O-Fe3^{5}	96.9(5)
Fe3-O2O-Fe3^{3}	89.18(13)	Fe4-O2O-Fe3	96.9(5)

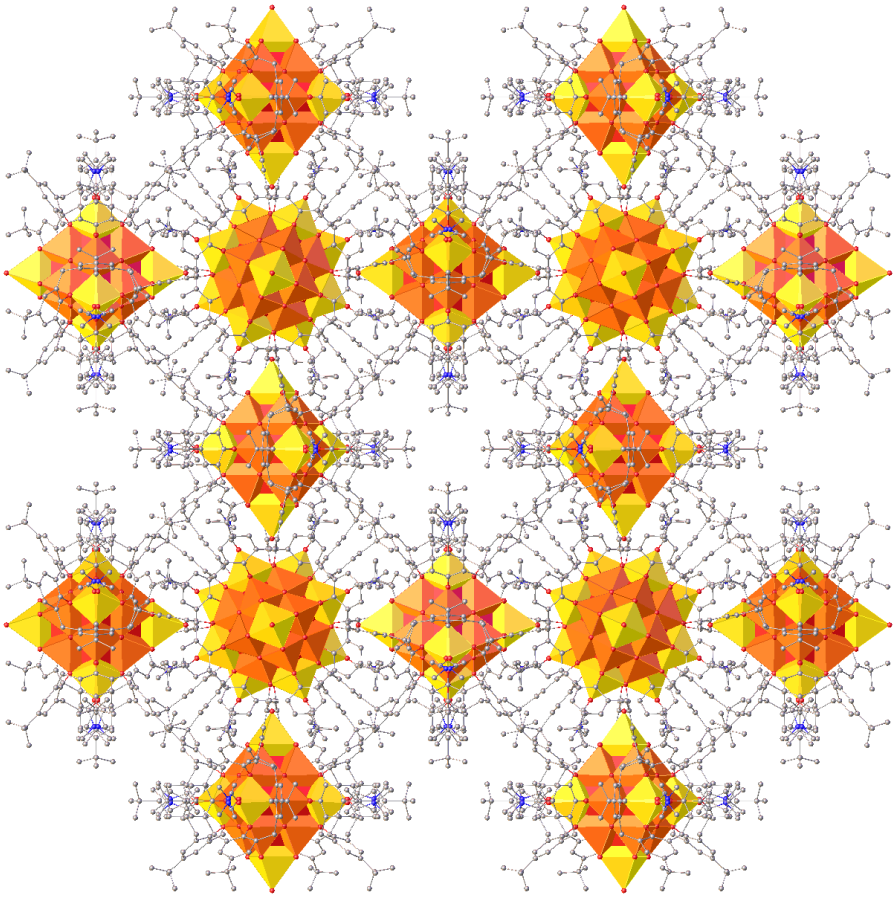

Figure S4.7- Extended structure of **36 s**hown down the *a*-axis highlighting the octahedral arrangement of clusters. Metal ions are shown in polyhedral format, the rest of the atoms in ball and stick. Colour code: Fe^{III} (octahedron)– yellow, Fe^{III} (cuboctahedron) – orange, N – dark blue, C – grey, O – red. H atoms omitted for clarity.

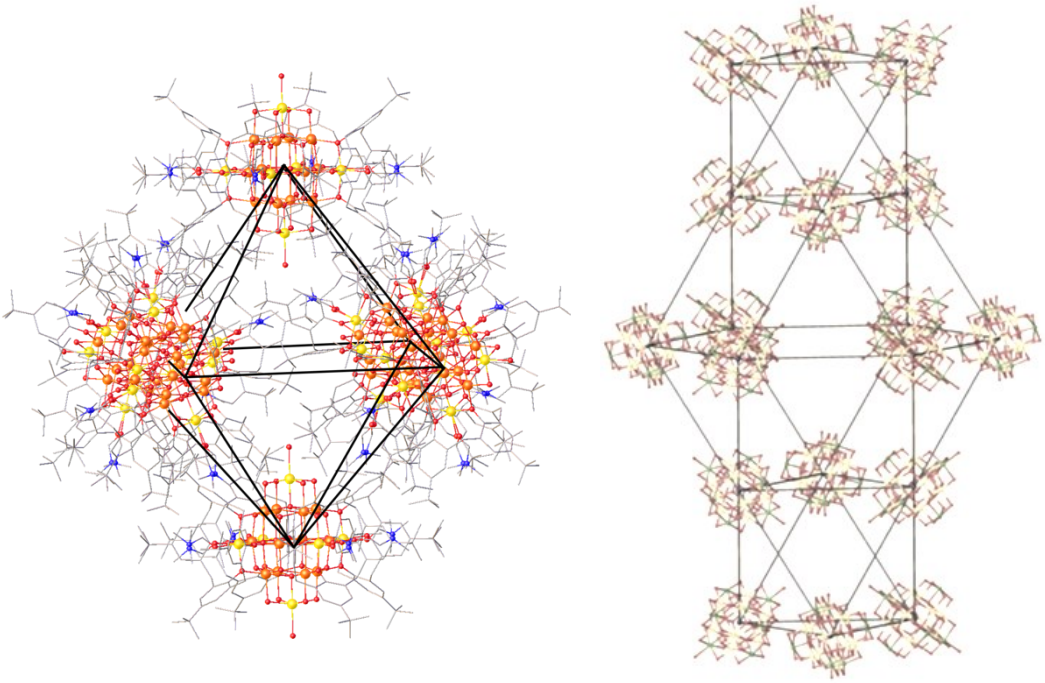

Figure S4.8- Packing diagrams of **36**, displaying an octahedral arrangement (left) and the alternating network of octahedra and cuboctahedra (right) in the extended structure. Colour code: Fe^{III} (octahedron)– yellow, Fe^{III} (cuboctahedron) – orange, N – dark blue, C – grey, O – red. H atoms omitted for clarity.

Table S4.9- Pertinent bond lengths and bond angles and Fe BVS values for **37**.

Fe1 / Å		**Fe2 / Å**	
Fe1-O8 (O)	1.983(2)	Fe2-O7 ($OR_{TBC[4]}$)	2.072(2)
Fe1-O8^{1} (O)	1.975(2)	Fe2-O9 (O)	1.9637(19)
Fe1-O10 (O)	2.0856(18)	Fe2-O9^{2} (O)	1.9638(19)
Fe1-O101 ($O_{dmc/f}$)	1.999(2)	Fe2-O13^{3} (O)	2.113(2)
Fe1-O1E^{1} (OEt)	2.018(2)	Fe2-O15^{3} (O)	2.039(3)
Fe1-O2E (OEt)	2.034(2)	Fe2-O3E (OEt)	1.964(2)
BVS(Fe1) = 3.012		BVS(Fe2) = 3.007	
Fe3 / Å		**Fe4 / Å**	
Fe3-O2 ($OR_{TBC[4]}$)	2.091(2)	Fe4-O4	1.983(10)
Fe3-O11 (O)	1.9615(17)	Fe4-O9	1.9572(19)
Fe3-O11^{2} (O)	1.9614(17)	Fe4-O10	2.0371(16)
Fe3-O13^{3} (O)	2.109(2)	Fe4-O12^{1}	1.9463(18)
Fe3-O14 (O)	2.031(2)	Fe4-O15^{3}	2.2323(5)
Fe3-O3E (OEt)	1.964(2)	Fe4-O2E	1.963(2)
BVS(Fe3) = 3.007		BVS(Fe4) = 3.060	
Fe5 / Å		**Fe6 / Å**	
Fe5-O1^{2} ($OR_{TBC[4]}$)	2.0265(19)	Fe6-O4 ($OR_{TBC[4]}$)	1.983(10)
Fe5-O10^{1} (O)	2.0404(18)	Fe6-O5 ($OR_{TBC[4]}$)	2.017(3)
Fe5-O11 (O)	1.9548(16)	Fe6-O6 ($OR_{TBC[4]}$)	1.979(10)
Fe5-O12 (O)	1.94779(17)	Fe6-O7 ($OR_{TBC[4]}$)	1.999(3)
Fe5-O14 (O)	2.2243(5)	Fe6-O15 (O)	1.990(2)
Fe5-O1E (OEt)	1.966(2)	Fe6-O1D (O_{dmf})	2.033(3)
BVS(Fe5) = 3.003		BVS(Fe6) = 3.131	
Fe7 / Å		**Fe8 / Å**	
Fe7-O3 ($OR_{TBC[4]}$)	1.991(3)	Fe8-O1 ($OR_{TBC[4]}$)	1.9855(18)
Fe7-O5 ($OR_{TBC[4]}$)	1.993(3)	Fe8-O1^{2} ($OR_{TBC[4]}$)	1.9854(18)
Fe7-O12 (O)	1.8871(19)	Fe8-O2 ($OR_{TBC[4]}$)	1.970(2)
Fe7-O12^{2} (O)	1.8871(19)	Fe8-O3 ($OR_{TBC[4]}$)	1.994(2)
Fe7-O14 (O)	2.242(2)	Fe8-O14 (O)	1.993(3)
Fe7-O15 (O)	2.229(3)	Fe8-O2D (O_{dmf})	2.016(3)

BVS(Fe7) = 3.032		BVS(Fe8) = 3.210	
Fe9 / Å		**Fe10 / Å**	
Fe9-O8 (O)	1.855(2)	Fe10-O10	1.8711(17)
Fe9-O9 (O)	1.8538(19)	Fe10-O10[1]	1.8710(17)
Fe9-O11 (O)	1.8515(17)	Fe10-O13	1.9610(16)
Fe9-Cl1 (Cl)	2.2346(8)	Fe10-O13[3]	1.9610(16)
BVS(Fe9) = 2.601		BVS(Fe10) = 2.636	
Fe-O-Fe / °			
Fe1-O8-Fe1[1]	91.942	Fe3[2]-O13-Fe10[2]	121.69(8)
Fe1-O8[1]-Fe[1]	91.942	Fe4[1]-O15-Fe4[2]	90.35(7)
Fe1-O10-Fe4	94.84(7)	Fe4[1]-O15-Fe4[2]	167.66(11)
Fe1-O2E-Fe4	98.84(8)	Fe4[1]-O12-Fe5	101.98(8)
Fe1-O10-Fe5	95.156	Fe4-O10-Fe5[1]	95.81(7)
Fe1-O1E-Fe5	99.71(8)	Fe4[2]-O15-Fe6	96.03(6)
Fe1-O8-Fe9	129.22(11)	Fe4[1]-O12-Fe7	108.31(9)
Fe1-O8[1]-Fe9[1]	127.720	Fe4[2]-O15-Fe7	88.29(7)
Fe1-O10-Fe10	114.60(9)	Fe4[1]-O15-Fe7	88.29(7)
Fe2-O3E-Fe3	98.31(10)	Fe4-O9-Fe9	125.12(10)
Fe2[2]-O13-Fe3[2]	89.87(8)	Fe4-O10-Fe10	124.41(9)
Fe2-O9-Fe4	101.32(9)	Fe5-O14-Fe5[3]	167.49(13)
Fe2[2]-O15-Fe4[1]	90.35(7)	Fe5-O12-Fe7	108.16(8)
Fe2[2]-O15-Fe6	99.03(10)	Fe5[3]-O14-Fe7	88.10(5)
Fe2[2]-O15-Fe7	167.19(11)	Fe5-O14-Fe7	88.11(5)
Fe2[2]-O15-Fe7	167.19(11)	Fe5-O14-Fe8	96.07(6)
Fe2-O9-Fe9	124.96(10)	Fe5[3]-O14-Fe8	96.07(6)
Fe2[2]-O13-Fe10[2]	121.09(8)	Fe5[3]-O1-Fe8	102.98(8)
Fe3-O11-Fe5	101.10(7)	Fe5-O11-Fe9	124.85(9)
Fe3-O14-Fe5	90.46(6)	Fe5[1]-O10-Fe10	124.82(8)
Fe3-O14-Fe5[3]	90.46(6)	Fe6-O5-Fe7	100.54(14)
Fe3-O14-Fe7	166.52(13)	Fe6-O15-Fe7	93.78(10)
Fe3-O2-Fe8	98.32(10)	Fe7-O3-Fe8	102.11(11)
Fe3-O14-Fe8	99.60(10)	Fe7-O14-Fe8	93.88(9)
Fe3-O11-Fe9	125.01(9)	Fe10-O13-Fe10[2]	85.25(9)

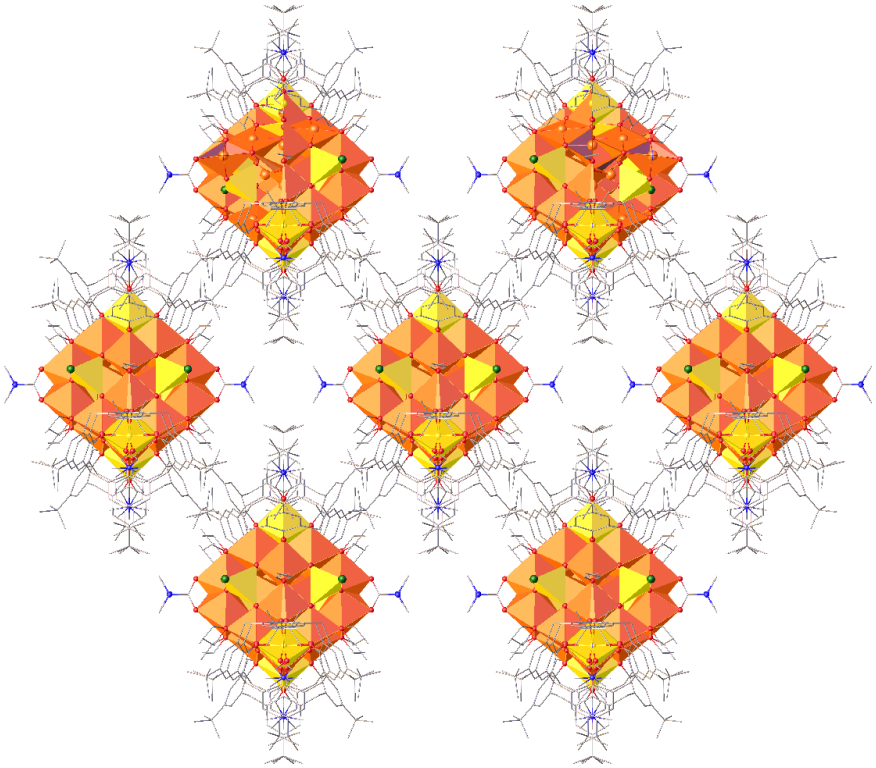

Figure S4.9- Extended structure of **37 s**hown down the *a*-axis. Metal ions are shown in polyhedral format, the rest of the atoms in ball and stick. Colour code: orange – Fe^{III} ions in the main unit, yellow – Fe^{III} ions capping the hexagonal/squares faces, Cl – dark green, N – dark blue, C – grey, O – red. H atoms omitted for clarity.

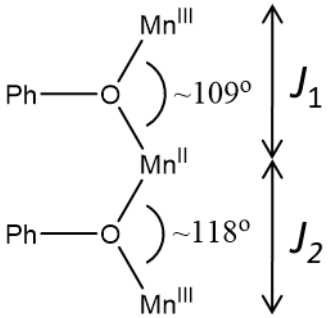

Figure S4.10- Model of the magnetic exchange interaction scheme used to simultaneously fit the susceptibility and magnetisation data for complex **35**.

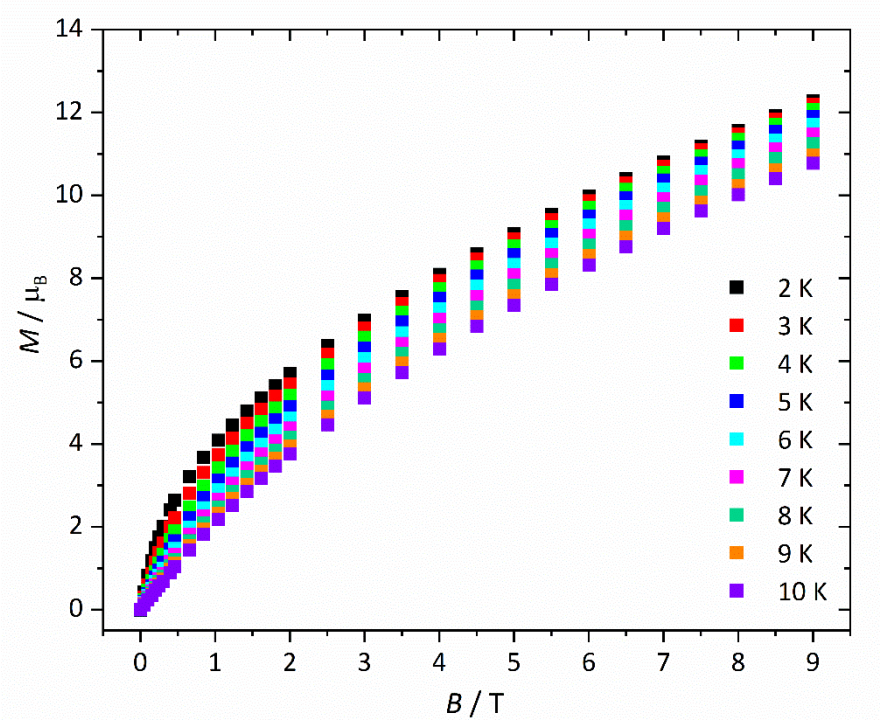

Figure S4.11- Variable-temperature-variable-field magnetisation measurements of **36** measured between T = 2-10 K and B = 0-9 T.

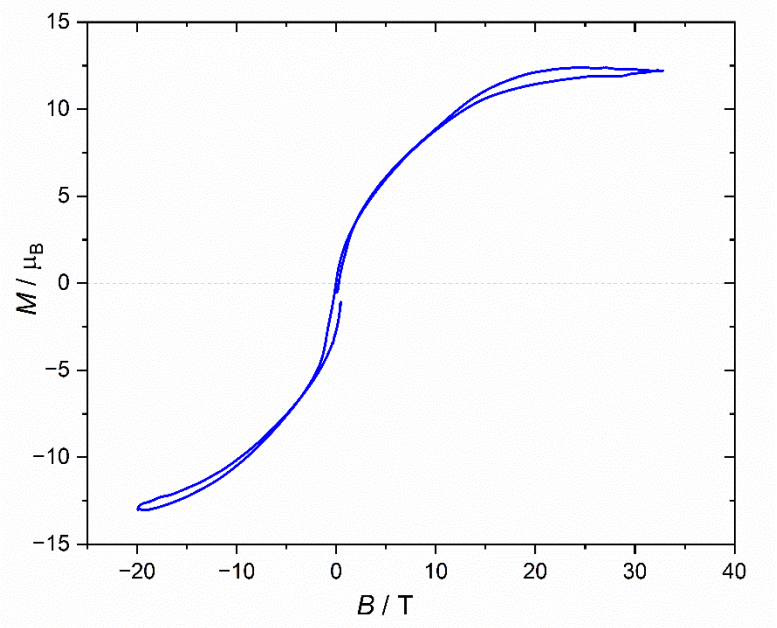

Figure S4.12- Low-temperature high-field magnetisation measurements of **36** performed at T = 0.4 K with fields up to 32.5 T, as discussed in main text.

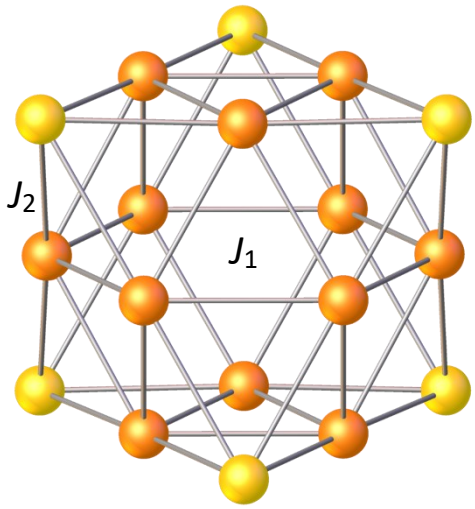

Figure S4.13- The exchange coupling model used to simulate the data of complex **36**, where J_1 represents exchange along the edges of the cuboctahedron (orange) and J_2 represents exchange along the edges of the square pyramids (yellow).

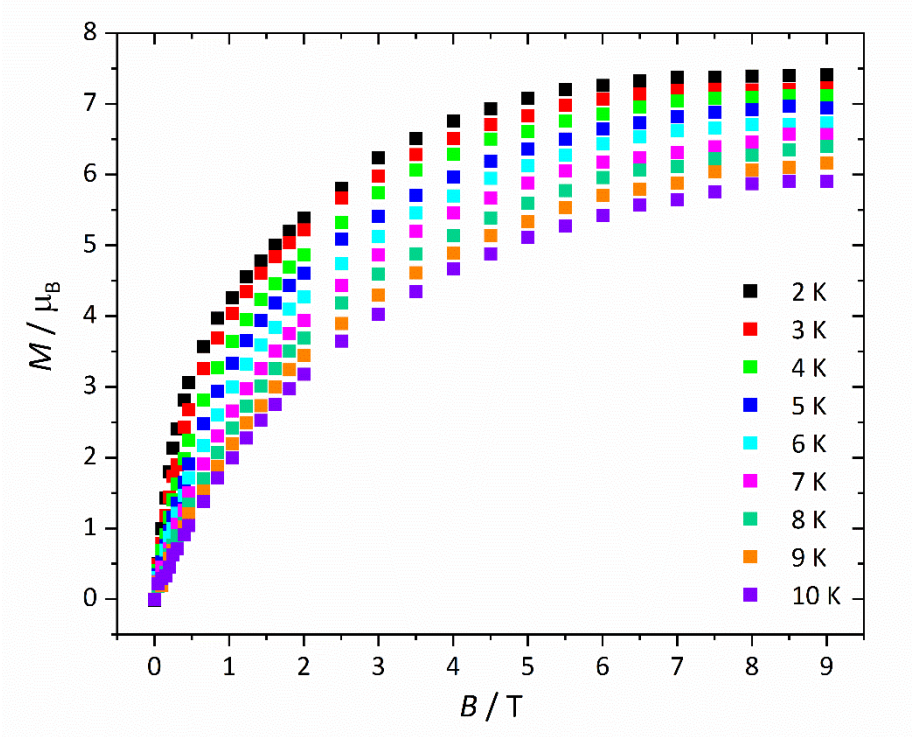

Figure S4.14- Variable-temperature-variable-field magnetisation measurements of **37** measured between T = 2-10 K and B = 0-9 T.